

EXPERIMENTAL AERODYNAMIC AND
STATIC ELASTIC DEFORMATION CHARACTERIZATION OF
LOW ASPECT RATIO FLEXIBLE FIXED WINGS
APPLIED TO MICRO AERIAL VEHICLES

By

ROBERTO ALBERTANI

A DISSERTATION PRESENTED TO THE GRADUATE SCHOOL
OF THE UNIVERSITY OF FLORIDA IN PARTIAL FULFILLMENT
OF THE REQUIREMENTS FOR THE DEGREE OF
DOCTOR OF PHILOSOPHY

UNIVERSITY OF FLORIDA

2005

ACKNOWLEDGMENTS

I would like to thank my advisor, Dr. Peter Ifju, for his support and friendship. I am grateful to Dr. Paul Hubner for his mentoring and to Dr. Bruce Carroll, Dr. R. Lind and Dr. D. O. Wu for their help.

Particular thanks go to Dr. N. Cristescu, and all my professors, for their encouragement and wonderful teaching. The author wishes also to acknowledge the technical contributions of Martin Waszak at the NASA Langley Research Center as well as funding. Furthermore I would like to thank AFOSR and AFRL at Eglin AFB for sponsorship.

Finally, and most importantly, I wish to thank my loved ones, who encouraged me throughout my career at the University. I thank them for their patience and support.

TABLE OF CONTENTS

	<u>page</u>
ACKNOWLEDGMENTS	ii
LIST OF TABLES	vii
LIST OF FIGURES.....	viii
ABSTRACT.....	xxii
CHAPTER	
1 INTRODUCTION.....	1
1.1 Motivation for this Research	4
1.2 Scope of the Present Research.....	7
1.2.1 Literature Survey.....	7
1.2.2 Development of the Experimental Apparatus and Techniques	7
1.2.3 Discussion of Aerodynamic Results	8
1.2.4 Application of Wind Tunnel Results to Aerodynamic Modeling.....	9
2 LITERATURE SURVEY.....	10
2.1 Aerodynamics Of LAR Rigid Wings At LRN	10
2.2 Aerodynamics Of LAR Flexible Wings At LRN	14
2.3 Considerations On Propulsion For MAVs	20
2.4 Aerodynamic Analytical Models.....	23
2.5 Static Elastic Deformations Of Flexible Wings	27
3 EXPERIMENTAL APPARATUS AND TESTS PROCEDURES	35
3.1 Description of the Models	35
3.1.1 Wings.....	36
3.1.1.1 Description.....	36
3.1.1.2 Fabrication.....	44
3.1.2 Complete Aerial Vehicles.....	46
3.2 Aerodynamic Coefficients.....	48
3.2.1 The Wind Tunnel	48
3.2.1.1 The open circuit wind tunnel	49
3.2.1.2 The close circuit wind tunnel.....	49

3.2.1.3	The sting balance and related hardware	52
3.2.2	The Signal Conditioning System and the Data Acquisition System.....	54
3.2.3	Sting Balance Set-Up	55
3.2.3.1	Data acquisition	55
3.2.3.2	Calibrations.....	55
3.2.4	Experimental Procedures.....	58
3.2.4.1	Computation of non-dimensional coefficients	59
3.2.4.2	Validation runs.....	62
3.2.4.3	Test procedures without propeller	64
3.2.4.4	Test procedures with powered propeller	65
3.2.5	Measurement Uncertainties	67
3.2.6	Wind Tunnel Corrections	69
3.3	Structural Deformation: Visual Image Correlation (VIC)	70
3.3.1	Introduction.....	70
3.3.2	The Principle of VIC	70
3.3.3	VIC Technique.....	72
3.3.3.1	Hardware and data acquisition system.....	72
3.3.3.2	Image processing	76
3.3.3.3	Calibrations.....	80
3.3.4	Experimental Procedures.....	81
3.3.4.1	Tests procedures without propeller.....	82
3.3.4.2	Tests procedures with powered propeller.....	84
3.3.4.3	Data post processing	86
3.3.5	Measurement Uncertainties	91
3.3.6	Wind Tunnel Corrections	92
4	EXPERIMENTAL RESULTS AND DISCUSSION.....	94
4.1	Introduction And General Observations	94
4.2	Static Elastic Deformation Of Wings.....	95
4.2.1	Global Change of Geometry	96
4.2.2	Displacement and Strains Fields.....	100
4.2.3	Camber	104
4.2.4	Geometric Wing Twist	107
4.3	Static Elastic Deformation Of Wings On MAV	112
4.3.1	Propeller Effects on the Geometry of the Wings.....	112
4.4	Aerodynamics Of Wings.....	119
4.4.1	Lift Curve Characteristics.....	119
4.4.2	Maximum Lift.....	121
4.4.3	L/D Characteristics.....	124
4.4.4	Pitching Moment Characteristics.....	125
4.4.5	Aerodynamic Center	127
4.4.6	Effects of Reynolds Number.....	131
4.5	Aerodynamics Of MAVs.....	133
4.5.1	Lift Curve Characteristics.....	133
4.5.2	Drag Characteristics	139
4.5.3	Pitching Moment Characteristics.....	146

4.5.4	Propeller Speed	151
4.5.5	Uninstalled Propeller Thrust and Power.....	154
4.6	Summary Of Results	158
4.6.1	Lift and Drag Characteristics of Wings.....	158
4.6.2	Lift and Drag Characteristics of MAVs	160
4.6.3	Pitching Moment Characteristics of Wings.....	162
4.6.4	Pitching Moment Characteristics of MAV	163
4.6.5	Elastic Deformation Results of Wings	164
4.6.6	Combining the Aerodynamic Result with the Elastic Deformation Results	166
4.6.7	Considerations on Propulsion	167
5	ANALYTICAL MODELS FROM WIND TUNNEL RESULTS	169
5.1	Introduction	169
5.1.1	Model Structure Determination	169
5.1.2	Propulsion Model.....	175
5.1.3	Aerodynamic Model.....	180
5.1.4	A Sample Application of the Models.....	185
5.2	Conclusions	187
6	SUMMARY AND RECOMMENDATIONS.....	189
APPENDIX		
A	EXPERIMENTAL DATA CORRECTIONS	194
A.1	Wind Tunnel Corrections	194
A.1.1	Solid Blockage	194
A.1.2	Wake Blockage	195
A.1.3	Streamline Curvature.....	196
A.1.4	Corrections to Measured Parameters.....	196
A.2	Structure Flexibility Corrections	198
A.2.1	Test Procedure and Preliminary Data Reduction	199
A.2.2	Data Analysis and Results	203
A.2.3	Final Correction of the Nominal AOA	206
B	UNCERTAINTY ANALYSIS	209
B.1	Wind Tunnel Measurements.....	209
B.1.1	Wind Tunnel Check Runs.....	209
B.1.2	Uncertainty Analysis	212
B.2	Visual Image Correlation	220
B.2.1	Theoretical Accuracy	220
B.2.2	Experimental Set-up.....	222
B.2.3	Experimental Results.....	223
B.2.4	Error Analyses	225

C	AERODYNAMIC AND PROPULSION RESULTS	231
C.1	Aerodynamic Results: Wings at Constant Flexibility.....	232
C.2	Aerodynamic Results: Wings at Constant Dynamic Pressure.....	241
C.3	Propeller Speed.....	250
C.4	MAV without Propeller.....	258
C.5	MAV with Propeller.....	265
C.6	Wings Arranged by Structural Design	275
C.6.1	Batten Reinforced Wings.....	276
C.6.2	Perimeter Reinforced Wings.....	280
D	WINGS' STATIC ELASTIC DEFORMATION RESULTS	285
D.1	Batten Reinforced Wings	286
D.2	Perimeter Reinforced Wings	293
E	SYMBOLS.....	302
E.1	English Symbols	302
E.2	Greek Symbols.....	305
E.3	Acronyms	306
E.4	Subscripts and superscripts.....	308
	LIST OF REFERENCES.....	309
	BIOGRAPHICAL SKETCH	317

LIST OF TABLES

<u>Table</u>	<u>page</u>
3-1. A brief description of the three basic wing structures tested.....	40
3-2. Table with a brief description of the wings tested in this work. The overall dimensions, airfoil shape and wing planform were the same.....	41
3-3. Table with a description of the complete aerial models subject of the analysis in this work.....	47
3-4. Sting balance rated loads	52
4-1. Table with summary of wings' characteristics and their designation.....	95
4-2. Table with a brief description of all the wings tested in this work. The overall dimensions, airfoil shape and wing planform were the same.....	95
B-1. Comparison of geometrical characteristics of flat plate models.....	210
C-1. Table with summary of wings' characteristics and their designation.....	232

LIST OF FIGURES

<u>Figure</u>	<u>page</u>
1-1. A typical MAV with carbon fiber structure and latex thin membrane wing skin.....	2
1-2. A typical 150 mm wingspan MAV with the characteristic flexible wing.....	3
3-1. Planform view of the wing and airfoil shape used in all the tests presented in this work.....	36
3-2. The structure's configurations of the wing tested.....	40
3-3. BR (batten reinforced) wing after demolding, on the left, and with spray paint applied, on the right.....	44
3-4. BR (batten reinforced) wing ready for the application of the latex skin.....	45
3-5. BR (batten reinforced) wing after the final application of the randomly speckled latex skin.....	46
3-6. A typical complete aerial vehicle equipped for tests in the wind tunnel.....	48
3-7. The open circuit wind tunnel.....	50
3-8. The closed circuit wind tunnel.....	51
3-9. A vehicle in the wind tunnel, mounted on the sting balance and on the aluminum pitching arm.....	53
3-10. Instrumentation and signal processing set-up installed on the side of the wind tunnel.....	54
3-11. Signals from the sting balance during calibration runs.....	58
3-12. Signals from the sting balance during calibration runs.....	58
3-13. Signals from the sting balance during calibration runs.....	59
3-14. Results for the drag of a sphere at the University of Florida wind tunnel compared with results from some publications.....	63

3-15. Results for flat plates at the University of Florida wind tunnel compared with results from Ref. [11].	64
3-16. Flow chart of a typical wind tunnel test procedure for a vehicle without a powered propeller.	65
3-17. Flow chart of a typical wind tunnel test procedure for a vehicle with a powered propeller.....	66
3-18. Uncertainties bounds for the coefficient of lift, at a free stream Reynolds number of 115,000.	68
3-19. Uncertainties bounds for the coefficient of drag, at a free stream Reynolds number of 115,000	68
3-20. Uncertainties bounds for the coefficient of pitching moment, at a free stream Reynolds number of 115,000.....	69
3-21. Measurement of displacements of object points on the specimen’s surface.	71
3-22. VIC system set-up for two-dimensional measurements (in-plane displacements and strains).....	73
3-23. VIC system set-up for three-dimensional measurements (out-of-plane displacements and strains).....	74
3-24. View from the top of the wind tunnel, showing the installation of the two cameras.....	74
3-25. View of the side of the wind tunnel, showing the installation of the two cameras on the aluminum frame.....	75
3-26. Lay-out of the digital image correlation system in the configuration used in this work.....	76
3-27. A square subset used for cross correlation function estimation.....	77
3-28. Schematic of the pinhole model leading to the central perspective projection.....	77
3-29. Schematic illustration of the stereo-triangulation scheme.....	78
3-30. Schematic depiction of matching between two images acquired at the same time and tracking of two pairs of images acquired at different times (and possibly at two different load statuses).....	79
3-31. Schematic depiction of calibration images	81
3-32. Schematic view of the procedure for the digital image correlation tests in the wind tunnel.	83

3-33. Schematic view of the procedure for the digital image correlation tests in the wind tunnel.	85
3-34. A sample of the automatic output file from the VIC system.	87
3-35. A sample of the final output file from the VIC system.	87
3-36. Two sections of the MAV wing, at the centerline (bottom) and at 50 mm on the X axis (top).	90
3-37. The same sections of the MAV wing, at the centerline (bottom) and at 50 mm on the X axis (top).	90
3-38. Best fit of the experimental values of the latex membrane displacements versus x coordinates.	91
3-39. Change of the AOA due to rigid body rotation versus C_L at four wind tunnel free stream velocities for a typical PR wing.	93
4-1. MAV wing type BR. The image shows the un-deformed structure reference image obtained by VIC at AOA=20, with no airflow.	97
4-2. MAV wing type BR. The view represents the deformed structure image for the VIC processing at AOA=20, at a free stream velocity of 13 m/s.	97
4-3. MAV wing type PR. The image shows the un-deformed structure obtained by VIC at AOA=22 degrees, with no airflow in the wind tunnel.	98
4-4. MAV wing type PR. The image shows the deformed structure obtained by VIC at AOA=22 degrees, at a free stream velocity of 13 m/s.	98
4-5. MAV wing type PR. The image shows the un-deformed structure obtained by VIC at AOA=22 degrees, with no airflow in the wind tunnel.	99
4-6. MAV wing type PR. The image shows the deformed structure obtained by VIC at AOA=22 degrees, at a free stream velocity of 13 m/s.	99
4-7. Wing type BR02, AOA=20, at a velocity of 13 m/s.	101
4-8. Wing type BR05, AOA=20, at a velocity of 13 m/s.	102
4-9. Wing type BR09, AOA=20, at a velocity of 13 m/s.	102
4-10. w displacement field for wing type BR05 at AOA=12 degrees, at three free stream velocities, from left 8, 10 and 13 m/s.	103
4-11. w displacement field for wing type BR09 at AOA=12 degrees, at three free stream velocities, from left 8, 10 and 13 m/s.	103

4-12. Variation of the value of camber for wings BR05 and BR09, versus AOA.....	105
4-13. Variation of the value of camber for wings BR05 and BR09, versus the free stream dynamic pressure..	105
4-14. Variation of the position of camber for wings BR05 and BR09, versus AOA.....	106
4-15. Variation of the position of camber for wings BR05 and BR09, versus the free stream dynamic pressure at the constant AOA of 12 degrees.	106
4-16. Angle of incidence for Rigid wing. Data are collected using VIC at three different free stream velocities and at a constant AOA of 12 degrees.....	108
4-17. Angle of incidence for wing BR05. Data are collected using VIC at three different free stream velocities and at a constant AOA of 12 degrees.....	108
4-18. Angle of incidence for wing BR09. Data are collected using VIC at three different free stream velocities and at a constant AOA of 12 degrees.....	109
4-19. Angle of incidence for wing BR05. Data are collected using VIC at five different angles of attack and at a constant free stream velocity of 13 m/s.	110
4-20. Maximum angle of incidence for wing BR05. Data are collected using VIC at five different angles of attack and at a constant free stream velocity of 13 m/s....	110
4-21. Change of angle of incidence (geometric twist) for wing BR05..	111
4-22. Change of angle of incidence (geometric twist) for wing BR09.	112
4-23. Displacements in Z direction (w) for BR Wing at AOA= 4°, velocity = 8 m/s. ..	114
4-24. Displacements in Z direction (w) for PR Wing at AOA= 4°, velocity = 8 m/s....	115
4-25. Geometry of two wing sections placed symmetrically at x = +/- 50 mm from the MAV's center line.....	116
4-26. Volume displacements ratios versus AOA for BR wing.....	118
4-27. Volume displacements ratios versus AOA for PR wing.	118
4-28. Lift curve slope versus free stream velocity for four wings	120
4-29. Lift curve slope versus free stream velocity for four wings	120
4-30. Maximum lift coefficient versus free stream velocity for four wings.....	122
4-31. Angle of attack for maximum lift coefficient versus free stream velocity for four wings.	122

4-32. Maximum lift coefficient versus free stream velocity for four wings type R, PR04, PR07 and PR12.	123
4-33. Angle of attack for maximum lift coefficient versus free stream velocity for four wings type R, PR04, PR07 and PR12.	123
4-34. Maximum L/D versus free stream velocity for four wings.	124
4-35. Maximum L/D versus free stream velocity for four wings type R, PR04, PR07 and PR12.	125
4-36. Longitudinal moment derivative versus free stream velocity for four wings.	126
4-37. Longitudinal moment derivative versus free stream velocity for four wings.	127
4-38. Position of the aerodynamic center as a function of the Reynolds number, for four different wings (R, PR07, BR09 and PR12).	129
4-39. Position of the aerodynamic center as a function of the Reynolds number, for the rigid and four PR type wings.	130
4-40. Position of the aerodynamic center as a function of the Reynolds number, for the rigid and four BR type wings.	130
4-41. Coefficient of lift versus angle of attack for the Rigid type wing at different Reynolds numbers.	132
4-42. Coefficient of drag versus angle of attack for the Rigid type wing at different Reynolds numbers.	133
4-43. Coefficient of lift versus angle of attack for the Rigid type wing compared with the same wing mounted on a MAV fuselage at $V_\infty = 13$ m/s.	134
4-44. Coefficient of lift versus angle of attack for the PR07 type wing compared with the same wing mounted on a MAV fuselage at $V_\infty = 13$ m/s.	135
4-45. Coefficient of lift versus angle of attack for the BR09 type wing compared with the same wing mounted on a MAV fuselage at $V_\infty = 13$ m/s.	135
4-46. Difference in coefficient of lift, versus AOA, due to the contribution of the fuselage to the wings type R, PR07 and BR09, at $V_\infty = 13$ m/s.	136
4-47. Difference in coefficient of lift, versus AOA, due to the contribution of the fuselage to the wings type R, PR07 and BR09, at $V_\infty = 10$ m/s.	137
4-48. Plot of total lift coefficient versus AOA, at three different free stream dynamic pressures, for the Rigid type wing with the powered propeller on.	138

4-49. Plot of total lift coefficient versus AOA, at three different free stream dynamic pressures, for the BR09 type wing with the powered propeller on.....	139
4-50. Coefficient of lift, versus coefficient of drag, in the two cases with and without fuselage for wing type R, at $V_\infty = 13$ m/s.....	140
4-51. Coefficient of lift, versus coefficient of drag, in the two cases with and without fuselage for wing type PR07, at $V_\infty = 13$ m/s.....	140
4-52. Coefficient of lift, versus coefficient of drag, in the two cases with and without fuselage for wing type BR09, at $V_\infty = 13$ m/s.	141
4-53. Difference in coefficient of drag versus coefficient of lift, due to the contribution of the fuselage to the wings type R, PR07 and BR09, at $V_\infty = 13$ m/s.....	142
4-54. Difference in coefficient of drag versus coefficient of lift, due to the addition of the fuselage to the wings type R, PR07 and BR09, at $V_\infty = 10$ m/s.	142
4-55. Coefficient of drag versus coefficient of lift, for the MAVR with powered propeller, at $V_\infty = 10$ m/s for different voltage motor settings.....	143
4-56. Coefficient of drag versus coefficient of lift, for the MAVR with powered propeller, at $E = 7.4$ Volt for different free stream velocities.	144
4-57. Coefficient of drag versus coefficient of lift, for the MAVPR07 with powered propeller, at $V_\infty = 10$ m/s for different voltage motor settings.....	144
4-58. Coefficient of drag versus coefficient of lift, for the MAVPR07 with powered propeller, at $E = 7.4$ Volt for different free stream velocities	145
4-59. Coefficient of drag versus coefficient of lift, for the MAVBR09 with powered propeller, at $V_\infty = 10$ m/s for different voltage motor settings.....	145
4-60. Coefficient of drag versus coefficient of lift, for the MAVBR09 with powered propeller, at $E = 7.4$ Volt for different free stream velocities.	146
4-61. C_m versus C_L for Rigid wing and MAVR at $V_\infty = 13$ m/s.....	147
4-62. C_m versus C_L for PR07 wing and MAVPR07 at $V_\infty = 13$ m/s.....	147
4-63. C_m versus C_L for BR09 wing and MAVBR09 at $V_\infty = 13$ m/s.....	148
4-64. Pitching moment coefficient, at three different free stream dynamic pressures, for MAV with the BR09 type wing without propeller.....	149

4-65. Pitching moment coefficient, at three different free stream dynamic pressures, for MAV with the BR09 type wing with propeller.....	150
4-66. Propeller speed versus AOA, for three motor's power settings, at a free stream velocity of 11.5 m/s.....	152
4-67. Propeller speed versus AOA, for three motor's power settings, at a free stream velocity of 11.5 m/s.....	152
4-68. Propeller speed versus AOA, at three free stream velocities, for a motor's power setting of 7.0 Volt.....	153
4-69. Propeller speed versus AOA, at four free stream velocities, for a motor's power setting of 7.0 Volt.....	153
4-70. Isolated propeller thrust versus propeller speed for three wind tunnel flow velocities.....	155
4-71. Isolated propeller power versus propeller speed for three wind tunnel flow velocities.....	155
4-72. Coefficient of thrust versus advance ratio for the isolated propeller.	157
4-73. Coefficient of power versus advance ratio for the isolated propeller.....	157
5-1. Overfit penalty, mean squared error and predicted squared error for the C_L model with various numbers of terms.	173
5-2. Comparison between experimental and estimated data.....	174
5-3. Plot of experimental data of propeller speeds versus AOA at three different levels of free stream dynamic pressure.	176
5-4. Plot of propeller speeds versus AOA and free stream dynamic pressure at three different levels of motor settings	177
5-5. Plot of propeller coefficient of thrust versus propeller speed and free stream dynamic pressure, at three different levels of motor settings.....	179
5-6. Total lift coefficient versus AOA at constant free stream dynamic pressure and motor setting	182
5-7. Total lift coefficient versus AOA at constant free stream dynamic pressure and motor setting.....	183
5-8. Drag coefficient versus AOA at constant motor setting.....	184
5-9. Drag coefficient versus AOA at constant motor setting. The experimental values are at 11.5 m/s.....	184

5-10. Trimmed flight angle of attack versus load factor at constant motor setting..	186
5-11. Trimmed elevator angle deflection versus load factor at constant motor setting.	187
A-1. Test sequence for AOA correction tests.	200
A-2. Reference image, at nominal AOA and airflow off.	201
A-3. Image with wing under loads, at nominal AOA and airflow on.	201
A-4. Reference image, at nominal AOA and airflow off.	202
A-5. Image with wing under loads, at nominal AOA and airflow on.	202
A-6. Plot of the displacements w in the Z direction in two conditions: reference state with airflow off (squares, all zeros) and in loaded state (triangles).	203
A-7. Reference and rotated wing sections at a selected nominal AOA and dynamic pressure.	204
A-8. Change of the AOA due to the flexibility of the holding structure versus the nominal testing AOA for one PR wing (15004), at three free stream velocities...	205
A-9. Change of the AOA due to rigid body rotation versus C_L at four wind tunnel free stream velocities for a typical PR wing.	206
A-10. Change of the AOA due to rigid body rotation versus C_L at four wind tunnel free stream velocities for a typical BR wing.	207
B-1. Experimental lift coefficient versus AOA for flat plates.	210
B-2. Coefficient of lift versus coefficient of drag for flat plates.	211
B-3. Difference of coefficients of drag between the published data and the experimental data, in function of the coefficient of lift, for flat plates.	212
B-4. Uncertainties bounds for the coefficient of lift at a Re number of 89,000.	217
B-5. Uncertainties bounds for the coefficient of lift at a Re number of 115,000.	217
B-6. Uncertainties bounds for the coefficient of drag at a Re number of 89,000.	218
B-7. Uncertainties bounds for the coefficient of drag at a Re number of 115,000.	218
B-8. Uncertainties bounds for the coefficient of pitching moment at a Re number of 89,000.	219
B-9. Uncertainties bounds for the coefficient of pitching moment at a Re number of 115,000.	219

B-10. The bar with the spherical head positioned close to the latex membrane.....	223
B-11. The complete test apparatus with the micrometer, the ring with latex membrane and the VIC cameras.	224
B-12. Latex membrane shape as recorded and processed by the VIC system.....	225
B-13. Error in w_{max} for a specific commanded displacement for two cases with same speckle sizes but different cameras positions.	226
B-14. Error in measured w_{max} versus commanded displacements for two cases with same cameras positions but different speckle sizes	227
B-15. Latex membrane profile versus X coordinate.	228
B-16. Error in % measured w_{max} versus commanded displacements for the two cases of peak value from each experiment and the maximum of the fitted curve for the same experiments.	228
B-17. Best fit of the experimental values of the latex membrane displacements versus X coordinates.	230
C-1. C_L versus α for R01 (Rigid) wing at $V_\infty = 8, 10, 11.5$ and 13 m/s.	233
C-2. C_L versus C_D for R01 (Rigid) wing at $V_\infty = 8, 10, 11.5$ and 13 m/s.	233
C-3. L/D versus C_L for R01 (Rigid) wing at $V_\infty = 8, 10, 11.5$ and 13 m/s.....	234
C-4. C_m versus C_L for R01 (Rigid) wing at $V_\infty = 8, 10, 11.5$ and 13 m/s.	234
C-5. C_L versus α for wing PR07 at $V_\infty = 8, 10, 11.5$ and 11.5 m/s.....	235
C-6. C_L versus C_D for wing PR07 at $V_\infty = 8, 10, 11.5$ and 11.5 m/s.....	235
C-7. L/D versus C_L for wing PR07 at $V_\infty = 8, 10, 11.5$ and 11.5 m/s.....	236
C-8. C_m versus C_L for wing PR07 at $V_\infty = 8, 10, 11.5$ and 11.5 m/s.	236
C-9. C_L versus α for wing BR09 at $V_\infty = 8, 10, 11.5$ and 10 m/s.....	237
C-10. C_L versus C_D for wing BR09 at $V_\infty = 8, 10, 11.5$ and 10 m/s.....	237
C-11. L/D versus C_L for wing BR09 at $V_\infty = 8, 10, 11.5$ and 10 m/s.....	238
C-12. C_m versus C_L for wing BR09 at $V_\infty = 8, 10, 11.5$ and 10 m/s.....	238
C-13. C_L versus α for wing PR12 at $V_\infty = 8, 10, 11.5$ and 10 m/s.	239

C-14. C_L versus C_D for wing PR12 at $V_\infty = 8, 10, 11.5$ and 10 m/s.	239
C-15. L/D versus C_L for wing PR12 at $V_\infty = 8, 10, 11.5$ and 10 m/s.....	240
C-16. C_m versus C_L for wing PR12 at $V_\infty = 8, 10, 11.5$ and 10 m/s.	240
C-17. C_L versus α for wings Rigid (01), PR07, BR09 and PR12 at $V_\infty = 8.0$ m/s.	242
C-18. C_L versus C_D for wings Rigid (01), PR07, BR09 and PR12 at $V_\infty = 8.0$ m/s.	242
C-19. L/D versus C_L for wings Rigid (01), PR07, BR09 and PR12 at $V_\infty = 8.0$ m/s. .	243
C-20. C_m versus C_L for wings Rigid (01), PR07, BR09 and PR12 at $V_\infty = 8.0$ m/s....	243
C-21. C_L versus α for wings Rigid (01), PR07, BR09 and PR12 at $V_\infty = 10.0$ m/s.	244
C-22. C_L versus C_D for wings Rigid (01), PR07, BR09 and PR12 at $V_\infty = 10.0$ m/s. ...	244
C-23. L/D versus C_L for wings Rigid (01), PR07, BR09 and PR12 at $V_\infty = 10.0$ m/s. .	245
C-24. C_m versus C_L for wings Rigid (01), PR07, BR09 and PR12 at $V_\infty = 10.0$ m/s. ...	245
C-25. C_L versus α for wings Rigid (01), PR07, BR09 and PR12 at $V_\infty = 11.5$ m/s.	246
C-26. C_L versus C_D for wings Rigid (01), PR07, BR09 and PR12 at $V_\infty = 11.5$ m/s. ...	246
C-27. L/D versus C_L for wings Rigid (01), PR07, BR09 and PR12 at $V_\infty = 11.5$ m/s. .	247
C-28. C_m versus C_L for wings Rigid (01), PR07, BR09 and PR12 at $V_\infty = 11.5$ m/s. ...	247
C-29. C_L versus α for wings Rigid (01), PR07, BR09 and PR12 at $V_\infty = 13.0$ m/s.	248
C-30. C_L versus C_D for wings Rigid (01), PR07, BR09 and PR12 at $V_\infty = 13.0$ m/s. ...	248
C-31. L/D versus C_L for wings Rigid (01), PR07, BR09 and PR12 at $V_\infty = 13.0$ m/s. .	249
C-32. C_m versus C_L for wings Rigid (01), PR07, BR09 and PR12 at $V_\infty = 13.0$ m/s. ...	249
C-33. Propeller speed versus AOA, at three free stream velocities, for a motor's power setting of 7.4 Volt.....	251
C-34. Propeller speed versus AOA, at three free stream velocities, for a motor's power setting of 7.0 Volt.	251
C-35. Propeller speed versus AOA, at two free stream velocities, for a motor's power setting of 6.6 Volt.....	252

C-36. Propeller speed versus AOA, for three motor's power settings, at a free stream velocity of 13.0 m/s.....	252
C-37. Propeller speed versus AOA, for two motor's power settings, at a free stream velocity of 11.5 m/s.....	253
C-38. Propeller speed versus AOA, for two motor's power settings, at a free stream velocity of 10.0 m/s.....	253
C-39. Propeller speed versus AOA, at four free stream velocities, for a motor's power setting of 7.4 Volt	254
C-40. Propeller speed versus AOA, at four free stream velocities, for a motor's power setting of 7.0 Volt.....	255
C-41. Propeller speed versus AOA, at three free stream velocities, for a motor's power setting of 6.6 Volt.....	255
C-42. Propeller speed versus AOA, for two motor's power settings, at a free stream velocity of 13 m/s.....	256
C-43. Propeller speed versus AOA, for three motor's power settings, at a free stream velocity of 11.5 m/s.....	256
C-44. Propeller speed versus AOA, for three motor's power settings, at a free stream velocity of 10 m/s.....	257
C-45. Propeller speed versus AOA, for three motor's power settings, at a free stream velocity of 8 m/s.....	257
C-46. C_L versus α for Rigid wing and MAVR at $V_\infty = 13$ m/s.	259
C-47. C_L versus C_D for Rigid wing and MAVR at $V_\infty = 13$ m/s.	260
C-48. L/D versus C_L for Rigid wing and MAVR at $V_\infty = 13$ m/s.....	260
C-49. C_m versus C_L for Rigid wing and MAVR at $V_\infty = 13$ m/s.	261
C-50. C_L versus α for PR07 wing and MAVPR07 at $V_\infty = 13$ m/s.	261
C-51. C_L versus C_D for PR07 wing and MAVPR07 at $V_\infty = 13$ m/s.	262
C-52. L/D versus C_L for PR07 wing and MAVPR07 at $V_\infty = 13$ m/s.....	262
C-53. C_m versus C_L for PR07 wing and MAVPR07 at $V_\infty = 13$ m/s.	263
C-54. C_L versus α for BR09 wing and MAVBR09 at $V_\infty = 13$ m/s.....	263

C-55. C_L versus C_D for BR09 wing and MAVBR09 at $V_\infty = 13$ m/s.	264
C-56. L/D versus C_L for BR09 wing and MAVBR09 at $V_\infty = 13$ m/s.....	264
C-57. C_m versus C_L for BR09 wing and MAVBR09 at $V_\infty = 13$ m/s.	265
C-58. C_L versus α for MAVR at $V_\infty = 11.5$ m/s and $E= 7.4, 7.0$ and 6.6 Volt.	267
C-59. C_L versus C_D for MAVR at $V_\infty = 11.5$ m/s and $E= 7.4, 7.0$ and 6.6 Volt.....	267
C-60. C_m versus C_L for MAVR at $V_\infty = 11.5$ m/s and $E= 7.4, 7.0$ and 6.6 Volt Volt....	268
C-61. C_L versus α for MAVR at $E = 7.4$ Volt and $V_\infty = 13, 11.5, 10$ and 8 m/s.	268
C-62. C_L versus C_D for MAVR at $E = 7.4$ Volt and $V_\infty = 13, 11.5, 10$ and 8 m/s.....	269
C-63. C_m versus C_L for MAVR at $E = 7.4$ Volt and $V_\infty = 13, 11.5, 10$ and 8 m/s.	269
C-64. C_L versus α for MAVPR07 at $V_\infty = 11.5$ m/s and $E= 7.4, 7.0$ and 6.6 Volt.	270
C-65. C_L versus C_D for MAVPR07 at $V_\infty = 11.5$ m/s and $E= 7.4, 7.0$ and 6.6 Volt.....	270
C-66. C_m versus C_L for MAVPR07 at $V_\infty = 11.5$ m/s and $E= 7.4, 7.0$ and 6.6 Volt.	271
C-67. C_L versus α for MAVPR07 at $E = 7.4$ Volt and $V_\infty = 13, 11.5, 10$ and 8 m/s. ..	271
C-68. C_m versus C_L for MAVPR07 at $E = 7.4$ Volt and $V_\infty = 13, 11.5, 10$ and 8 m/s. .	272
C-69. C_L versus α for MAVBR09 at $V_\infty = 10$ m/s and $E= 7.4, 7.0$ and 6.6 Volt.....	272
C-70. C_L versus C_D for MAVBR09 at $V_\infty = 10$ m/s and $E= 7.4, 7.0$ and 6.6 Volt.....	273
C-71. C_m versus C_L for MAVBR09 at $V_\infty = 10$ m/s and $E= 7.4, 7.0$ and 6.6 Volt.....	273
C-72. C_L versus α for MAVBR09 at $E = 7.4$ Volt and $V_\infty = 13, 11.5, 10$ and 8 m/s. ..	274
C-73. C_L versus C_D for MAVBR09 at $E = 7.4$ Volt and $V_\infty = 13, 11.5, 10$ and 8 m/s. .	274
C-74. C_m versus C_L for MAVBR09 at $E = 7.4$ Volt and $V_\infty = 13, 11.5, 10$ and 8 m/s. .	275
C-75. C_L versus α for wings BR03, BR05 and BR02 at $V_\infty = 8$ m/s.....	276
C-76. C_L versus C_D for wings BR03, BR05 and BR02 at $V_\infty = 8$ m/s.....	277
C-77. L/D versus C_L for wings BR03, BR05 and BR02 at $V_\infty = 8$ m/s.	277

C-78. C_m versus C_L for wings BR03, BR05 and BR02 at $V_\infty = 8$ m/s.....	278
C-79. C_L versus α for wings BR03, BR05 and BR02 at $V_\infty = 13$ m/s.....	278
C-80. C_L versus C_D for wings BR03, BR05 and BR02 at $V_\infty = 13$ m/s.....	279
C-81. L/D versus C_L for wings BR03, BR05 and BR02 at $V_\infty = 13$ m/s.	279
C-82. C_m versus C_L for wings BR03, BR05 and BR02 at $V_\infty = 13$ m/s.....	280
C-83. C_L versus α for wings PR04, PR07 and PR12 at $V_\infty = 8$ m/s.....	280
C-84. C_L versus C_D for wings PR04, PR07 and PR12 at $V_\infty = 8$ m/s.	281
C-85. L/D versus C_L for wings PR04, PR07 and PR12 at $V_\infty = 8$ m/s.	281
C-86. C_m versus C_L for wings PR04, PR07 and PR12 at $V_\infty = 8$ m/s.....	282
C-87. C_L versus α for wings PR04, PR07 and PR12 at $V_\infty = 13$ m/s.....	282
C-88. C_L versus C_D for wings PR04, PR07 and PR12 at $V_\infty = 13$ m/s.	283
C-89. L/D versus C_L for wings PR04, PR07 and PR12 at $V_\infty = 13$ m/s.....	283
C-90. C_m versus C_L for wings PR04, PR07 and PR12 at $V_\infty = 13$ m/s.	284
D-1. Local angle of incidence distribution in the X direction from centerline for wing BR09 at $\alpha = 18$ degrees.....	287
D-2. Undeformed (flow off) and deformed (flow on) wing sections for wing BR09 at $\alpha = 18$ degrees	288
D-3. w contour plots for wing BR09 at $\alpha = 18$ degrees.....	289
D-4. Local angle of incidence distribution in the X direction from centerline for wing BR05 at $V_\infty = 13$ m/s.....	290
D-5. Undeformed (flow off) and deformed (flow on) wing sections for wing BR05 at $V_\infty = 13$ m/s.	291
D-6. w contour plots for wing BR05 at $V_\infty = 13$ m/s.....	292
D-7. Undeformed (flow off) and deformed (flow on) wing sections for wing PR07 at $V_\infty = 13$ m/s.	294
D-8. w contour plots for wing PR07 at $V_\infty = 13$ m/s.	295

D-9. Contour plots with the strain in the X direction for wing PR07 at $V_\infty = 13$ m/s. ...	296
D-10. Undeformed (flow off) and deformed (flow on) wing sections for wing PR12 at $V_\infty = 13$ m/s.	297
D-11. Undeformed (flow off) and deformed (flow on) wing sections for wing PR12 at $V_\infty = 8$ m/s.	298
D-12. w contour plots for wing PR12 at $V_\infty = 13$ m/s.	299
D-13. Contour plots with strain in the X direction for wing PR12 at $V_\infty = 13$ m/s.....	300
D-14. Local angle of incidence distribution in the X direction from centerline for wing PR07 at $\alpha = 20$ degrees and at $V_\infty = 13$ m/s.....	301

Abstract of Dissertation Presented to the Graduate School
of the University of Florida in Partial Fulfillment of the
Requirements for the Degree of Doctor of Philosophy

EXPERIMENTAL AERODYNAMIC AND
STATIC ELASTIC DEFORMATION CHARACTERIZATION OF
LOW ASPECT RATIO FLEXIBLE FIXED WINGS
APPLIED TO MICRO AERIAL VEHICLES

By

Roberto Albertani

December 2005

Chair: Peter G. Ifju

Major Department: Mechanical and Aerospace Engineering

The concept of micro aerial vehicles (MAVs) is for a small, inexpensive and sometimes expendable platform, flying by remote pilot, in the field or autonomously. Because of the requirement to be flown either by almost inexperienced pilots or by autonomous control, they need to have very reliable and benevolent flying characteristics drive the design guidelines.

A class of vehicles designed by the University of Florida adopts a flexible-wing concept, featuring a carbon fiber skeleton and a thin extensible latex membrane skin. Another typical feature of MAVs is a wingspan to propeller diameter ratio of two or less, generating a substantial influence on the vehicle aerodynamics.

The main objectives of this research are to elucidate and document the static elastic flow-structure interactions in terms of measurements of the aerodynamic coefficients and wings' deformation as well as to substantiate the proposed inferences regarding the

influence of the wings' structural flexibility on their performance; furthermore the research will provide experimental data to support the validation of CFD and FEA numerical models.

A unique facility was developed at the University of Florida to implement a combination of a low speed wind tunnel and a visual image correlation system. The models tested in the wind tunnel were fabricated at the University MAV lab and consisted of a series of ten models with an identical geometry but differing in levels of structural flexibility and deformation characteristics.

Results in terms of full-field displacements and aerodynamic coefficients from wind tunnel tests for various wind velocities and angles of attack are presented to demonstrate the deformation of the wing under steady aerodynamic load.

The steady state effects of the propeller slipstream on the flexible wing's shape and its performance are also investigated. Analytical models of the aerodynamic and propulsion characteristics are proposed based on a multi dimensional linear regression analysis of non-linear functions.

Conclusions are presented regarding the effects of the wing flexibility on some of the aerodynamic characteristics, including the effects of the propeller on the vehicle characteristics. Recommendations for future work will conclude this work.

CHAPTER 1 INTRODUCTION

Micro aerial vehicles (MAVs) represent a new challenge for aerodynamics and controls. A typical MAV has a wing-span of the order of 15 cm or less, has a total mass around 50 g and flies at speed around 15 m/s (typical Reynolds number from 60,000 to 150,000). The operational concept of MAVs is for a small, inexpensive and sometimes expendable platform, flying autonomously or by remote pilot, usually in the field. Because of the requirement to be flown either by almost inexperienced pilots or by autonomous control, reliable and benevolent flying characteristics drive the design guidelines. A widely used propulsion system is electric motor with propeller. The extensive use of high strength composites for manufacturing their structure is critical. The primary mission for these vehicles is surveillance, in a vast variety of different facets. Other missions include detection, placement of unattended sensors or wildlife management. It is equally important that deployment in the field be made easy, to quickly respond to operational needs such as imaging in real time on the battlefield (“over the hill” problem) or in urban areas (“around the corner” problem). Since MAVs are essentially small flying wings the design goal is to develop an efficient low Reynolds number (LRN), low aspect ratio (LAR) wings that can fly easily and with agility, but not be too sensitive to wind shear and gusty conditions.

The propulsion system is equally challenging, with a demand for relatively high velocity motors spinning small propellers (diameters are typically around 80 mm or less,

with local Reynolds number from 10,000 to 30,000, based on the typical blade mean chord of 10 mm).

To address the design challenges, the University of Florida researchers have developed a series of MAVs that incorporate a unique, thin, flexible wing design with reflex airfoil. Figure 1-1 shows a typical MAV configuration



Figure 1-1. A typical MAV with carbon fiber structure and latex thin membrane wing skin. The wing has a span of 15 cm with an AR of about 1.3; maximum take off weight is 65 g.

The wings of these vehicles are manufactured of a flexible carbon fiber skeleton and a thin elastic membrane; their general configuration resembles the wings of a bat. Simulations of the flight dynamics are perhaps the most useful tools for pre-flight mission planning. These simulations estimate the responses to commanded maneuvers and allow the resulting flight paths to be rigorously evaluated. Such a tool is thus invaluable for mission preparation; however, its value is tightly correlated to the fidelity of the models that represent the aerodynamics of the vehicle. Figure 1-2 illustrates the characteristic elastic flexibility of the wing of a MAV.

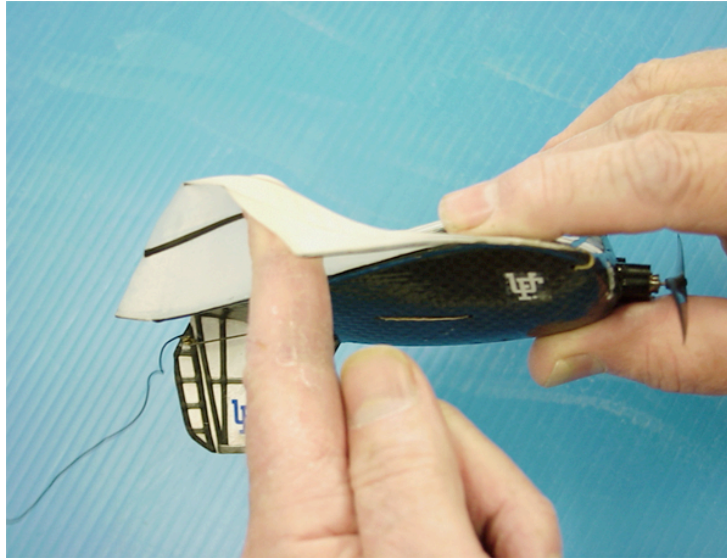


Figure 1-2. A typical 150 mm wingspan MAV with the characteristic flexible wing.

Several techniques are commonly used to generate models of the MAV's aerodynamic characteristics. Analytical estimates are available because of advances in computational fluid dynamics, but they are reliable only in the case of rigid wings. Attempts were made to model the flexible wing characteristics with computational fluid dynamics and finite element analysis; however, there was only limited experimental validation of the wing deformation. Experimental and analytical estimates are often combined to determine a single model for the aircraft. The field of MAVs is still relatively immature and systematic and reliable experimental data are sparse. Consequently, high-fidelity simulations do not yet exist for most vehicles.

It is desirable to perform parametric wind tunnel investigations to document the aerodynamic behavior of the flexible membrane wings. A better knowledge of the aeroelastic properties and deformation of flying structures, either in vehicles or biological systems, is of primary interest. Projection moiré interferometry (PMI) and

photogrammetry were used to experimentally quantify wing deformation in wind tunnel tests. The information from the PMI provided useful out-of-plane displacements but could not yield the in-plane displacements and strains. Photogrammetry provided only sparse data.

The design of flexible wing MAVs must consider the critical issues of aerodynamics and structures. A notable feature of this approach is adaptive washout which provides gust alleviation and stall delay. The experimental investigation of the relationship between wing flexibility and performance for this class of vehicle is not yet available. The combination of structural design and aerodynamic design is inherently linked and must be considered simultaneously.

Other areas of interest for MAV physics are the effects of the propulsion system. The contribution of the running propeller can have profound effects on both the equilibrium equations and the stability equations. The relatively high propeller thrust compared to the aircraft's total weight and the high ratio of the propeller diameter to wingspan make the propeller effects more relevant on MAV than on standard size airplanes. Furthermore the miniature DC electric motors used in MAVs are highly sensitive to the AOA and free stream velocity. Those characteristics applied to rigid wings or coupled with flexible wings could play a decisive role in the MAV flight mechanics and dynamics, yet they are not fully documented.

1.1 Motivation for this Research

The original University of Florida flexible MAV wing design, in comparison to a traditional rigid wing, offers operational advantages. These are a considerable resistance to crashes, a relatively simplicity in the fabrication, the possibility to adopt wing warping

or morphing for control and the capability to fold the wing (in the case this is a requirement).

In the past few years a steady progress has been achieved in the study of LAR wing aerodynamics at LRN by developing powerful CFD tools and by improving the wind tunnel experimental techniques required for force measurements at low velocities.

Advances in dynamic flow-structure numerical solvers and in MAV flight tests offer a clear path of evidence leading to beneficial effects of wing flexibility on flying qualities. Nevertheless a complete experimental proof of static elastic effects and advantages of the flexible wing over the rigid counterpart has not been performed.

It is the goal of this work to address the need of a systematic characterization of the aerodynamics of LAR wings at LRN including the effects of varying flexibility. The experimental work utilizes the low speed wind tunnel at the University of Florida using a six-component sting balance for the measurements of the aerodynamic coefficients and a visual image correlation (VIC) system for measurements of full field structural displacements. The latter system represents an original and unique application of a VIC system in a wind tunnel. The aerodynamic results will be compared and correlated with the flexibility of the structure, experimentally characterized for all the designs of the wings. The data are based on wind tunnel experiments of LAR wings with identical geometric features but with different structural design, thus various elastic properties.

The elastic energy stored by the deformed wing has many potential ramifications in flight mechanics, flight dynamics and control design. The existing experimental work was carried out mainly with wings constituted by flexible structures but without the

elastic skin membrane. The importance of the strain energy in the membrane was featured in some experimental work and practical applications on MAV.

Propulsion tests were performed with the complete aircraft, and the results were used to assess the effects of the propeller on aerodynamic force, moment coefficients and static longitudinal stability.

Micro aerial vehicle research involves expanded flight envelopes, as a result of the requirements for improved vehicle maneuverability and agility for tactical advantages and unmanned flight operational characteristics. The expansion of the flight envelope requires nonlinear aerodynamics, which must be modeled accurately.

Since nonlinear aerodynamics are much more complex than linear aerodynamics, more extensive experimentation is required using statistical analysis to accurately characterize the functional dependencies. These considerations emphasize the need to develop efficient wind tunnel testing and modeling techniques to accurately characterize nonlinear aerodynamics, with possible interactions effects amid a substantial number of independent variables.

The problem of obtaining reliable aero models is addressed by using the results from the wind tunnel tests to identify polynomial functions for the aerodynamic coefficients. The effects of the distinctive structural design of the wings are accounted for; comparisons and correlations are made using the results from the structural deformation characterization obtained with the VIC system.

The direct contributions of this work is the following: 1- support the development of high-fidelity nonlinear simulation to be used for control law design, flight envelope expansion, flight experiment design and pilot training, 2- support tuning and validation of

FEA codes, 3- support tuning and validation of CFD codes including structure-flow interactions, 4- provide an efficient aerodynamic characterization for new vehicles (with flexible geometries), 5- provide static elastic structural data to support servo mechanisms design, passive and active servoelasticity techniques or active skin control strategies, 6- tuning and validation of hardware in the loop (HIL) systems.

1.2 Scope of the Present Research

The present work is divided into four different parts linked together from the overall objective. They are as follows: 1- Literature survey, 2- Development of the Experimental Apparatus and Techniques, 3- Discussion of Aerodynamic Results, 4- Application of Wind Tunnel Results to Aerodynamic Modeling.

1.2.1 Literature Survey

This section presents a review of some influential literature related to the aerodynamics of LAR wings applied to LRN conditions and with MAV applications, with rigid and flexible structure. Some works on the propeller effects on aerodynamics of flying vehicles are also discussed followed by the section covering the modeling techniques of the aerodynamic coefficients applied by other researchers. A section dedicated to the mechanical facets of the elastic flexibility of the wings, with numerous correlations to biological systems, will conclude the literature survey. Analytical as well as experimental works are reviewed in this analysis.

1.2.2 Development of the Experimental Apparatus and Techniques

The experimental apparatus and the procedures used in the experiments in the wind tunnel are presented in Chapter 3. The chapter is divided into two main parts describing the two experimental techniques used in this work: the section on the aerodynamic forces

and coefficients and the section on the measurements of the structural deformations of the wings.

The experimental data, obtained from models of identical geometric dimensions, focus on the effects of different structural design, and thus various flexibilities, using AOA sweeps at selected free stream velocities and, in the case of complete aerial vehicles, the power settings. The section presents a complete description of the models used in the tests with the key details of fabrication and preparation. A brief explanation of the results, the wind tunnel corrections and the uncertainties in the experimental data is also presented.

Systematic lists of results are presented in Appendix C; more details on the wind tunnel data corrections and measurements uncertainties analysis are explained in Appendix A and B, respectively.

1.2.3 Discussion of Aerodynamic Results

The first part of Chapter 4 is dedicated to the discussion of the results of the measurements of the static elastic deformations of the wings. The main features addressed are the geometric characteristics of the wings resulting from the deformations due to the aerodynamic loads, in terms of maximum camber, the maximum camber's position and the wing wash-out (wing twist).

In the second part of the chapter the results from the sting balance measurements are discussed, in terms of the typical aerodynamic coefficients and derivatives and compared for different wing structural configurations. Degree of merit for each wing design is proposed for direct comparison of the performance of wings with different structural flexibility. Further analysis of data includes wings with fuselage installed and

aerial vehicles with propeller running at different power settings. A summary of results and conclusions complete the chapter.

1.2.4 Application of Wind Tunnel Results to Aerodynamic Modeling

A modeling technique used to develop accurate analytic models for the aerodynamic and propulsion force and moment coefficient dependencies from the wind tunnel data is presented in Chapter 5. The resulting models embrace a set of smooth differentiable functions for the non-dimensional aerodynamic force and moment coefficients in terms of ordinary polynomials in the independent variables, suitable for nonlinear aircraft simulation. Validation runs of the model using dedicated wind tunnel tests are exhibited.

CHAPTER 2 LITERATURE SURVEY

2.1 Aerodynamics Of LAR Rigid Wings At LRN

Theoretical research on the subject of rigid, LAR wings and at LRN dates back to the early 1900's with the Prandtl's lifting line theory for finite wings, which replaces the wing by a series of horseshoe vortices of infinitesimally small circulation strength [1]. The bound parts of those vortices buckles to a single line, the lifting line. Early experimental work on low aspect ratio wings by Zimmerman [2] and Winter [3] in the late 1930's showed some anomalies of the lift in respect to the theory developed by Prandtl, Tietjens and Hartjog [1] at the beginning of the 20th century. In particular Winter's results showed the existence of a specific range of aspect ratios (between 1.00 and 1.25) in which the lift was not obeying the current linear theory and the maximum lift coefficient was abnormally high [2]. Winter also proposed an approximation to the Prandtl's lifting-line theory based on a Fourier series approximation. According to Hoerner [4] as the aspect ratio becomes smaller, it reaches the area of the "fully" developed vortex system interfering with the wing circulation; the vortex field in turn affects the flow past the foil sections.

Hoerner [5] added to the non-linear lift factors, the wing's lateral edges and the component of velocity normal to the free stream and parallel to the wing span direction. It was believed (Hoerner, [5]) that the non-linear component of lift was caused by the drag based on the normal velocity component. From this idea came the concept of cross flow on the wing and the influence of the leading-edge shape on the cross-flow separation

at low angles of attack. Bartlett and Vidal [6] in 1955 gave a semi empirical formula for correction of the coefficient of lift (C_L) based on the cross-flow coefficient (C_{dc}), established in wind tunnel tests on wings with aspect ratio below 2 and different plan form shapes. The above tests were performed at a range of Reynolds numbers between 800,000 and a few million.

For lower Reynolds numbers, typical of MAV operations, significant experimental work was done by Jacobs [7] and Schmitz [8] with Re numbers in a range between 40,000 and 105,000. Jacobs performed the tests in a relatively high turbulence wind tunnel, while Schmitz instead used a low turbulence tunnel. By comparing the results of the two researchers it was proposed by Hoerner [5] that gains could be made by making the flow turbulent. On the subject of thickness ratio (t/c) and camber, in the case of infinite span wing (two dimensional models) the conclusion by Hoerner [4] was that for best performance at low Reynolds numbers the thickness ratio should be low and camber high, whereas at Re numbers $> 1.0 \cdot 10^5$ a regular airfoil with thickness distribution, Clark Y or similar, gives better performance. Large collections of experimental results on different airfoils was published by Riegels [9] including data on thick airfoil sections with infinite aspect ratio at LRN on tests performed in the late '40s and '50s and more recently by Selig [10] and Carmichael [11]. The three publications consist in the typical lift, drag and longitudinal moment coefficients measured at different Reynolds numbers and are a valuable reference for data comparisons.

Pelletier and Mueller [12,13] performed a systematic experimental investigation on the combination of small aspect ratio wings and low Reynolds number, less than 200,000. This early work was remarkable and effective representing an important

reference for the instrumentation set-up and data acquisition for tests in the wind tunnel at low velocities. Several tests were performed with semi-span models and this characteristic caused some problems due to the relative large vortical structures forming, at the lower Reynolds numbers, in the area of the side plates. Pellettier and Mueller concluded that cambered plate wings offer better aerodynamic characteristics than flat plate wings for a given Reynolds number. The researchers also studied the effect of free stream turbulence and trailing edge geometry, concluding that both parameters had little effect on the aerodynamic performances, including the longitudinal pitching moment. The result, different from the conclusion reported by Hoerner [5] on the experiments results obtained by Jacobs [7] and Schmitz [8], shows the important role played by the combination of LRN and LAR wings.

More recently Torres and Mueller [14] and Torres [15] extended the experimental study of low aspect ratio wings (between 0.5 to 2), with different planform shapes and at Reynolds numbers below 200,000. The results confirmed the non-linearity for the lift curve for aspect ratio at or below 1.00, with also high values of lift coefficient and the associated angle of attack. The study showed also that the planform shape has a significant effect on the aerodynamic performance. In particular the inverse Zimmerman [1] gave the best results for aspect ratios below 1 and at high angles of attack. For higher aspect ratios the elliptical planform is superior, especially for moderate angle of attacks. Another noteworthy finding by Torres [15] is the rear shift toward the trailing edge of the aerodynamic center as the angle of attack increased. The Reynolds number was found to have a negligible effect on the aerodynamic lift and drag characteristics, at least for Re numbers between 100,000 and 200,000, in conditions sufficiently away from stall.

Torres also analyzed the influence of the wing camber, confirming its trend to be similar to the higher aspect ratio wings. The leading edge shape also was found very influential, especially on the longitudinal pitching moment. Furthermore this behavior was found highly dependent from the Reynolds number. Sharp leading edges seemed to perform better than rounded ones.

The second and third part of Torres' [15] work was a proposed application of the experimental data to predict MAV performances and to perform an optimization of the design using a genetic algorithm.

While Torres work had a lower bound of the Reynolds number of 70,000, Laitone [16] published experimental data at Reynolds numbers of 20,000 and 50,000, for wings with various planform shapes and aspect ratios between 1 and 8. Laitone's results suggested an increase in L/D by using a 5% camber airfoil section, respect to the flat counter parts, for Reynolds numbers below 20,000, but also suggested to perform further studies to explain the contemporaneous increase in drag.

Many updates followed the original Prandtl's lifting line theory, including the lifting surface theory and empirical formulation by Hoerner [4 and 5]. In more recent work Lian, Shyy and Ifju [17] and Viieru, Shyy and Ifju [18] performed a full analysis of LAR wings with reflex camber. They developed a CFD code with a novel Navier-Stokes equations solver and one objective was the study of the effects of the tip vortices at a typical Reynolds number of 90,000. Results showed that the tip vortex induces a downwash that reduces the effective angle of attack; the induced drag, caused by the vortex, reduces the L/D. The use of an endplate was investigated and showed benefits for

small and medium angles of attack. Further work by Viieru, Albertani, Shyy and Ifju [19] found an agreement between CFD results and wind tunnel results within 5%.

A less sophisticated but systematic study was published by Kellogg [20], using XFOIL to perform a number of runs on five airfoils at various t/c ratios between 1.2 to 12 %, at Reynolds numbers of 60,000, 100,000 and 150,000 in both laminar and turbulent flow. The results showed that laminar flow produces greater aerodynamic efficiency than turbulent flow at those Reynolds numbers. The results also predicted better performance for the thin (2%) airfoil with respect to the thick one (12%) and the difference, less than 10% in laminar flow conditions became more than 20% in turbulent flow conditions.

Boughton, Attari and Kozak [21] proposed more empirical formulas and CFD tuning, based on wind tunnel data. By studying an inverse Zimmerman wing with flat plate and with S5010 airfoil as test cases with low aspect ratio and Reynolds numbers in the 100,000 range. The proposed CFD mesh configuration can predict C_L values to within 10% of the experimental wind tunnel results. Some differences of the C_D values were observed although the C_{D0} values were within few percent. Numerical and empirical estimations gave similar results at low angles of attack.

2.2 Aerodynamics Of LAR Flexible Wings At LRN

The design of the flexible wing, distinctive of the biologically inspired University of Florida MAVs, introduces more variables in the overall wing characterization process, in comparison to the design of the same rigid wing. The correlation between wing deformation and aerodynamic characteristics has been for sail designers and sail makers a paramount subject for many years. Some earlier computational work by Greeley,

Kirkman, Drew, and Cross-Whiter [22] demonstrated good results, but also evinced the limitations of a relatively simple pseudo 3D surface lift theory applied in a truly 3D environment. The cost and construction techniques of sails, based at that time on flat panels, were also a limitation to the use of more sophisticated computational solvers for flow-structure interaction problems.

Shyy and Smith [23] demonstrated the development of a computational methodology to handle the fluid flow and flexible massless membrane structure interaction in the context of a moving boundary problem. The analytical study, performed on three types of two-dimensional airfoils with zero thickness (rigid, flexible and hybrid rigid-flexible) showed that the flexible airfoil exhibits higher maximum lift-to-drag ratios but it can also cause the lift-to-drag ratio to fluctuate more in an unsteady flow environment. Furthermore the study predicted that the hybrid rigid-flexible wing consistently performs better than either a rigid or a completely flexible wing. Sugimoto [24] also performed studies on two-dimensional membrane airfoils. Shyy, Klevebring, Nilsson, Sloan, Carrol and Fuentes [25] extended the previous study to comparisons of custom design sections, to well documented NACA 0012 and Clark-Y airfoils. The wing section had various values of camber, between 0% and 8.89%, and thickness, between 6 and 12.9%; the free stream conditions were set at low Reynolds number with steady and unsteady conditions. The results predicted that an increased camber and reduced thickness provide more favorable L/D characteristics when the Reynolds number becomes lower and also that in an oscillating free stream a flexible profile yields better overall performance than a similar rigid profile.

Lian, Shyy and Ifju [26] further extended the previous work with a three-dimensional model for the interaction between a membrane wing and its surrounding viscous flow. In addition, the membrane had mass and the proper elastic characteristics. Lian and Shyy [27] coupled the non-linear membrane solver and the Navier-Stokes equations solver through moving boundary technique and time synchronization. This work confirmed the important role played by the tip vortices and predicted that the separation, due to an adverse pressure gradient, occurs first near the root. Dynamic results could be obtained, and a vibration of the wing membrane at a frequency of 100 Hz was predicted under steady state free stream conditions.

A thorough survey of the available literature confirmed that an experimental study on a series of flexible LAR wings at LRN having a parametric structural design and performing the aerodynamics measurements concurrent with out-of-plane static elastic deformation does not exist.

The first generation of MAV, designed and fabricated at the University of Florida, was tested at the NASA Langley Research Center. Waszak, Jenkins and Ifju [28] tested, at the low-speed wind tunnel, a vehicle with 152 mm (6 inches) wingspan, standard configuration with wing and low mounted cruciform tail and equipped with three different wing structures. The purpose of the research was to investigate the benefits of the flexible wing concept, already predicted by numerical methods. The wings were made by a carbon fiber skeleton and by a thin latex membrane or with an inextensible skin. The various structures were obtained by varying the number of longitudinal stiffeners, or battens. Part of the investigation consisted also in the measurements of the wing surface deformed by the aerodynamic load by a videogrammetry system; this part

of the experiments will be explained in the section 2.5. The tests were conducted with a complete aircraft equipped with an internal combustion engine with propeller. The results with the model without propeller proved that the flexible membrane wing allowed the vehicle to achieve higher angles of attack without stalling. It was also proposed that there was a link between the wing tip vortices structure and the deformation of the wing, the membrane billowing and the stall resistance of the latex membrane wing. The vehicle showed relatively modest L/D ratios and was stable in all axes with static stability derivatives larger than typical manned aircraft. The vehicle was also trimmed near to the maximum L/D ratio.

The dependence of the aerodynamic characteristics of a flexible wing on its initial settings, as membrane pre-tension and trailing edge tension, is a well-known trimming mechanism instinctively used by the sailors. Marchaj [29] listed one of the first experimental and empirical data on sails showing the importance of a self regulation of the airfoil camber to optimize the aerodynamic efficiency of the sail; more recently various observation during full scale tests of the last generation America's Cup sailboats decisively pointed out the importance of the combination of the sail with the flexibility of the carbon mast, 35 m tall.

The combination of the pitching of the boat sailing upwind, with the natural deflection modes of the mast-sail system, was proven to be an important factor for improving the rig efficiency and, ultimately, the boat's speed. During tests of a full-scale sail wing at the NASA Langley wind tunnel, Fink [30] proved the benefits of a soft wing in comparison to the rigid counterpart. In particular the maximum lift and lift-drag ratio resulted higher for the soft wing. A lateral control device based on the wing-warp

principle was also tested; it demonstrated to be effective and with linear characteristics at angle of attack below stall. At angles of attack near stall it became nonlinear revealing a decrease of effectiveness.

More interesting Fink concluded [30] that the lift curve had the characteristic of an unusually steep lift curve slope at low angles of attack, from -8 to -5 degrees, attributed to the rapid increase in camber with increasing angle of attack. The lift curve slope became closer to a standard value at high angles of attack when the wing fabric and rigging became taut; in this condition the sail wing experienced only minor changes of camber. Furthermore it was observed that the aerodynamic center of the sail wing was unusually rearward, at about 40% of the chord, because of the wing characteristic of increasing camber with increasing of lift. Other work, in the field of sail wings, was done by Sneyd [31] focusing on the aerodynamic coefficients and longitudinal stability.

Waszak, Davidson and Ifju [32] investigated flight control characteristics and strategies for MAVs using wind tunnel data. Their work consisted in the development of a dynamic simulation model used to estimate vehicle trim, longitudinal stability and control properties. The analysis proved that the vehicle had acceptable stability and good controllability, a not surprising result for an already flight-tested aircraft. The aforementioned works by Waszak suggested the presence of benevolent characteristics induced by the wing flexibility, in terms of ability to adapt to atmospheric disturbances and to provide smoother flight, a very desirable attribute for an unmanned surveillance platform but yet no experimental evidence was offered to prove that statement.

De Luca [33] tested in the wind tunnel at the Air Force Institute of Technology (AFIT) two versions of the same MAV design with 610 mm (24 inches) wingspan. The

aircraft had identical geometry but two different wing structures, one made by solid carbon fiber and the other by a flexible carbon fiber skeleton with a parachute membrane material covering the planform area. Results showed the expected delay of the stall angle, typical of flexible wings, and better static stability characteristics in comparison to the rigid counterpart. It was also suggested that the previous attributes lend to a more stable and responsive flight. Thrust tests with the powered aircraft did not lead to any reliable result. The flight qualities of MAV equipped with flexible wings were observed and heuristically improved during a large number of flight tests and MAVs international competitions, almost systematically won by the University of Florida's team.

Ettinger, Nechyba, Ifju and Waszak [34] estimated the difference of the lift curve versus airspeed between a flexible and a rigid wing. Jenkins, Ifju, Abdulrahim and Olipra [35] recorded during flight tests the pilot controls input to two identical vehicles, one with rigid wing and the other with flexible wing giving comparative flight handling qualities. Results in terms of spectral analysis of control input movement rates at different center of gravity location were presented. Considering the elevator rate data, it was shown that differences developed between the vehicle with the good handling qualities and the other configurations (aft CG and Rigid wing), even in the presence of gusty wind conditions. Important differences appeared throughout the whole stick inputs frequency range presented, but most convincingly between 1 and 10 Hz.

The benefits of a thin and elastically flexible wing were demonstrated by flight tests with a morphing aerial vehicle [36]. In the case of a thin and flexible wing, it would be very difficult to install and operate ailerons for roll control, therefore the option with a morphing wing is practical and proved to be very effective. The authority implemented

by the morphing wing allowed a decoupled lateral-directional and longitudinal flight dynamics. The vehicle demonstrated benevolent flight characteristics while allowing for extreme maneuvers.

The elasticity of the wing demonstrated to play an important but elusive role in the flight mechanic, dynamic and the energetics of a MAV with a flexible wing.

2.3 Considerations On Propulsion For MAVs

A survey of the available literature proved that an experimental study on powered MAVs, at different levels of wing's flexibility, with the aerodynamics measurements concurrent with out-of-plane static elastic deformation, does not exist.

The unsteady flow at the onset of stall previously mentioned was clearly evident by visual inspection of the models during the wind tunnel. Without the propeller, evident wing's vibrations have started with every wing about 8 to 10 degrees before the angle of attack for maximum lift. With the propeller on, the angle for maximum angle of attack was dramatically increased from about 24 degrees up to 36 or more. Interestingly enough, the vibrations of the wing disappeared during powered tests.

Many authors addressed the influence of the propeller on the aircraft aerodynamics and flight characteristics. Prandtl, in an early work performed at the Gottingen Laboratory [37] in the early 20's, measured the lift and drag characteristics of a three-dimensional airfoil in various positions respect to a propeller; data of the propeller thrust was also recorded and the wing was not mechanically connected to the propeller. The wing had an AR of 6 and the wingspan to propeller diameter ratio was 3.6; the wind tunnel velocity was kept constant at 20 m/s and the ratio of the propeller tip speed to the

free-stream velocities was 4.86. The propeller shaft was at a constant angle with the flow while the wing could change the position and AOA.

Prandtl could distinguish two kinds of influences: one due to the variations in free stream velocity and the other due to the variation in direction of the velocity. In particular the thrust of the propeller was higher when positioned below the wing or downstream to the wing. He noted also a marked decrease in drag when the propeller axis was the farthest above the airfoil. The variations in the airfoil pitching moment, due to the influence of the propeller, were very small in all cases.

Of particular interest are the early analysis and experiments by Von Mises [38]. He pointed out the effects of interference of the fuselage with the propeller, and the importance of the relative size of the propeller and fuselage. This relative size, as we will see later, proved to be a paramount factor in the MAV characteristics. Von Mises introduced also the concept of combined efficiency in wind tunnel tests, as a parameter that will account for the resultant thrust T_r as combination propeller-fuselage.

Formally introduced and derived by Von Mises [38] and Hoerner [5], the normal component of a propeller at an angle of attack is analytically derived using a quasi steady approximation for the propeller blade local C_L by McCormick [39]. He plotted C_z as a function of the propeller advance ratio for constant values of C_L . The pitching moment generated by the propeller normal force has a positive contribution to the static stability margin, Perkins and Hage [40]. Early theory and experiments on the wing-induced upwash on the propeller, and slipstream effects of the propeller on the wing, were presented by Hoerner [5], who also presented experimental evidence of the effects of the propeller slipstream on tail surfaces. A MAV is typically very sensitive to the pitching

moment characteristics, therefore, of particular interest, are the effects of the propeller's force component normal to the shaft that develops when the velocity is inclined about the X axis.

Experimental results by Kuhn and Draper [41] on the propeller-wing interactions indicated that increasing the coefficient of thrust increased the wing angle of attack for maximum lift and greatly diminished the reduction in lift above the angle of attack for maximum lift. An appreciable direct pitching moment was found at high angle of attack on the propeller itself. Such moment contribution doubled when in the presence of the wing and corresponded to a downward movement of the effective center of thrust of about 20% of the propeller radius. In an attempt to experimentally measure the propeller thrust by a wake survey, Pendley [42] reported that for small AOAs, large changes occurred in the energy distribution in the propeller wake creating an asymmetry of the thrust distribution over the propeller disk thus shifting the propeller thrust axis with pitch.

The work by the aforementioned researchers considered a typical aircraft with a wingspan-propeller ratio of 10 or more; in the case of a MAV, that ratio could easily be 2 or less, and the airflow accelerated by the propeller has an important mass flow compared to the mass flow interested by the wing. The above characteristics may require a different approach in the experimental techniques, which need to be designed with a generous number of combinations of free stream velocities, and propeller speeds as explained in chapter three.

Some experimental work for high thrust and high flow propulsion systems, typical for STOL aircraft, was presented by Trebble [43], offering some advises for testing V/STOL models. The case of micro aerial vehicles equipped with DC motors has not

been fully experimentally explored. Propeller-wing mutual effects can be properly exploited to develop V/STOL techniques with fixed wing MAV; perched take off and landing for example was analytically studied and discussed by Crowther [44].

Waszak et al. [32] experimentally estimated the change in the aerodynamic derivatives due to the propeller operation using a MAV of the first generation, with an internal combustion engine and a single flexible design wing. This paper is considered an important reference of wind tunnel experimental work on MAVs including proposals of analytical models of the aerodynamics and propulsion.

2.4 Aerodynamic Analytical Models

The problem to devise analytical models for the main aerodynamic characteristics of a rigid LAR wing at LRN, was suggested by Polhamus [45, 46] and Raymer [47]. Hoerner [4, 5] proposed some empirical equations, based on experimental data, suggesting a nonlinear second lift component of lift, which can be isolated from the total values of lift or normal force.

More recently, Torres [14, 15] used specific wind tunnel data on LAR wings to fit an analytical expression with the objective of modeling the nonlinear dependence of C_L with the angle of attack. Torres [15] based his model on the expressions listed by Polhamus [46] and Raymer [47], which were derived from the DATCOM [48] empirical equations, using wind tunnel results of wings with AR from 0.5 to 2.0. Torres found Polhamus' expression the most suitable and derived the coefficients of the linear expression of C_L , nonlinear in the angle of attack, using the statistical tools in Excel. The approximation of the experimental results, obtained with this method, was satisfactory.

Boughton, Attari and Kozak [21] also formulated empirical expressions for lift and drag based on wind tunnel experiments.

When in the presence of a number of dependent variables, as in the case of a powered MAV with a flexible fixed wing, and with various independent variables and complex system responses, not necessarily linear, the approaches that seem most appropriate are a multiple curve fittings or multiple regression analysis. More recently modern experiment design and RSM techniques have been appropriately applied to wind tunnel tests.

The first concept of the fundamental mathematical problem in determining the parameters which best fit observational equations was studied by Rudjer Josip Boscovich in the year 1757 (Boscovich, a Croatian mathematician, is more famous for addressing for the first time, in the year 1750, the idea that the atom is formed by sub particles, opposing the concept by Democritus, accepted at that time, that the atoms were “uncuttable”). The basic criterion for selecting the best regression equation is illustrated by Draper [49], suggesting that the process of selecting the best regression equation is not unique, and personal judgment is a necessary part of any of the statistical methods proposed and used. Dodge and Jureckova [50] listed four of the most common and effective regression methods (LAD regression, LS regression, TLS regression and M-regression) but indicating that none of them are good for all purposes; they proposed an adaptive regression method. The technique consisted in a construction of an adaptive combination of several pairs of these estimation methods. The problem in wind tunnel testing is less statistically driven and more defined in the physical entities involved in the results.

Draper [49] suggested a more pragmatic approach by defining the multiple regression and mathematical model building problem as a structured model building procedure. He also warned that no scientist should be persuaded to abandon his or her scientific insight and principles in favor of some computerized statistical screening procedure. The aforementioned regression techniques should be considered part of the more general experiments planning and analysis. Some insights on modeling techniques are also offered by Steffen [51] about RSM methods and Giunta and Watson [52] on the comparison between polynomial and interpolating models.

The MAVs, similarly to other non-conventional aircraft as V/STOL's vehicles or the F18 HAARV, have the capability to operate in a region of the flying envelope far beyond the maximum AOA of the airplane in dry configuration. Furthermore, in the wind tunnel experiments, the effects of the propeller slipstream on the global vehicle's aerodynamics are correlated to a series of independent variables with complex effects on the aerodynamic coefficients. Indeed, linear and nonlinear regions of the lift curve were of primary interest in the present research scope of work, especially considering the fact that in some test cases with the propeller on, results demonstrated only a moderate loss of linearity of the lift curve up to 36 degrees AOA, but not a clear and definite wing's stall. A technique for global modeling of nonlinear aerodynamic coefficients, proposed by Morelli [53], applies multivariate orthogonal functions generated from the experimental data.

The technique uses multivariate orthogonal modeling functions to determine non-linear model structure and expands each retained modeling function in an ordinary multivariate polynomial [54]. The orthogonality of the modeling functions allowed

straightforward determination of an adequate model structure and the associated parameter values. The terms to be retained in the final polynomial form were selected using a minimum predicted squared-error criterion. Morelli [54] indicated also that partial derivatives of the formulated models could be used to assemble globally useful linear parameter varying models. Smooth analytic derivatives of any order can be simply calculated and the final result was a compact, global analytical model of the nonlinear functional dependence intrinsic of the experimental data with good predictive capabilities. As suggested by Draper [49] a robust modeling capability should be combined with an efficient planning and experiment design.

Modern techniques of experimental design, applied to wind tunnel tests, were developed by DeLoach [55] at NASA LARC and applied in numerous test cases. One project considered remarkably interesting for the subject of this research was a wind tunnel experiment for characterizing the aerodynamic and propulsion forces and moments of a model airplane. Morelli and DeLoach [56] performed a combination of conventional and MDOE tests at the NASA Langley 12 foot LSWT using a modeling technique that applied multivariate orthogonal functions and expanding them in terms of ordinary polynomial functions. From those experiments the researchers evinced the need, for a better efficiency of the modeling process, the capability to set the AOA of the model at arbitrary values during a test run. Particularly useful was the predefinition of the subspace boundaries by the use of one factor at a time (OFAT) sweeps however, as clearly stated by the authors, even in the most automated optimized procedure, the human analyst would be needed to provide high-level oversight of the entire process.

Another problem that is addressed in this research is the characterization of the flexibility of the wing structure.

2.5 Static Elastic Deformations Of Flexible Wings

Flexible design and flexible materials have been a natural study subject for biologists for many years. Wainwright, Biggs, Currey and Gosline [57] have described pliant materials as a class of materials that function in supportive systems by being deformed and compliant materials, which use the opposite strategy of a rigid material by complying with a state of stress. While the latter are the main scope of this work, the former concept is potentially of great interest in many applications like the use of flexible structure for control or for stored elastic energy.

Pawlowski, Belvin, Raney, Su, Harrison and Siochi [58] have demonstrated the feasibility of lightweight, electrically responsive wing skins for MAV flexible airframe design. Schmit, Glauser, Gorton [59] used a low dimensional tool to solve flow-structure interaction problems based on POD and modified LSE techniques. The method employed the dynamic strain measurements from the membrane wing to estimate the POD expansion coefficients. From those coefficients they derived an estimation of the velocity in the wing's wake. A similar system was proposed for a possible use for MAV control purposes.

Zheng and Ramaprian [60] have demonstrated an actively controlled flexible wing skin control technique by using a commercially available piezo-ceramic bender inside the flexible wing molded out of polyurethane foam. The study estimated the feasibility of the design of a piezo electrically deformable wing that can fly at constant altitude and ground speed in moderately fluctuating winds in the order of +/- 10% of velocity. One

important feature of the flexible wing is the capability to absorb, to store and eventually release energy in the form of elastic energy. Such characteristics could play a key role in the flight dynamics of the MAV. The use of active control systems in MAVs is a promising way to take a positive advantage of an elastically deformable wing.

In the case of the flexible wing of the MAV, without any active control system, the wing acts in a way more similar to an insect than a bird. Birds, due to the presence of muscles in their wings, have a different power and control mechanism than insects. According to Combes and Daniel [61] the insects' wing deformations during flight are largely passive, and are controlled primarily by the architecture and material properties of the wing. Their work was experimental, using *Manduca sexta* wings, with the derivation of stiffness distribution on the wing from static deformation measurements. They found how wings from different species have highly tailored structural characteristics according to the insects' natural functions, or requirements. Combes and Daniel [62, 63], in subsequent works, added to their research the study of fluid-dynamic force effects and inertia forces. Their conclusion was that the elastic interactions between a wing, and the fluid-dynamic forces it generates, are minor compared to the effects of wing inertia. Fluid damping, rather than aerodynamic forces, was the major player, a not surprising result considering the low Reynolds number below 10,000.

Steppan [64] studied slightly larger wings, typically in butterflies as the *Vanessa Cardui*. He documented the "passive" properties of deformability of the wing and his results showed that flexural stiffness scales with wing loading to nearly the fourth power (exponent equal to 3.9) and is highly correlated with the wing area cubed (exponent equal to 3.1). It was also proposed that the insect selection for a consistent dynamic wing

geometry (angular deflection) in flight might be a major factor controlling general wing stiffness and deformability. Elastic energy management plays a fundamental role in biology systems as well as in MAV flight dynamics.

Sensenig and Shultz [65] documented an efficient elastic energy storage system in leg joints lacking extensor muscles in arachnids. The muscles during propulsion act as dampers and shock absorbers during climbing or other deviations from walking on smooth horizontal surfaces. They also suggested the use of the muscles as energy dampers for controls purposes.

Another proposal of an elastic energy application is by Pennycuick and Lock [66], on the hovering flight of pigeons. It was proposed that the kinetic energy of the pigeon's wing, in hovering or in slow forward flight, is transferred to the air at the end of the down stroke by a mechanism involving temporary storage of elastic energy in bent primary feather shafts. The authors experimentally measured the amount of elastic energy stored in the feathers, estimated the elastic efficiency and compared that with the energy, or power, necessary for the flight conditions considered.

Applications of elastic energy balance are well known in the MAVs community. Pornsin-Sirirak, Tai, Nassef, and Ho [67] documented the study of a parylene diaphragm electrostatic actuator valves and the use of this flexible parylene actuator for micro adaptive flow control. In their conclusion the authors recommended that to further improve the aerodynamic performance of MEMS wings, a selective stiffness distribution control on the membrane is desired. This feature will help to actively control the flexibility of the wings and the shedding of the vortices.

Ho, Nassef, Pornsinsirak, Tai and Ho [68] studied a 15 cm wingspan-flapping wing MAV, in the Reynolds number range of 10,000-100,000. In this flow regime, rigid fixed wings drop dramatically in aerodynamic performance while flexible flapping wings gain efficacy hence they are the preferred propulsion method for small natural fliers. One of the conclusions of their work was that the flexible wing produced more mechanical power than the rigid wing. The advantage of the increase of the output of mechanical power that the flexible wing enjoys is revealed that when the two wings carry the same payload. The flexible wing has excess power and therefore it can accelerate, perform maneuvers, or simply extend its range by reducing its power consumption, while the rigid wing has no spare power to match the flexible wing performance. The above concept is clearly better exploited in unsteady flow regimes typically for a flapping wing or for a fixed wing during unsteady flight and high g's transient maneuvers.

A flexible wing should dramatically eclipse the rigid counterpart when unsteady flow and motion are manifested, which are an important part of a flight profile of a MAV, and yet not very well documented. Some studies on highly unsteady flying conditions were made at NACA in the early and mid 40s, prompted by the fighter pilots in World War II pushing the envelope of their airplanes. Hoerner [5] documented the increase of lift during dynamic pitch up tests in the wind tunnel, with respect to the steady tests in the same conditions. The increase of lift in dynamic conditions was attributed to the delay of the adverse pressure gradient, allowing the airfoil to support greater lift than during the steady case. Those early tests also offered some knowledge to the dynamic lift stall.

More recently Broeren and Bragg [69] performed a systematic wind tunnel study on various types of thin airfoils. The models were two-dimensional with thicknesses

between 18.6 and 6.7% and camber between 0 and 5.94%. The test's Reynolds number was 300,000. The results highlighted the different stall patterns typical of thin airfoils. Airfoils having the thin-airfoil stall type exhibited highly unsteady stall characteristics. The combination thin-airfoil/trailing-edge stall type had the highest levels of lift fluctuations at stall; nearly double that of the pure thin-airfoil stall cases. A laminar-separation bubble was a common feature in the airfoil flow fields for both stall types.

Cummings, Morton, Siegel and Bosscher [70] documented a different dynamic lift behavior. They performed wind tunnel tests and carried out a numerical solution of the unsteady, laminar, compressible Navier-Stokes equations applied to a model of an UCAV Boeing 1301. The model reference chord was 133 mm and the tests Reynolds number was 142,000. The model, with delta wing, was able to develop lift up to 25 degrees angle of attack, well inside the post stall region. The dynamic lift characteristics were found quite unusual compared to other experimental evidence with different delta wing configurations. Instead of gaining lift during a pitch-up maneuver the UCAV loses lift, compared to the steady case, until the post stall region is reached. During the pitch down phase, the model gains lift with respect to the steady case.

Dynamic pitching tests were also conducted by Brandon [71] at the Langley Low Speed Wind Tunnel, using models of rectangular and delta planform wings with flat plate airfoil shape, in addition of a model of the F-18 jet fighter. Substantial increments in lift, drag, and pitching moment due to dynamic effects were measured for the rapid large-amplitude pitching motions. The conclusion, applied to a F-18 class aircraft, was that natural persistence of the dynamic lift effects were seen to be too short to significantly

affect turn performance; however, longitudinal and lateral stability were significantly impacted by dynamic effects.

An invaluable support to aerodynamic wind tunnel tests of flexible wings is offered by the measurements of the structure's deformation. Burner, Fleming and Hoppe [72] used experimental techniques to measure the deformation of a model under wind tunnel tests, usually a nuisance for the wind tunnel experimenter, but a primary goal for experiments with flexible wings applied to MAVs. The authors compared three optical systems: custom video photogrammetry, projection moiré interferometry and the commercial photogrammetry Optotrak system, listing their advantages and disadvantages.

Fleming, Bartram, Waszak and Jenkins [73] performed more specific work on wing deformation during wind tunnel tests, acquiring the MAV's wing deformation using the PMI technique. During those tests it was found that a 6-batten monofilm covered wing, deformed approximately 65% less than a 2-batten, latex covered wing. No force coefficients were presented to better assess the differences between the various wing structural configurations.

One of the main topics to address when working on the structural deformation of the wings is the definition of the material characteristics of the wing's components. The flexible wings are designed in a similar style than bat's wings, with a skeleton made by carbon fiber and a thin membrane skin, made by latex rubber or other elastic materials. Mooney [74], in a milestone work on large elastic deformation of rubber material, proposed a novel general strain energy function using H as a new elastic constant. Mooney's equation was validated with experimental data on soft rubber from 400 percent

elongation to 50 percent compression. The specific case of a rubber thin membrane was formally addressed by Fulop [75], working on a thin elastic rubber membrane stretched by a small shaft normally to the pre-stressed surface. Fulop proposed and validated, using experimental data that Laplace's equation for the membrane holds without restriction. Interestingly enough he observed that the motion of any point in the membrane is purely vertical, for vertical displacements of the shaft. This suggested that the horizontal component of the tension remains constant and equal to the tension in the initial undisplaced position.

Inspired by the basic work done by Mooney and Fulop other researchers developed experimental techniques for efficient methods for thin membrane characterization. Yang and Hsu [76] used a system of indentation using a sphere and solved two sets of three first order nonlinear differential equations for membrane displacements, applied to the area of contact between the sphere and the membrane and the free membrane area. The membrane was considered as a Mooney type material. Wan and Liao [77] and Liu and Ju [78] proposed a procedure to find the mechanical properties of a thin flexible membrane from measurements of its displacement obtained by applying an external load to the membrane center via a rigid spherical capped shaft or a rigid sphere. Liu and Ju assumed the non-linear membrane to be an isotropic three-dimensional incompressible (rubber-like) material exercising a Mooney-Rivlin constituent behavior. A theoretical model is constructed to quantitatively correlate the elasticity to the deformation profile of the membrane. The measurements of the deformation of the membrane were achieved by a computerized microscope-enhanced image system with a CCD camera. Data were analyzed using homemade imaging software based on the LabView platform. The

experimental validation was good for thin membrane for which bending stresses were insignificant, according to one of the assumptions proposed in the theory.

Having evaluated the most relevant concepts related to rigid and flexible wings at LRN, it is now apropos to describe the methodology used in the present work to evaluate this topic. The following chapters review the experimental systems, present the test results and propose some applications of the data.

CHAPTER 3 EXPERIMENTAL APPARATUS AND TESTS PROCEDURES

It is apparent from the literature review illustrated previously that a systematic experimental characterization of LAR flexible wings at LRN, including the effects of the propeller, is required. Because of the flexibility of the wings, the aerodynamic characteristics cannot be fully comprehended without a static aeroelastic characterization of the system, performed in parallel to the aerodynamic measurements. Two main experimental arrangements were used in the wind tunnel for this research: a strain gauge sting balance, for force measurements, with the subsequent computation of aerodynamic coefficients, and the Visual Image Correlation (VIC) system, for geometric and structural deformations characterization.

This chapter describes the two experimental techniques, with the two different apparatuses, test procedures and data analyses. The first section illustrates the models used in the wind tunnel, common for both experimental techniques.

3.1 Description of the Models

The main objective of the presented research is the experimental characterization, both aerodynamic and geometric, of LAR wings at LRN, as affected by the following parameters:

1. Elastic characteristics of the structure and the skin
2. Free stream dynamic pressure
3. Propeller's slipstream, when applicable
4. Reynolds number

The following section explains the geometric, the structural and the manufacturing features of the models used in the wind tunnel tests.

3.1.1 Wings

One wing planform with the associated airfoil shape were chosen from the flight line of the University of Florida MAV lab. The geometry was kept constant for all the models tested. In this way the changes in any aerodynamic characteristic, at the same dynamic pressure or Reynolds number, was only due to the wing flexibility and the consequent shape when loaded.

3.1.1.1 Description

The wing's planform is a modified Zimmerman type with straight leading edge (Charles H. Zimmerman, conceived the innovative wing's design in the early 1930's; he won the NACA design competition with his disc-shaped wing concept capable of flying at high speeds or hovering), as illustrated in Figure 3-1. The aerial vehicle configuration is tailless without wing sweep angle; therefore an ad-hoc autostable airfoil section was used.

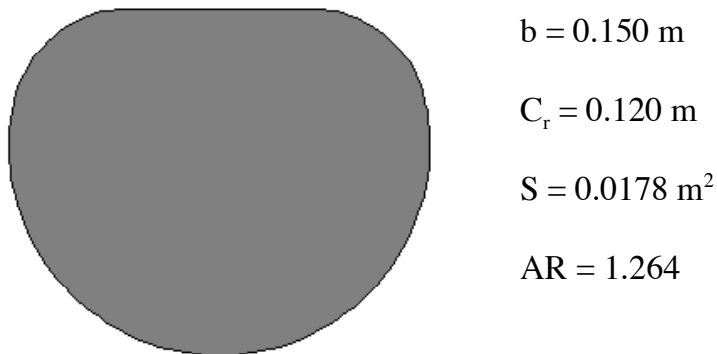
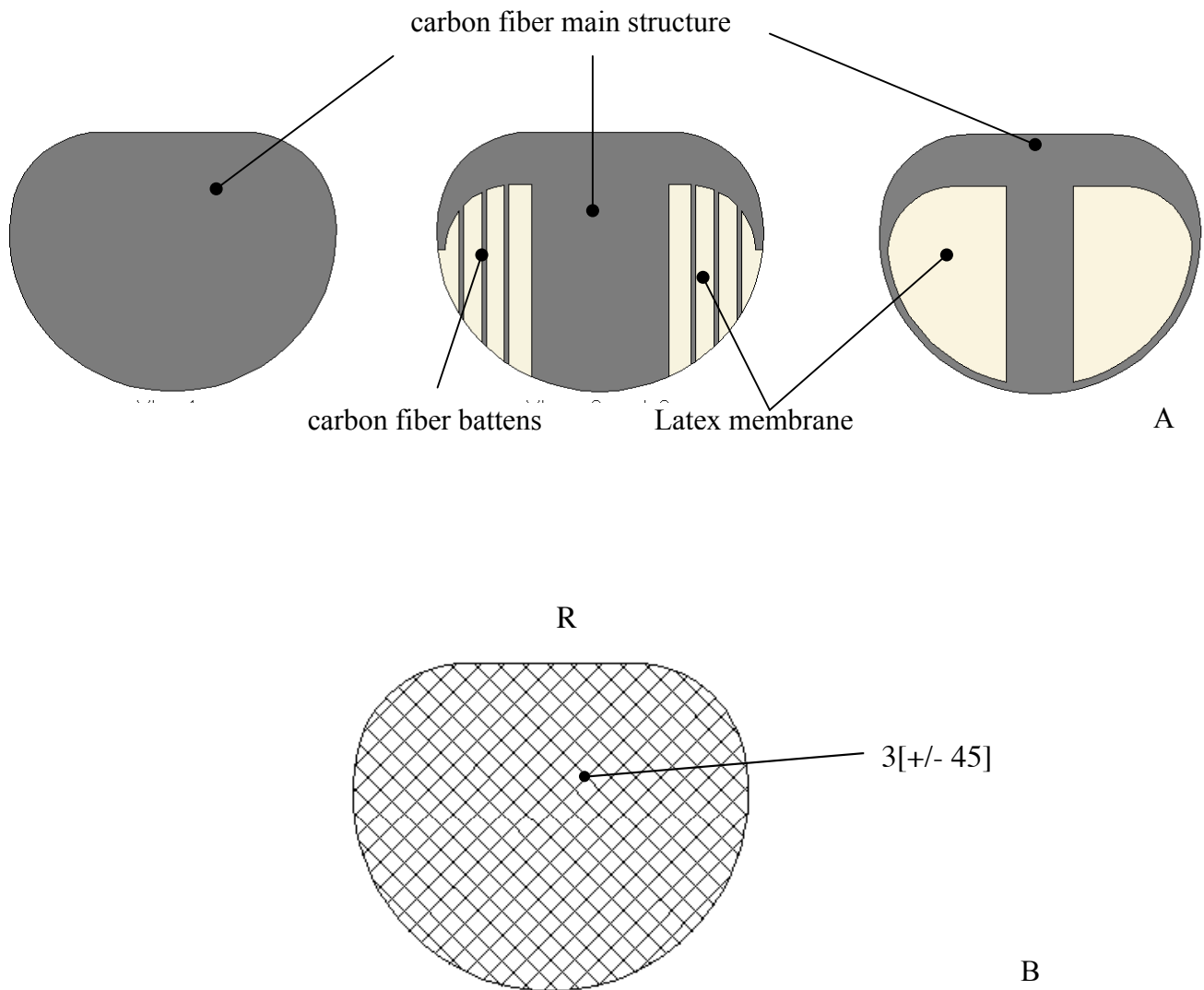
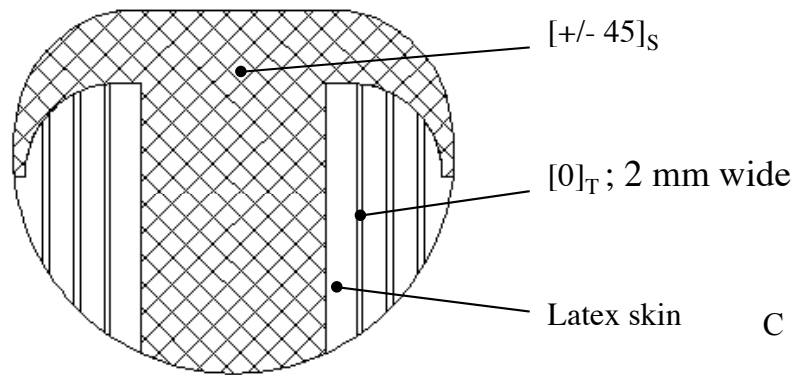


Figure 3-1. Planform view of the wing and airfoil shape used in all the tests presented in this work. The geometrical data were used for the computation of the coefficients.

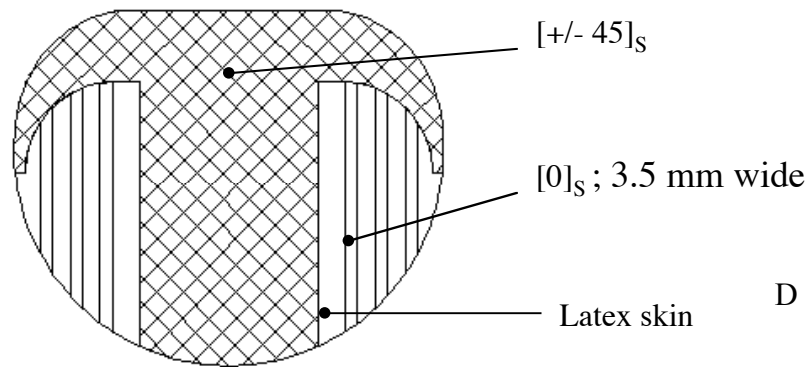
The structures of the MAV wings are constructed out of carbon fiber composites. This is accomplished utilizing a CNC machined mold and carbon fiber pre-preg [80]. The wings were manufactured from the same mold, thus have the same nominal shape. The difference in the flexibility of the structure was relatively simple to obtain by using the anisotropic characteristics of the composite materials. This work presents results for several models obtained from three basic wing configurations, schematically described in Figure 3-2 and illustrated in Table 3-1.



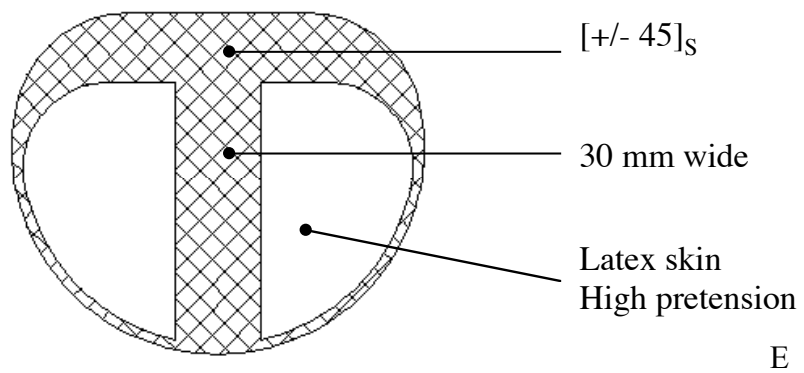
BR02



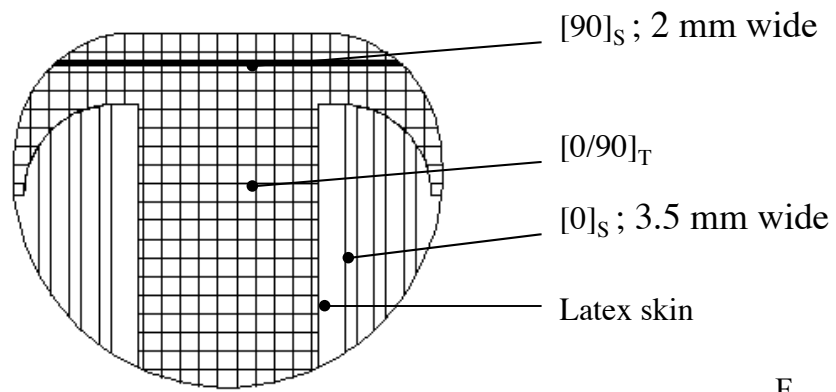
BR03



PR04

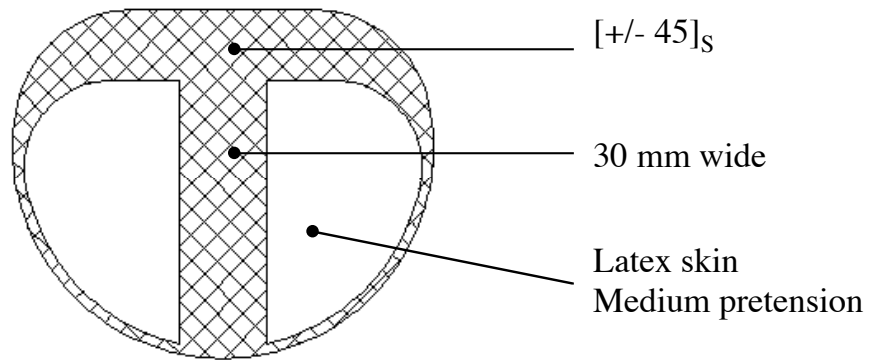


BR05



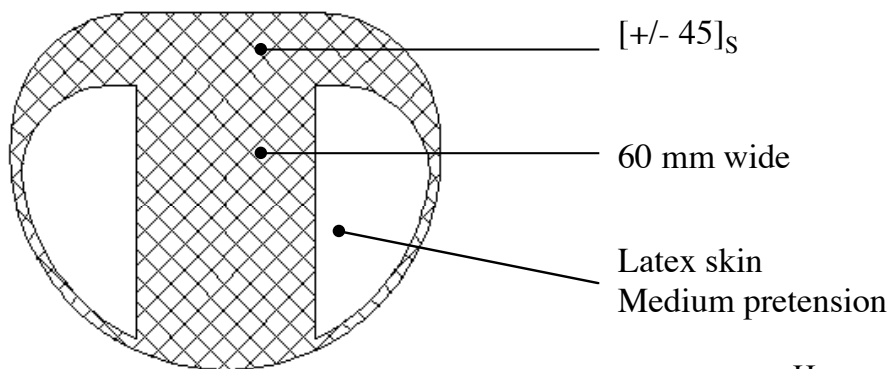
F

PR06



G

PR07



H

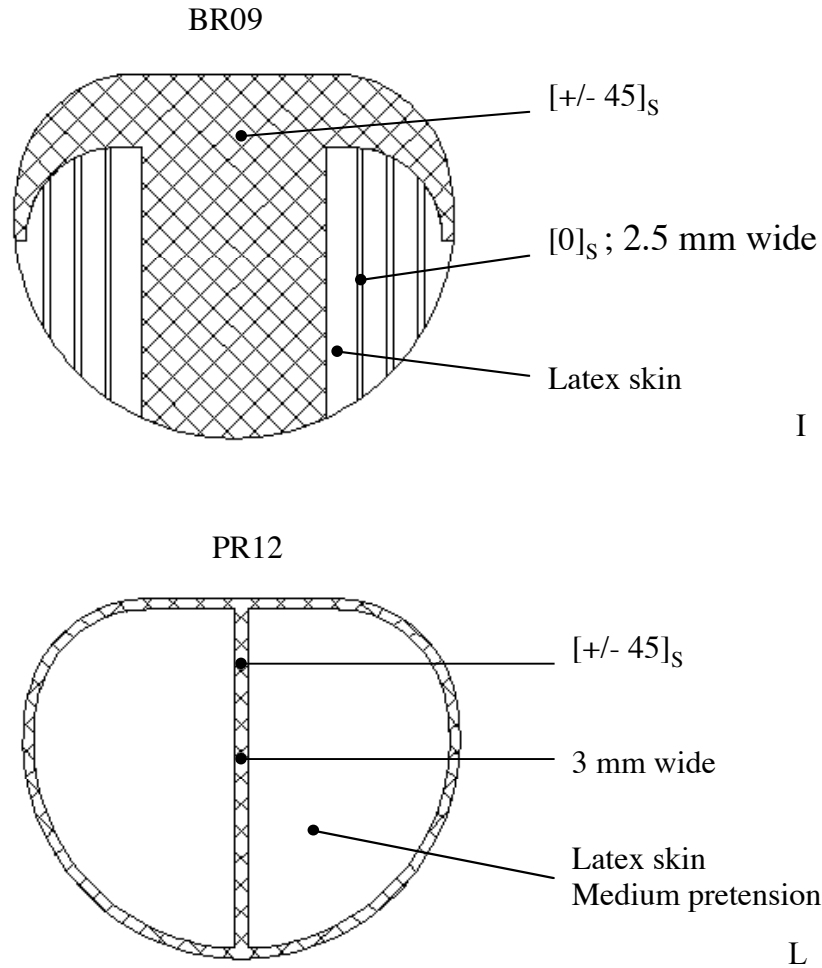


Figure 3-2. The structure's configurations of the wing tested. A) the three main groups, from left to right, rigid (R), batten reinforced (BR) and perimeter reinforced (PR) type, B) R, C) BR02, D) BR03, E) PR04, F) BR05, G) PR06, H) PR07, I) BR09, L) PR12.

Table 3-1. A brief description of the three basic wing structures tested.

Wing	Description
R	Wing made by Solid Carbon Fiber (Rigid)
PR	Wing with Rigid Leading Edge and reinforced with Carbon Fiber Perimeter
BR	Wing with Rigid Leading Edge and reinforced with Battens

The R wing, the solid carbon fiber configuration without latex membrane, was used as a nominally rigid benchmark model for reference measurements; the carbon fiber distribution was $[(+/- 45)_3]_T$. The flexible models were obtained from the two other basic structural designs using a variety of different carbon fiber layouts and wing skin configuration combinations, according to Table 3-2. The general design was with two carbon fiber plies in the central part and the leading edge and, in the case of the BR wing, six battens were added with a variable number of plies, depending of the wing models. All wings had an elastic latex wing skin with a thickness of 0.2 mm.

Table 3-2. Table with a brief description of the wings tested in this work. The overall dimensions, airfoil shape and wing planform were the same.

Type	Model	Description
R	1	Wing made by Solid Carbon Fiber (Rigid)
BR	2	Thin battens (one ply 0), 2 mm wide, LE +/- 45
BR	3	Thick battens (two plies 0/0), 3.5 mm wide, LE +/- 45
PR	4	Perimeter and LE +/- 45, skin pretension high, middle part 30 mm wide
BR	5	Thick battens (two plies 0/0), 3.5 mm wide, LE 0/90, wingspar 90/90 2 mm wide
PR	6	As 15004 with medium skin pretension
PR	7	As 15004 with middle part 60 mm wide
BR	9	Thick battens (two plies 0/0), 2.5 mm wide, LE +/- 45
PR	12	Rigid thin perimeter, narrow middle part, LE +/- 45

The following description of the wings refers to Figure 3-2-B. The wing BR02 is characterized by a relatively rigid leading edge (LE) with a carbon fiber lay-out $[(+/- 45)_s]$ and thin battens with only one ply $[0]_T$, 2 mm wide. This wing has the most flexible battens of the entire series therefore the flexibility of the carbon fiber structure in this case is distributed to the six battens. The wing BR05 was designed with the same concept of wing 02 but obtained in a different way. In this case the LE is fabricated with

a $[0/90^0]_T$ laminate schedule and reinforced by a transverse unidirectional spar $[90]_S$, 2 mm wide; the battens are thicker than the standard with $[0]_S$, 3.5 mm wide. This configuration gave the wing a good torsional flexibility around the LE maintaining the battens relatively stiff. The wings BR02 and BR05 were designed to attain the wing deformation style characterized by the maximum geometric twist.

The wing BR03 has the same thick ($[0]_S$) and wide battens than BR05 but the LE with carbon fiber $[+/- 45]_S$. The wing BR09 is the configuration most used for flight testing and it is characterized by thick ($[0]_S$) but narrow (2.5 mm) battens and the standard $[+/- 45]_S$ carbon fiber LE. The wing BR03 was designed to be the stiffest wing with battens; the wing BR09 was designed to have a combination of the two deformation styles, billowing and geometric twist.

The PR wings were realized with a nominally rigid central part with an integral rigid perimeter to give the planform shape, as illustrated in Figure 3.2-A. The relatively high stiffness of the perimeter do not allow for a significant geometric twist and the deformation is concentrated on the latex membrane skin giving the deformation shape the characteristic billowing. The different levels of deformation were obtained by varying the ratio of area interested by the latex over the rigid carbon fiber and, in one case (wing PR004), the pretension of the skin. The wing PR04 and PR06 have a rigid central part 30 mm wide, in the wing PR07 the middle carbon body is 60 mm wide and finally the wing PR12 has the largest area of latex with a 3 mm rigid part on the center line, as illustrated in Figure 3.2-B.

The wings' design ensured the proper variations of global structural flexibility and the difference of deformation styles, namely geometric wing twist (or wash-out),

billowing (or increasing of maximum camber) and combinations of the two was obtained, as illustrated in Chapter 4 and Appendix D. Span wise deflection was negligible for all the designs, a typical feature of LAR wings; the ability of the wing's skin to stretch was also a parameter. Referring to the Figures 3.2-A and 3.2-B and Table 3.2, the wings' deformation characteristics can be summarized as follows:

Wing type R, nominally rigid wing.

Wing type BR02, thin battens, the deformation will be both shapes geometric twisting (GT) and billowing (B) and on battens and latex.

Wing type BR03, thick and wide battens, the deformation will be moderate GT and moderate on latex (this is the most rigid wing with battens).

Wing type BR05, thick and wide battens and torsionally elastic LE, the deformation will be mainly GT and moderate on latex.

Wing type BR09, intermediate size battens and LE, the deformation will be a combination of GT, B and blended on the battens and latex.

Wing type PR04, rigid perimeter and latex with high pretension, medium size middle rigid part (30 mm), the deformation will be moderate on the latex and no GT.

Wing type PR06, rigid perimeter and latex with medium pretension, medium size middle rigid part (30 mm), the deformation will be significant on the latex and no GT.

Wing type PR07, rigid perimeter and latex with medium pretension, wider rigid middle part (60 mm), the deformation will be significant on the latex and no GT.

Wing type PR12, rigid perimeter and latex with medium pretension, the narrowest rigid middle part (3 mm), the deformation will be of great magnitude on the latex and no GT.

3.1.1.2 Fabrication

The preparation of the specimen is relatively straight-forward, but requires attention to some important details, like the choice of the background color on the target surface (to blend with the wing skin) and skin finish (diffuse) to minimize, or eliminate, noise that can result during image processing. The following steps describe the model preparation.

Step 1. After the carbon fiber wing is connected to a holder suitable for installation in the wind tunnel, the top surface is spray painted with a light-colored paint, similar to the color of the skin. In this way, the optical effects of the wing battens, normally black, being photographed by the cameras through the partially transparent wing skin, will be minimized. Figure 3-3 shows the wing carbon fiber skeleton with and without the light colored paint.



Figure 3-3. BR (batten reinforced) wing after demolding, on the left, and with spray paint applied, on the right.

Furthermore because the thickness of the paint is only few hundredths of millimeter and its modulus of elasticity is negligible compared to the carbon fiber the elastic characteristics of the wing are not affected by the application of the paint.

Step 2. The wing skin, consisting of a strip of thin, lightly colored and partially transparent latex rubber is speckled with a flat black paint. The random speckle pattern, illustrated in Figure 3-4 is obtained by increasing the size of the nozzle's diameter on a regular can of spray paint. After the paint has dried, a coat of dulling spray is applied to the same side of the latex. The single speckles have a size of less than one millimeter and they are not connected together. The dulling spray with a thickness of few hundredth of millimeter when dry has a very low elastic modulus thus they do not significantly change the mechanical properties of the latex skin. If information concerning the state of the pre-strain in the MAV wing is desired, a picture of the latex is captured, for later use as a reference in the VIC system.



Figure 3-4. BR (batten reinforced) wing ready for the application of the latex skin. The latex is illustrated without speckle, to the right, and after the spray application of the random black speckle, to the left.

Step 3. The latex is stretched out around a frame, and the four borders are pinned to hold the desired tension on the skin. The latex is fastened with the speckled side facing down. Spray mount adhesive is applied to the painted side of the carbon fiber skeleton wing. The wing is then attached to the clean side of the latex and allowed to dry. Care is taken to keep the portion of un-bonded latex free of spray glue. The excess latex rubber is then trimmed away. The model, depicted in Figure 3-5, is now ready for testing in the wind tunnel.



Figure 3-5. BR (batten reinforced) wing after the final application of the randomly speckled latex skin. The model is now ready for wind tunnel testing.

3.1.2 Complete Aerial Vehicles

The complete aerial vehicle for wind tunnel testing is essentially a flight ready vehicle without the payload and the on-board electronics (motor controller, radio,

batteries). In the specific case of this research, some of the wings that were previously tested, see Table 3-2, were installed on a partial vehicle complete with fuselage, vertical stabilizer, DC motor Maxon RE-10 and the selected propeller U-80. The diameter of the propeller was reduced to 58 mm and kept constant for all the experiments.

The partial vehicle and its components were constructed out of the same composite materials used for the wings but with a different technique [79, 80]; all the vehicles tested shared the same fuselage and components with assorted wings. Table 3-3 briefly describes the models that were tested in the wind tunnel.

Table 3-3. Table with a description of the complete aerial models subject of the analysis in this work.

Model	Wing	Description
MAV10501	R	Wing made by Solid Carbon Fiber (Rigid)
MAV10507	PR	Perimeter and LE +/- 45, skin pretension high, middle part 60 mm wide
MAV15009	BR	Thick battens (two plies 0/0), 2.5 mm wide, LE +/- 45

In this way the only difference between the different complete models was only the wing. Figure 3-6 shows a model with a batten reinforced (BR) wing ready for testing in the wind tunnel.

The models were equipped with controls and operational servo actuators for tests with control deflections; the actuators were not energized and the desired deflection was set manually for each experiment. The deflection angle was kept fixed during the tests by the resistance offered by the actuator. The motor was powered by an external high-resolution DC power supply to avoid the inevitable problems of battery discharge. The electrical connection to the motor was via a thin wire with a very low stiffness loop to cross the sting balance; tests with and without wire proved that the power wire had a

negligible influence on the measured aerodynamic axial forces (drag and thrust) in the conditions included in the test matrix.

The motor was set to run at the desired voltage, the measurement of the absorbed current was obtained from the power supply and the propeller speed was measured with a laser tachometer through the wind tunnel's window.

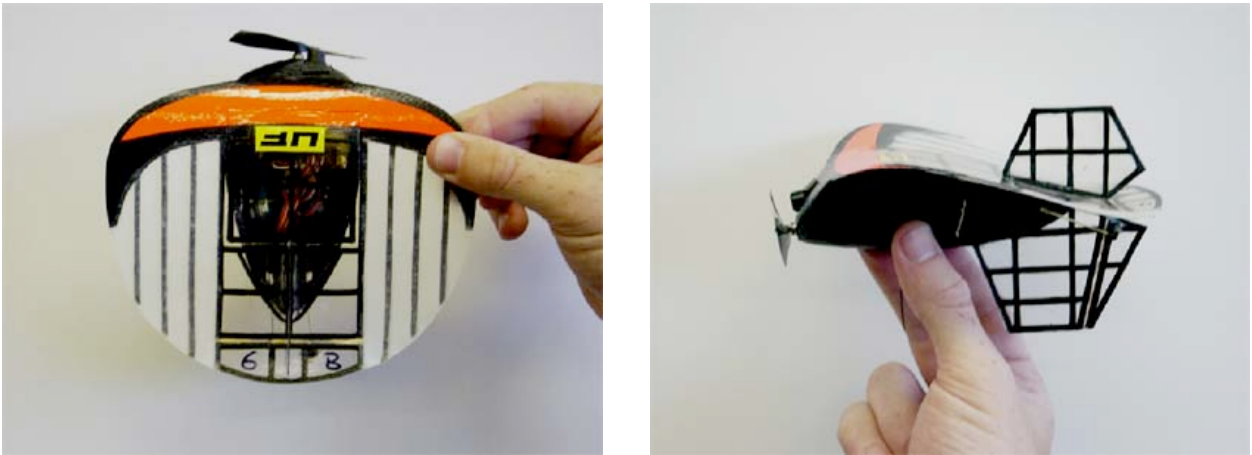


Figure 3-6. A typical complete aerial vehicle equipped for tests in the wind tunnel. The wing in this case is a BR type (Figure 3-3); for structural tests, using the VIC, the upper vertical stabilizer was removed to avoid shadows on the upper wing surface.

3.2 Aerodynamic Coefficients

This section will review the part regarding the measurement of the aerodynamic and propulsion forces on the vehicles with the computation of the related coefficients.

3.2.1 The Wind Tunnel

Historically, Leonardo da Vinci [81], circa 1500, was the first to propose the idea behind a wind tunnel. He wrote that the effects of air flowing on an object are the same as the object moving in still air. Although the first practical wind tunnel was designed and used by Francis Herbert Wenham in 1870, the Wright brothers, in 1901, performed the

first systematic experiments on airfoils characteristics in an operational and technically effective wind tunnel [82].

Because of the scheduled decommissioning of the old wind tunnel at the University of Florida with the purpose of installing a new one, the results presented in this work were obtained from both facilities, with the vast majority, more than 95 %, obtained by using the old open circuit configuration. The new wind tunnel is a closed circuit type and all data were corrected in order to have a full homogeneity and compatibility of results.

3.2.1.1 The open circuit wind tunnel

The facility used during the first phase and the majority of tests, located at the Mechanical and Aerospace Engineering Department of the University of Florida, was a horizontal, open circuit, low speed wind tunnel. The wind tunnel, Figure 3-7, with an overall length of 10 m, had a square section entrance with a bell mouth inlet type and several anti-turbulence screens. The contraction section was designed to provide low turbulence levels in the test section, less than 0.1%. The test section is 914 by 914 mm and a length of 2 meters. A centrifugal type fan is installed downstream and its speed is regulated by a variable frequency controller operated remotely by a personal computer (PC) via the data acquisition (DAQ) system used for the experiments and LabView software. The maximum velocity for test purposes is approximately 15 m/s, with a subsequent maximum Re number of approximately 200,000, based on the model under test.

3.2.1.2 The close circuit wind tunnel

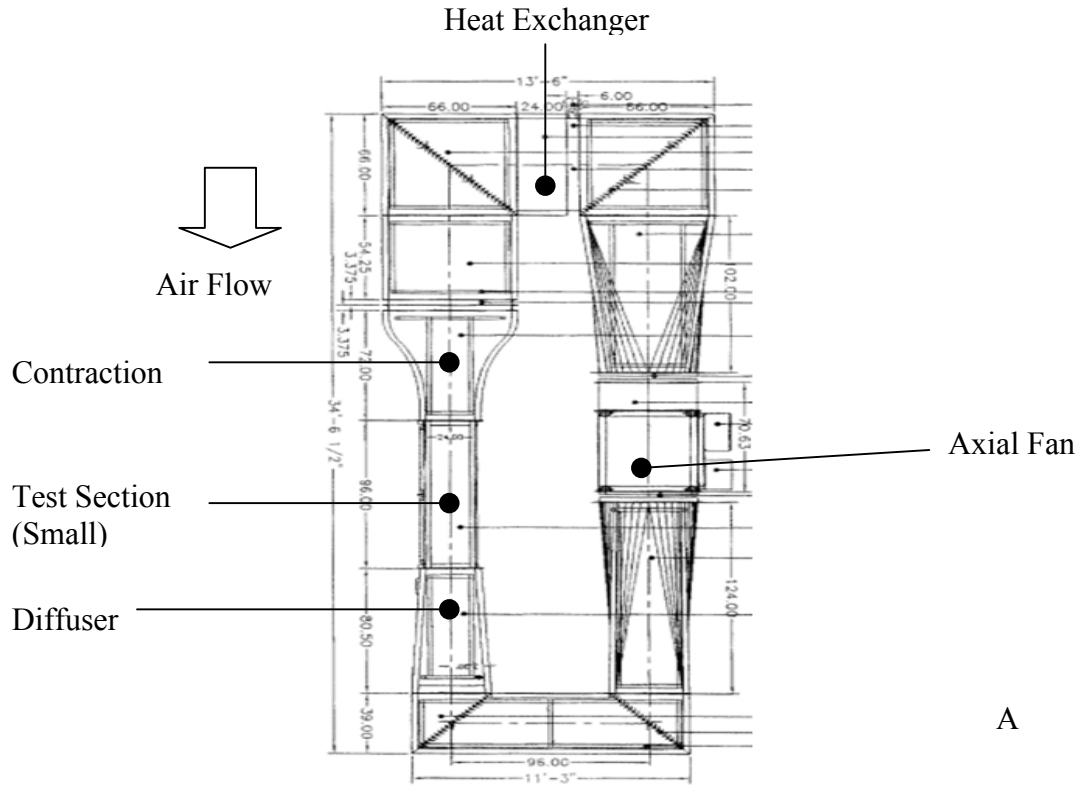
In the course of the implementation of the Mechanical and Aerospace Engineering Department's plan to upgrade the experimental aerodynamic facilities, the open circuit

wind tunnel described in the previous paragraph was decommissioned and a new equipment was purchased and set in operation.

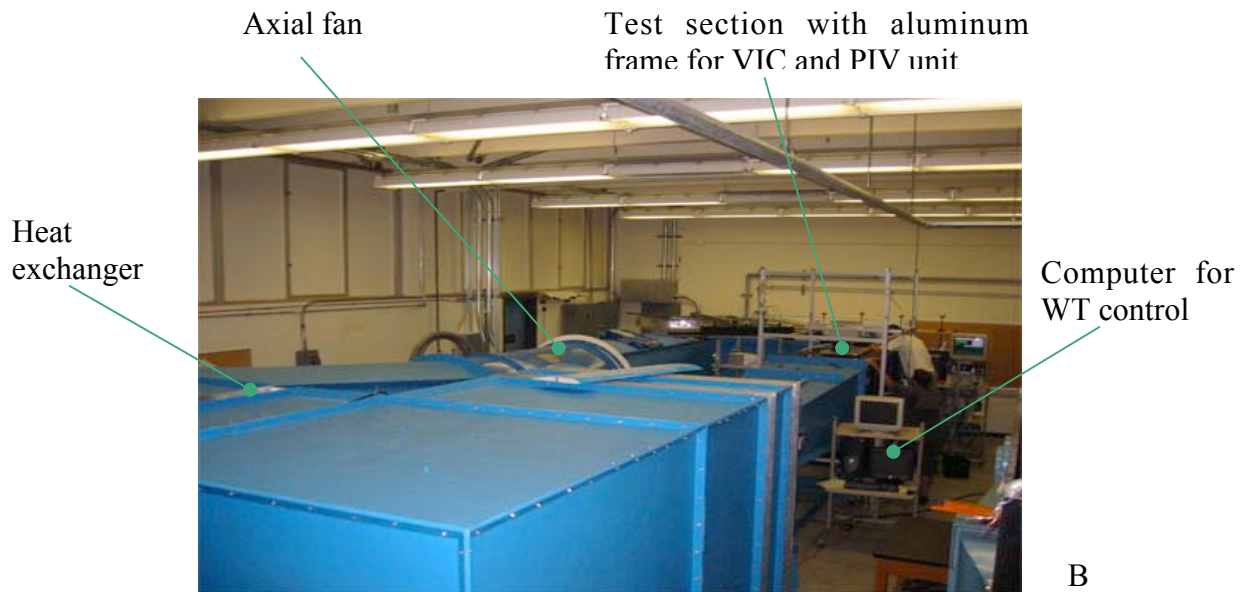


Figure. 3-7. The open circuit wind tunnel.

The new wind tunnel is a Gottingen-type, closed, recirculating design with the flow loop arranged in a horizontal configuration. The overall dimensions of the unit are length 10.72 m, height 2.21 m, width 4.12 m; an axial fan runs the wind tunnel and the flow conditioning is achieved using hexagonal aluminum honeycomb cell, high porosity (60%) stainless steel screen and high efficiency turning vane cascades in the elbows. The airflow temperature can be cooled using the installed heat exchanger, connected to a chilled water system and controlled by a modulating valve with temperature feedback. The system includes two different test sections, one with a square section of nominal side of 24" (60.64 cm) and the other a side of 33" (83.82 cm), to accommodate larger models. The maximum speeds are in the order of 91 m/s and 53 m/s, respectively, with Reynolds numbers achievable in the order of 3.7 and 2.7 millions. Total measured turbulence level is .08 %. Schematic and panoramic views of the wind tunnel are portrayed in Figure 3-8.



A



B

Figure 3-8. The closed circuit wind tunnel. A) schematic top view, B) panoramic image; overall dimensions are 10.72 m, height 2.21 m, width 4.12 m.

3.2.1.3 The sting balance and related hardware

To measure forces and moments, on MAV wings and complete models, an Aerolab 01-15 6-component sting balance was procured and installed in the wind tunnel. The balance, with six channels in a full Wheatstone-bridge configuration, is an internal 5 forces and 1 moment sting balance. Two forces are normal to the balance's axis on a vertical plane (i.e. lift), two forces are normal to the balance's longitudinal axis on a plane perpendicular to the previous plane (i.e. side force), one force is in the axial direction and the only moment is around the longitudinal axis, typically the roll axis. The design of a wind tunnel balance is of necessity a compromise between the required maximum load capability of all components and the accuracy required for minimum loads. In our case, because of a combination of different requirements, the maximum design load capability of the balance exceeds the typical MAV maximum loads. Table 3-4 gives the manufacturer rate loads.

Table 3-4. Sting balance rated loads

Normal Force	± 44.5 N	Pitching Moment	± 2.63 kN·m
Side Force	± 44.5 N	Yaw Moment	± 2.63 kN·m
Axial Force	± 17.8 N	Roll Moment	± 8.77 kN·m

The forces generated by our aircraft utilize only 0.1% to 2.5% of the full-scale range of the balance thus the level of the electrical signals from the strain gauges are very low, in the range of the microvolt, making the data processing particularly challenging.

The balance, which holds the model under test, is connected to an aluminum custom designed arm, illustrated in Figure 3-9. The arm is connected to a gearbox and a brushless servomotor.

A single axis motion controller runs the servomotor, with the driver connected to the personal computer via the RS232 for firmware uploading. A zero to 10 volt analog signal is generated by the DAQ system and sent to the driver via a wire to command the pitching motion. A high precision absolute encoder provides the AOA feedback. The system has been designed to perform tests at steady or unsteady AOA. Dynamic pitching tests can be performed to investigate a variety of phenomena, including vertical gust effects.

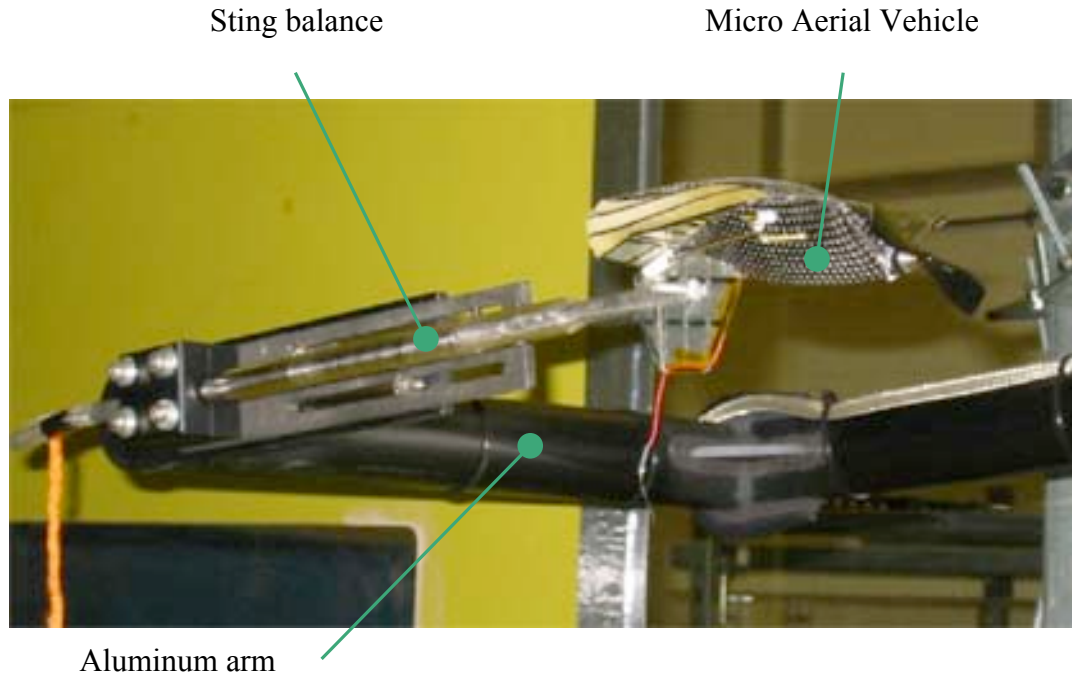


Figure 3-9. A vehicle in the wind tunnel, mounted on the sting balance and on the aluminum pitching arm.

The typical pitching velocity for an AOA sweep in steady tests is 1 degree per second; for unsteady tests the pitching frequencies can be up to 3 to 5 Hertz with amplitudes up to 90 degrees. The balance has a frequency response of several hundreds

of Hertz. All components are assembled on a test rig stand next to the side of the wind tunnel, as depicted in Figure 3-10

3.2.2 The Signal Conditioning System and the Data Acquisition System

The DAQ is a typical National Instruments modular system; the main element is a NI SCXI 1520 8 channels programmable strain gauge module, with full bridge configuration, 2.5 excitation volt and gain 1,000 as typical settings. Other modules include SCXI 1121 signal conditioner module, 1180 feed through with 1302 breakout and 1124 D/A module. A NI 6052 DAQ PAD Firewire provides A/D conversion, multiplexing and PC connection.

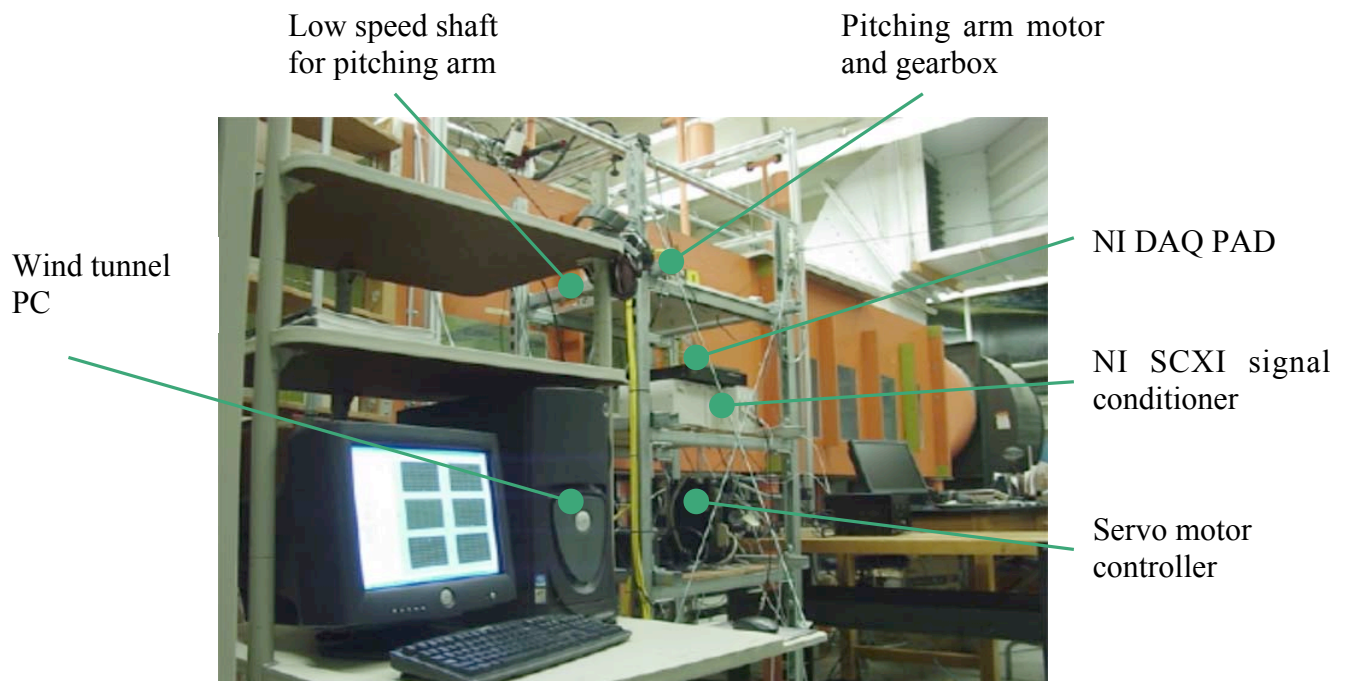


Figure 3-10. Instrumentation and signal processing set-up installed on the side of the wind tunnel.

A 4 wire RTD thermocouple for airflow temperature measurement and the analog output from the US Digital absolute encoder for AOA measurement were connected with

the SCXI 1121 module. A Heise differential pressure sensor, for dynamic pressure readings via a pitot tube, was connected to one of the PC RS 232.

3.2.3 Sting Balance Set-Up

3.2.3.1 Data acquisition

At each angle of attack, the output signals from the 6 channels of the sting balance were sampled 500 times at a frequency of 1,000 Hz. The average and standard deviation were computed repeating this process four times for each test point, for a total of 2,000 samples in a continuous sampling time of 2 seconds; a total average and standard deviation were calculated and stored for following data analysis. The averages were used for the calculation of the loads and the standard deviations were used for the uncertainty analysis. In addition, the signals from the six channels of the balance were recorded with airflow off, at the beginning and at the end of each test sequence (i.e. angle of attack sweep), in order to account for any drift that may occur. The drift was supposed to have a linear behavior with time, also recorded and should be noted that the drift in the signal, in the short time of each experiment, was negligible.

3.2.3.2 Calibrations

An external balance requires a careful calibration. The calibration is of paramount importance for mainly two reasons, to find the relationship between output signal and applied load (or loads) and, in the case of a multi-component balance, to characterize the interactions between channels. The calibration was achieved by loading the balance with certified weights, typically from 1 g to 100 g, at precisely defined loading points and directions, using a special calibration rig. The voltage signals from the balance, on the order of few microvolts, were recorded for each load. At this point a choice was required about the desired accuracy of data and the subsequent data analysis. The requirements

for accuracy on testing MAVs was established in the order of up to 40 % on the minimum drag or, in terms of load, about .01 N.

The above goal and the consideration of the small mechanical deflections led us to neglect second order balance interactions at this stage of testing [83]. Considering the above assumptions, a 6 by 6 calibration matrix was assembled to provide a set of equations for signals as function of loads. The evaluation of the signals from the balance during the tests is performed by the inverse version of that matrix, obtaining the final loads as function of signals. The calibration matrix obtained is valid for the sting balance body axis. The loads from the balance were, in real time, shifted and turned relative to the wind axis, the model's reference system relative to the airflow. The signal of the strain gauge bridge for the component "i" is given by the equation

$$S_i = R_{0i} + \sum_{j=1}^6 A_{ij} F_j \quad (3.1)$$

The obtained system of equations is inverted to

$$[F_j] = [S_i]^{-1} - \{R_{0i}\} \quad (3.2)$$

A preliminary display of the data is performed in real time by a program showing the results on the computer screen fitted with a least square line. The operator has the option, according to the conditions, to accept the test point or to refuse it, without interrupting the test.

The results of the single runs are stored and later analyzed using a custom spreadsheet performing the recommended linear regressions [84, 85] and some statistical measures to quantify the uncertainty in the balance load estimation. For each run a calibration sheet was produced and a file was stored in a database.

A sample of a calibration run is presented in the Figures 3-11 to 3-13. The balance is loaded only in the axial direction. It can be noted the small and linear first order interaction with the roll component in Figure 3-13; the signals in the other channels, normal forces and side forces in Figures 3-11 and 3-12 respectively, were so low that can be considered only noise. Furthermore, the standard deviations in the axial applied force and in the rolling moment are negligible, Figure 3-13, while in the other four channels normal and side forces, Figure, 3-11 and 3-12, are more significant relative to the signals. The voltage resolution in all cases was one microvolt (absolute value).

When loaded in other directions, the interactions were negligible; when the roll component was loaded, a very small and linear interaction in the axial component was detected. The above considerations were used to form the six by six calibration matrix [A] used in Equation 3.1.

Using certified weights, in controlled points and directions, the calibration matrix was later assessed by applying simultaneous loads to the balance. The good agreement between the applied loads and the measured loads was the final acceptance check before the tests in the wind tunnel. A certain level of hysteresis was detected in the axial component for small loads during calibration tests. The problem is probably caused by wire insulation inside the balance and was avoided by changing the AOA always in one direction.

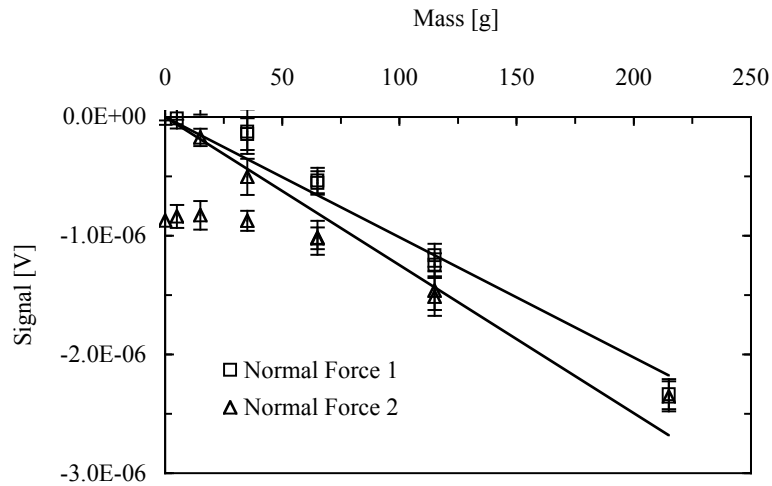


Figure 3-11. Signals from the sting balance during calibration runs. The load was the axial force and the plots represent the first order interactions.

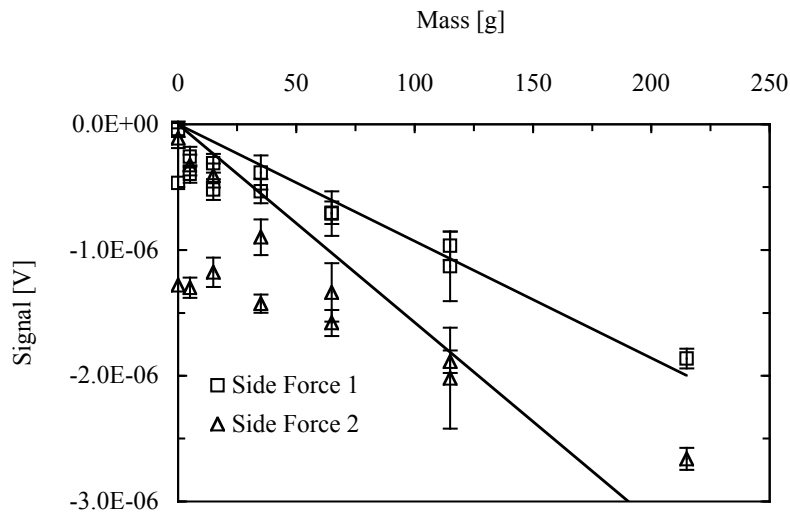


Figure 3-12. Signals from the sting balance during calibration runs. The load was the axial force and the plots represent the first order interactions.

3.2.4 Experimental Procedures

The procedures designed and used for the experiments conducted in the wind tunnel had different goals with a step-by-step approach. The general goal was the check and validation of the overall performance of the system, with the final objective to

establish the capability to perform wind tunnel tests at low and very low Reynolds numbers on a broad variety of aerodynamic situations. The specific goal of this research, and for the experiments conducted during this work, was the characterization of the aerial vehicle systems, divided in two main categories, without and with a working propeller.

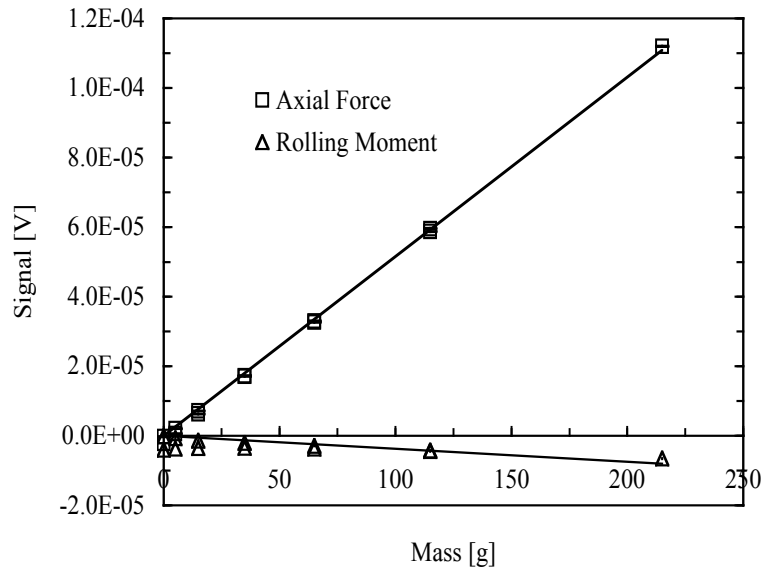


Figure 3-13. Signals from the sting balance during calibration runs. The applied load was the axial force and the plots show the signals from the loaded channel and its main interaction (rolling moment). Note the scale of the plot is two orders of magnitude greater than Figures 3-11 and 3-12.

3.2.4.1 Computation of non-dimensional coefficients

The previous description of the data acquisition process was applied at each angle of attack in a specific test matrix at specified airflow velocity (and Reynolds number) and, if applicable, at predetermined propeller speed. The flow velocity and air density were computed using pressure and temperature recorded inside the wind tunnel at each angle of attack; a high precision absolute barometer located in an adjacent laboratory indicated the static reference pressure. The velocity and dynamic pressure values at the

specific angles of attack, with the reference area of the wing, were used to nondimensionalize the forces and compute the aerodynamic coefficients with the following formulas.

The lift coefficient

$$C_{L,u} = \frac{L}{\frac{1}{2} \rho V_{\infty}^2 S_w} \quad (3.3)$$

The drag coefficient

$$C_{D,u} = \frac{D}{\frac{1}{2} \rho V_{\infty}^2 S_w} \quad (3.4)$$

The pitching moment coefficient

$$C_{m,u} = \frac{M}{\frac{1}{2} \rho V_{\infty}^2 S_w c} \quad (3.5)$$

The side force coefficient

$$C_{y,u} = \frac{Y}{\frac{1}{2} \rho V_{\infty}^2 S_w} \quad (3.6)$$

The yawing moment coefficient

$$C_{n,u} = \frac{\mathcal{N}}{\frac{1}{2}\rho V_{\infty}^2 S_w c} \quad (3.7)$$

And the rolling moment coefficient

$$C_{l,u} = \frac{\mathcal{L}}{\frac{1}{2}\rho V_{\infty}^2 S_w b} \quad (3.8)$$

The propulsion coefficients were computed using two different techniques. From experiments carried with the isolated propeller, the thrust coefficient is

$$C_T = \frac{T}{\rho n^2 D^4} \quad (3.9)$$

The power coefficient

$$C_P = \frac{P}{\rho n^3 D^5} \quad (3.10)$$

Most of the experiments with the active propeller were carried out using a complete MAV. A set of forces were defined by algebraic summation of the aerodynamic lift and drag including the effects of the propeller and solving on the body axes [84] as follows

$$\begin{Bmatrix} N \\ X \end{Bmatrix} = \begin{bmatrix} \Delta D & \Delta L \\ \Delta L & -\Delta D \end{bmatrix} \begin{Bmatrix} \cos \alpha \\ \sin \alpha \end{Bmatrix} \quad (3.11)$$

Using the proceeding forces in the body reference, the following thrust and normal force coefficients were defined, respectively, as

$$C_x = \frac{X}{\frac{1}{2}\rho V_\infty^2 S_w} \quad (3.12)$$

$$C_N = \frac{N}{\frac{1}{2}\rho V_\infty^2 S_w} \quad (3.13)$$

The lift, drag and pitching moment, used in Equation (3.3) to Equation (3.5), when used in the case of the powered MAV, were the “total” aerodynamic forces in the wind axes reference, therefore including the propeller thrust and normal force.

3.2.4.2 Validation runs

Numerous tests were conducted, at the early stage of this work and in the open circuit wind tunnel, using models in which results could be found in the literature, with the purpose to check the validity of our results. Results for a sphere were compared with data from Refs. [4, 86]. Figure 3-14 shows a general convergence of data; the scatter in the experimental points was attributed to a combination of the turbulence level of the free stream in the wind tunnel and to the particular Re number region in which we are operating, prone to whimsical changes of the coefficient of drag.

The results were more accurate at higher Re number, where the drag force is higher compared with the lower velocities.

Additionally, tests conducted using flat plates were compared with data from Ref. [14]. In Figure 3-15 we can see very good correlation between published data and results

from our experiments. The flat plate used in these tests were slightly different from the model used in Ref. [14] in the thickness (1.2 % of c and 2% respectively) and in the leading and trailing edges, elliptical type sanded by hand the first and machined by CNC machine the second. Note that in the area of low lift coefficient, the drag forces are in the order of .05 N and the difference between published data and our experiments is in the order of .01 and .02 N. Additional tests were run with a Clark-Y airfoil with excellent match between actual and published data.

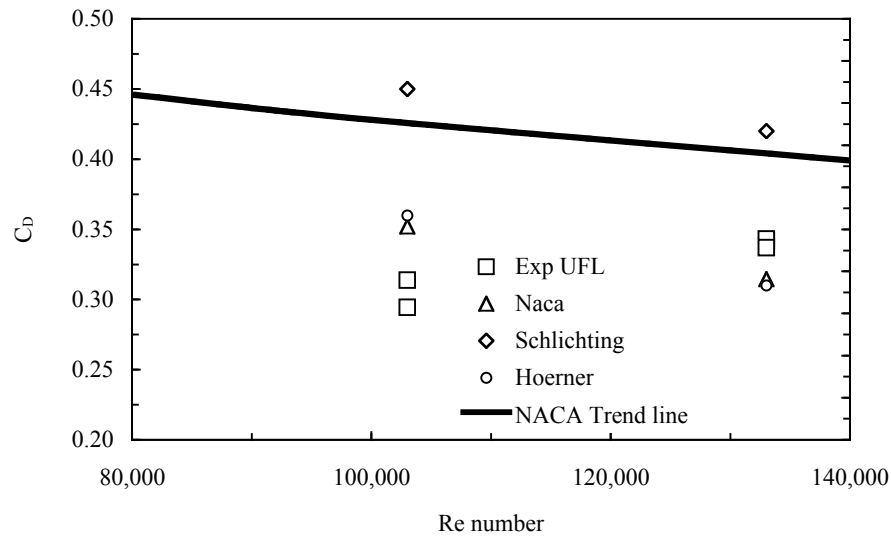


Figure 3-14. Results for the drag of a sphere at the University of Florida wind tunnel compared with results from some publications.

The aerodynamic loads on the isolated sting balance, without any model attached, were evaluated at different dynamic pressure and were found insignificant compared to the minimum forces produced by the wings. Accurate tares were always performed before every test series.

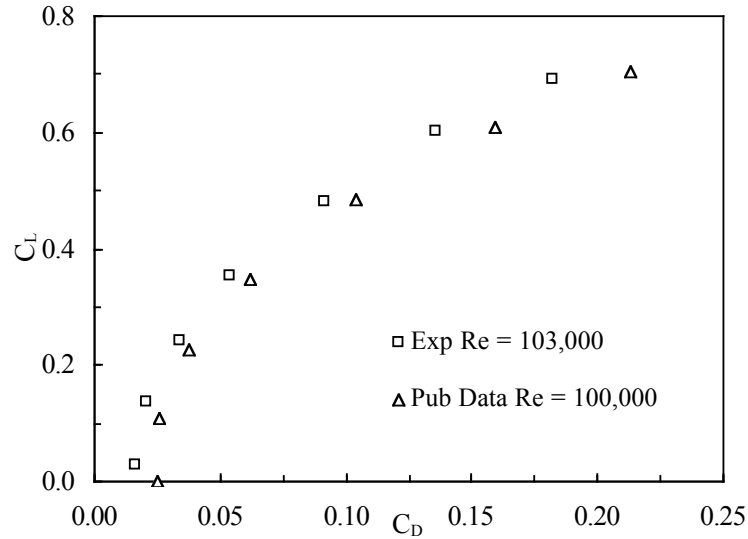


Figure 3-15. Results for flat plates at the University of Florida wind tunnel compared with results from Ref. [11].

3.2.4.3 Test procedures without propeller

A typical test starts with the input in the software of the model position in the reference to the sting balance center, the sequence of the desired AOAs and the model geometric characteristics. This is followed by the acquisition of the tares with the wind off, at each angle of attack. A set of zeros are acquired at the start and at the end of the run for further analysis, and eventual corrections due to the drifting of the signals. The tare matrix will be selected and the tests can start with the airflow on and repeated at every desired dynamic pressure.

The software performs all data conversions in forces and displays, in real time, the six coefficients (C_L , C_D , C_y , C_l , C_m , C_n) vs. AOA. At the end of the run the data were stored in a file for further analysis. The procedure is schematically illustrated in Figure 3-16.

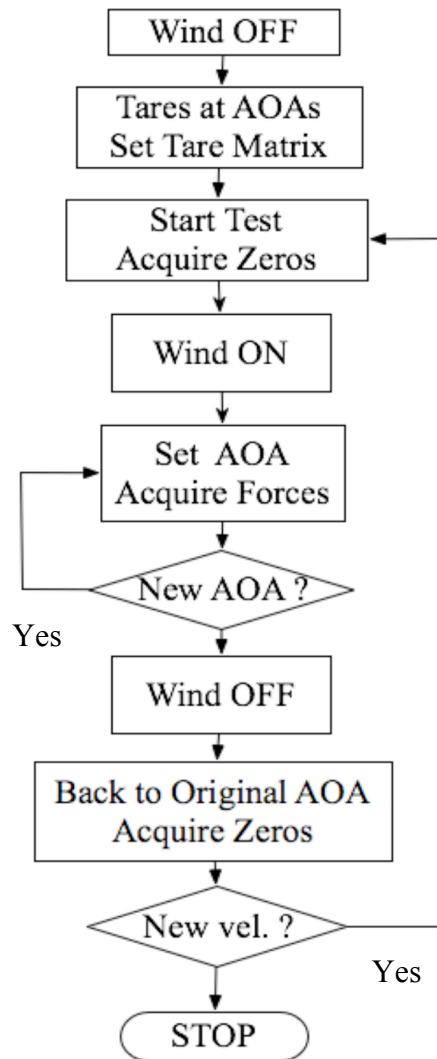


Figure 3-16. Flow chart of a typical wind tunnel test procedure for a vehicle without a powered propeller.

3.2.4.4 Test procedures with powered propeller

The basic procedure with the propeller running is the same then the one without propeller. The set-up requires a power supply for the electric motor and measurements of voltage, current usage and propeller speed at each test point. The test points are defined as a sweep of angles of attack at specified voltage settings. The propeller speed was

measured at each AOA using a laser tachometer. At the end of the run the data were stored in a file for further analysis. The procedure is schematically depicted in Figure 3-17.

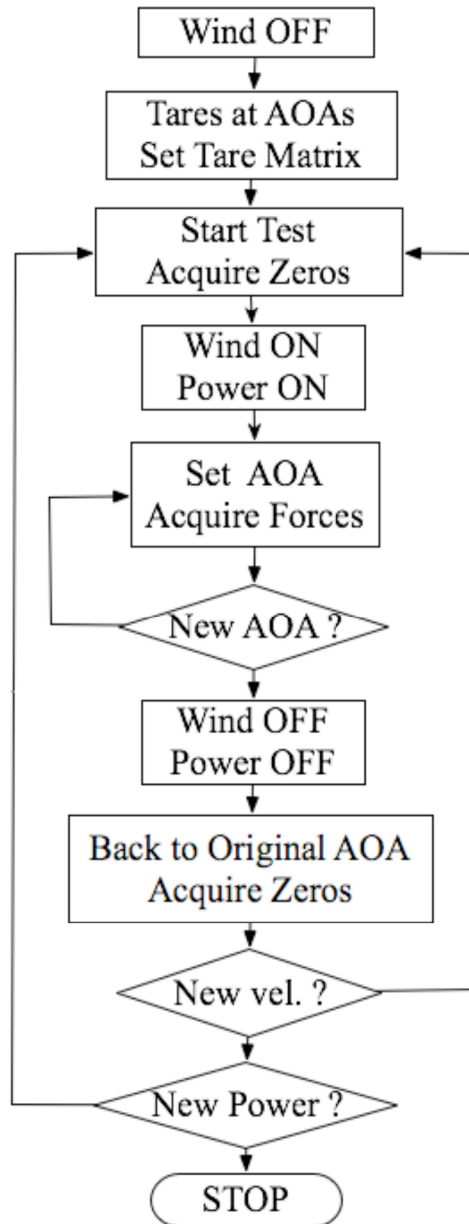


Figure 3-17. Flow chart of a typical wind tunnel test procedure for a vehicle with a powered propeller.

3.2.5 Measurement Uncertainties

An error sensitivity analysis was performed for the three aerodynamic coefficients C_L , C_D and C_m , as explained in Appendix B. The largest sources of uncertainty were the quantization error and the uncertainty deriving from the standard deviation of a given output signal. The quantization error, due to the use of 16 bit DAQ cards, was found negligible. Other minor sources of uncertainty were identified as the errors associated with solving the balance forces and moments, the AOA measurements and the free stream velocity determination deriving from dynamic pressure measurements using a pitot tube and temperature readings.

Less important error factors are also uncertainties in the determination of model geometric quantities such as wing area and reference chord. The sting balance was designed for loads in the order of 50 N, much higher than the loads measured with MAVs (in the order of 0.5 N) therefore even with the use of very precise instrumentation it is reasonable to expect the main source of error to be the balance [28]. A preliminary estimate of error was done by running calibration check runs, giving the necessary confidence in the results to go ahead and run tests. A complete analysis on the uncertainties, based on Ref [87], was performed and is available in Appendix B.

Some examples of results are in Figure 3-18, 3-19 and 3-20, in the form of plots of the aerodynamic coefficients C_L , C_D and C_m with their respective error bound about each data points. The error bound generally increased with the decreases of the loads, but it was always within acceptable limits as showed in Appendix B.

The following plots are relevant samples at a medium free stream velocity corresponding to cruise flight speed for the vehicle.

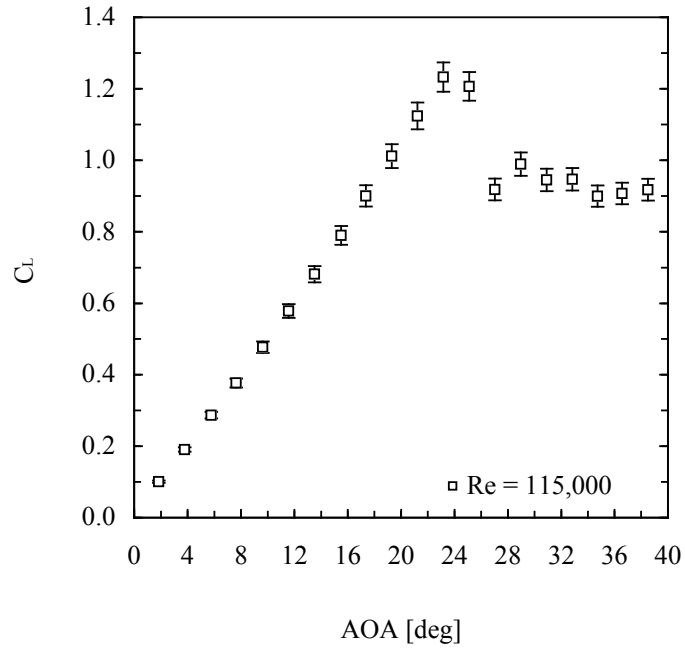


Figure 3-18. Uncertainties bounds for the coefficient of lift, at a free stream Reynolds number of 115,000.

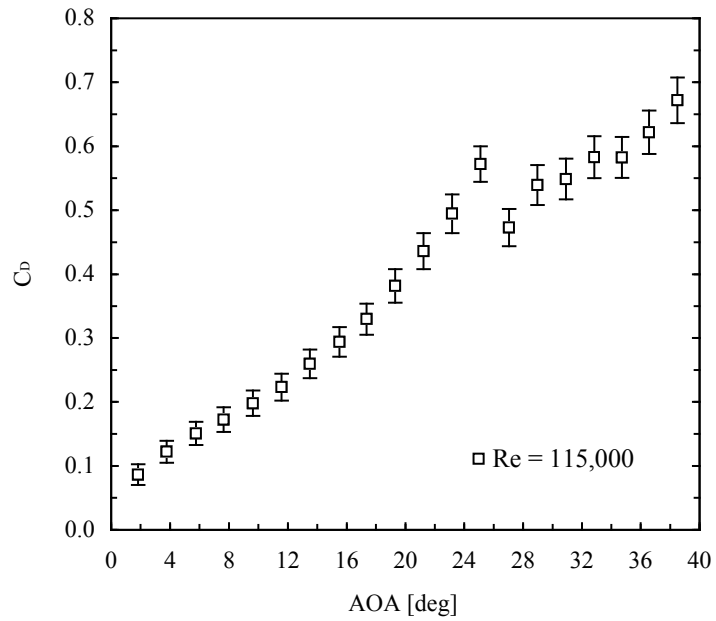


Figure 3-19. Uncertainties bounds for the coefficient of drag, at a free stream Reynolds number of 115,000

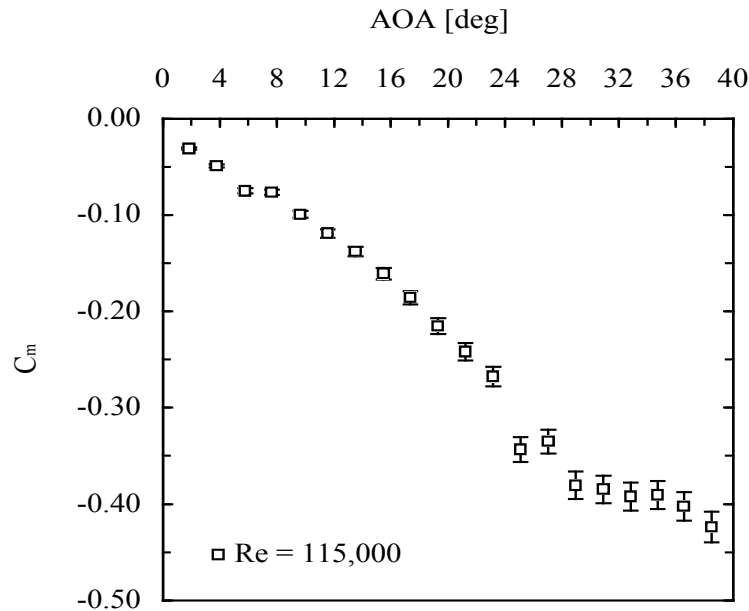


Figure 3-20. Uncertainties bounds for the coefficient of pitching moment, at a free stream Reynolds number of 115,000.

3.2.6 Wind Tunnel Corrections

The wind tunnel corrections applied to the coefficients of lift, drag and pitching moment are the classical for wind tunnel blockage (streamline curvature, solid blockage and wake blockage), as described in [84, 88 and 10] and explained in details in Appendix A.

The Reynolds numbers computed in this work were based on the nominal chord at the wing root, without any correction. The effects of wall interference during AOA sweeps was not an issue, even at high angle of attack, because the pitching axis of the models could be set at the leading edge or at 25% of the \bar{C} (or in any other position) as desired. The reference free stream velocity in the test section was always set with the model close to zero degree AOA to determine the reference Reynolds number.

3.3 Structural Deformation: Visual Image Correlation (VIC)

This section will review the part regarding the measurement of the static aeroelastic deformations of the wing's structure including the effects of the propulsion system. A brief introduction will be followed by a description of the experimental system used, the post processing of the data, the experimental procedures and a description of the models.

3.3.1 Introduction

A comprehensive experimental investigation of the characteristics of a MAV with flexible lifting surface, performed in a wind tunnel, requires not just the measurement of the aerodynamic coefficients, but necessitates also an accurate experimental description of the deformation of the wing. The flexibility of the wing's structure and the thin and in most cases highly elastically stretchable wing skin makes the air flow-structure interactions a paramount factor in the aerial vehicle aerodynamic and flight characteristics. In this work the visual image correlation (VIC), a non-contacting full-field measurement technology, was implemented and used in the wind tunnel characterization of the micro aerial vehicles.

3.3.2 The Principle of VIC

The digital image correlation method was originally introduced in the early '80s by researchers from the University of South Carolina [89-91]. The principle of the technique is to devise the displacement of the material under test by tracking the deformation of a random speckle pattern applied to the specimen's surface in digital images acquired during the loading, as schematically depicted in Figure 3-21.

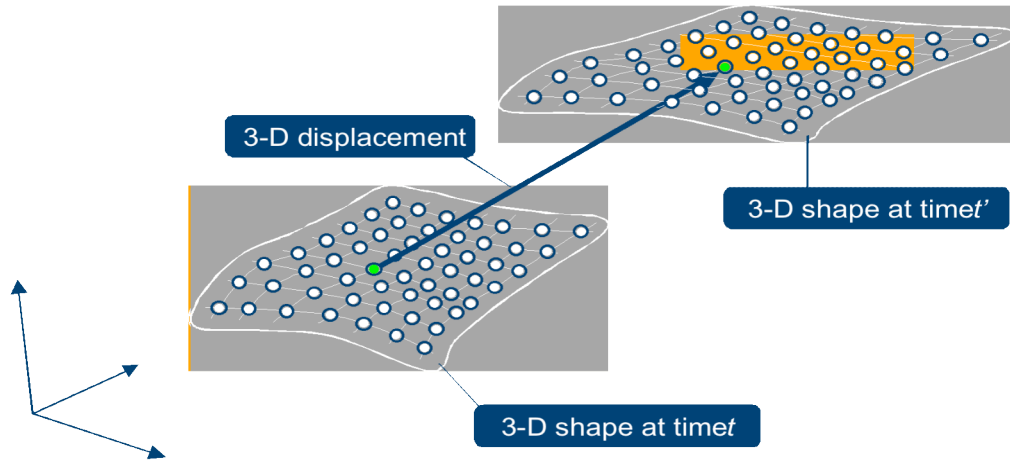


Figure 3-21. Measurement of displacements of object points on the specimen's surface.

Analytically, the task is achieved by finding the region, in an image of the deformed specimen that maximizes the normalized cross-correlation function $C(x_p, y_p, u, v)$ corresponding to a small subset of the reference image, taken when no load was applied. The correlation function assumes the following form

$$C(x_p, y_p, u, v) = \sum_{i, j=-n/2}^{n/2} (I(x_p + i, y_p + j) - I'(x_p + u + i, y_p + v + j))^2 \quad (3.14)$$

Where x_p and y_p are the Pixel coordinates in the reference image (with no load applied).

By repeating this procedure for a large number of subsets, full-field deformation will be obtained. The strains will be obtained by finding the gradient of the displacements. In dyadic notation, the strain tensor is

$$\mathbf{E} = \frac{1}{2}(\mathbf{u}\bar{\nabla} + \bar{\nabla}\mathbf{u}) \quad (3.15)$$

The system used in this work uses two cameras, enabling the characterization of three-dimensional shape as well as the measurement of the three dimensional deformation [91, 92]. The three dimensional technique requires using at least two synchronized cameras acquiring images of the specimen from different viewing angles. By determining reciprocal image locations across views from the cameras, and tracking the movement throughout the loading cycle, the shape and deformation of the specimen can be reconstructed, based on a simple cameras calibration.

3.3.3 VIC Technique

This section will provide a description of the VIC technology in general principles, since a detailed in depth analysis of this technique was not the scope of this work and will be referenced to specialized publications. The section will also provide a detailed description of the data post-processing, experimental procedures and models preparation used in this research.

3.3.3.1 Hardware and data acquisition system

The experimental set-up for the VIC is relatively simple. In the two-dimensional case, when only in-plane displacements measurements are required, only one camera is needed, as schematically depicted in Figure 3-22. For three-dimensional measurements, two cameras are necessary and sufficient, as represented in Figure 3-23, to capture the off-plane geometries, before and after the application of the loads.

For the specific case of this project, two cameras were installed at the top of the wind tunnel, Figure 3-24. Optical access into the test section was through a float glass window. Schreirer, Braasch and Sutton [94] have carefully investigated the effects of a glass interface; the cameras are calibrated through the window to ensure minimal

distortion effects. Two continuous 250 Watt lamps illuminate the model, enabling the use of camera exposure times of 5 to 10 ms.

Energy emitted by the lights, a potential hazard for the specimen, was not a concern due to the cooling effect of the wind tunnel flow rate, typically from 8 to 13 m³/s. Images are digitally stored for later processed. The cameras and the lights were mounted on an aluminum frame completely independent from the wind tunnel's structure, with the purpose to isolate them from the inevitable vibrations of the wind tunnel when running, Figure 3-25.

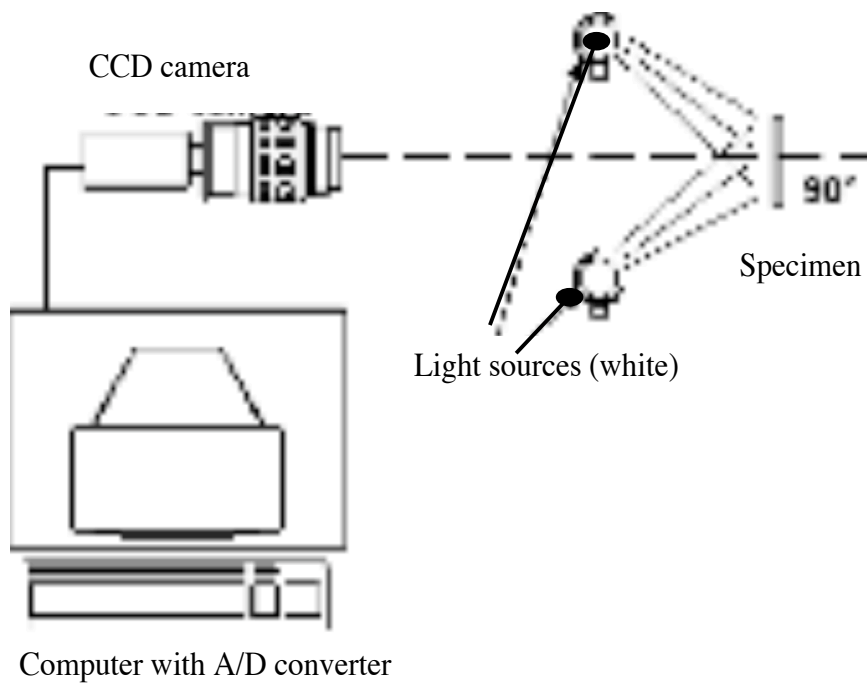


Figure 3-22. VIC system set-up for two-dimensional measurements (in-plane displacements and strains).

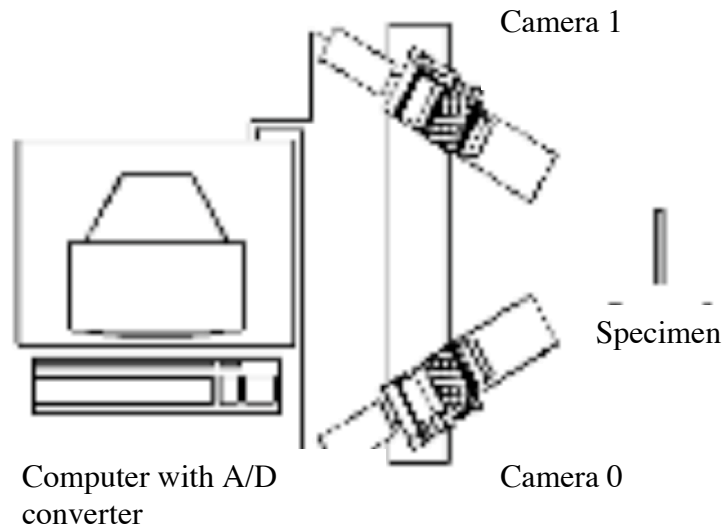


Figure 3-23. VIC system set-up for three-dimensional measurements (out-of-plane displacements and strains).

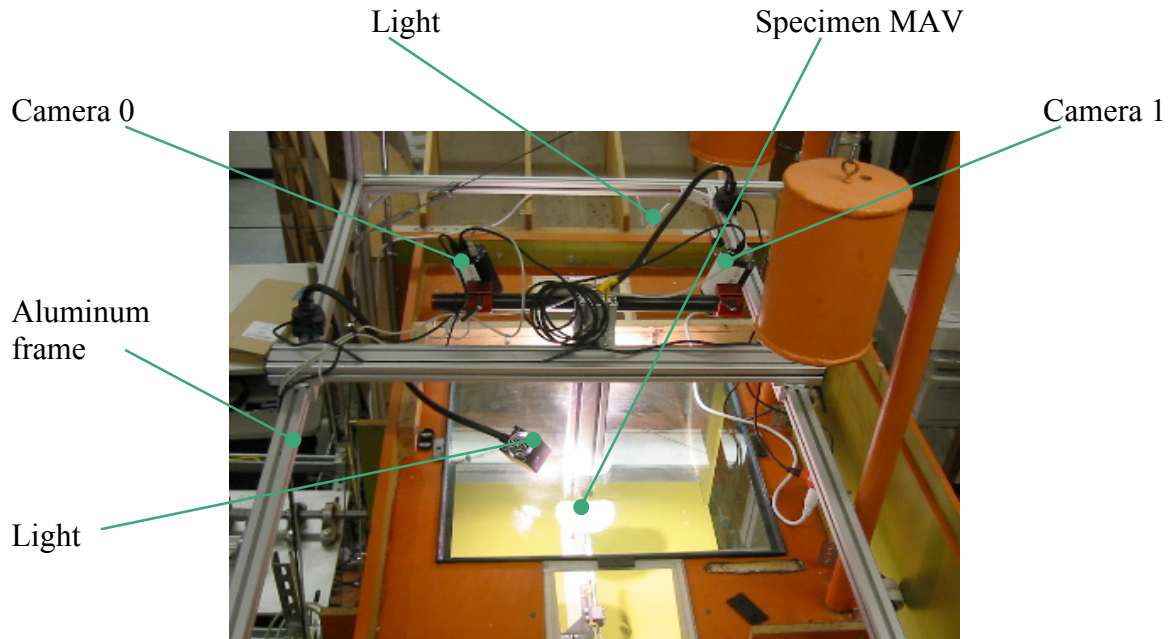


Figure 3-24. View from the top of the wind tunnel, showing the installation of the two cameras.

According to the standard specifications [93] from the company that developed and delivered the VIC system, the cameras were connected with the computer via IEEE 1394 (Firewire) and synchronized for instantaneous shots. A standard acquisition board installed in the computer performs the digitalization of the images, and the image processing is carried out by custom software [93]. Although the exposure time could be very short (10 ms or less) and the acquisition rate can be quite fast, in the order of 50 frames per second or more, the maximum achievable acquisition rate is three frames per second. The limiting factor is the storage of the pictures, which in the described system is performed by the computer's hard disk. To achieve faster rates, on the order of thousands of Hertz, cameras with on-board memory need to be used. A schematic view of the layout of the system is depicted in Figure 3-26.

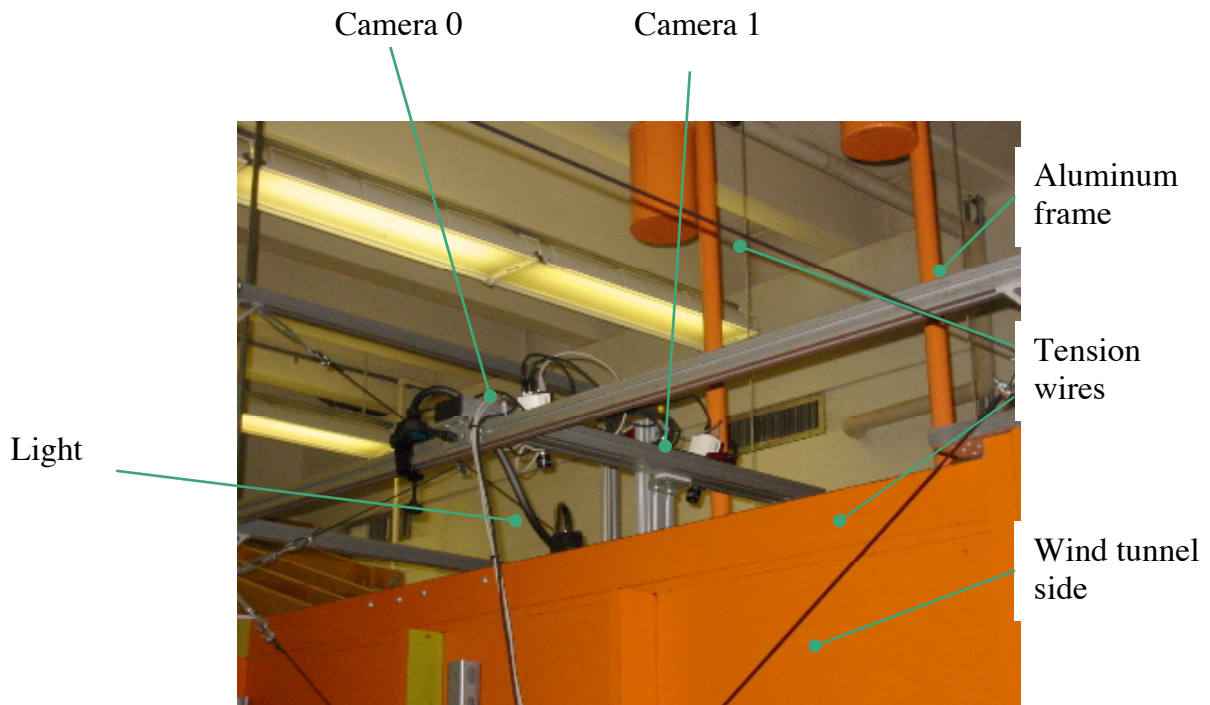


Figure 3-25. View of the side of the wind tunnel, showing the installation of the two cameras on the aluminum frame.

3.3.3.2 Image processing

Among the available techniques a particular method [91] has established itself as the preferred method for deformation analysis due to its reliability, excellent accuracy, simple application and capability to measure arbitrarily large rotations and strains in excess of 500%. The algorithm is based on an iterative solution procedure for finding the maximum of the cross-correlation coefficient in an n-dimensional parameter space. The parameter space is swept by the parameters of a mapping function that transforms coordinates from the original image frame to coordinates in the deformed image and typically include the mean displacement in the horizontal and vertical direction, as well as the four gradients of the displacements with respect to the coordinate axes. Using this parameterization, an originally square area in the un-deformed image, Figure 3-27, can be mapped to a subset in a deformed image, after being subjected to any combination of deformation and motion.

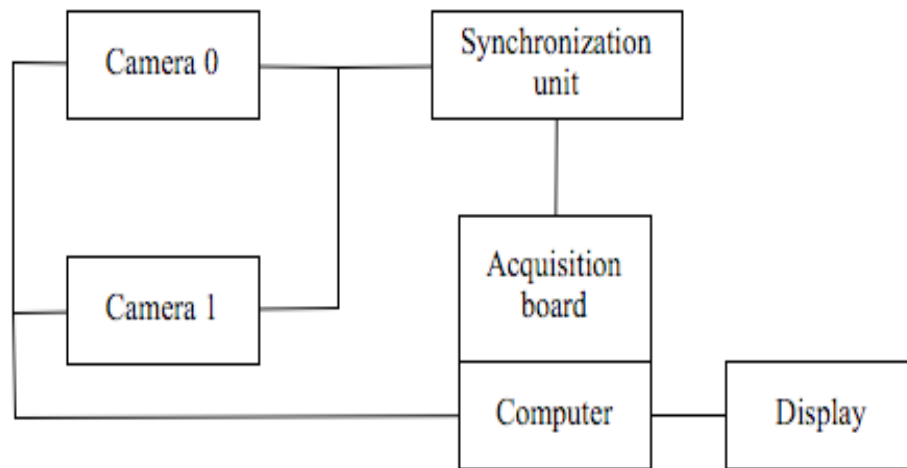


Figure 3-26. Lay-out of the digital image correlation system in the configuration used in this work. The cameras do not have data storage capabilities.

As the deformed coordinates will not fall onto the sampling grid of the image, accurate grey-value interpolation procedures [94] are performed to achieve optimal sub pixel accuracy without bias. A schematic description of the scheme is illustrated in Figure 3-28.

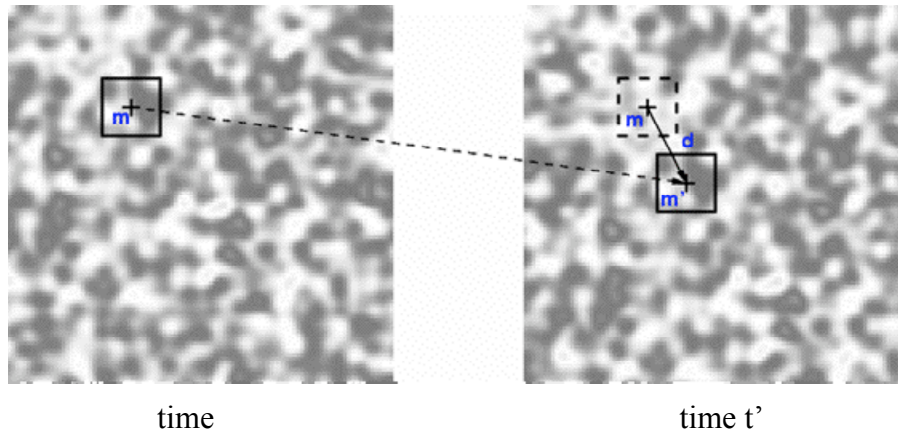


Figure 3-27. A square subset used for cross correlation function estimation. The two images represent the two cases at time t (reference image) and at time t' (deformed image).

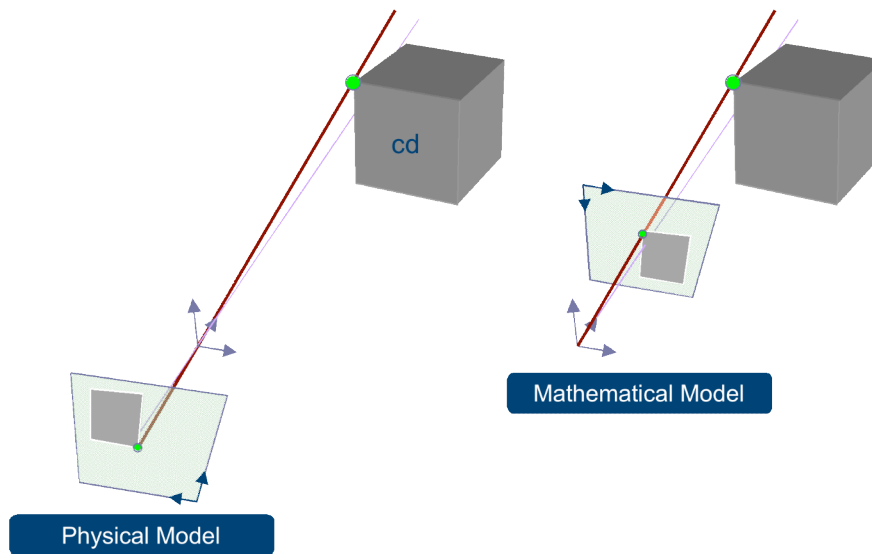


Figure 3-28. Schematic of the pinhole model leading to the central perspective projection.

For the three-dimensional case, a minimum of two cameras is used and a similar algorithm is used. However, the acquisition of the images is based on the stereo-triangulation technique and the computing of the intersection of two optical rays is required. The optical-geometric diagram of stereo-triangulation is schematically illustrated in Figure 3-29.

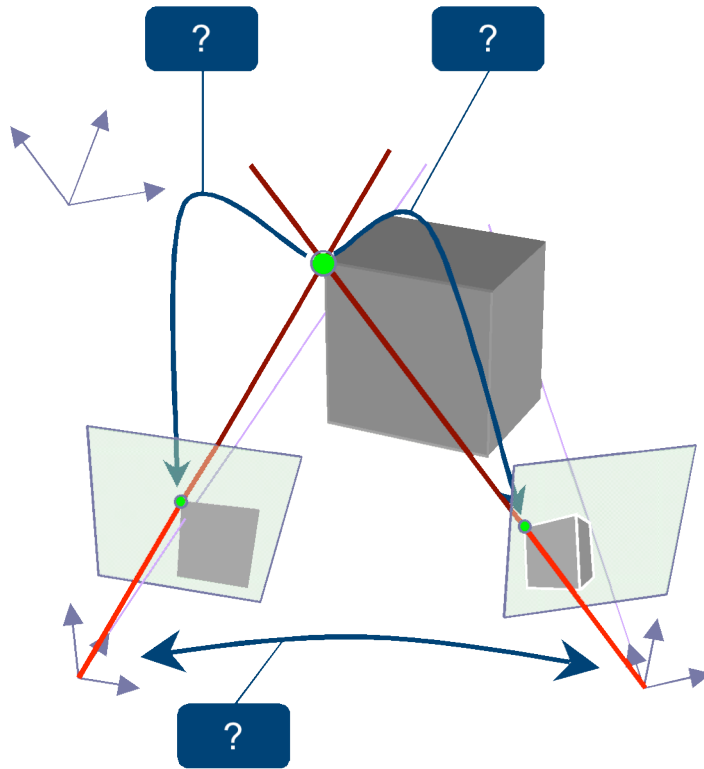


Figure 3-29. Schematic illustration of the stereo-triangulation scheme. Question marks represent the required intersections of optical rays.

The mapping function is now based on the known parameters of the cameras, and the sought parameters are the location and orientation of a segment of the surface assumed to be locally planar. For deformation measurements, additional parameters are added to the mapping functions, describing the orientation and position of the surface

segment after the deformation as well as parameters describing higher-order deformation terms. This process is called projection / back-projection technique. If we envision a fictitious two-dimensional frame, with the two images from the two cameras acquired at the same instant as one coordinate (called axis 1) and time as the other coordinate (called axis 2), the three-dimensional reconstruction of the object is obtained using matching by stereo-correlation applied in the direction 1, combined with tracking (temporal matching) applied in the direction 2, as illustrated in Figure 3-30.

Both processes need the application of the previously described stereo-triangulation, and a careful cameras calibration is required.

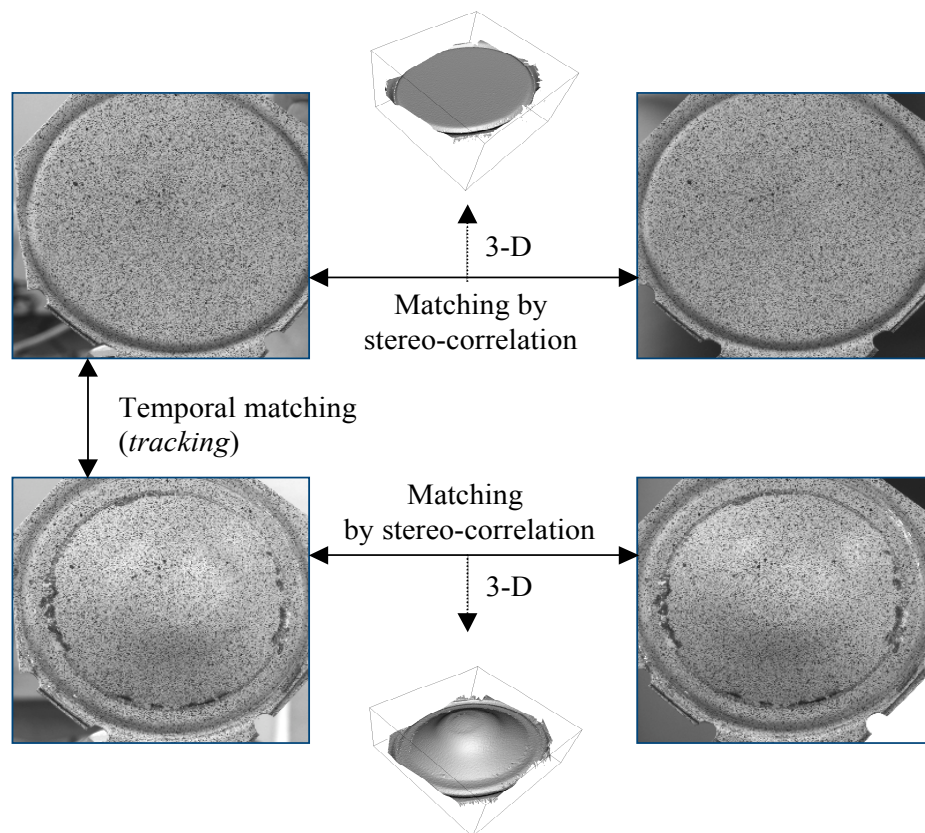


Figure 3-30. Schematic depiction of matching between two images acquired at the same time and tracking of two pairs of images acquired at different times (and possibly at two different load statuses).

3.3.3.3 Calibrations

In contrast to the two-dimensional case, where camera calibration is simply the determination of a scale factor, three-dimensional systems must be calibrated. The two cameras have to be mounted on a rigid support to avoid relative motion of the cameras during and after the calibration. An aluminum bar mounted on a frame around the wind tunnel was used, as illustrated in Figure 3-24 and 3-25. The cameras were not moved for the duration of the tests. The calibration process consists of the acquisition of a series of images of a calibration target in random orientations and roughly at the same distance between the cameras and the specimen. Rotations can be around all the three axes and one image (for each camera) was acquired at every position, for a random number of times (generally between twenty and thirty). The geometric characteristics of the target were selected according with the distance and dimension of the area investigated on the specimen and the lenses size.

Examples of some images of the calibration target are portrayed in Figure 3-31; from those images calibration parameters for the two cameras, as well as their relative orientation, were determined fully automatically [93].

The calibration process is a simple and straightforward procedure; a paramount detail is the quality of the target, usually black with extra precise and very sharp white dots. The opposite configuration, black dots in a white background, is a possibility and it was used in the early stage of this research.

At the conclusion of the calibration routine, in less than a minute, a table of calibration quality parameters, one for each image and one global are listed; the operator

will decide the goodness of the calibration and, if accepted, those parameters will be stored and later used by the system during the post processing of the tests.

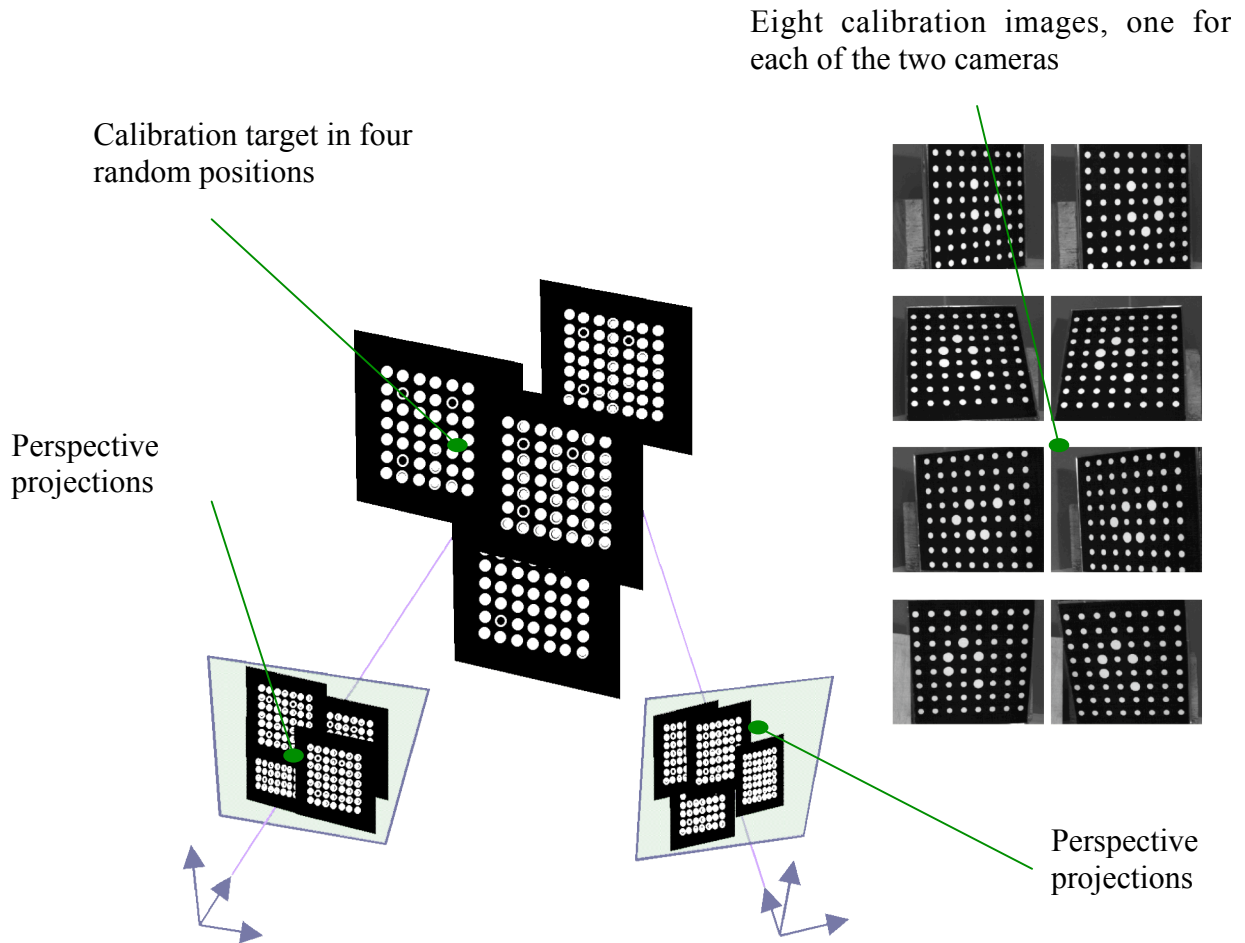


Figure 3-31. Schematic depiction of calibration images. The target is moved four times, and eight images, one for each camera, are stored and processed for calibration parameters identification.

3.3.4 Experimental Procedures

Two test procedures were developed to achieve the main objectives of this research: to ascertain the aerodynamic characterization at different free stream velocities and at different motor settings, and to determine the deformation of the wings under

steady aerodynamic loads. This section will describe the structural part of the procedures. With both the experimental techniques used, the sting balance for force measurements and the VIC, for structural deformation measurements, the deciding factor for a different procedure was the presence of the powered propeller.

3.3.4.1 Tests procedures without propeller

The objective was to determine the deformation of the wings under steady aerodynamic loads, in different steady conditions of AOA and free stream velocity. The reference to measure the displacement was the wing at the specified angles of attack, with zero free stream velocity. In this case, the wing will be only loaded by the skin pretension applied during the fabrication. Because this condition was used to take the reference images for VIC, the pretension will not appear in our results. This condition needs to be carefully considered in the evaluation of the results, because this can generate areas of “virtual” compression in the skin membrane, which is physically impossible, due to areas of relaxation of the pre-existing tension.

Some experiments were performed using as reference the latex skin before the application on the wing, thus in a relaxed unloaded status. In that case it was possible to measure an “absolute” strain situation when the loads were applied. The sequence of events, graphically illustrated in Figure 3-32 was first to take a picture of the model at the set angle, with wind off. Next was to start the wind tunnel up to the desired dynamic pressure, and when stable conditions were reached, take the picture of the deformed wing. Then the airflow was stopped, and the model was automatically moved to the next AOA. At the same time, the system was recording the aerodynamic loads. This sequence was repeated for the selected angles of attack, 5 or 6 levels (from 4 degrees up to the limit

of the linear part of the lift curve, 20 or 22 degrees) at the selected flow velocities, typically 13, 11.5, 10 and 8 m/s.

The aerodynamic characteristics and the deformations of the different wings have also been compared to a nominally rigid wing built, from the same mold, by several layers of solid carbon fiber.

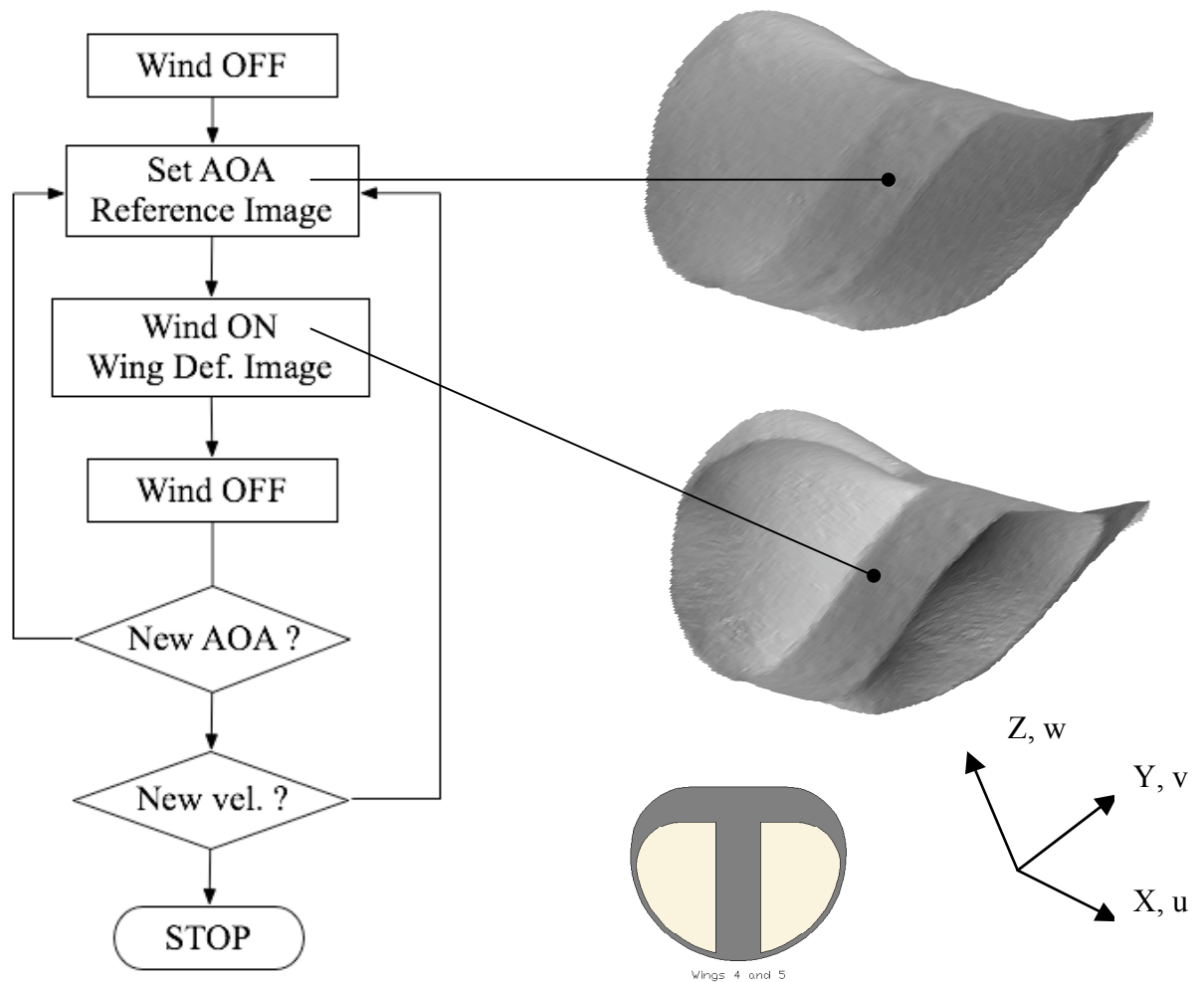


Figure 3-32. Schematic view of the procedure for the digital image correlation tests in the wind tunnel. This sequence was applied for every AOA tested with isolated wings. The wing depicted in the Figure is a PR model.

3.3.4.2 Tests procedures with powered propeller

The objective was to determine the deformation of the wings induced by the propeller slipstream under steady aerodynamic loads. As for the previous section, a reference was needed to measure the displacements of the wing. For that purpose an image with motor off and wind tunnel flow off was taken at selected AOA in the test matrix.

For every test run and at each AOA, a sequence of three steps was performed. First was to take the reference image with wind tunnel flow off and motor off. Then the wind tunnel was set to the desired dynamic pressure and another picture was taken. Finally, the vehicle's motor was set to the required input voltage. When stable conditions were achieved, another set of images of the deformed wing was captured. At the same time, the forces were measured by the sting balance. The input voltage to the motor was attained using a high precision DC power supply with overload control for precise current measurement and the propeller speed was obtained by a laser tachometer.

Next the motor and the wind tunnel flow were turned off, and the model was automatically set to the next AOA. This sequence was repeated for the selected angles of attack, at the selected flow velocities (typically 8, 10, 11.5 and 13 m/s), and at the planned motor settings (7.4, 7.0 and 6.6 Volt). A schematic representation of the experiments procedure is depicted in Figure 3-33.

The aerodynamic characteristics and the deformations of the vehicles with flexible wings have also been compared to the same vehicle equipped with a nominally rigid wing manufactured by the same mold, using several layers of solid carbon fiber.

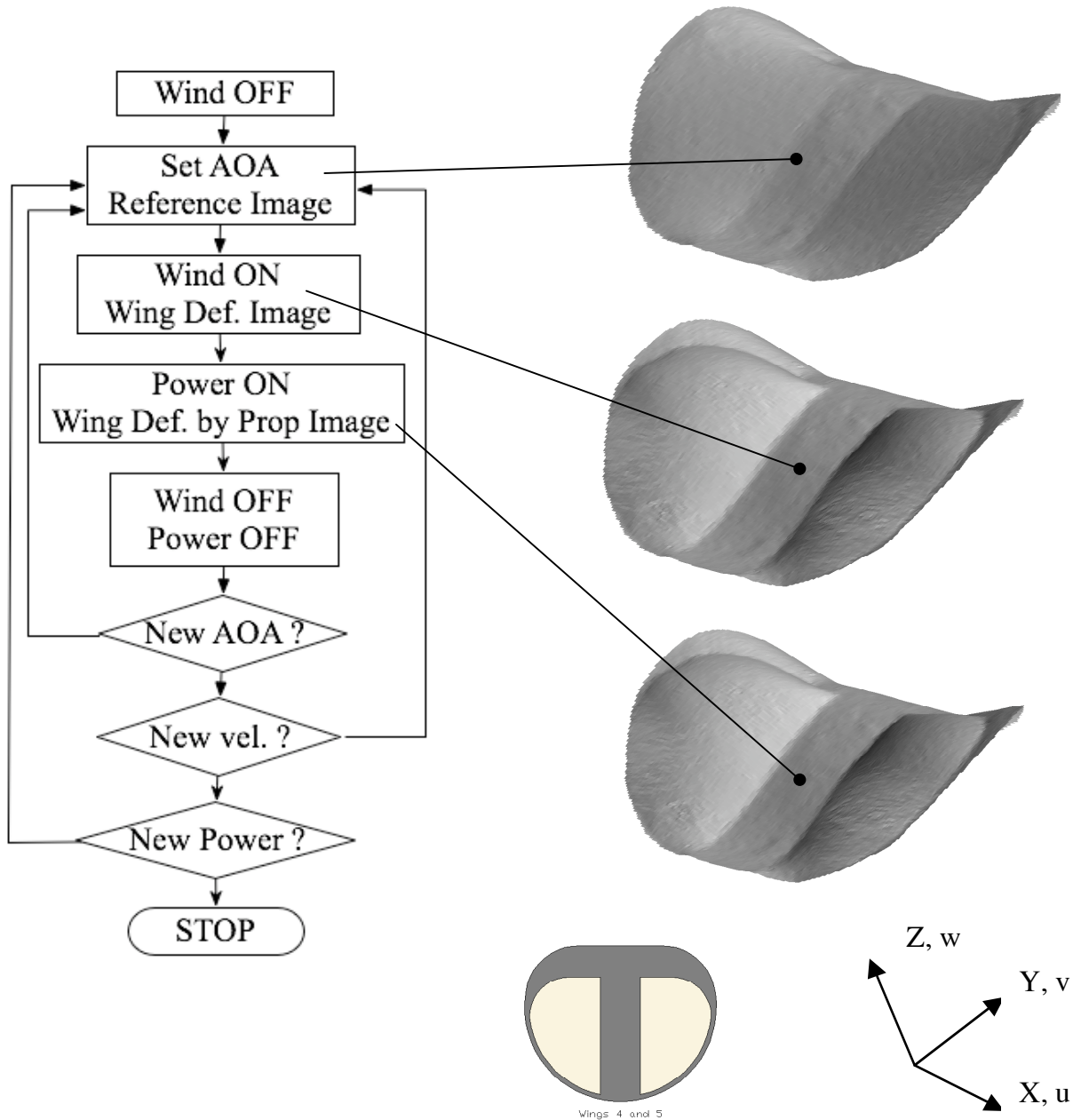


Figure 3-33. Schematic view of the procedure for the digital image correlation tests in the wind tunnel. The wing depicted in the Figure is a PR model.

3.3.4.3 Data post processing

The data analysis was performed for every test run, consisting of the reference picture and the related deformed images, by using the post processing included in the VIC system software [93]. Figure 3-33, in the previous section, is an example of the 3D geometry of one wing, in this case was the type PR. The coordinate reference system (X , Y , Z) is a body system. The unloaded (and non deformed) state is the top image. This is considered the reference image. The same wing under deformation due to the free stream dynamic pressure is portrayed in the middle image. The image at the bottom shows the deformation, if any, due to the propeller slipstream superimposed to the free stream velocity in the wind tunnel. The billowing of the wing skin, due to the acting dynamic pressure, is very evident.

The system software computes the main variables, namely the body coordinates, the displacements (u , v and w), the strains in the reference axes and the principal strains. Any variable could be visualized in three-dimensional plots or in the two-dimensional plane X - Y , on a section chosen by the operator using a menu driven procedure. The two-dimensional data could be plotted or saved in an Excel file.

The most basic output of the system is a file with the three-dimensional grid of the model with the values X_d , Y_d and Z_d of the geometry and the displacements u , v and w , in the same coordinate reference system. The grid points are approximately 15,000 and their number is roughly dependent by the density of the random speckle applied to the surface. As previously discussed in section 3.2.2, the grid density is automatically selected by the system with the purpose to obtain the optimal sub-pixel accuracy. Strains in X , Y and W directions, as well as principal strains, are also an option in the same

output file. The file is automatically created by the VIC system, and contains random rows of zeros, as indicated in Figure 3-34.

0	0	0	-1	546	21	0	0	0
0	0	0	-1	551	21	0	0	0
0	0	0	-1	556	21	0	0	0
0	0	0	-1	561	21	0	0	0
0	0	0	-1	566	21	0	0	0
0	0	0	-1	571	21	0	0	0
-3.71631	49.0871	-0.156135	6.06138	576	21	0.00144465	-0.00328507	0.0143088
-3.2035	49.1014	-0.152586	5.29447	581	21	0.00186861	-0.00427438	0.018368
-2.69282	49.113	-0.134632	5.65631	586	21	0.00196816	-0.00369174	0.0154242
-2.17741	49.1304	-0.142561	5.35025	591	21	0.00162562	-0.00417173	0.0165634
-1.6644	49.1446	-0.134574	5.22733	596	21	0.00205726	-0.00337883	0.0115327
-1.14901	49.1609	-0.138317	5.06904	601	21	0.00135704	-0.00332471	0.0125057

Figure 3-34. A sample of the automatic output file from the VIC system. The rows containing the zeros need to be filtered out.

The rows containing the zeros are spurious; therefore they needed to be eliminated from the file. The filtering was obtained using a LabView or Matlab code and a new file was obtained, as depicted in Figure 3-35.

"X"	"Y"	"Z"	"correlatio	"x"	"y"	"U"	"V"	"W"
-10.3448	9.66153	-0.183683	4.77381	324	214	0.018153	0.004107	1.42431
-10.171	9.66194	-0.182116	5.00978	329	214	0.017827	0.003849	1.43782
-9.99755	9.66219	-0.178652	4.97372	334	214	0.01798	0.004114	1.44919
-9.82345	9.66208	-0.178723	4.96774	339	214	0.017858	0.004657	1.46514
-9.65014	9.66091	-0.173729	4.8909	344	214	0.017917	0.005292	1.47422
-9.47628	9.66286	-0.171833	4.6942	349	214	0.018773	0.004763	1.48509
-9.30245	9.66254	-0.169536	5.15979	354	214	0.018651	0.004246	1.49643
-9.1291	9.66406	-0.16411	5.89599	359	214	0.018152	0.004187	1.50592
-8.95501	9.66442	-0.162845	6.33504	364	214	0.01775	0.003813	1.52177
-8.781	9.66509	-0.160912	6.20364	369	214	0.017371	0.00363	1.53623

Figure 3-35. A sample of the final output file from the VIC system. The spurious rows were filtered out and the data are now ready for post-processing.

The geometry and displacements from the output file were used to make custom contour plots of the displacement fields in any of the three directions. Using the displacement information, it was possible to calculate the discrete strain field in the MAV wing through the classic large strain/displacement equations. The u , v , and w displacement fields are mapped onto an unstructured quadrilateral mesh resembling the specific topology of the wing. At each quadrilateral, the mapped displacement vectors at all four nodes are fit into appropriate shape functions. The strain field in each quadrilateral is then calculated as:

$$\epsilon_{xx} = \frac{\partial u}{\partial x} + \frac{1}{2} \left[\left(\frac{\partial u}{\partial x} \right)^2 + \left(\frac{\partial v}{\partial x} \right)^2 + \left(\frac{\partial w}{\partial x} \right)^2 \right] \quad (3.16)$$

$$\epsilon_{yy} = \frac{\partial v}{\partial y} + \frac{1}{2} \left[\left(\frac{\partial u}{\partial y} \right)^2 + \left(\frac{\partial v}{\partial y} \right)^2 + \left(\frac{\partial w}{\partial y} \right)^2 \right] \quad (3.17)$$

$$\epsilon_{xy} = \frac{1}{2} \left[\frac{\partial v}{\partial x} + \frac{\partial u}{\partial y} + \frac{\partial u}{\partial x} \frac{\partial u}{\partial y} + \frac{\partial v}{\partial x} \frac{\partial v}{\partial y} + \frac{\partial w}{\partial x} \frac{\partial w}{\partial y} \right] \quad (3.18)$$

In the above equations, u , v , and w , are the displacements in the X, Y and Z directions, respectively.

Because the model, and the structure that holds it, are not perfectly rigid, care must be taken to check for any rigid body rotation or translation and, if necessary, apply the appropriate corrections to some of the results. When the wing is subjected to

aerodynamic loads, a certain amount of rigid rotation or translation can be expected. In order to obtain an accurate assessment of the displacement field of a MAV under certain dynamic pressure load, the rigid body translation and rotation, if substantial, must be accounted for.

The strains, by definition, are independent from rigid body rotation and translation, and thus the strain field is presumed to be unaffected, if the proper system calibration was obtained. In addition, displacements in the X and Y directions are assumed to be free of rigid movement, thus only Z displacements will be adjusted. The technique presented in this work to account the unwanted displacements is to assume that the mid-plane of the MAV wing is rigid, and will not deform. An assumption fairly accurate due to the solid skin carbon fiber longitudinal structure, with a large inertia in the Z-Y plane, used to attach the wing to the sting balance. In the case of the complete aerial vehicle, the wing is rigidly connected to the fuselage in the middle part of the wing for a width of 60 mm. The displacements along this centerline are then averaged, and this number is subtracted from the w displacement field of the entire wing. This technique is demonstrated in Figure 3-36 and Figure 3-47, at two sections in the Z-Y plane at the centerline and 50 mm off the centerline.

In Figure 3-36, the topology of two wing sections is examined, both with and without aerodynamic loads. The same two sections are presented in Figure 3-37, with the corrections for the rigid body rotation and translation applied. As intended, the relative displacement of the centerline can be seen to approach zero, and the shapes are the real shapes as resulted only from the true deformation of the wing.

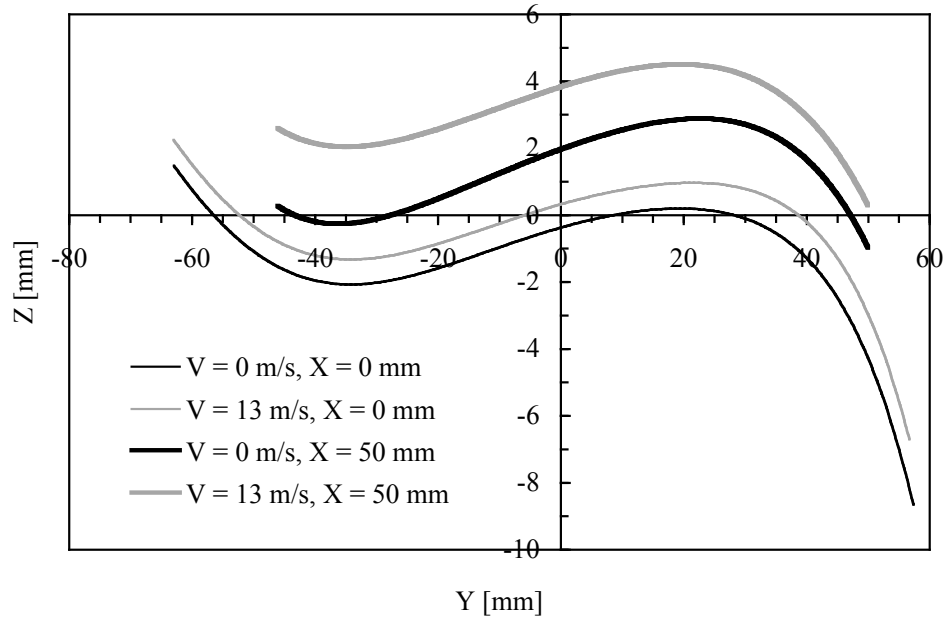


Figure 3-36. Two sections of the MAV wing, at the centerline (bottom) and at 50 mm on the X axis (top). The leading edge is on the right, airflow runs from right to left. The grey profiles are displaced from the original off-wind position (black) due to the elastic deformation and rigid body motion.

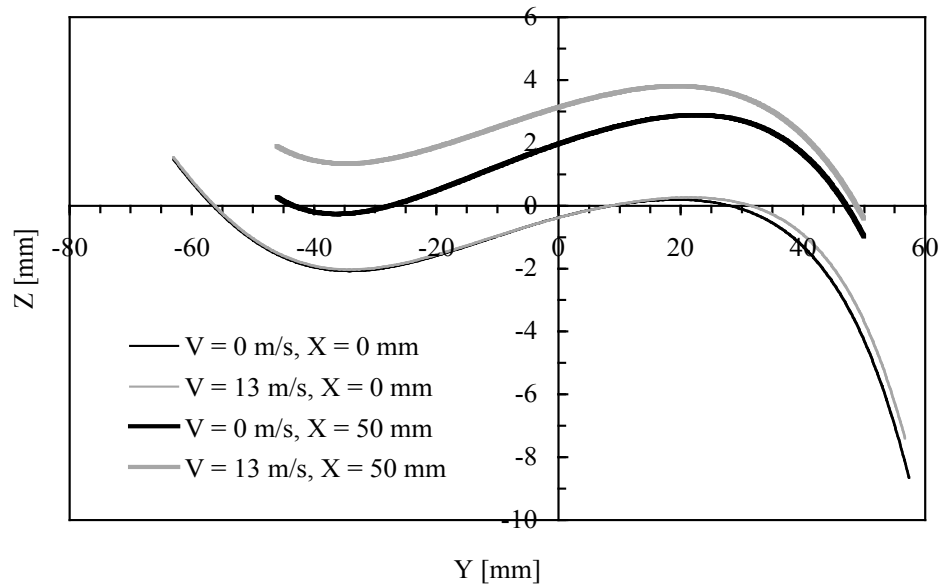


Figure 3-37. The same sections of the MAV wing, at the centerline (bottom) and at 50 mm on the X axis (top). The wind on positions were corrected for the rigid body motion. The profiles at the centerline (bottom) are virtually coincident, therefore the central part of the wing is not experiencing any deformation during the tests.

3.3.5 Measurement Uncertainties

Because the VIC system is a close system, with proprietary software not accessible to the operator, the decision was made to perform an accuracy analysis, and error assessment, by carrying out an ad hoc set of experiments. Details of the proposed technique are reported in Appendix B. The error assessment experiments, performed during this work, consisted in the measurement of the displacements and the deformed surface of an original plane latex membrane, when subjected to a known deformation.

The typical average error bound resulted to be less than $\pm .003$ mm, with a commanded maximum displacement of 0.1 mm. A sample from the results of those tests, with the uncertainty bound, is depicted in Figure 3-38.

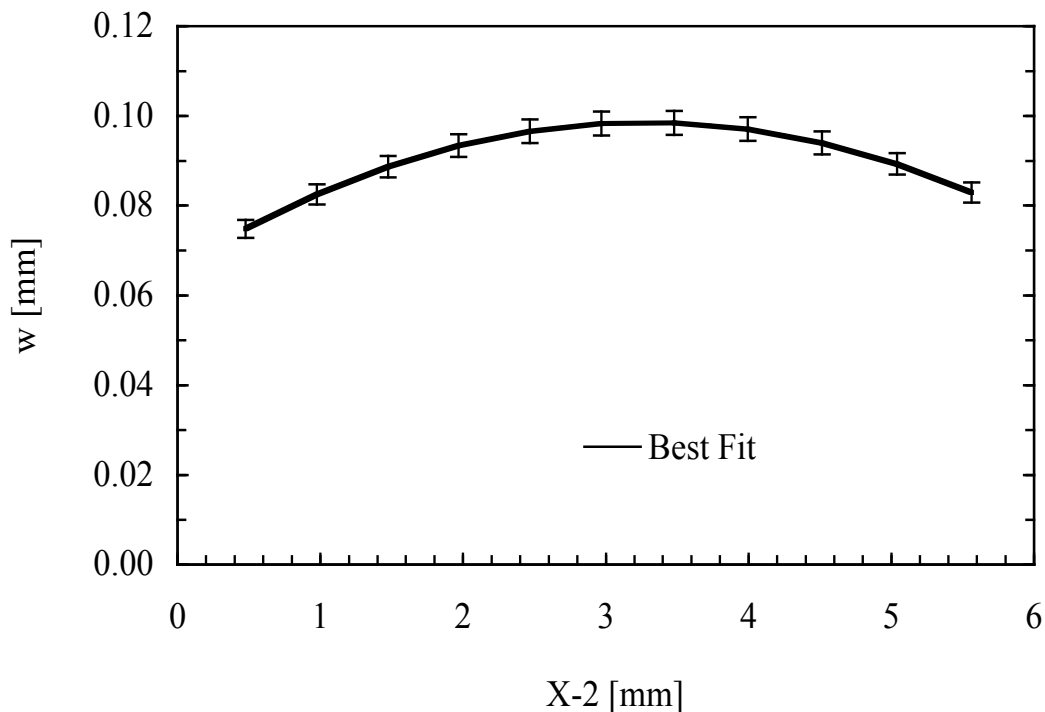


Figure 3-38. Best fit of the experimental values of the latex membrane displacements versus x coordinates. The average error bound is less than $\pm .003$ mm.

The membrane was the same used for the wing skin and it was glued with a selected pretension on a rigid thick aluminum ring. The same VIC set-up was used during these experiments and the tests, with roughly the same distance between the lenses and specimen with the same speckle color and density.

3.3.6 Wind Tunnel Corrections

The corrections used in this section were applied to the nominal values of the angle of attack. The measurements of the AOA errors and the computation of the corrections are explained in Appendix A. In the general case, any change in the model position and shape during wind tunnel tests may be considered as the summation of the flexibility of the holding structure, of the sting balance (if an external balance is used) and the model itself.

Specific tests were conducted with the three different types of wings and the change in the AOA of the model as a rigid body rotation was measured using the VIC system. In the linear region of the lift curve the values of $\Delta\alpha_{AV}$ were plotted versus C_L at the available test flow velocities for the two types of flexible wings, PR and BR (see Appendix A). An example of one plot is depicted in Figure 3-39.

With the assumption that the wing rigid body rotation is caused mainly by the lift component of the aerodynamic resultant, the corrections for the full range of AOA and velocities were estimated as a function of the lift coefficient using linear regressions (see Appendix A). Using the linear equations expressions, the correction for the AOA for a particular type of wing was found as

$$\Delta\alpha = f(C_L, q) \quad (3.19)$$

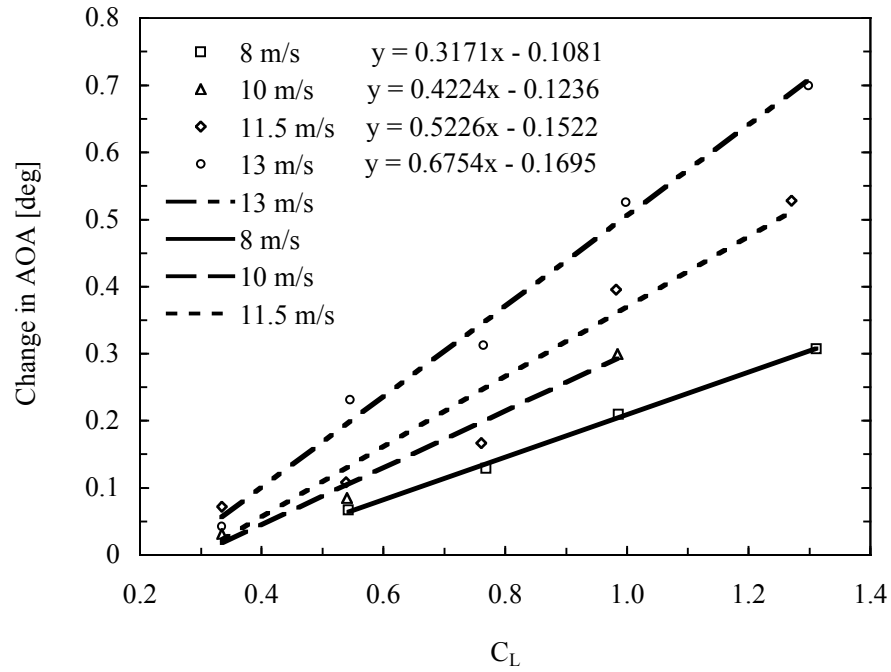


Figure 3-39. Change of the AOA due to rigid body rotation versus C_L at four wind tunnel free stream velocities for a typical PR wing.

The effective value of the AOA finally is

$$\alpha_E = \alpha + \Delta\alpha \quad (3.20)$$

CHAPTER 4 EXPERIMENTAL RESULTS AND DISCUSSION

4.1 Introduction And General Observations

This chapter is devoted to a comprehensive inspection of the experimental results with some insights of trends and particular phenomena that can be evinced only by the observation and cross correlation of multiple tests results. The processing of the data is part holistic and part formal or mathematical, according to the appropriate cases.

The aerodynamic and propulsion characteristics tests results are reported in Appendix C and in Appendix D the elastic deformation results of the wings. In general the results presented in the appendices are organized in two main groups: plots of characteristics at constant structural flexibility and plots of characteristics at constant dynamic pressure. In this way it is easy evaluate the features of the different wings and their merits. The propulsion plots consist of angle of attack and power sweeps at different dynamic pressures.

The reader is encouraged to review the results presented in the Appendices C and D before continuing with the considerations in this chapter. The main objective of this work is to correlate the aerodynamic features of the wings with their structural properties, thus it is useful before proceeding with comments on the results to show the basic physical characteristics of the wings in Table 4-1 and Table 4-2.

The chapter is organized in four main parts: the static elastic deformations of the wings, the aerodynamic of the wings, the aerodynamic and propulsion characteristics of the micro aerial vehicles and the summary of results and conclusions.

Table 4-1. Table with summary of wings' characteristics and their designation.

Model	Type	Description	Design.
15001	R	Wing made by Solid Carbon Fiber (Rigid)	Rigid
15007	PR	As 15004 with middle part 60 mm wide	PR07
15009	BR	Thick battens (two plies 0/0), 2.5 mm wide, LE +/- 45	BR09
15012	PR	Rigid thin perimeter, no middle part, LE +/- 45	PR12
MAV15001	R	Vehicle with wing 15001	MAVR
MAV15007	PR	Vehicle with wing 15007	MAVPR07
MAV15009	BR	Vehicle with wing 15009	MAVBR09

Table 4-2. Table with a brief description of all the wings tested in this work. The overall dimensions, airfoil shape and wing planform were the same.

Type	Model	Description
R	1	Wing made by Solid Carbon Fiber (Rigid)
BR	2	Thin battens (one ply 0), 2 mm wide, LE +/- 45
BR	3	Thick battens (two plies 0/0), 3.5 mm wide, LE +/- 45
PR	4	Perimeter and LE +/- 45, skin pretension high, middle part 30 mm wide
BR	5	Thick battens (two plies 0/0), 3.5 mm wide, LE 0/90, wingspar 90/90 2 mm wide
PR	6	As 15004 with medium skin pretension
PR	7	As 15004 with middle part 60 mm wide
BR	8	As 15005 with skin made by parachute material (very stiff, not elastic)
BR	9	Thick battens (two plies 0/0), 2.5 mm wide, LE +/- 45
PR	12	Rigid thin perimeter, no middle part, LE +/- 45

4.2 Static Elastic Deformation Of Wings

The present study constitutes an expansion of the work by Waszak, Jenkins and Ifju [28] and Fleming, Bertram, Waszak and Jenkins [73] by the original use of the visual image correlation technique in wind tunnel tests, by which the full three-dimensional displacement field of the membrane wing could be captured. Furthermore, the tests were performed on a series of wings with various flexibilities. This section presents the wings' global deformation and some characteristics features that can be estimated from the

deformed wing's geometry, as camber and the wash-out effect (change of geometric twist); they both are characteristics of a flexible wing subjected to aerodynamic load.

4.2.1 Global Change of Geometry

Typical results obtained from the VIC system consist of the geometry of the wing surface in discrete X, Y, and Z coordinates and the corresponding displacements u, v, and w, if any deformation of the structure occurred [95-97]. Figures 4-1 and 4-2 represent two states of the wing type BR09, the batten reinforced wing, at an AOA of 20 degrees, with airflow off, Figure 4-1, and with airflow on, Figure 4-2.

The deformation of the wing, due to the aerodynamic load, is evident from Figure 4-2 showing the carbon fiber battens acting as flexible beams with the latex skin as elastically extensible lateral boundary conditions on the sides. The dimensional resolution of the system, estimated to be on the order of .1-.05 mm, can reveal some details like the battens on the wing under dynamic pressure loads.

The elastic displacement field along the MAV wing can be considered a variable of three factors: the flow dynamic pressure, the angle of attack of the wing and the slipstream wash created by the propeller, when applicable. The influence of wind speed and AOA has been well documented [96, 97]; the flow-structure interactions produced by the propeller will be explored in the following chapters. The maximum displacement found within a flexible MAV wing will increase with the increase of wind speed and, up to the level tested during this work (22^0), with higher angle of attack. In addition, the absence of any propeller will lead to a displacement field that is relatively symmetric about the centerline of the MAV.

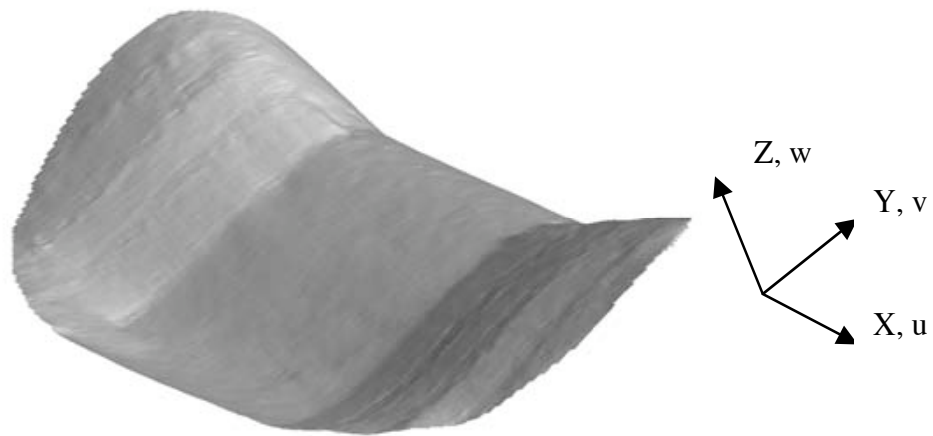


Figure 4-1. MAV wing type BR. The image shows the un-deformed structure reference image obtained by VIC at AOA=20, with no airflow.

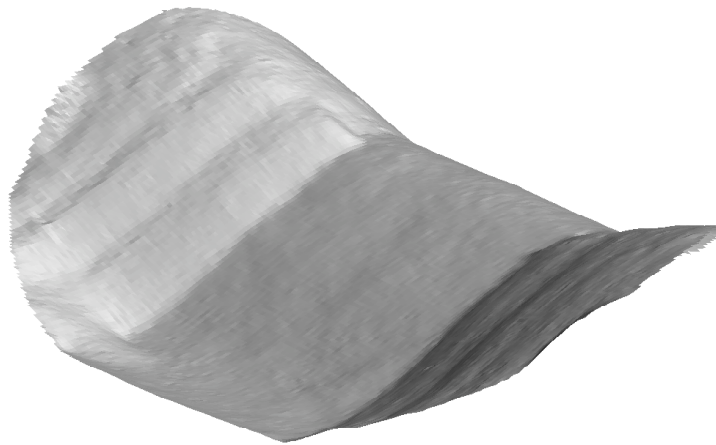


Figure 4-2. MAV wing type BR. The view represents the deformed structure image for the VIC processing at AOA=20, at a free stream velocity of 13 m/s.

Figures 4-3 to 4-6 represent the three-dimensional geometry of wing PR07. The coordinate reference system (X, Y, Z) is a body system. The unloaded (and non deformed) state is in Figure 4-3 and Figure 4-5. This is considered the reference image.

The same wing subjected to aerodynamic load is Figure 4-4 and Figure 4-6. It is useful to remind to the reader that the structure of the PR wings consisted of a carbon fiber perimeter around the entire wing, with the latex inside. The billowing of the skin is very evident.

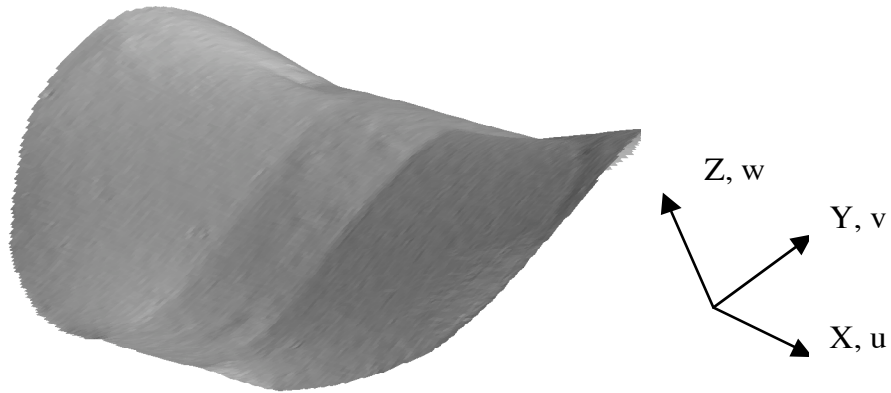


Figure 4-3. MAV wing type PR. The image shows the un-deformed structure obtained by VIC at AOA=22 degrees, with no airflow in the wind tunnel. The geometry is used as reference geometry.

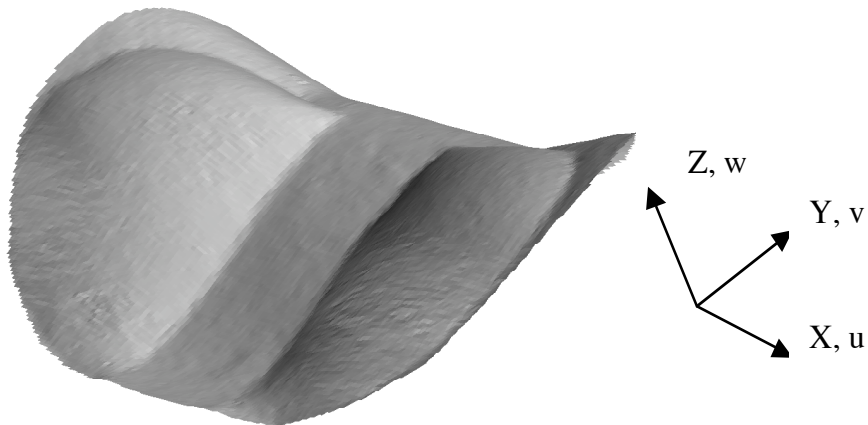


Figure 4-4. MAV wing type PR. The image shows the deformed structure obtained by VIC at AOA=22 degrees, at a free stream velocity of 13 m/s.

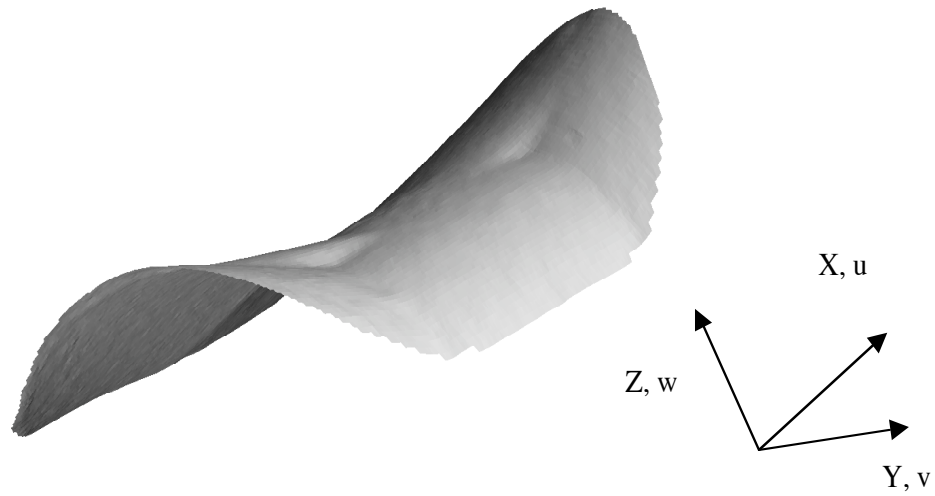


Figure 4-5. MAV wing type PR. The image shows the un-deformed structure obtained by VIC at AOA=22 degrees, with no airflow in the wind tunnel.

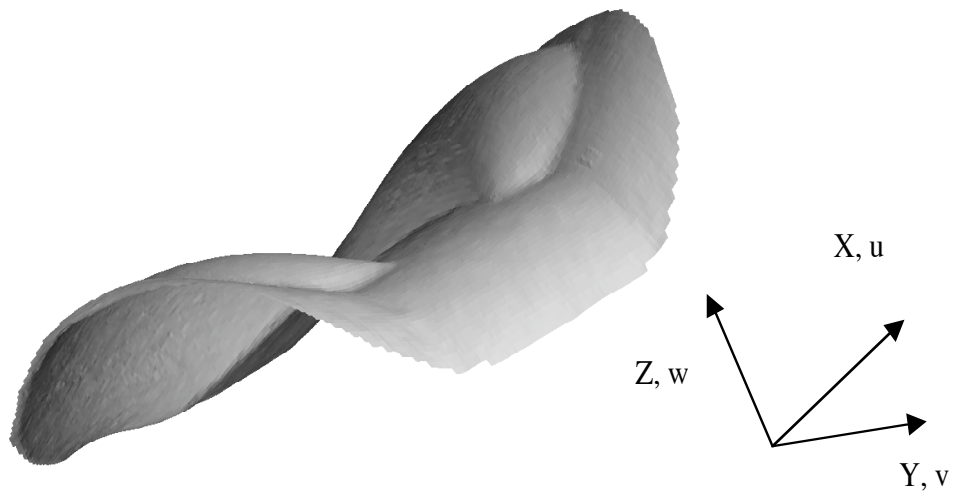


Figure 4-6. MAV wing type PR. The image shows the deformed structure obtained by VIC at AOA=22 degrees, at a free stream velocity of 13 m/s.

The displacements inherent within the PR wing are appreciably dissimilar to those observed in the BR wing, at the same free stream dynamic pressure and AOA. This is caused by the significantly different boundary conditions presented to the latex membrane; the PR wing is, like a drumhead, affected by an in-plane diffused pretension while the longitudinal battens of the BR wing provide a stiffer foundation but in only one preferred direction.

4.2.2 Displacement and Strains Fields

Displacement data in all three Cartesian directions is available. This data is best realized in color contour form, and several examples can be seen in Figure 4-7 through Figure 4-11. Referencing to Figure 4-7, the top two contour plots are displacements in the X (perpendicular to the free stream and horizontal) and Z (normal to the wing) directions, respectively. It can be seen that displacement is largely negligible in the area composed of rigid carbon fiber, and maximum in the latex section of the wing. The lower plots display the discrete strain field that accumulates on the wing, calculated directly from the displacement field [96, 97].

The in-plane strains give the physical interpretation of the deformation in the latex wing skin, originated by stretching the rubber thin membrane. The carbon fiber parts, in the load range interested by the tests in the wind tunnel, are virtually strain free. Indeed, the carbon fiber battens exhibit deflection but no stretch.

Figure 4-8 (wing BR05) and Figure 4-9 (wing BR09) give examples of displacement contours found on another wing configuration, but under analogous flight conditions to those presented in Figure 4-7. Both display similar contour maps, but the

wing BR05, in particular shows greater inherent flexibility than the BR02 wing. Table 4-2 shows a description of the structural features of the wings.

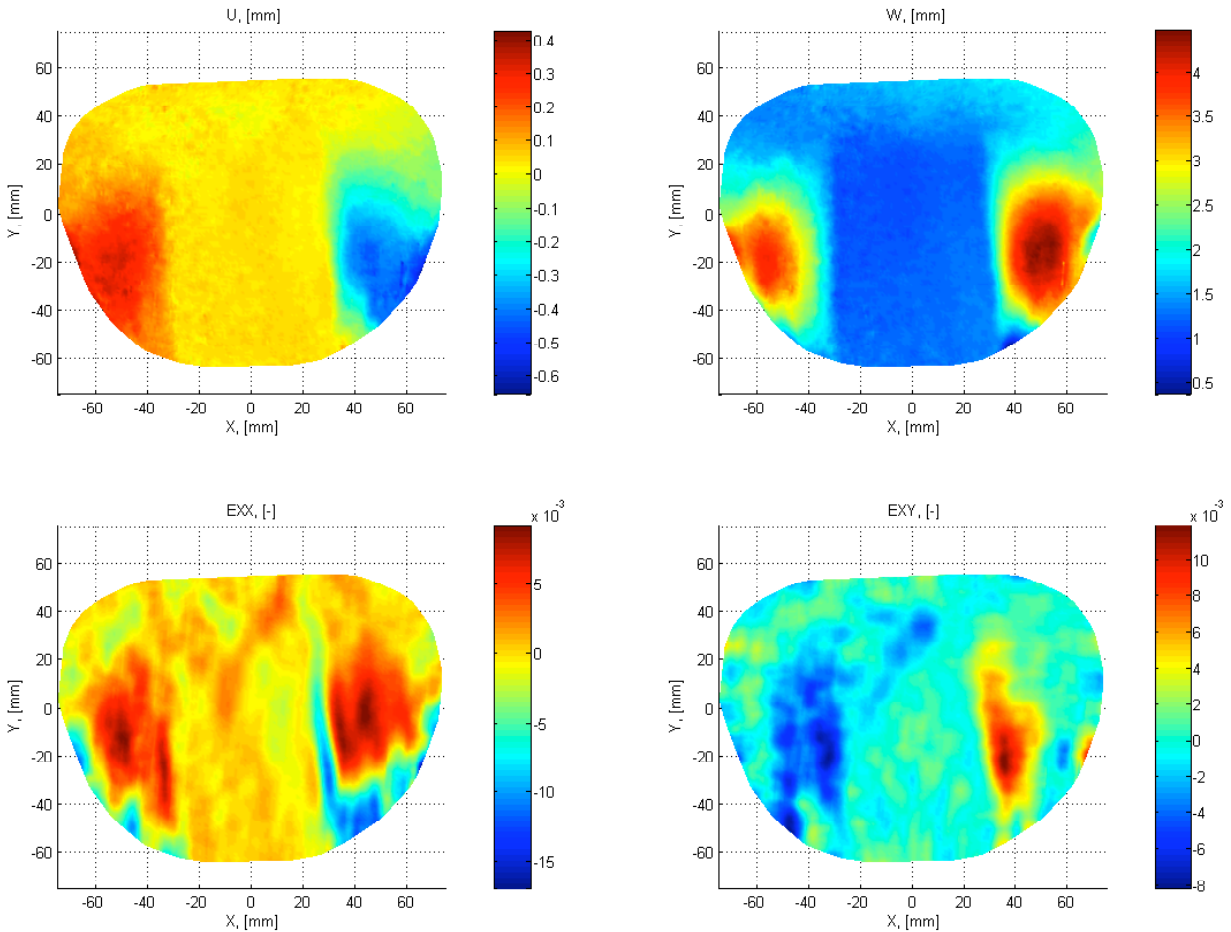


Figure 4-7. Wing type BR02, AOA=20, at a velocity of 13 m/s. From top left, clockwise, u [mm], w [mm] and in-plane strains in X direction and XY plane (shear).

Peak out-of-plane displacements (w) in wing BR05 reaches 6 mm, compared to 4 mm found in wings BR02 and BR09. This large displacement field is presumed to be a direct result of the flexible, in torsion, leading edge of wing BR05. The peak out-of-plane displacement, for both Figure 4-8 and Figure 4-9 occurs at an edge of the wing that

exhibited low frequency large vibrations, possibly caused by the presence, in that area, of the tip vortices.

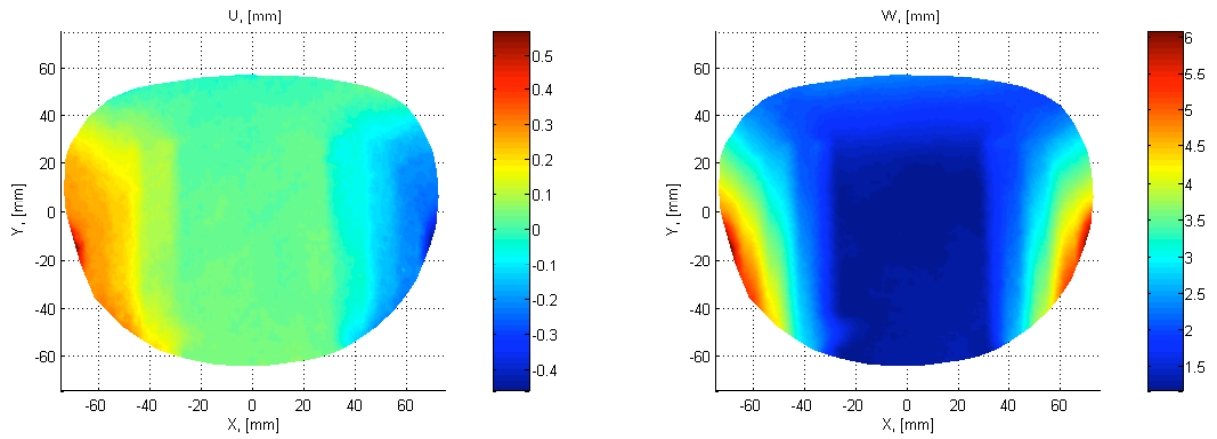


Figure 4-8. Wing type BR05, AOA=20, at a velocity of 13 m/s. From left, u [mm] and w [mm].

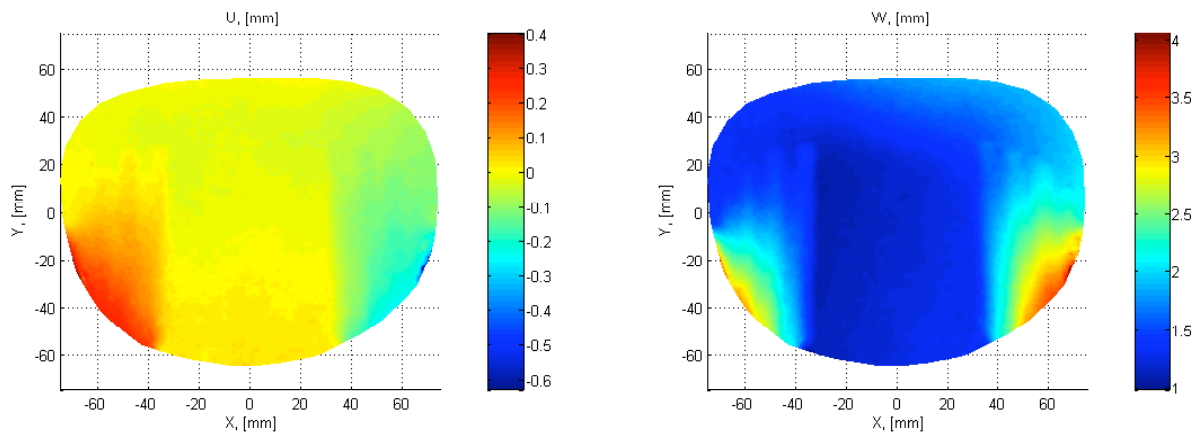


Figure 4-9. Wing type BR09, AOA=20, at a velocity of 13 m/s. From left, u [mm] and w [mm].

The w displacement fields found at three different wind speeds can be directly compared for greater insight into the fluid-structure interaction. This is achieved in Figure 4-10 and Figure 4-11, for wings 05 and 09, respectively. Predictably, higher free stream speeds generate larger wing deflection. Sharp color gradients give information about the location of battens within the wing (particularly in Figure 4-11). The superior flexibility of wing 05 over wing 09 can again be seen in these comparison contour plots. As explained in section 3.1.1.1, the wing BR05 is more flexible of the wing BR09 due to the torsionally elastic LE.

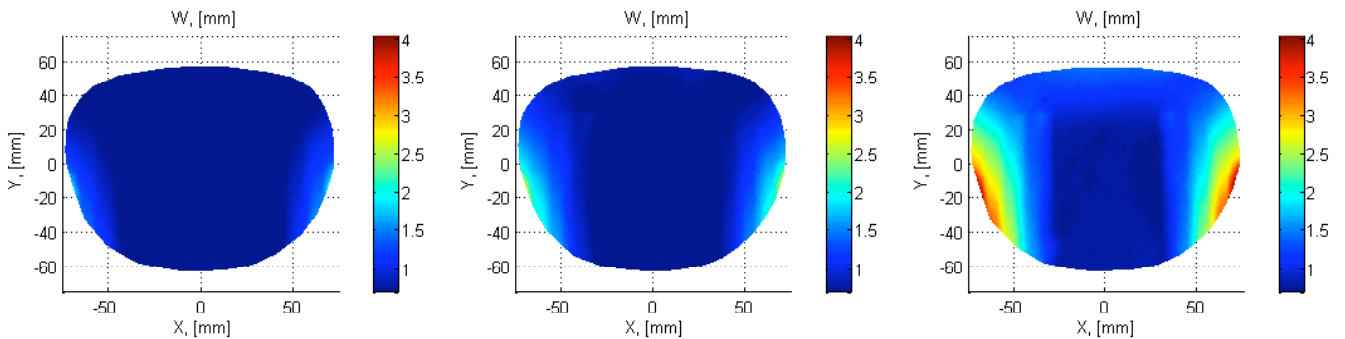


Figure 4-10. w displacement field for wing type BR05 at AOA=12 degrees, at three free stream velocities, from left 8, 10 and 13 m/s.

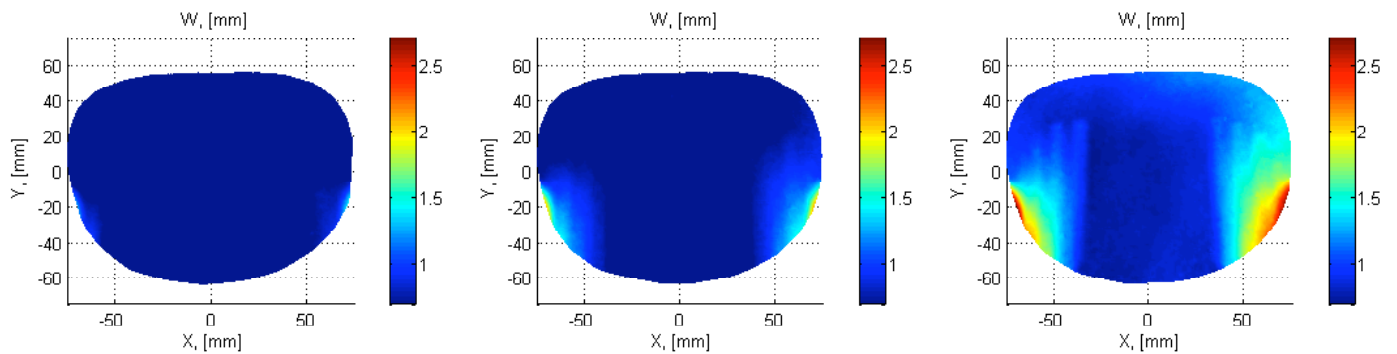


Figure 4-11. w displacement field for wing type BR09 at AOA=12 degrees, at three free stream velocities, from left 8, 10 and 13 m/s.

4.2.3 Camber

One important feature of flexible wings is how the overall shape is changed, with the change of aerodynamic conditions like AOA or dynamic pressure. Sail makers and sail designers epitomize the significance of the flexible wing concept. Optical systems to detect the sail shape while sailing have been used but they have never been of real practical value while the development of computational methods [22, 29] gained more importance in the sailing research community. More recently, theoretical work was performed specifically on MAV latex membrane wings [25, 26, 27] and experimental work was performed on sail-wing concepts [30, 31] and on micro aerial vehicles [28, 73].

Using the results, in terms of the three-dimensional geometry of the wing's structure under deformations, some important features of the wings' shape were detected. Figure 4-12 and Figure 4-13 show the change in the magnitude of the camber at a section at 50 mm from the vehicle's center-line (5/6 of the semi-span) for the wings BR05 and BR09. The change is from the reference condition, at the same AOA and with zero free stream velocity. The airfoil's section has virtually zero thickness; the camber is the maximum distance of the wing surface from the chord line and it will be referred as t or t/c when normalized with the wing chord. The variation of the camber (t) is plotted versus the AOA at the maximum tested free stream velocity (13 m/s), Figure 4-12, and versus the dynamic pressure, at a constant AOA of 12 degrees, Figure 4-13.

Figure 4-14 and Figure 4-15 show, for the same wings and conditions of Figure 4-12 and Figure 4-13, the change in the position of camber along the chord. The plots again clearly show a linear trend with AOA and q .

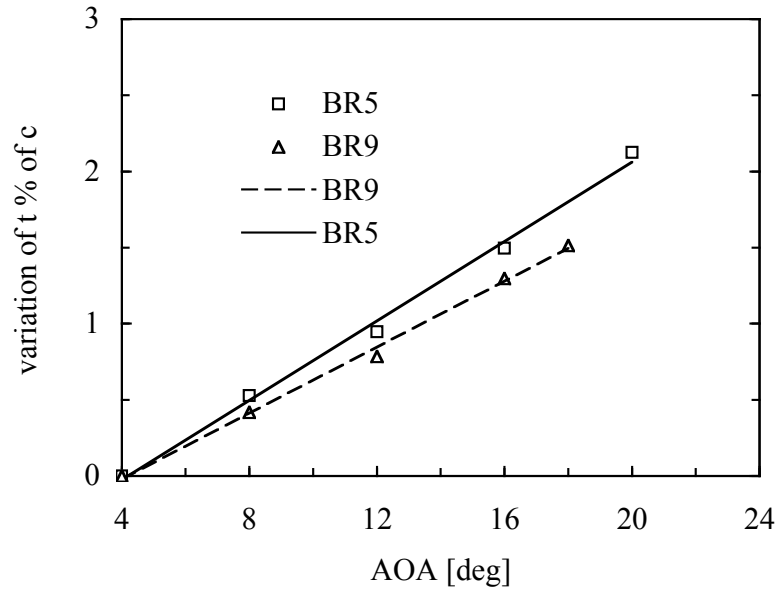


Figure 4-12. Variation of the value of camber for wings BR05 and BR09, versus AOA. The data, at the same wing section, are measured using the VIC. The free stream velocity was at the constant value of 13 m/s.

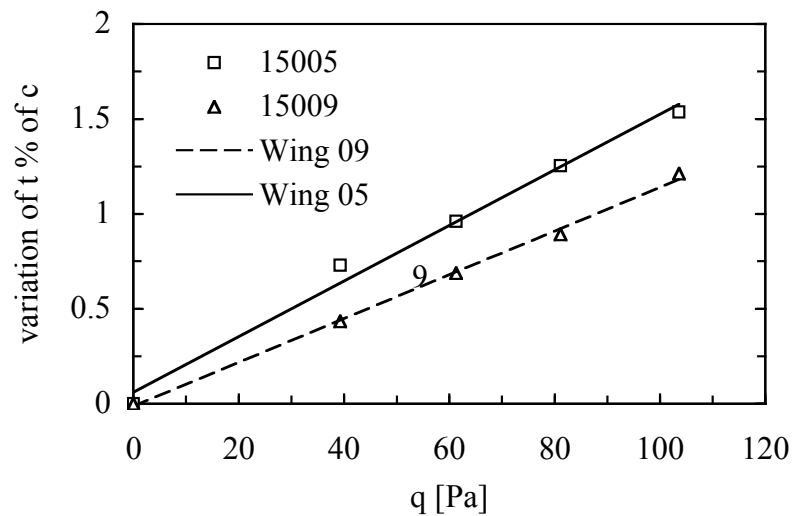


Figure 4-13. Variation of the value of camber for wings BR05 and BR09, versus the free stream dynamic pressure. The data, at the same wing section, are measured using the VIC. The AOA was at the constant value of 12 degrees.

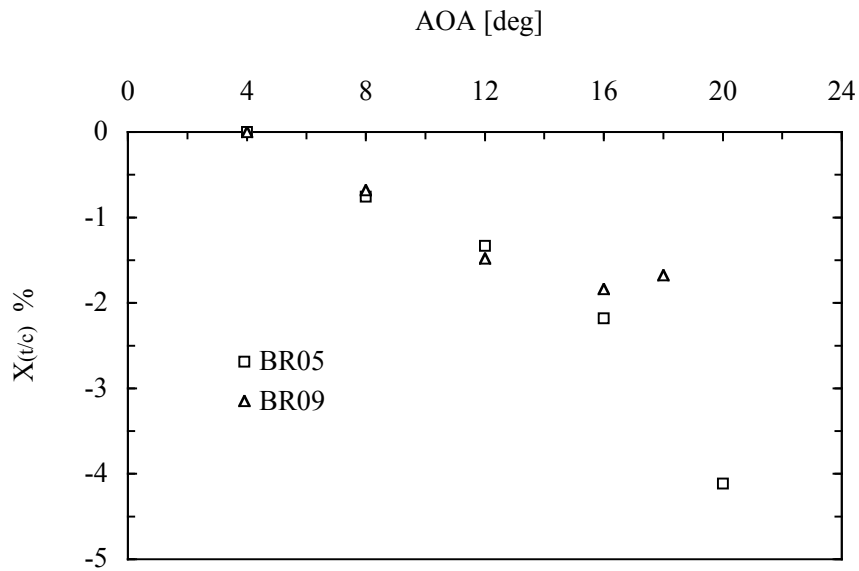


Figure 4-14. Variation of the position of camber for wings BR05 and BR09, versus AOA. The data, at the same wing section, are measured using the VIC. The free stream velocity was at the constant value of 13 m/s.

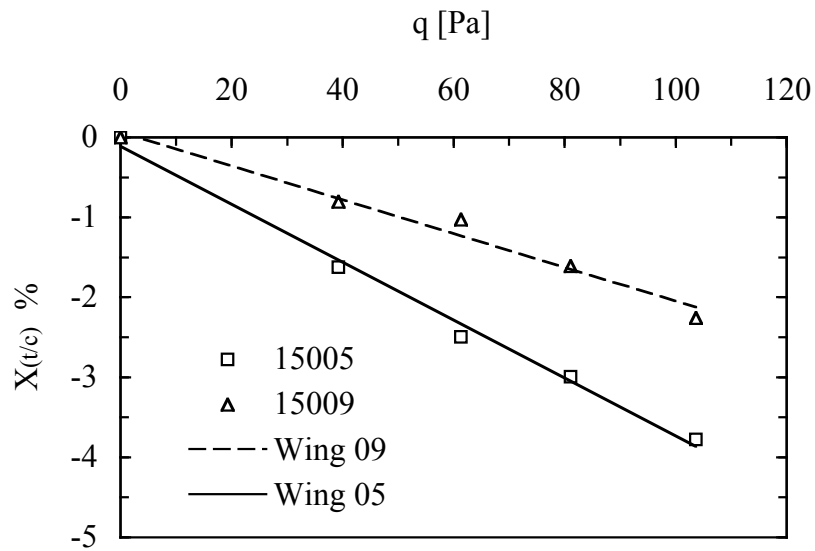


Figure 4-15. Variation of the position of camber for wings BR05 and BR09, versus the free stream dynamic pressure at the constant AOA of 12 degrees.

4.2.4 Geometric Wing Twist

Structural torsion, or elastic twist, around the X-axis, is an important characteristic of a flexible wing known as washout. The washout, a significant factor in sail aerodynamics [29], is also an important player in the flight mechanics of a MAV. The elastic torsion of wind tunnel models wings has been studied mainly as an undesired effect that needed to be characterized [99, 100]. The wing twist is quantified by the change along the X-axis of the angle of incidence, i_w , of the wing. The angle of incidence is the angle between a fixed reference line, typically the MAV longitudinal body axis and the chord line of the local airfoil section.

The chord is the line connecting the airfoil's leading edge with the trailing edge, on a plane parallel to the Y-Z plane. Figure 4-16, 4-17 and 4-18 show, for the wings type R, BR09 and BR05 respectively, the value of i_w along the half-span of the wing, at three values of the free stream velocities. As we should expect the change in i_w with the dynamic pressure for the rigid wing, Figure 4-16, is negligible.

Interestingly enough the wings include a design wash-in, due to the wing twist angle (both aerodynamic and geometric). This design angle of incidence is represented by the curves in wind off conditions (Figures 4-16, 4-17 and 4-18). The maximum negative change in the angle i_w , as expected, is for wing BR05, Figure 4-18. It is useful to remind to the reader that the wing BR05 was designed with thicker battens and the leading edge with only one ply 0/90, giving the wing a particular low torsional rigidity (Table 4-2). It needs to be mentioned also that the angle i_w , for the three wings in Figures 4-16, 4-17 and 4-18, start to show a variation at a station of over 30 mm from the

centerline, where the angle of incidence curves start to diverge from the reference at wind off conditions.

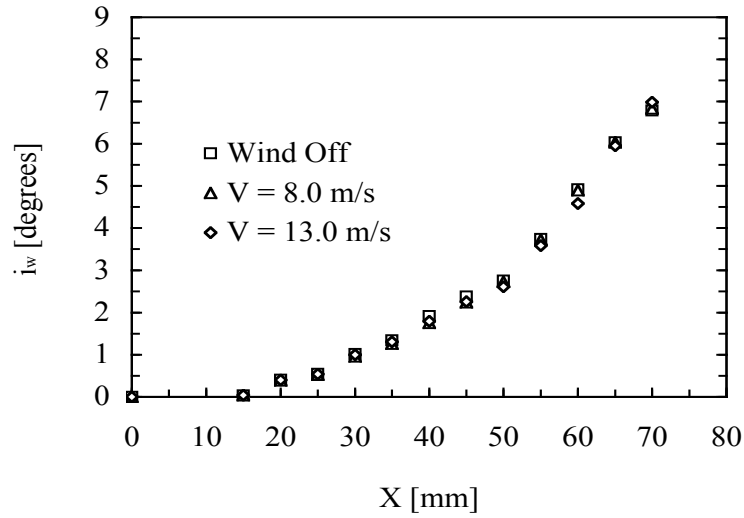


Figure 4-16. Angle of incidence for Rigid wing. Data are collected using VIC at three different free stream velocities and at a constant AOA of 12 degrees. The vehicle center line is at $X=0$, the wing's tip is at $X=75$.

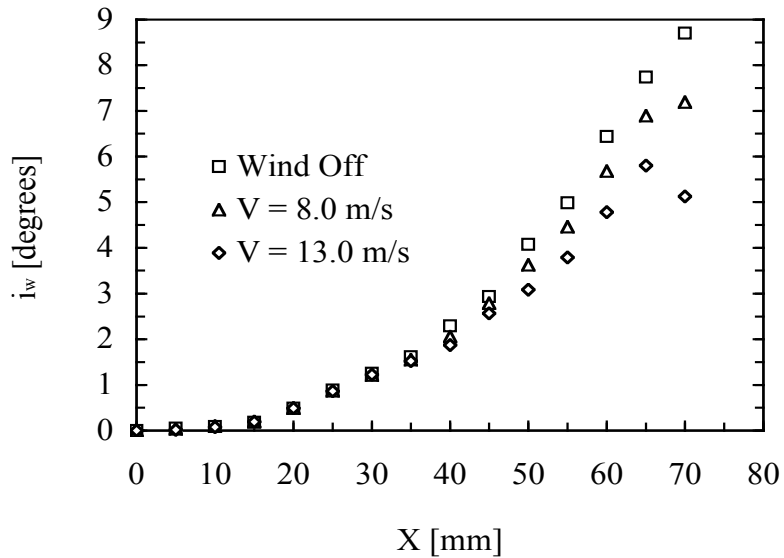


Figure 4-17. Angle of incidence for wing BR05. Data are collected using VIC at three different free stream velocities and at a constant AOA of 12 degrees.

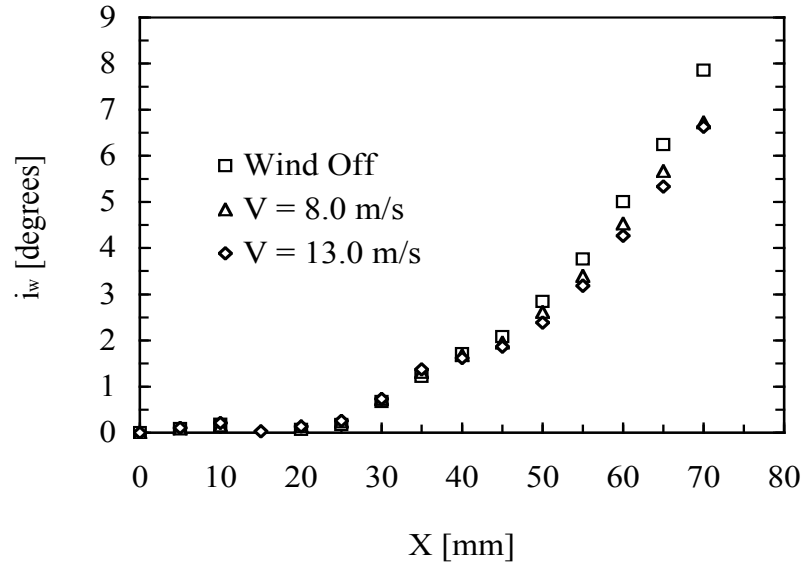


Figure 4-18. Angle of incidence for wing BR09. Data are collected using VIC at three different free stream velocities and at a constant AOA of 12 degrees.

The reason for this response is that the central part of the wing, 60 mm wide, is made of solid carbon fiber (Figure 3-2 and Figure 3-3), therefore practically rigid. The variation of the angle of incidence along the wingspan at different values of the angle of attack, for wing BR05, at a constant free stream velocity, is depicted in Figure 4-19. It is evident, from Figure 4-19, how the angle of incidence decreases, due to the twist of the wing (wash-out) with the increase of the AOA. The wash-out is generally caused, in steady conditions, by either an increase of dynamic pressure, an increase of AOA or both.

The reference configuration is given by finding the local angle of incidence of the airfoil, at wind off conditions, and using that value as the base condition. The change in local angle of incidence is used to quantify the absolute washout, regardless the built-in angle of incidence.

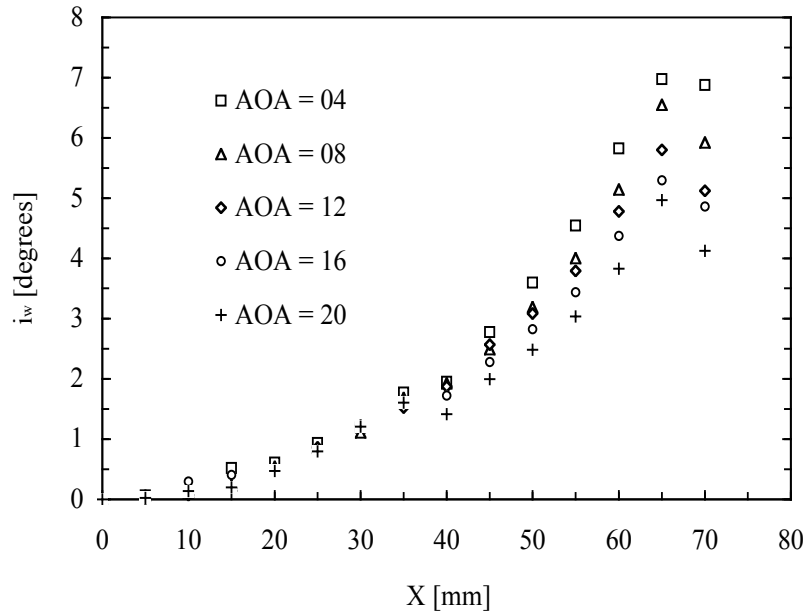


Figure 4-19. Angle of incidence for wing BR05. Data are collected using VIC at five different angles of attack and at a constant free stream velocity of 13 m/s.

A plot of the maximum value of the angle of incidence versus AOA, obtained from the data of Figure 4-19, is depicted in Figure 4-20.

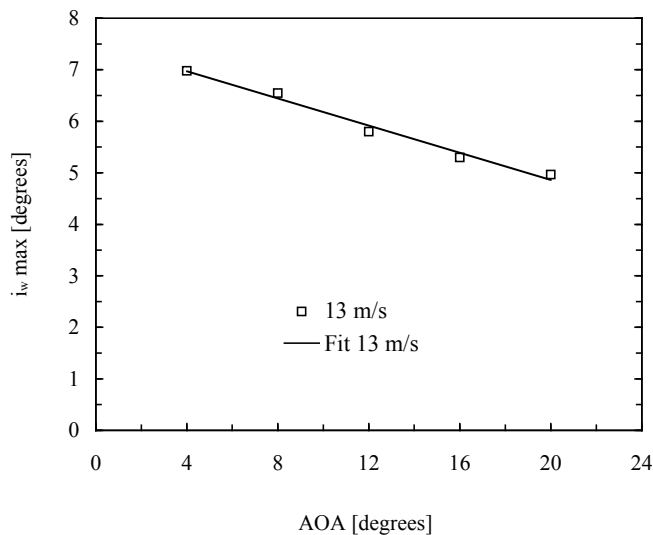


Figure 4-20. Maximum angle of incidence for wing BR05. Data are collected using VIC at five different angles of attack and at a constant free stream velocity of 13 m/s.

Interestingly, the maximum angle of incidence for the wing BR05 at a free stream velocity of 13 m/s is linear with the AOA.

Figure 4-21 and Figure 4-22 show the change in local angle of incidence, instead of the absolute values in the previous plots, along the X axis (span wise direction) for the wings BR05 and BR09 respectively.

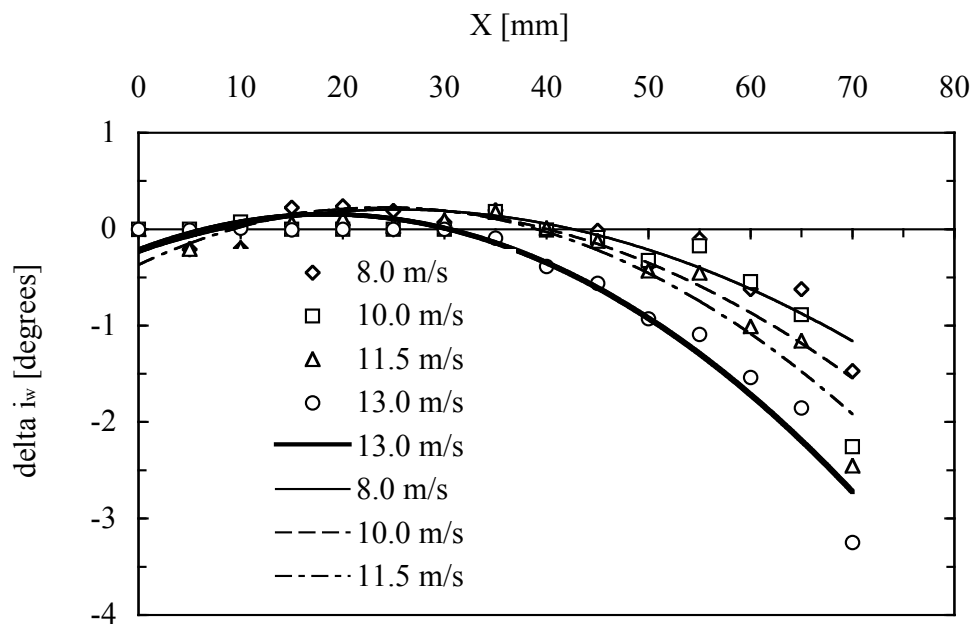


Figure 4-21. Change of angle of incidence (geometric twist) for wing BR05. Data are collected using VIC, at four different free stream velocities and at a constant angle of attack of 12 degrees. The reference condition is wind-off.

The largest change in local angle of incidence, Figure 4-21, is relative of wing BR05, designed to have the largest amount of torsional flexibility of all the wings subject to the present work.

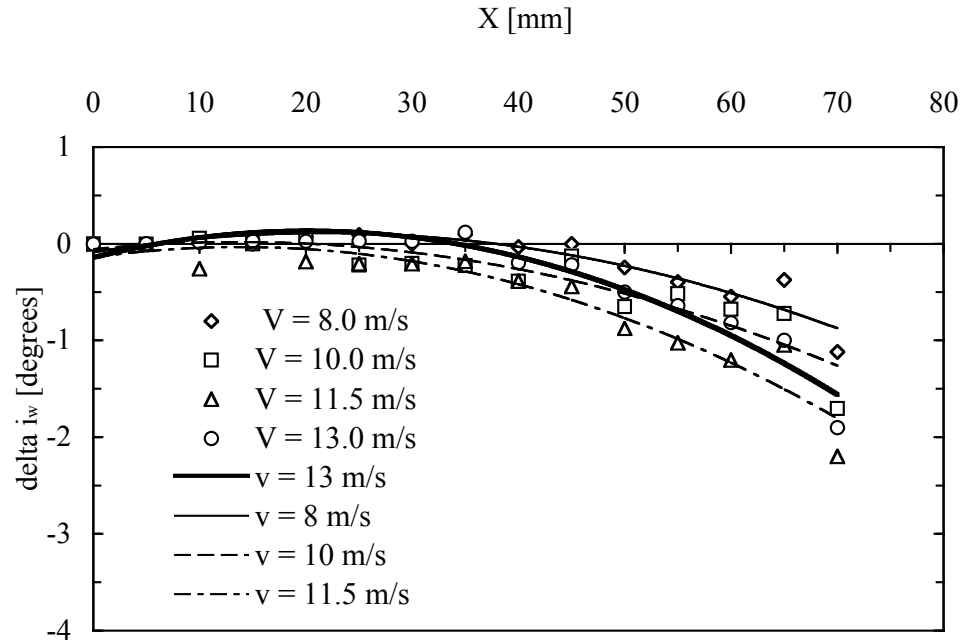


Figure 4-22. Change of angle of incidence (geometric twist) for wing BR09. Data are collected using VIC, at four different free stream velocities and at a constant angle of attack of 12 degrees. The reference condition is wind-off.

4.3 Static Elastic Deformation Of Wings On MAV

In the previous chapters the deformation of the isolated wings (clean configuration) were presented, as a function of their structural design and the two independent variables angle of attack and free stream velocity. In this section the complete MAV will be considered thus the effect of the propeller slipstream will be evaluated and the propeller speed, commanded by the voltage setting to the electric motor, will be added as another independent variable.

4.3.1 Propeller Effects on the Geometry of the Wings

The elastic displacement field along the MAV wing, for a constant structural configuration, can be considered a variable of three factors: the flow dynamic pressure,

the angle of attack of the wing and the slipstream wash created by the propeller. The influence of wind speed and AOA has been well documented for the wings type BR in the previous sections; the flow-structure interactions produced by the propeller will be presented in this section. The wings type PR will be illustrated in Appendix D. The maximum displacement found within a flexible MAV wing will increase with higher flow velocities and, up to a certain level, with higher angle of attack.

In addition to this, the absence of any propeller will lead to a displacement field that is relatively symmetric about the centerline of the MAV. Results with asymmetries will also be found because of experimental uncertainties and due to the inevitable manufacturing irregularities. These ideas lead to the question if the asymmetric effect of a spinning propeller upstream to the wing plays any role in the displacement field of the elastic wing downstream and, if so, if it can be detected and characterized by the proposed experimental technique.

The displacements inherent within the PR wing, as presented in Appendix D, are appreciably dissimilar to those observed in the BR wing, at the same dynamic pressure and AOA. This is caused by the significantly different boundary conditions presented to the latex membrane; the PR wing is, like a drumhead, affected by an in-plane diffused pretension while the longitudinal battens of the BR wing provide a stiffer foundation but in only one preferred direction. Contour plots of displacement results from both wings are presented in Appendix D, in Figure 4-23 and Figure 4-24.

These specific results were garnered at an AOA of 4° , at a wind tunnel flow velocity of 8 m/s; the plot on the left is with the propeller in windmill conditions and on the right with a 7.4 V motor setting.

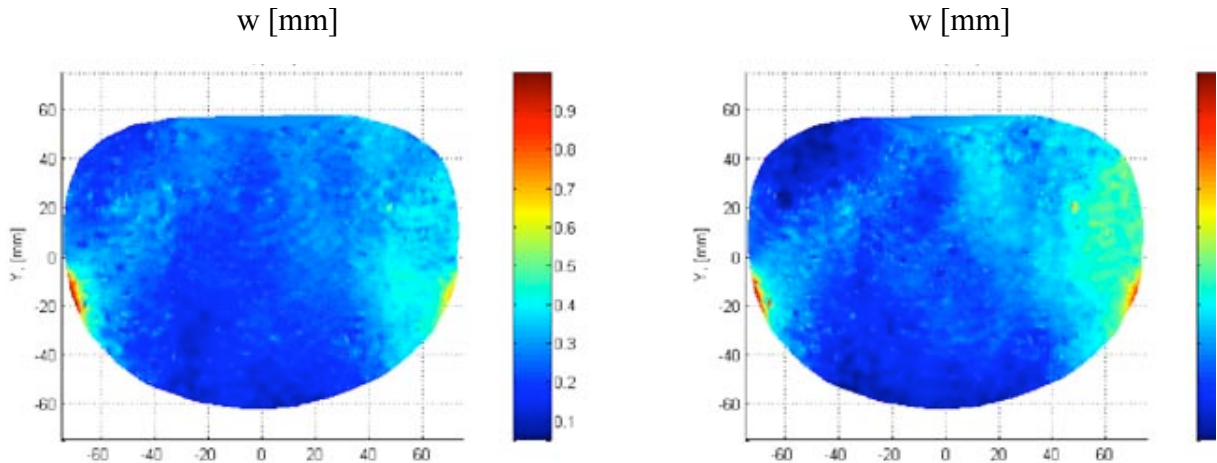


Figure 4-23. Displacements in Z direction (w) for BR Wing at $AOA = 4^\circ$, velocity = 8 m/s. The conditions on the left are with the propeller in windmill conditions and on the right with the motor setting at 7.4 V DC. Propeller's rotation is clockwise.

The propeller used had a diameter of 80 mm with a vehicle wingspan to propeller diameter ratio of 1.5 and rotating clockwise. These test conditions represent a configuration that places the emphasis on the propeller's slipstream, as 4° AOA and 8 m/s were the lowest values in the corresponding flight test matrix, while 7.4 volts applied to an 80 mm propeller were the largest values of the voltage settings applied to the motor in the test matrix.

From the basis of the those Figures, it appears that the presence of a propeller does have significant effects on the displacement field along a MAV's flexible wing. The batten reinforced (BR) wing shows a mild asymmetry in its displacement field when power is applied to the motor. Some asymmetry is also revealed under the effect of a freely spinning propeller, but it is most likely a result of experimental noise.

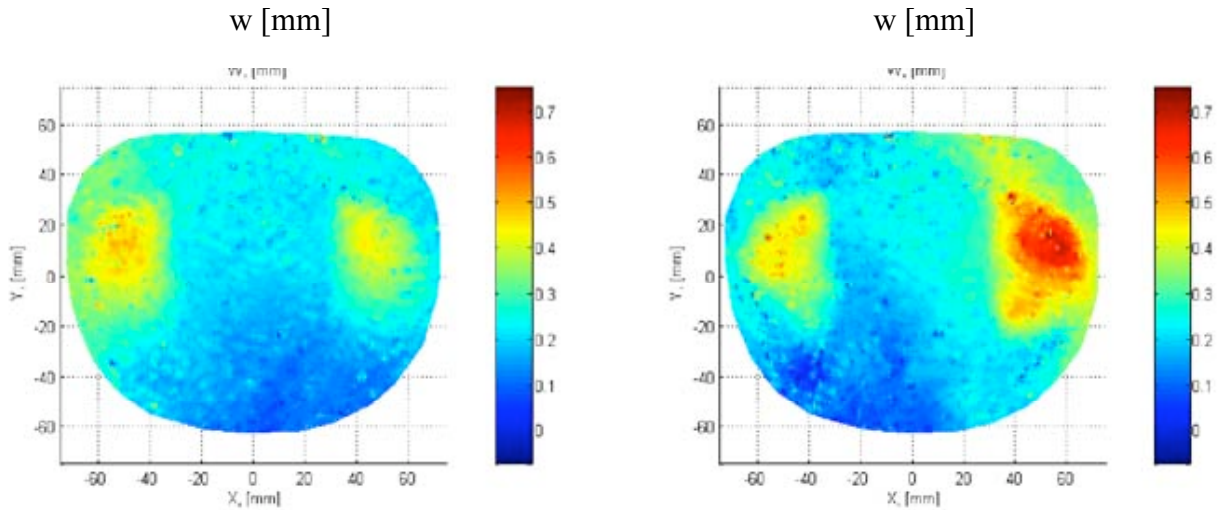


Figure 4-24. Displacements in Z direction (w) for PR Wing at $AOA=4^\circ$, velocity = 8 m/s. The conditions on the left are with the propeller in windmill conditions and on the right with the motor setting at 7.4 V DC. Propeller's rotation is clockwise.

The propeller's effect on the perimeter reinforced (PR) wing is more drastic, showing substantial shape differences when the propeller is powered at 7.4 V DC.

One important feature about a flexible wing is how the wing airfoil shape is altered with the change of aerodynamic conditions like AOA or dynamic pressure and with the change of motor setting, effectively changing the aerodynamic twist. Using the geometry of the structure under deformations, some important features of the wings can be detected, like the change in the wing section maximum camber and its position along the chord. A closer look is provided by Figure 4-25, which compares two sections of the PR wing under the effects of a powered propeller. The sections were taken symmetrically at $x = \pm 50$ mm thus on two Z-Y planes located at 50 mm symmetrically from the centerline of the vehicle.

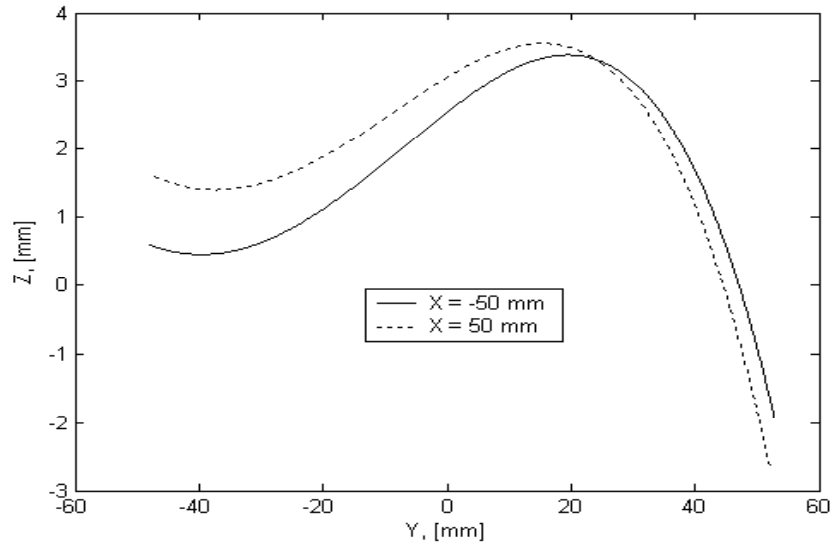


Figure 4-25. Geometry of two wing sections placed symmetrically at $x = \pm 50$ mm from the MAV's center line. The leading edge is on the left. It is evident the difference in shape produced by the propeller slipstream.

The conditions presented in Figure 4-25 show the maximum of the detected difference in shape of the two semi-wings subjected to symmetric aerodynamic loads and with powered propeller. As expected, the effects of the propeller on the out of plane displacement field of a MAV's wing in different flow conditions is less important and has the tendency to be overshadowed by the effects of the aerodynamics of the higher angles of attack and higher dynamic pressures. A simple but more effective quantitative assessment to determine the global effect of a propeller's slipstream wash on the wing deformation in more general flow conditions is proposed. Fleming, Bertram, Waszak and Jenkins [73] published results using a similar methodology but applied to different experimental conditions and using different experimental techniques (PMI).

If the wing is divided into two halves symmetrically around the centerline of the MAV, the ratio of the average displacement found on the left side of the wing to the one found on the right should give a reasonable indication of the asymmetry within the displacement field and thus a quantitative evaluation of the propeller slip stream wash.

This ratio is given by:

$$R = \frac{\int_A w(x, y) dA \Big|_{Left}}{\int_A w(x, y) dA \Big|_{Right}} \quad (4.1)$$

Physically, each integral represents the volume bounded between the deformed and reference wing surfaces. Ideally, steady flow conditions in the absence of a propeller should yield a ratio of approximately unity, taking into account experimental noise and materials or fabrication asymmetries. With the knowledge that the VIC system produces a discrete scheme with equal grid spacing (on the order of 0.5 mm) in both the X and Y directions, this ratio can be fairly well approximated by:

$$R \approx \frac{\sum_{i=1}^N w_i \Big|_{Left}}{\sum_{i=1}^N w_i \Big|_{Right}} \quad (4.2)$$

Results of the computed ratios for both the batten reinforced (BR) wing and the perimeter reinforced (PR) wing are depicted in Figure 4-26 and Figure 4-27, respectively. The noise reported in the plot was estimated by performing the evaluation of R from tests data obtained using the rigid wing, which should give a nominal value of $R = 1$. The noise is the difference between the measured value of R and 1.

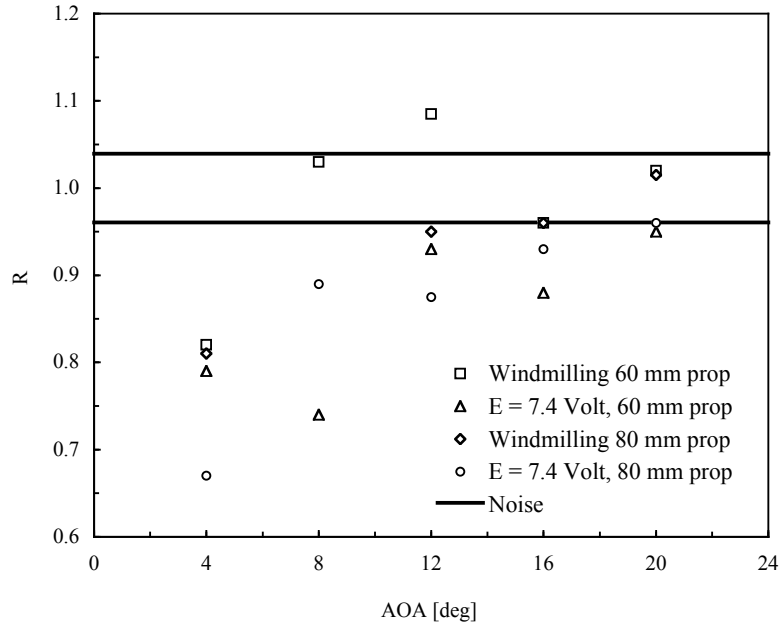


Figure 4-26. Volume displacements ratios versus AOA for BR wing. The plot represents two propellers sizes of 60 and 80 mm of diameter with and without power.

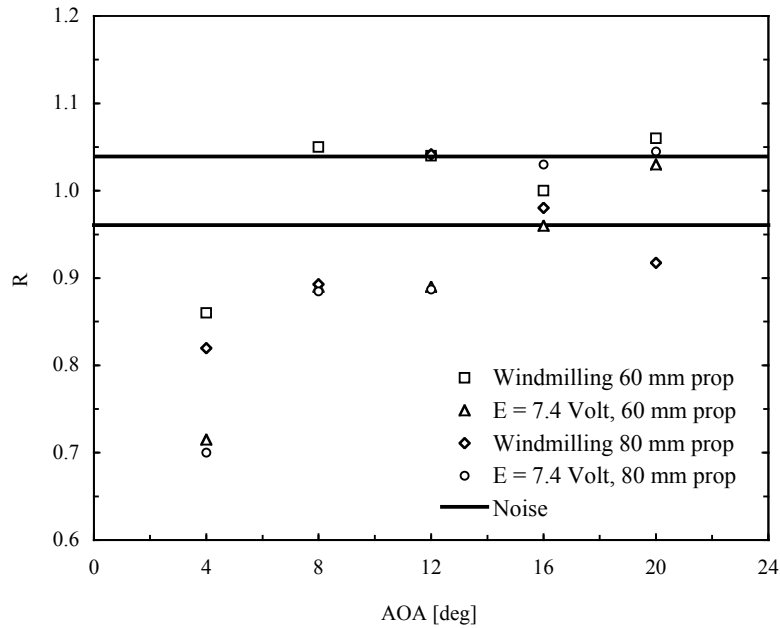


Figure 4-27. Volume displacements ratios versus AOA for PR wing. The plot represents two propellers sizes of 60 and 80 mm of diameter with and without power.

Despite some noise in the data gathered with the 80 mm propeller in wind milling conditions, the ratio described above appears to function as intended. Ratios on the order of 0.6 (indicating an important asymmetric displacement field along the wing) were detected for low angles of attack. Data at higher AOAs approach unity, as expected, due to the increasingly higher dominant effect of the AOA over the propeller slipstream.

4.4 Aerodynamics Of Wings

In the following sections, some of the aerodynamics features regarding the isolated wings, without fuselage or propeller, will be examined. The data are stored in a database and the plots of the general aerodynamics characteristics are listed in the Appendix C.

4.4.1 Lift Curve Characteristics

Possibly one of the most significant parameter applicable to the lift curve that can be linked to the elastic static flexibility of the wing is the lift curve slope. Figure 4-28 shows the derivative $dC_L / d\alpha$ versus the free stream velocity, for the four wings. Contrary to the expectation, the change in this derivative with the increase of the free stream velocity is relatively small, despite the decrease of the effective AOA due to the decrease of the local angle of incidence (Figure 4-21 and Figure 4-22).

It is postulated that in the flexible BR wings, the decrease in lift due to the wash-out is compensated by the simultaneous increase of wing camber (Figure 4-13) therefore the lift curve slope is not affected (or mildly affected) by an increase of dynamic pressure.

The PR wings as it will be illustrated in the following plots do not exhibited any appreciable geometric twist in load conditions (Appendix D) but they were affected by an important aerodynamic twist.

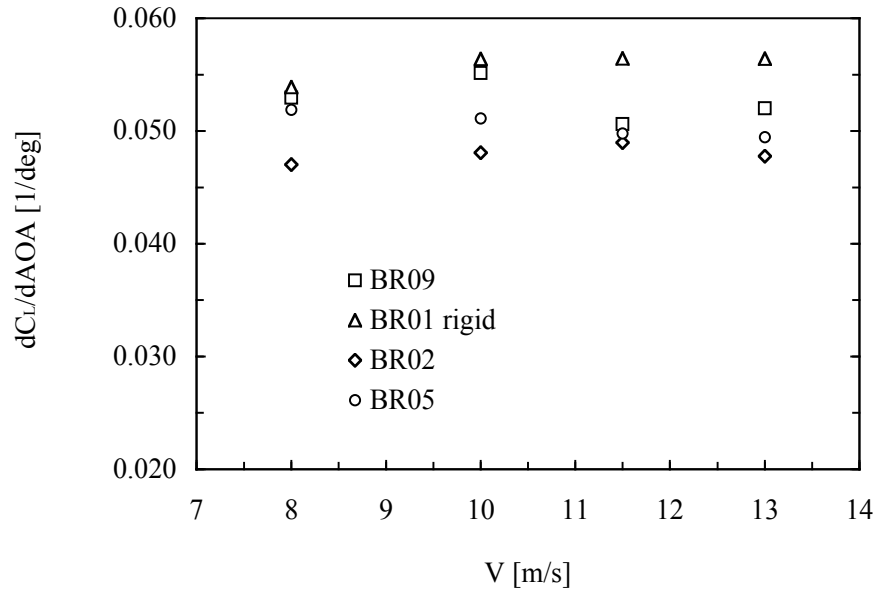


Figure 4-28. Lift curve slope versus free stream velocity for four wings. Data are collected using the wind tunnel sting balance.

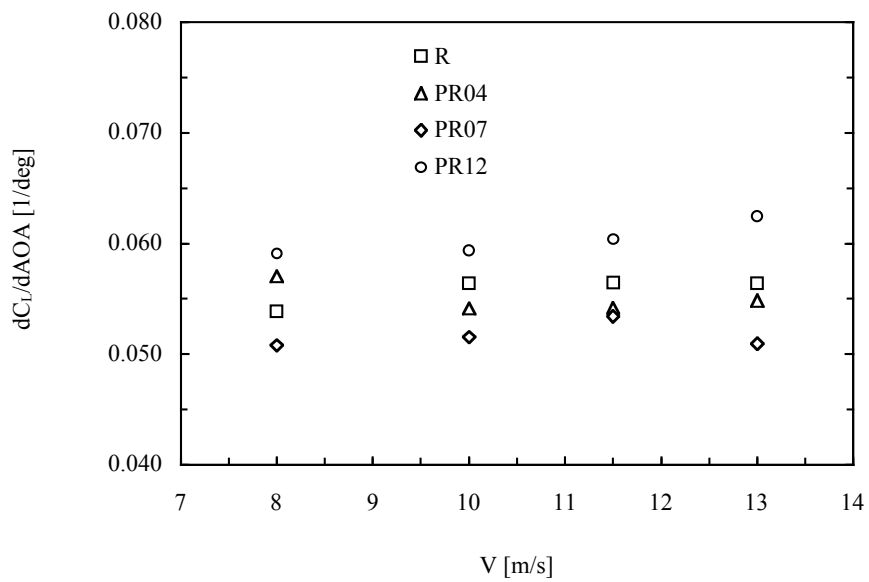


Figure 4-29. Lift curve slope versus free stream velocity for four wings. Data are collected using the wind tunnel sting balance.

4.4.2 Maximum Lift

Figure 4-30 shows the maximum lift coefficient versus the free stream velocity and Figure 4-31 shows the angle of attack for the maximum lift versus the free stream velocity, for four types of wing. As we could anticipate the absolute value of $(C_L)_{\max}$ (Figure 4-30) is lower for more flexible wings (BR05 and BR02). The explanation can be traced to the significant value of twist for those wings, as depicted in Figure 4-19 for wing BR05. The twist causes a decrease of the i_c thus a decrease of the AOA compared to more rigid wings (r and PRs) at the same nominal AOA. The decrease of effective max AOA in the wing tip area limits the global $(C_L)_{\max}$ for the entire wing. The $(C_L)_{\max}$ values are relatively constant with the velocity, with the exception of wing 09.

The angle of attack for $(C_L)_{\max}$ (Figure 4-31), as expected, increases the value with an increasing of flexibility, due to the washout effect. The case for AOA for $(C_L)_{\max}$ is characterized by the same genesis of the aforementioned case of $(C_L)_{\max}$. The decrease of the i_c in the wing's tip region for the BR wings (see Figure 4-19 as a sample case) causes a local decrease of AOA thus the entire wing can reach a higher nominal AOA without stall. This is one of the desired features of the flexible wings, which can delay the onset of stall. The apparent incongruous behavior of wing 09 requires further investigations. It is interesting to observe that the values for $(C_L)_{\max}$ (Figure 4-31) and the values for the angle of attack for $(C_L)_{\max}$ (Figure 4-30), for the rigid wing BR01, remain remarkable constant with the change of the free stream velocity, confirm the irrelevant effects over the limits of the range of the Reynolds number covered by the tests (See section 4.4.6).

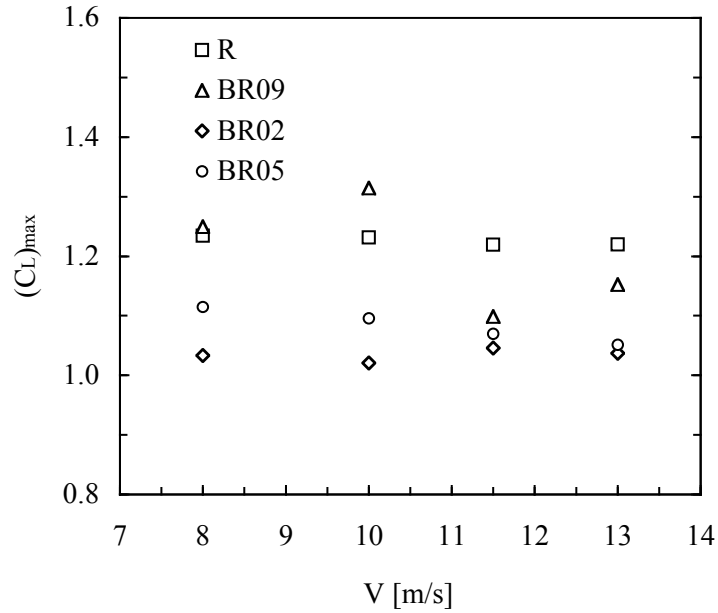


Figure 4-30. Maximum lift coefficient versus free stream velocity for four wings. The level of flexibility of the wings is BR01, BR09, BR05 and BR02, in order from the least (rigid) to the most flexible.

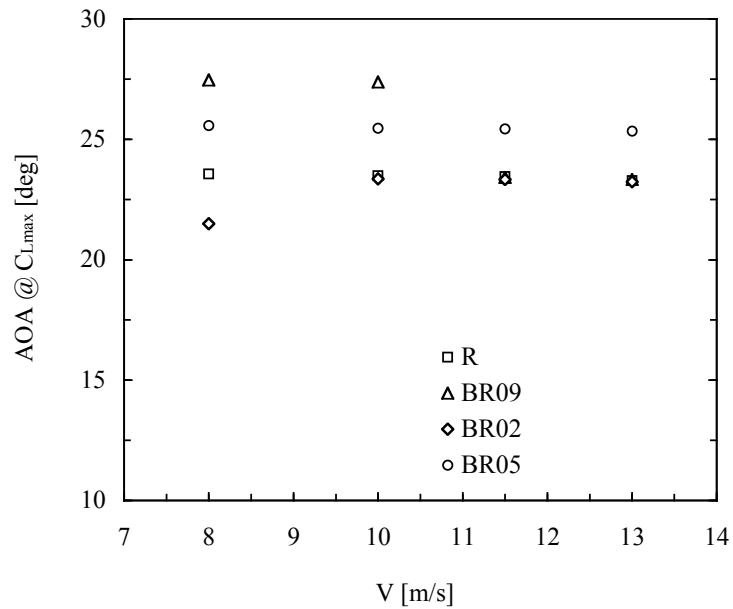


Figure 4-31. Angle of attack for maximum lift coefficient versus free stream velocity for four wings. The level of flexibility of the wings is BR01, BR09, BR05 and BR02, in order from the least (rigid) to the most flexible.

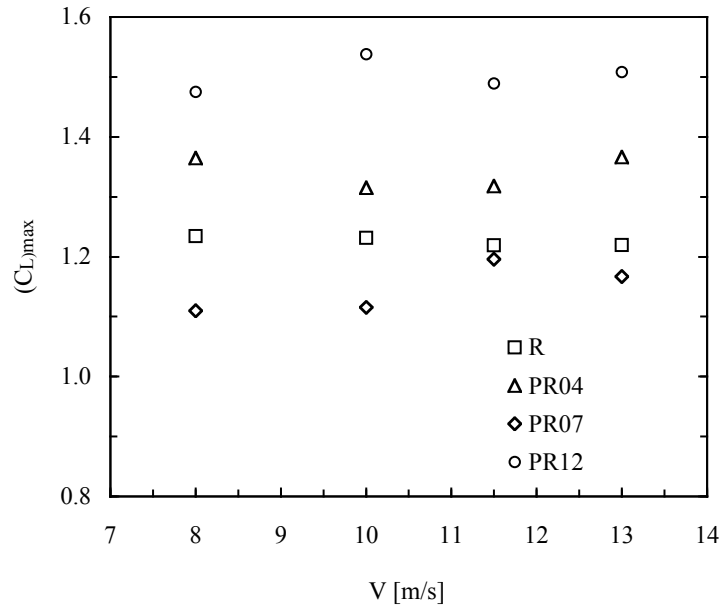


Figure 4-32. Maximum lift coefficient versus free stream velocity for four wings type R, PR04, PR07 and PR12.

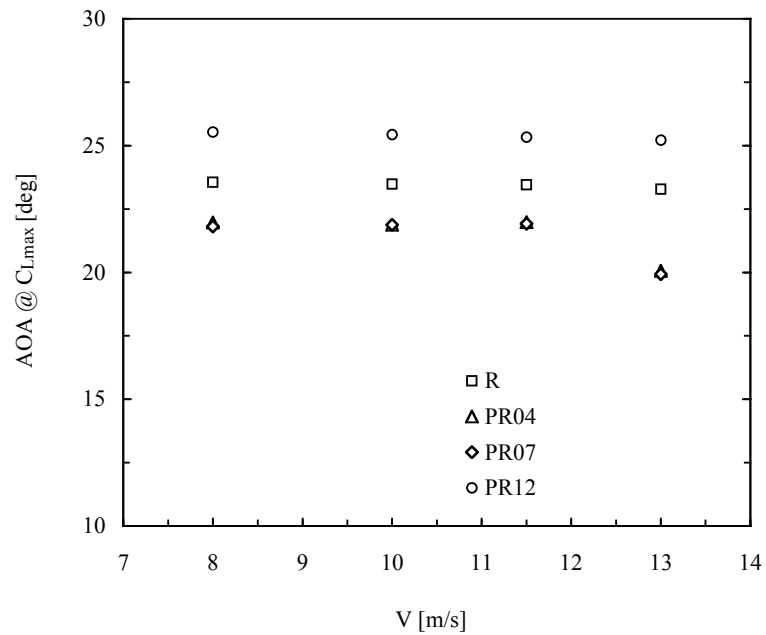


Figure 4-33. Angle of attack for maximum lift coefficient versus free stream velocity for four wings type R, PR04, PR07 and PR12.

It is noticeable the generally higher $C_{L_{max}}$ of the PR wings respect to the R wing, Figure 4-32. The AOA for $C_{L_{max}}$ shows less scatter than the BR type wings remaining closer to the R wing.

4.4.3 L/D Characteristics

An important parameter for the wing's performances is the aerodynamic efficiency, or L/D. Plots of L/D are listed for all wings in Appendix C, for wings of different flexibilities and for different dynamic pressures. Figure 4-34 shows the maximum aerodynamic efficiency, or $(L/D)_{max}$, for the four BR wings versus the free stream velocity, Figure 4-35 shows the same parameter for the wings type PR. The rigid wing (BR01) shows the smallest change in value, as expected.

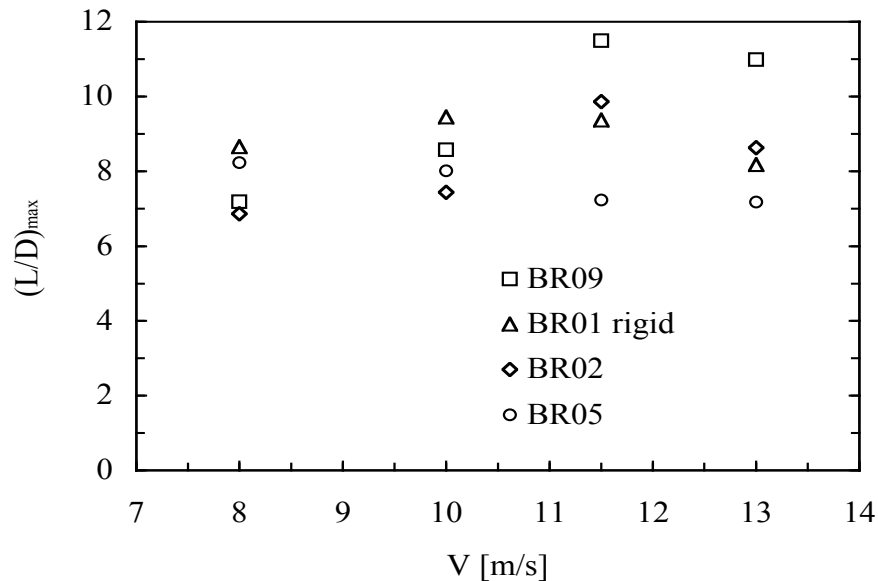


Figure 4-34. Maximum L/D versus free stream velocity for four wings. The level of flexibility of the wings is BR01, BR09, BR05 and BR02, in order from the least (rigid) to the most flexible.

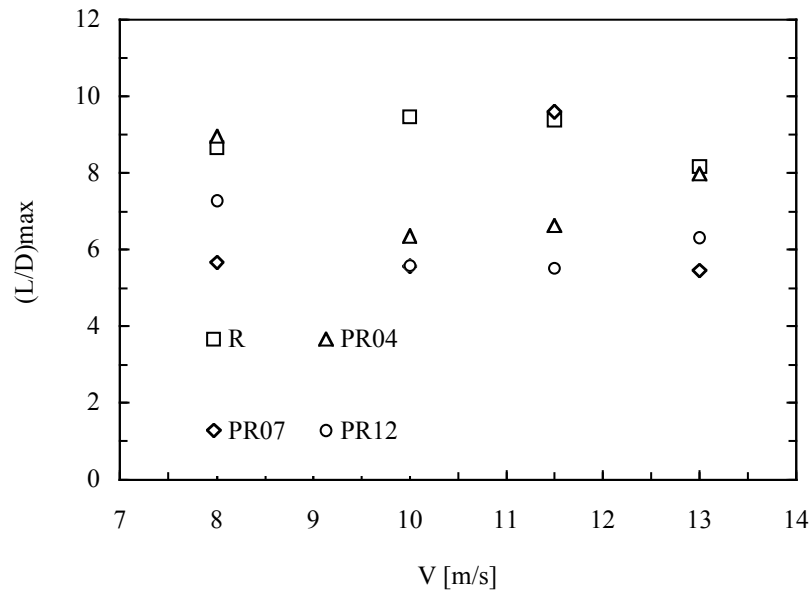


Figure 4-35. Maximum L/D versus free stream velocity for four wings type R, PR04, PR07 and PR12.

Those results need particular attention, considering the fact that they are affected by both aerodynamic lift and drag with their combined experimental accuracies. The change for flexible wings is relatively significant, but with opposite trends for wing 05 and for wings 01 and 09. The $(L/D)_{\max}$ for wing BR05 increases with the increase of free stream velocity, wings BR09 and BR02 decreases.

4.4.4 Pitching Moment Characteristics

Figure 4-36 and 4-37 show the derivative dC_m/dC_L versus the free stream velocity, for the wings type BR and PR, respectively. The change in the longitudinal moment derivative with the free stream velocity is evident, and reflects the high sensitivity of the pitching moment to the change in the position of the maximum camber, with the velocity, illustrated in Figure 4-14 and Figure 4-15.

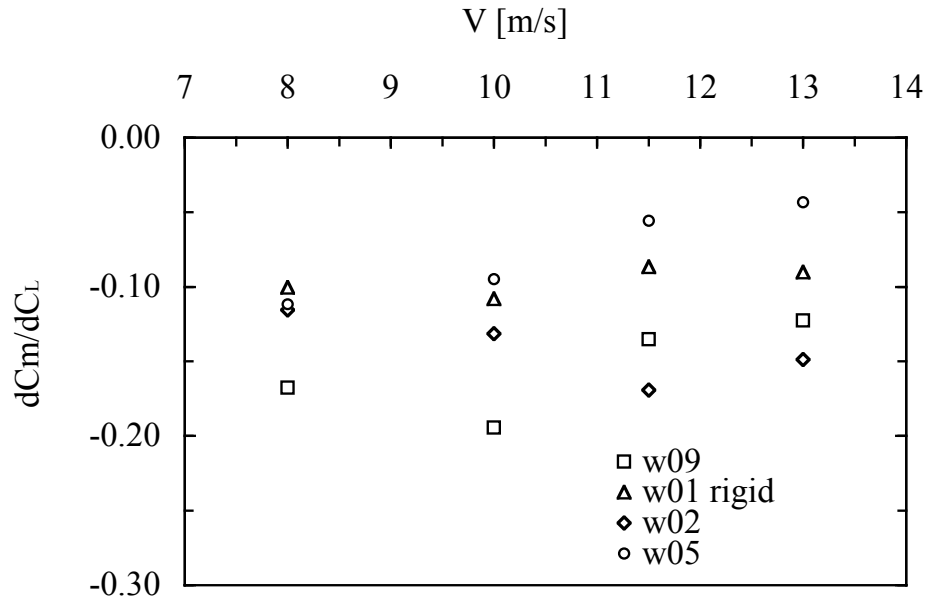


Figure 4-36. Longitudinal moment derivative versus free stream velocity for four wings. The level of flexibility of the wings is BR01, BR09, BR05 and BR02, in order from the least (rigid) to the most flexible.

The wing type PR04 has the pitching moment derivative close to the rigid wing while the wings PR07 and PR12 have the highest negative (nose down) measured values. This is reflected by the important downstream shift of the point of maximum camber experienced by those wings. In the next section the position of the aerodynamic center will be presented, a characteristic intimately related to the pitching moment and the position of maximum camber.

The longitudinal moment characteristics are one of the biggest challenges for MAVs. The vehicles are generally highly sensitive in flight test to the center of gravity (CG) position and the range of the flyable CG location is, in absolute metric terms, a few millimeters long; to meet this hard requirement can result in a formidable weight management design and fabrication challenge.

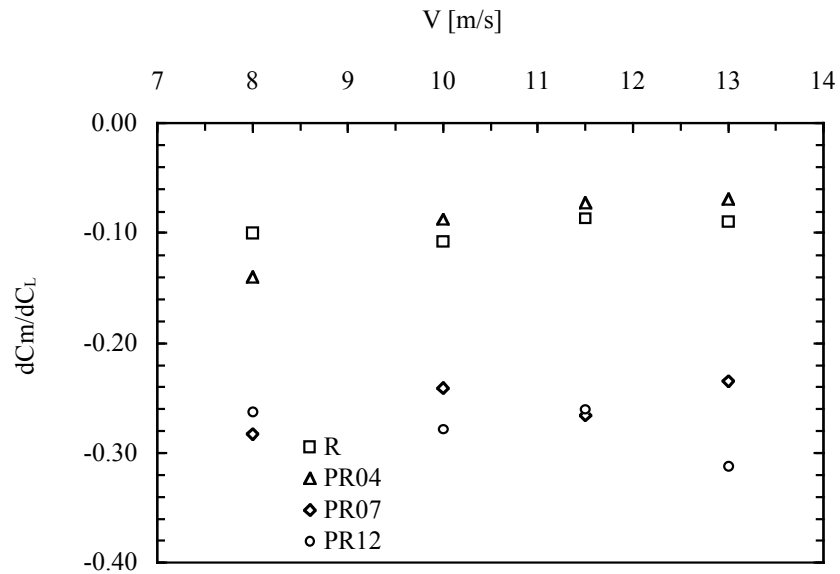


Figure 4-37. Longitudinal moment derivative versus free stream velocity for four wings. The wings depicted are PR04, PR07 and PR12; rigid wing is considered as reference.

4.4.5 Aerodynamic Center

One important parameter in the aerodynamics of the LAR wings and in the flight characteristics of the entire aircraft is the location of the aerodynamic center (ac). The scope of this section is to elucidate the location of the ac as a function of the dynamic pressure and of the type of the wing, namely its structure thus its flexibility.

The location of the ac was calculated using the sting balance data of normal force and longitudinal moment, measured around one quarter of the root chord. The calculation of the location of the ac is important in the entire range of AOA and especially in the non-linear regime however, the main scope of this work is to find correlations between the flexibility of the wing's structure and the aerodynamic characteristics, therefore only the area with linear behavior will be presented. With the same rationale of the scope of the work the assumption of independence of the ac

location from the angle of attack will be made. This postulation is generally true for high aspect ratio wings and not normally acceptable for LAR wings [15]. Analysis and observations in the non-linear regime will be discussed in the section related to the formulation of analytical models with the extension of non linear dependence of ac location with AOA.

The ac is defined as the point (X_{ac} , normalized with c [%] or $\bar{X}_{ac} = x_{ac}/(c/4)$) along the chordwise direction of the wing at which the pitching moment is independent of angle of attack, therefore

$$\partial C_{m_{ac}} / \partial \alpha = 0 \quad (4.3)$$

Considering the generic aerodynamic moment and the normal force applied at $c/4$, the transfer of the force and moment from $c/4$ to the ac yields the following expression for the pitching moment about the ac

$$M_{ac} = M_{c/4} - (X_{c/4} - X_{ac})N \quad (4.4)$$

Equation 4.4 can be nondimensionalized by using the dynamic pressure and can be presented in the following coefficients form

$$C_{m_{ac}} = C_{m_{c/4}} - (.25 - \bar{X}_{ac})C_N \quad (4.5)$$

The location of the ac can be calculated by differentiating the Equation (4.5) with the assumption that \bar{X}_{ac} is independent from the angle of attack

$$\text{Solving Equation (4.6) for } \bar{X}_{ac} \text{ we obtain } \frac{\partial C_{m_{ac}}}{\partial \alpha} = \frac{\partial C_{m_{c/4}}}{\partial \alpha} - (.25 - \bar{X}_{ac}) \frac{\partial C_N}{\partial \alpha} = 0 \quad (4.6)$$

$$\bar{X}_{ac} = .25 - \frac{\partial C_N}{\partial C_{m_{ac}}} \quad (4.7)$$

Equation (4.7) applied to the aerodynamic coefficients measured with the sting balance results in a constant location of the ac in respect to the AOA. In this way it is possible to observe the effects of the change of dynamic pressure and wing structure's flexibility on the ac location.

The following plots represent the results of the ac location for the different type of wings at the different testing Reynolds numbers. The plots are presented in a series of three with the ac location of different wings as a function of the Reynolds number in three groups:

- wings BR09, PR07 and PR12 with the rigid wing as reference
- the PR wings (04, 06, 07 and 12) with the rigid wing as reference
- the BR wings (02, 03, 05 and 09) with the rigid wing as reference

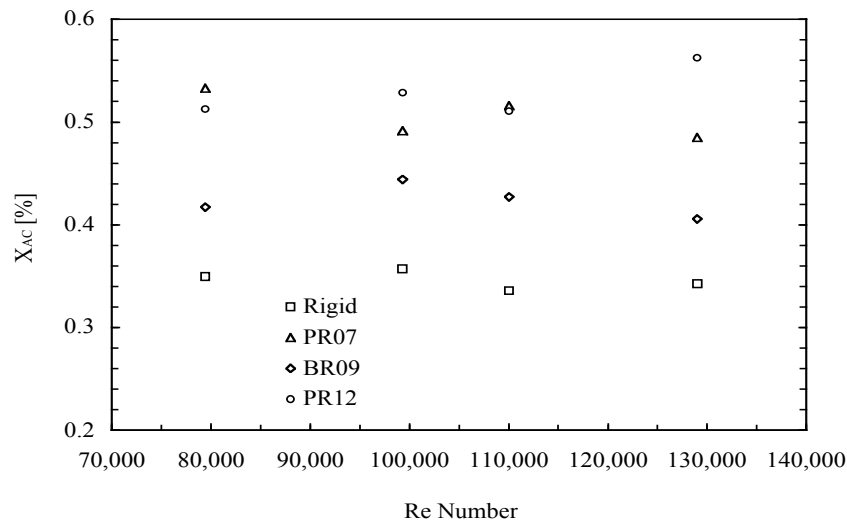


Figure 4-38. Position of the aerodynamic center as a function of the Reynolds number, for four different wings (R, PR07, BR09 and PR12).

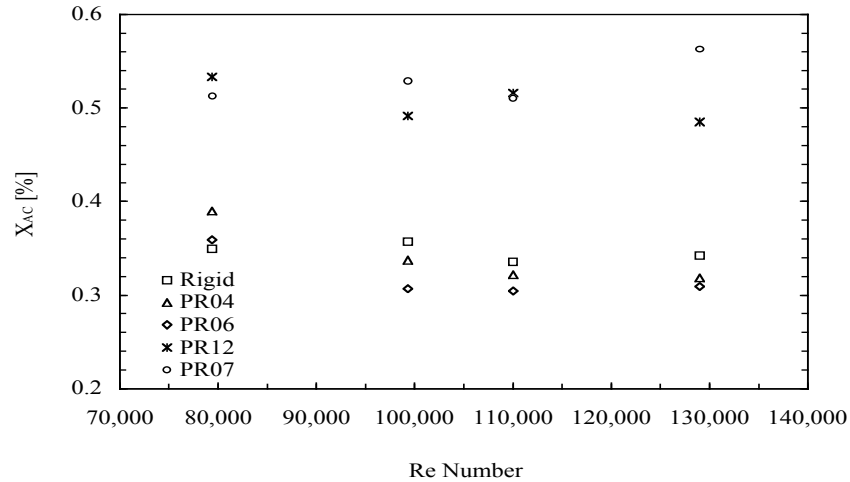


Figure 4-39. Position of the aerodynamic center as a function of the Reynolds number, for the rigid and four PR type wings.

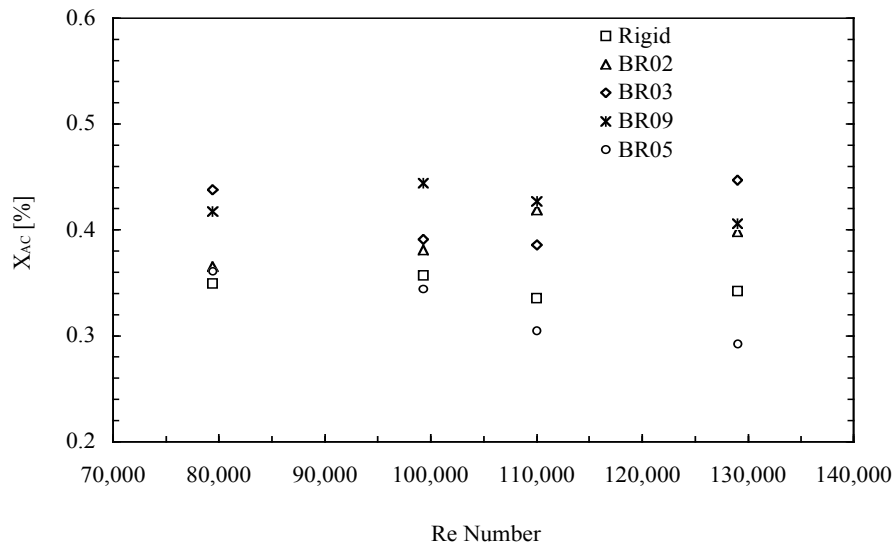


Figure 4-40. Position of the aerodynamic center as a function of the Reynolds number, for the rigid and four BR type wings.

Figure 4-38 illustrates the ac location for the three wings that have been also tested in the complete aircraft configuration (fuselage, vertical stabilizer and propeller) and flight tested, therefore are the wings for which the most amount of data is available. The other wing is the PR12, with the most amount of latex. The three flexible wings are compared with the rigid wing.

The evident trend of the plots of Figure 4-38 shows that in all cases the ac is located downstream of the 25% of the chord; as expected, by observing the downstream shift of the location of the maximum camber from the VIC results, the move of the ac is higher for the PR (perimeter reinforced) type wings in respect to the BR (batten reinforced) and rigid wing. Exceptions of the general trend are wings PR04 and PR06 (Table 3-2) with the ac location upstream respect to the rigid wing, Figure 4-39. The common feature of the two wings is the rigid central part 30 mm wide, instead 60 mm of the wing PR07. Another exception is wing BR05 with the ac location upstream respect to the rigid wing; the wing BR05 is the one with the least torsional stiffness (leading edge with carbon fiber 0/90, Table 3-2) and this causes the highest wash-out and twist, as measured by the VIC tests.

4.4.6 Effects of Reynolds Number

Because of the flexibility characteristics of the wings and the subsequent change in their shape when loaded, the Reynolds number effects must be investigated using only the rigid type wing. In that case the fluid dynamic effects can be isolated and observed.

It was observed [4, 9, 11, 14 and 15] that in general, for LAR wings, the effect of varying the Reynolds number on the lift and drag coefficients (at the same wind tunnel free stream turbulence level) can be considered small. In particular for the range of Reynolds numbers used in this work, from approximately 80,000 to 130,000, the effects are practically insignificant. Figure 4-41 shows the lift coefficient for the rigid wing versus AOA at different Reynolds number. The difference in the lift coefficient at the different Reynolds numbers is irrelevant and well inside the uncertainty bound (Appendix B).

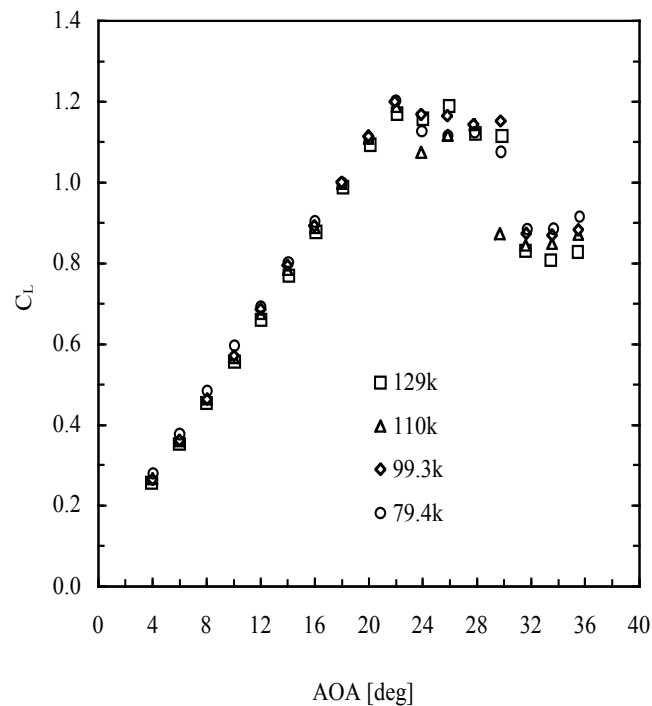


Figure 4-41. Coefficient of lift versus angle of attack for the Rigid type wing at different Reynolds numbers.

Similar behavior is presented in Figure 4-42 for the coefficient of drag. The values of the coefficients at different Reynolds number are close together for all the region of linear lift, with a tendency of a slightly higher drag at higher velocities. In the non-linear region a moderate scatter with velocity is observed, but with the same drag versus velocity trend than the linear region. Because of the small Reynolds number range for the tests, it was decided not to perform velocity sweeps.

Furthermore, because of the dynamic elastic vibrations observed on the flexible wings, it was decided not to address possible Reynolds number effects on the boundary layer regions; the assumption was that any drag characteristics derived by laminar bubbles and boundary layer interactions with the high frequency wings' vibrations will be

automatically accounted with the global drag measurements but not specifically addressed.

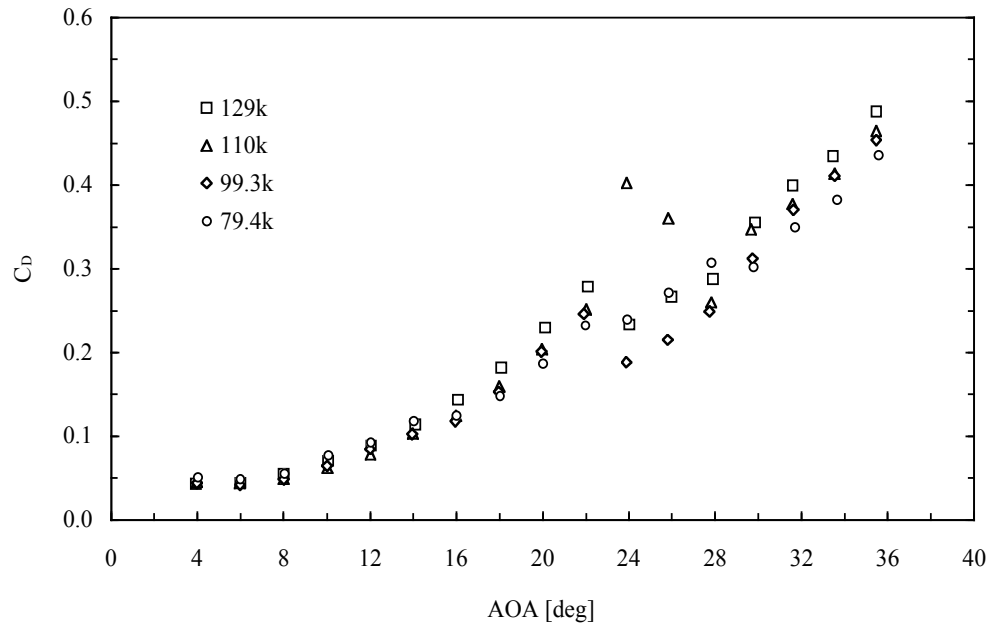


Figure 4-42. Coefficient of drag versus angle of attack for the Rigid type wing at different Reynolds numbers.

4.5 Aerodynamics Of MAVs

This section will examine the aerodynamic characteristics of the MAV. The MAV is a complete aircraft with some selected wings installed on the same fuselage and same tail surfaces, thus only the effects of different wings, with their distinctive structural flexibility, can be evinced. Tests were conducted without propeller, to account of the change in the aerodynamic properties of the basic wing due to the addition of the fuselage and vertical tale surface, and with the powered propeller.

4.5.1 Lift Curve Characteristics

The first step of the study of a complete MAV was to test three selected wings, the Rigid, the PR07 and BR09 mounted on the same fuselage and with the same vertical

stabilizer. The configuration obtained was a realistic flying configuration with only the propeller missing. The two flexible wings were selected for their relevance in the flight test program and the rigid wing was used as reference.

A series of tests were performed at the four standard Reynolds number and samples of the results are reported in Appendix C. It is interesting to note the general decrease in lift, at the same AOA, caused by adding the fuselage. Figures 4-43, 4-44 and 4-45 show an example of lift versus AOA duplicated from the plots in Appendix C. Interestingly enough the decrease in lift at the same AOA seems to be smaller with the flexible wings in respect to the rigid wing.

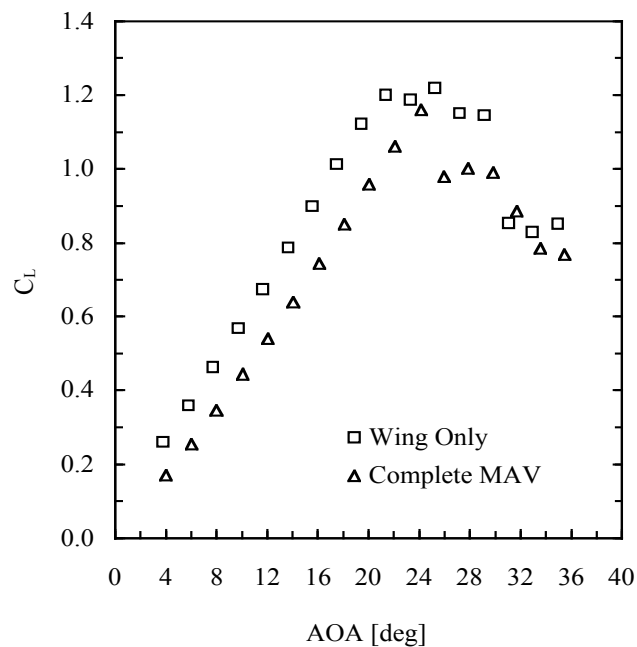


Figure 4-43. Coefficient of lift versus angle of attack for the Rigid type wing compared with the same wing mounted on a MAV fuselage at $V_\infty = 13$ m/s.

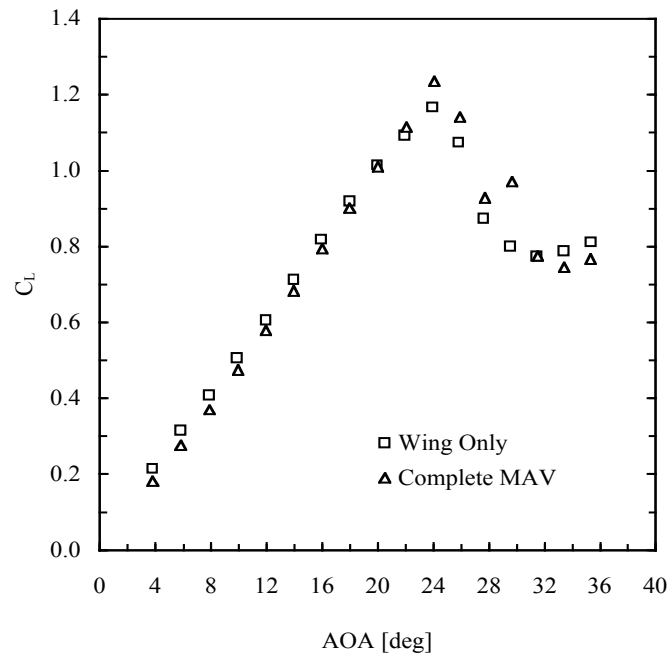


Figure 4-44. Coefficient of lift versus angle of attack for the PR07 type wing compared with the same wing mounted on a MAV fuselage at $V_\infty = 13$ m/s.

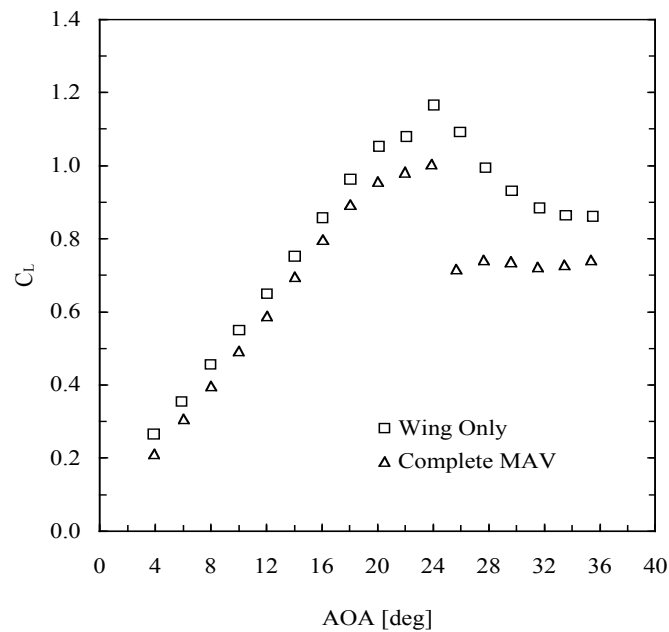


Figure 4-45. Coefficient of lift versus angle of attack for the BR09 type wing compared with the same wing mounted on a MAV fuselage at $V_\infty = 13$ m/s.

It is evident from Figures 4-43, 4-44 and 4-45 that the rigid wing is more sensitive than the two flexible wings to the effects of adding a fuselage. In particular the loss of lift in the cases of the flexible wings, at the same angle of attack, is lower for the flexible wings and the PR07 wing exhibits the least loss of lift. From the data in Appendix C was possible to calculate the change in lift at the same AOA as

$$DC_L = (C_L)_{MAV} - (C_L)_{wing} \quad (4.8)$$

Figure 4-46 and Figure 4-47 show the plots with the function from Equation (4.8) for a free stream velocity of 13 m/s and 10 m/s, respectively, for the wings type Rigid, PR07 and BR09.

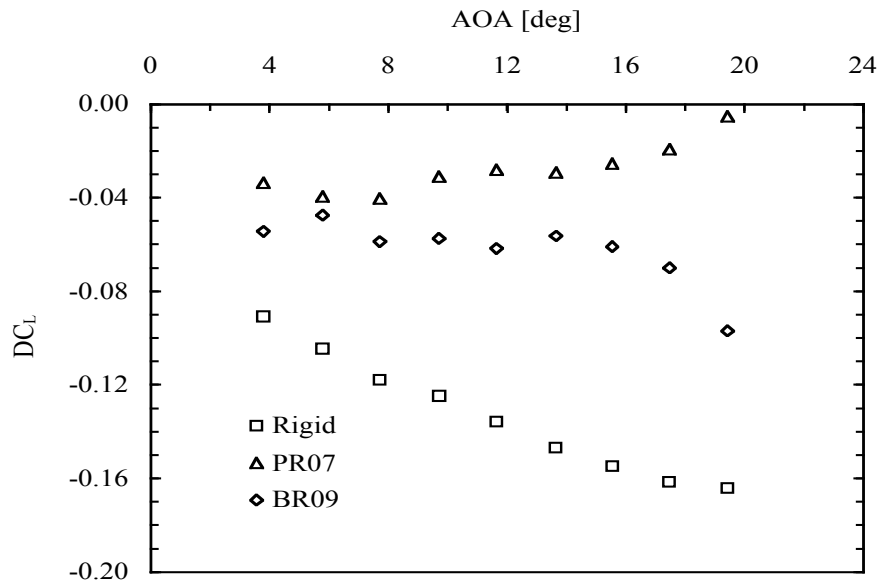


Figure 4-46. Difference in coefficient of lift, versus AOA, due to the contribution of the fuselage to the wings type R, PR07 and BR09, at $V_\infty = 13$ m/s.

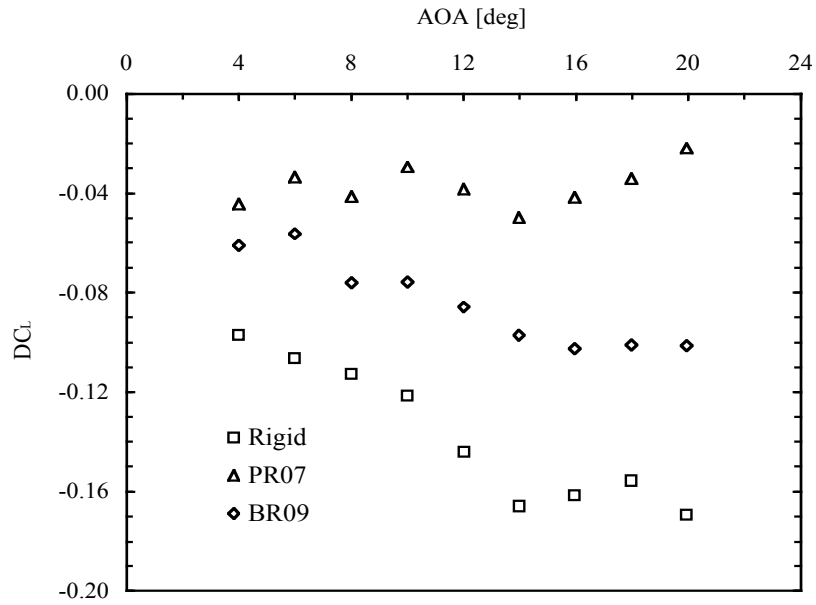


Figure 4-47. Difference in coefficient of lift, versus AOA, due to the contribution of the fuselage to the wings type R, PR07 and BR09, at $V_\infty = 10$ m/s.

From the previous Figures it is apparent the different behavior of the lift for the three wings when the same fuselage is added. Furthermore the batten reinforced wing BR stands in between the rigid and the perimeter reinforced wing PR. The loss of lift in the rigid wing is the highest and AOA dependent whereas it is low and independent from AOA for the PR wing. The BR wing acts in an intermediate fashion, with an intermediate loss of lift mildly AOA dependent.

In the case of the MAVs with a powered propeller, the lift and drag coefficients were found to be predominantly dependent on the thrust coefficient or, in other words, it is clear the very significant influence of the propeller in the overall aerodynamics of the vehicle. Furthermore, the propeller effects are generally non-linear.

An example of the aerodynamic data, in terms of total lift coefficient versus AOA, is depicted in Figure 4-48 and Figure 4-49, for a rigid wing and for a BR (batten reinforced) wing, respectively.

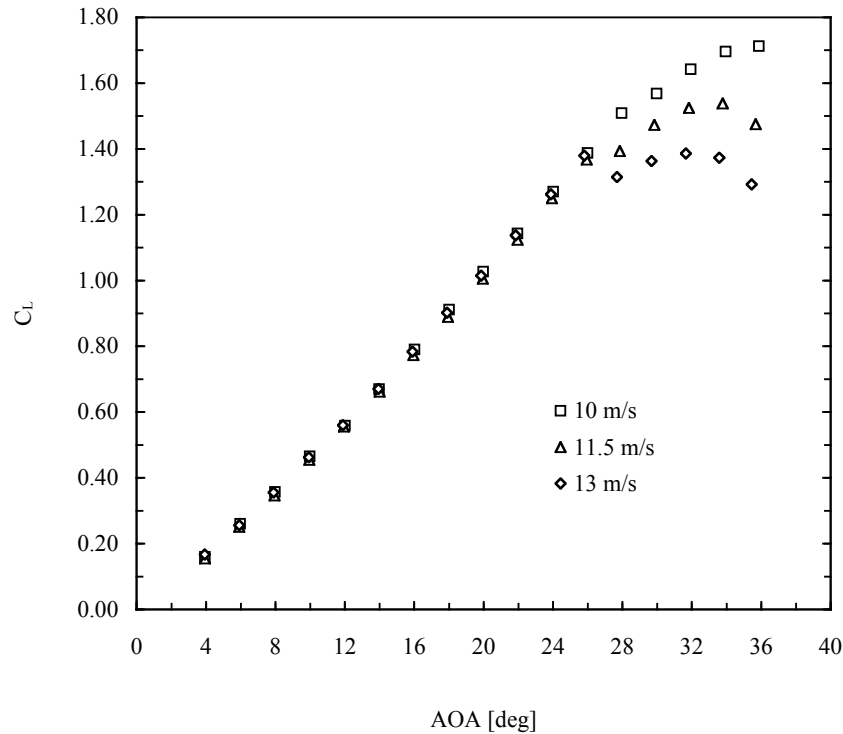


Figure 4-48. Plot of total lift coefficient versus AOA, at three different free stream dynamic pressures, for the Rigid type wing with the powered propeller on. The total lift coefficient includes the thrust component. It is evident the nonlinear dependence of the coefficient with the dynamic pressure.

A noticeable variation of the lift curve slope with the dynamic pressure, already observed in other works [56, 95 and 98], is evident in Figure 4-49. This is not consistently evident, in the rigid wing, as illustrated in Figure 4-48. The variation of the lift curve slope with the dynamic pressure is therefore attributable to the flexibility of the wing's structure.

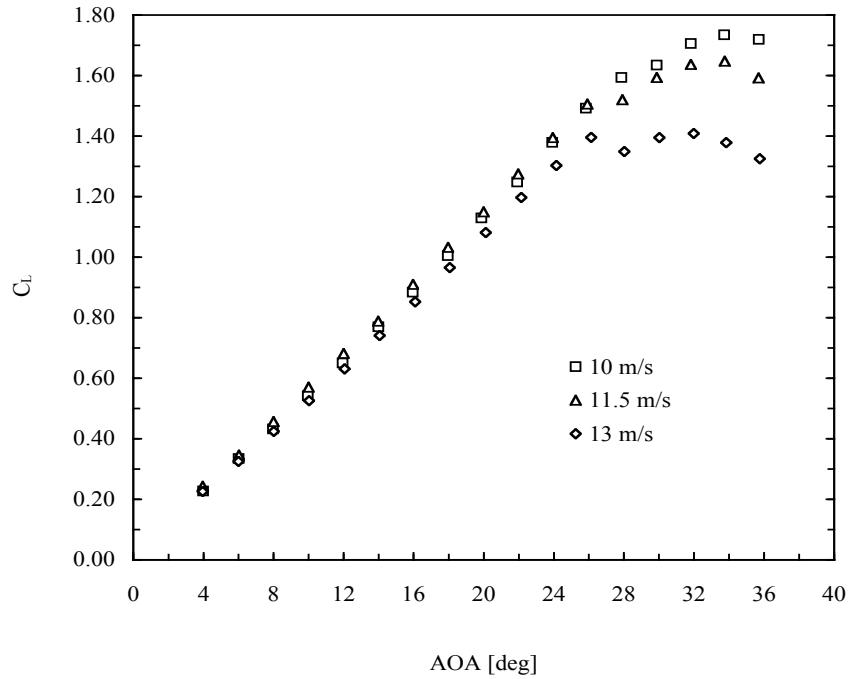


Figure 4-49. Plot of total lift coefficient versus AOA, at three different free stream dynamic pressures, for the BR09 type wing with the powered propeller on. The total lift coefficient includes the thrust component. It is evident the nonlinear dependence of the coefficient and the lift slope with the dynamic pressure.

Another significant effect observed on the aerodynamic coefficients at a fixed motor voltage at various dynamic pressures is the change in the maximum lift coefficient, as shown in Figure 4-48 and Figure 4-49.

4.5.2 Drag Characteristics

From the tests mentioned in the previous section and reported in Appendix C data about the effects of adding the fuselage on drag were gathered. From the same Appendix, Figures 4-50 and 4-51 and 4-52 show three sample plots relative to the drag versus lift for the same wings with and without fuselage.

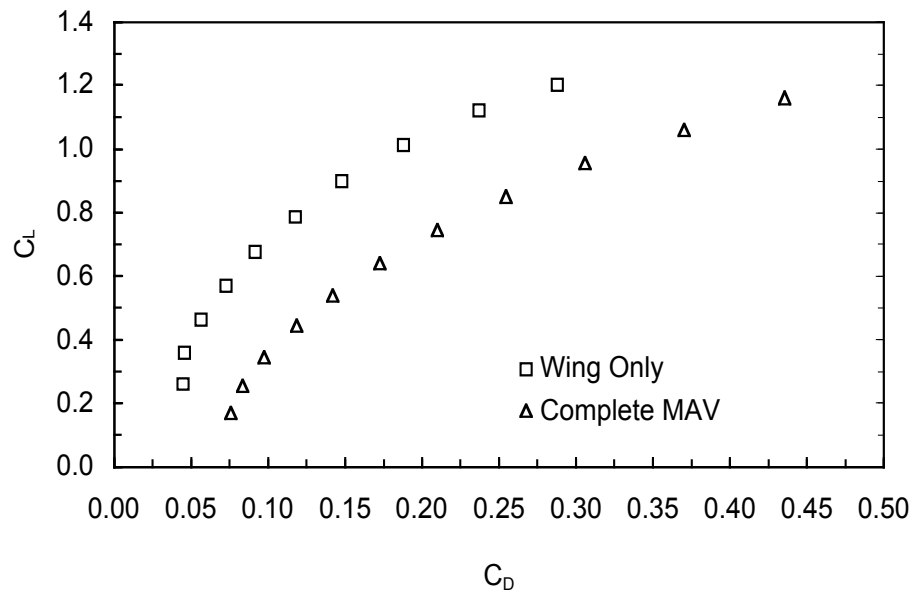


Figure 4-50. Coefficient of lift, versus coefficient of drag, in the two cases with and without fuselage for wing type R, at $V_\infty = 13$ m/s.

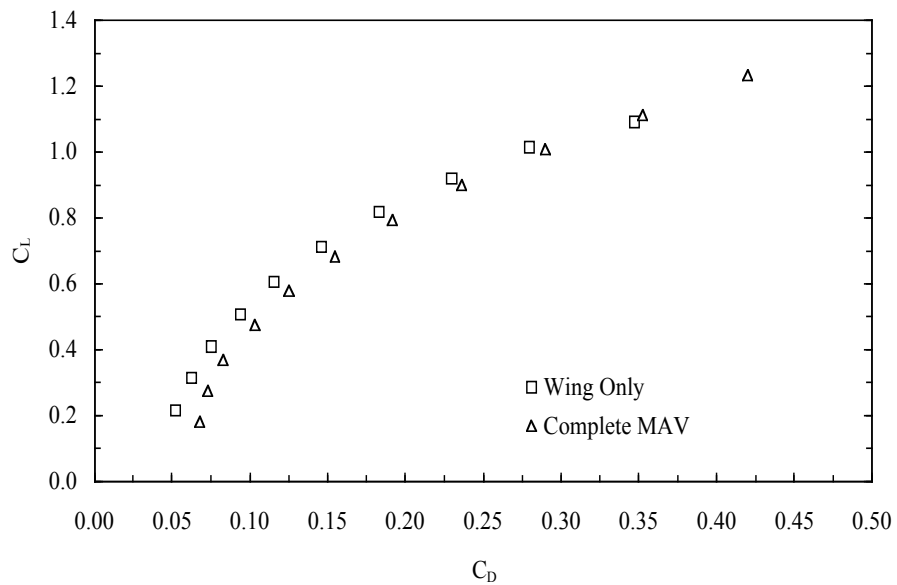


Figure 4-51. Coefficient of lift, versus coefficient of drag, in the two cases with and without fuselage for wing type PR07, at $V_\infty = 13$ m/s.

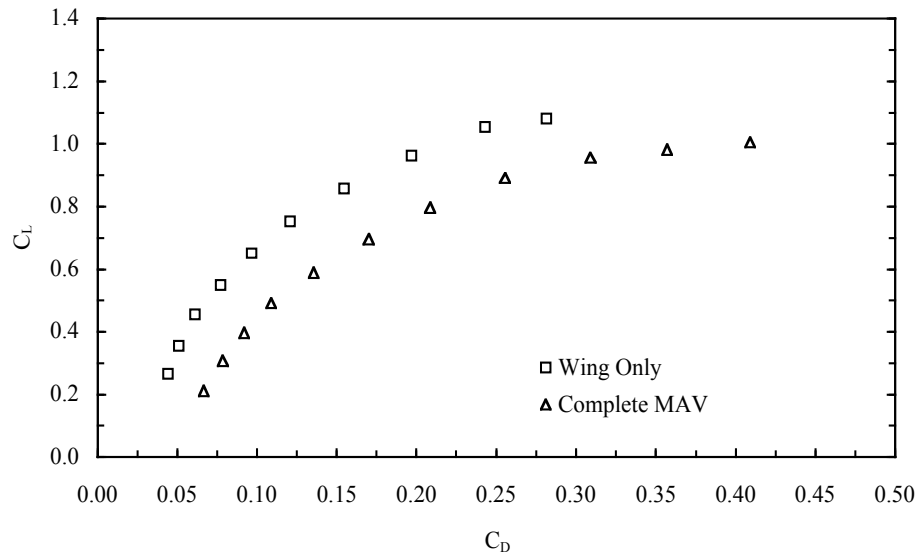


Figure 4-52. Coefficient of lift, versus coefficient of drag, in the two cases with and without fuselage for wing type BR09, at $V_\infty = 13$ m/s.

Using the aforementioned lift and drag data and the same post processing technique presented in the previous section, the change in the coefficient of drag between the wing alone and the same wing mounted on the fuselage was defined as

$$DC_D = (C_D)_{MAV} - (C_D)_{wing} \quad (4.9)$$

The plots with the difference in drag coefficient, obtained from Equation (4.9), versus lift coefficient are presented in the Figures 4-53 and 4-54 for the three types of wing and at the free stream velocities of 13 and 10 m/s.

It useful to remind to the reader the presence of a free stream velocity error bound in the aerodynamic coefficients, which should be considered in the interpretation of the results presented; the error bound is presented in Appendix B Figures B-4 to B-9.

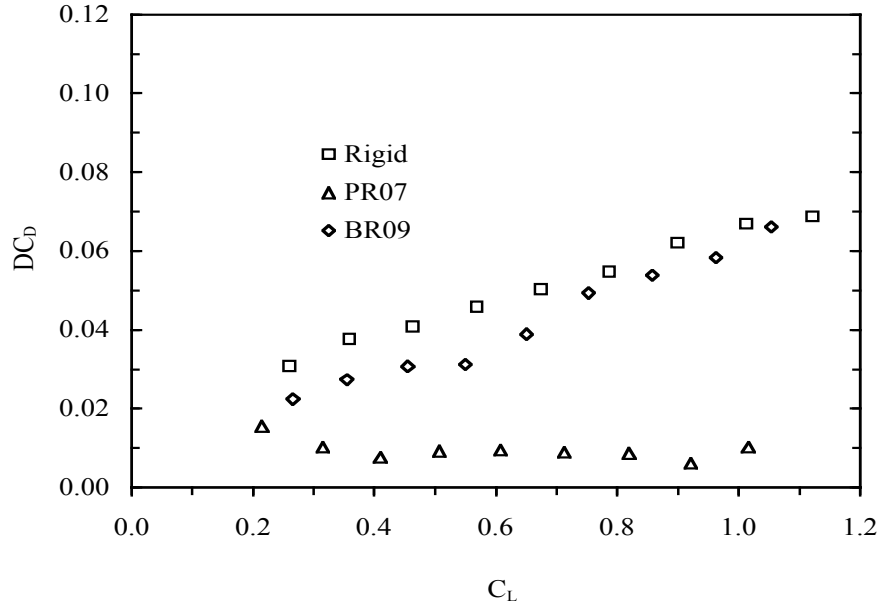


Figure 4-53. Difference in coefficient of drag versus coefficient of lift, due to the contribution of the fuselage to the wings type R, PR07 and BR09, at $V_\infty = 13$ m/s.

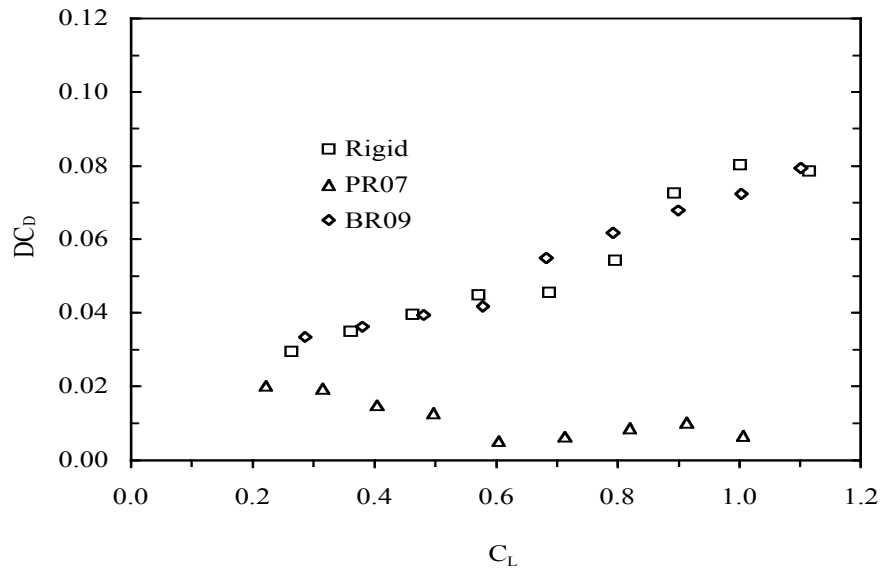


Figure 4-54. Difference in coefficient of drag versus coefficient of lift, due to the addition of the fuselage to the wings type R, PR07 and BR09, at $V_\infty = 10$ m/s.

The case with the powered propeller is more complex than the case without propeller, regarding the design and carry out of the experiments and the interpretation of

the results. The main source of complexity is represented by the fact that the added independent variable, the propeller speed, set by the DC motor voltage input, is in reality also an independent variable, being strongly dependent from the AOA and free stream velocity. Furthermore, the dependency is non-linear in the cases with lower input voltage and lower dynamic pressure, as reported in the Appendix C.

Because of this intimate input voltage-AOA-dynamic pressure non-linear dependency, the author decided to proceed with an analytical modeling technique in order to obtain a simulation model of the propulsion and aerodynamic coefficients based on wind tunnel tests. The modeling effort is described in Chapter 5. Several examples of the drag versus lift at different free stream velocities and at different voltage motor settings are reported from Figure 4-55 to Figure 4-60 for the wings type R, PR07 and BR09.

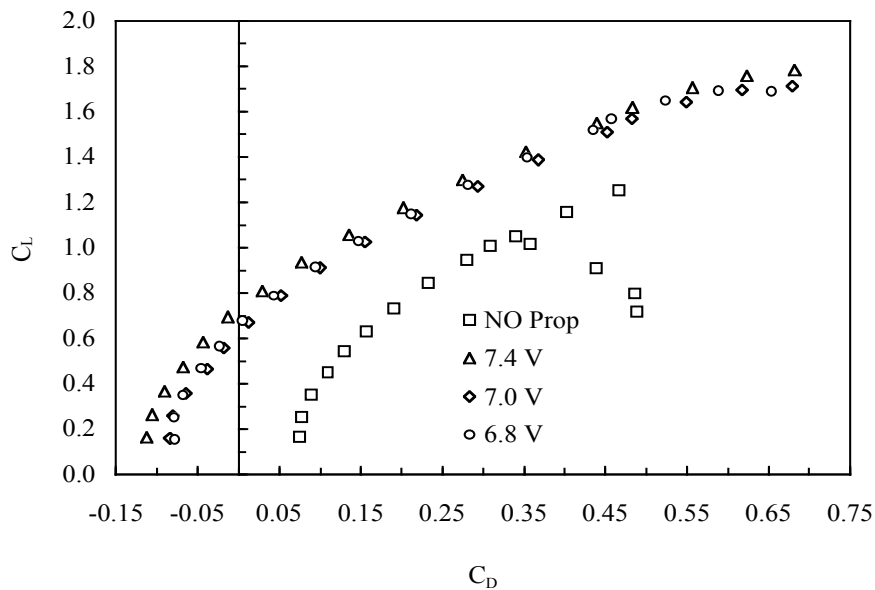


Figure 4-55. Coefficient of drag versus coefficient of lift, for the MAVR with powered propeller, at $V_\infty = 10$ m/s for different voltage motor settings. The negative C_D denotes a positive net thrust.

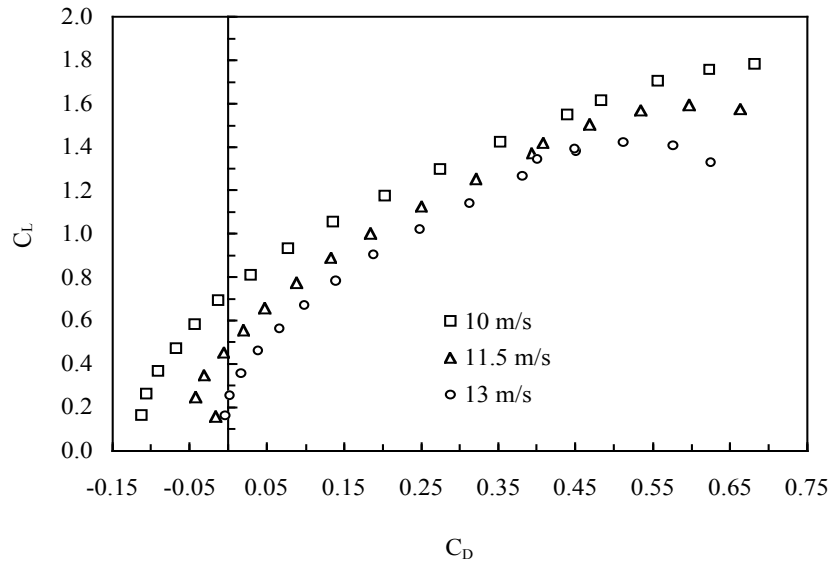


Figure 4-56. Coefficient of drag versus coefficient of lift, for the MAVR with powered propeller, at $E = 7.4$ Volt for different free stream velocities. The negative C_D denotes a positive net thrust.

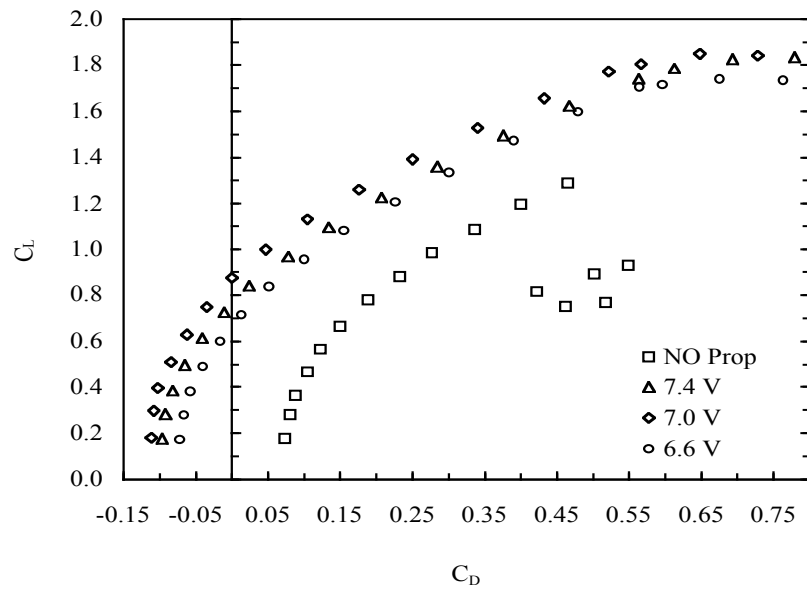


Figure 4-57. Coefficient of drag versus coefficient of lift, for the MAVPR07 with powered propeller, at $V_\infty = 10$ m/s for different voltage motor settings. The negative C_D denotes a positive net thrust.

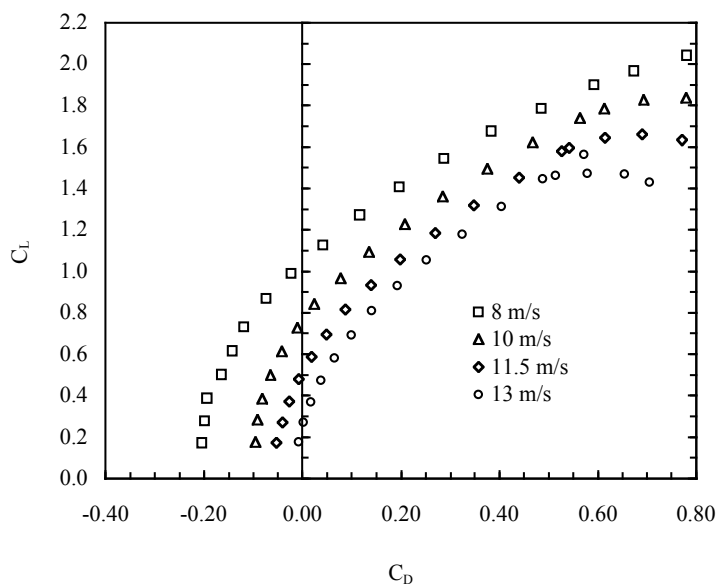


Figure 4-58. Coefficient of drag versus coefficient of lift, for the MAVPR07 with powered propeller, at $E = 7.4$ Volt for different free stream velocities. The negative C_D denotes a positive net thrust.

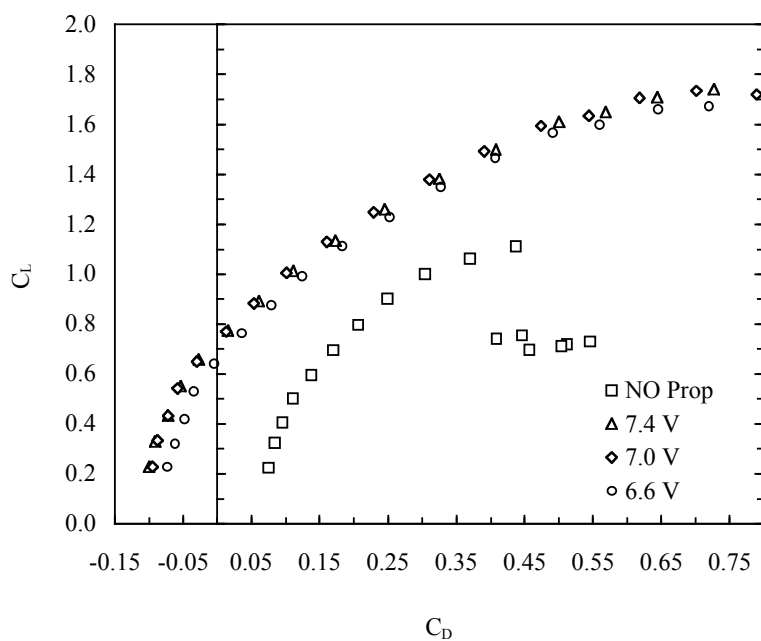


Figure 4-59. Coefficient of drag versus coefficient of lift, for the MAVBR09 with powered propeller, at $V_\infty = 10$ m/s for different voltage motor settings. The negative C_D denotes a positive net thrust.

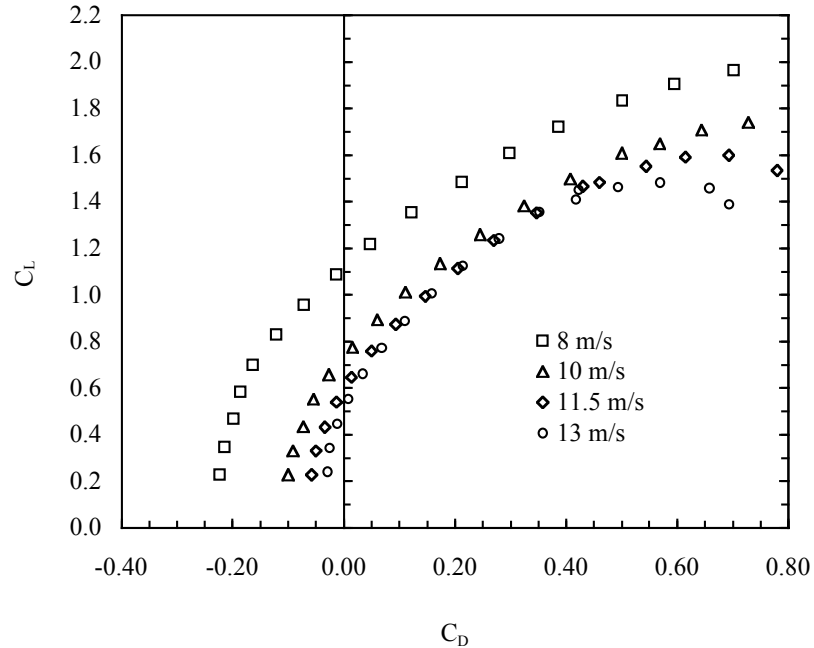


Figure 4-60. Coefficient of drag versus coefficient of lift, for the MAVBR09 with powered propeller, at $E = 7.4$ Volt for different free stream velocities. The negative C_D denotes a positive net thrust.

It is evident from the plots in Figures 4-55, 4-57 and 4-59 at different voltage inputs that, for all the three types of wing, there is the obvious significant distance between the drag coefficient curves without and with propeller however the curves with propeller are relatively close together. Observing the three plots at the same motor voltage input but at different free stream velocities, Figures 4-56, 4-58 and 4-60, it can be noted the scatter of the drag coefficient curves, with a perceptible non-linear tendency at the different dynamic pressures. There is no appreciable differences or trends regarding the different flexibility characteristics of the three wings.

4.5.3 Pitching Moment Characteristics

Similarly to the case of lift and drag characteristics, the effects on the longitudinal moment of adding the same fuselage and the same vertical stabilizer to the wing were

investigated with the three standard types of wing. From the group of plots presented in Appendix C, it is possible to discern interesting conclusions. Figures 4-61, 4-62 and 4-63 present plots with the coefficient of pitching moment around the 25% of the root chord versus the coefficient of lift, for the three wings type R, PR07 and BR09, at the free stream velocity of 13 m/s.

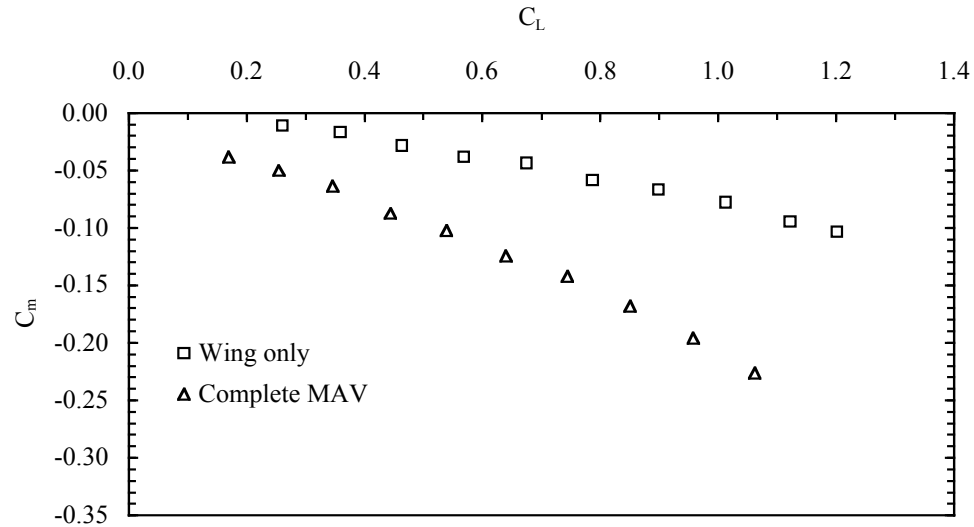


Figure. 4-61. C_m versus C_L for Rigid wing and MAVR at $V_\infty = 13$ m/s.

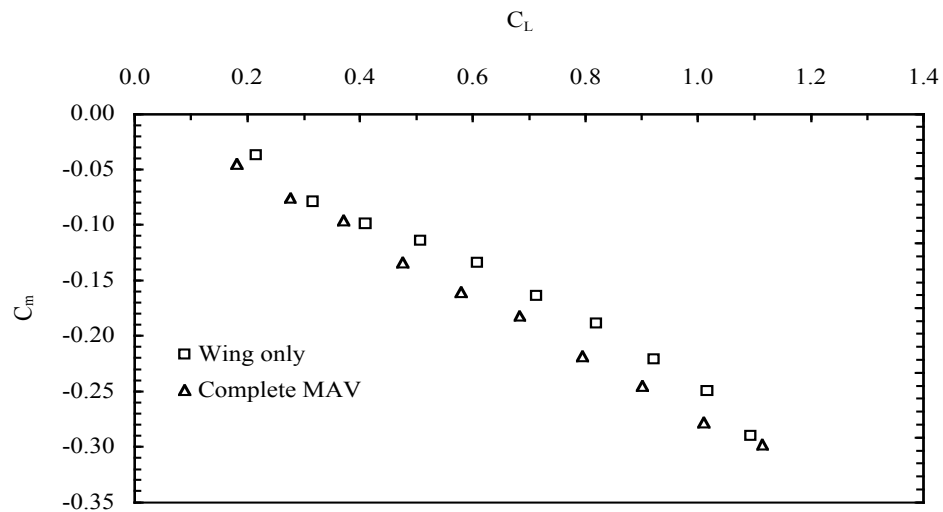


Figure 4-62. C_m versus C_L for PR07 wing and MAVPR07 at $V_\infty = 13$ m/s.

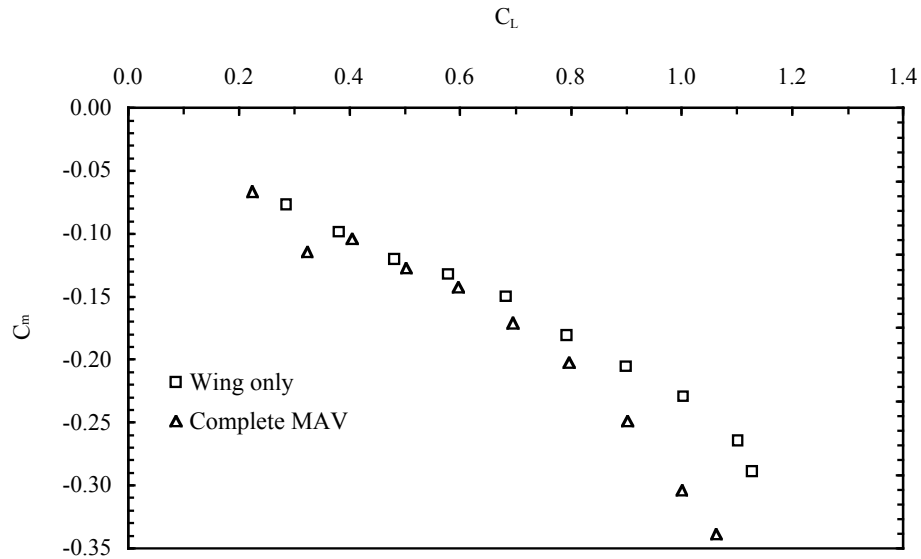


Figure 4-63. C_m versus C_L for BR09 wing and MAVBR09 at $V_\infty = 13$ m/s.

Comparing Figure 4-61 (rigid wing) and Figure 4-62, PR wing, it is evident that the PR wing has in general a higher pitching moment in respect to the rigid wing, as already mentioned in the section on the isolated wings. However the effect of the addition of the fuselage is not severe in the PR wing as for the rigid wing, in particular adding the fuselage on the rigid wing increases the static stability margin (the derivative of the coefficient of pitching moment in respect to the coefficient of lift) and increases also the moment; in the PR wing otherwise the moment increases by adding the fuselage, but the static stability margin does not appreciably change. Similar conclusions can be found by inspecting Figure 4-63 about the BR wing, with the difference that the curve seem to be slightly not linear.

In the case of the MAVs with powered propeller, the longitudinal pitching moment coefficient is significantly and consistently affected by the change in dynamic pressure,

but interestingly enough, the aforementioned dynamic pressure effects are moderately dependent from the wing flexibility and robustly affected by the change in the propeller operating conditions. The changes in the propeller operating conditions are originally caused by the change in the dynamic pressure and AOA, at a constant motor voltage input.

Figure 4-64 and Figure 4-65 illustrate tests results with the coefficient of pitching moment versus coefficient of lift, for wing BR09 (batten reinforced), without and with propeller, respectively.

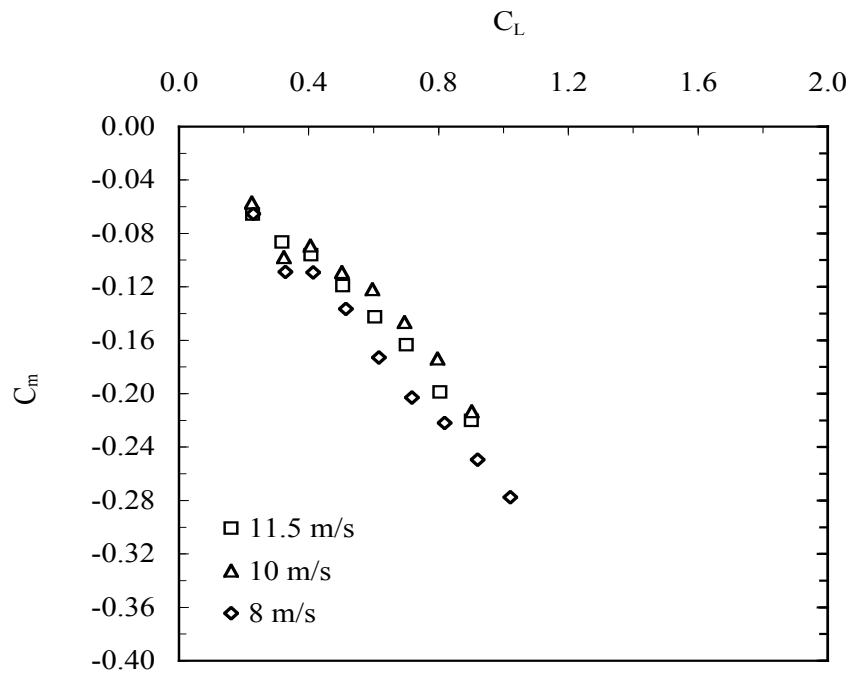


Figure 4-64. Pitching moment coefficient, at three different free stream dynamic pressures, for MAV with the BR09 type wing without propeller.

In the case of non-powered tests, Figure 4-64, the pitching moment curves at different dynamic pressures are relatively close together. In the powered case, Figure 4-65, the static stability remains similar to the un-powered case and the vehicle exhibits a

modest, but consistent, nose up moment attributed to the propeller effects. The relatively high scatter of the pitching moment curves with the dynamic pressure observed in Figure 4-65 is motor voltage dependent; with the increase of the voltage (or the propeller speed) the curves become closer together, without any important change in the stability derivative.

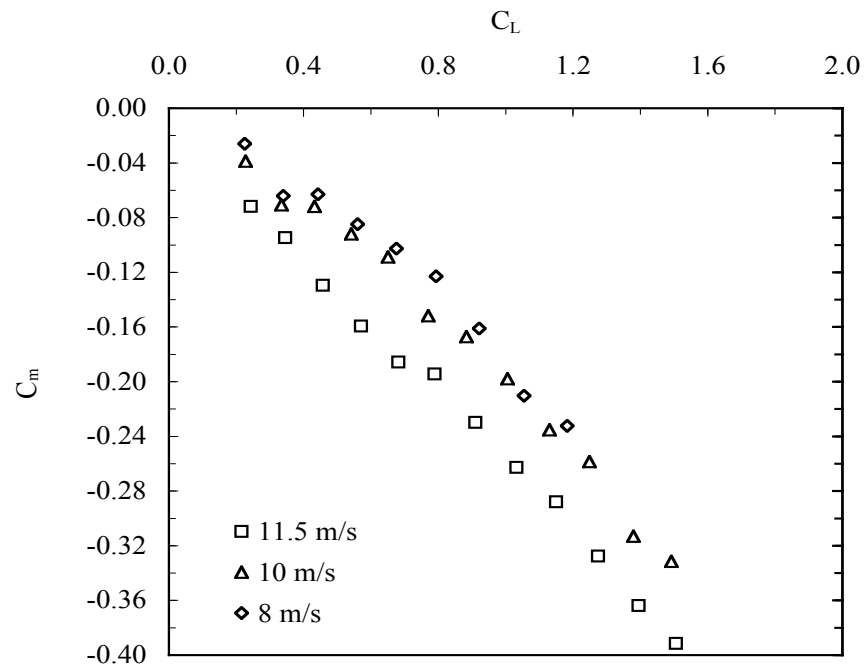


Figure 4-65. Pitching moment coefficient, at three different free stream dynamic pressures, for MAV with the BR09 type wing with propeller. The motor setting is 7.0 Volt.

In the case of the powered tests, the linear part of the pitching moment coefficient curve is extended up to a lift coefficient of 1.5, while in the non-powered case the linear limit is 1.0. The results described above confirmed the need for dynamic pressure

dependent terms in fitting functions for lift, drag and pitching moment. Experimental data were plotted and carefully checked for experimental noise or bad data.

The significant coupling between pitching moment and propeller speed, or motor setting, makes the throttle management a good candidate for an advanced longitudinal control system.

4.5.4 Propeller Speed

The control of the propeller speed was obtained by setting the DC motor input voltages at several pre-selected values through the DC power supply. At the same time the absorbed current was read on the power supply display while the propeller speed was obtained by a non-contact laser tachometer. With the described arrangement the real independent value was the voltage, and the propeller speed was strongly dependent from the test conditions such the AOA and the free stream velocity. In this way when the voltage input to the motor was set, the wind tunnel flow velocity was set and the test called for an AOA sweep, the propeller speed would change at every AOA. Since the propeller thrust is strongly RPM dependent, the thrust would also change with the AOA.

A series of propeller speed plots is presented in Appendix C; four samples from the series are depicted in Figure 4-66, 4-67 and 4-68. In general the propeller speed, at constant motor voltage setting, decreases with an increase of the AOA and increases with an increase of the free stream velocity.

The propeller speed is also significantly affected by the propeller diameter. Tests with isolated propellers in the wind tunnel revealed that with larger diameters, in the order of 70 or 80 mm, the propeller speed was lower and there is no gain in thrust in respect to the smaller diameters (in the range of 60 mm).

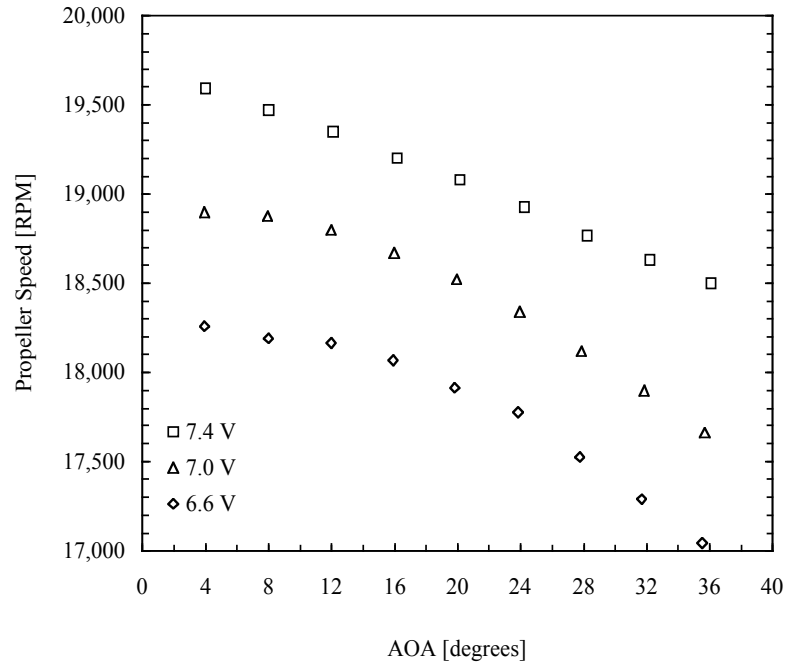


Figure 4-66. Propeller speed versus AOA, for three motor's power settings, at a free stream velocity of 11.5 m/s. The wing used on the MAV is the Rigid type.

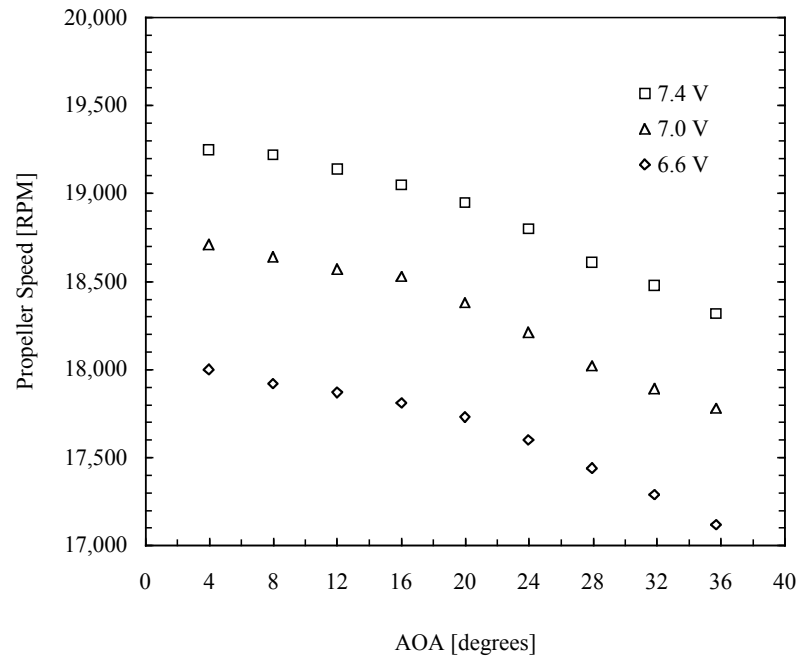


Figure 4-67. Propeller speed versus AOA, for three motor's power settings, at a free stream velocity of 11.5 m/s. The wing used on the MAV is the BR09 type.

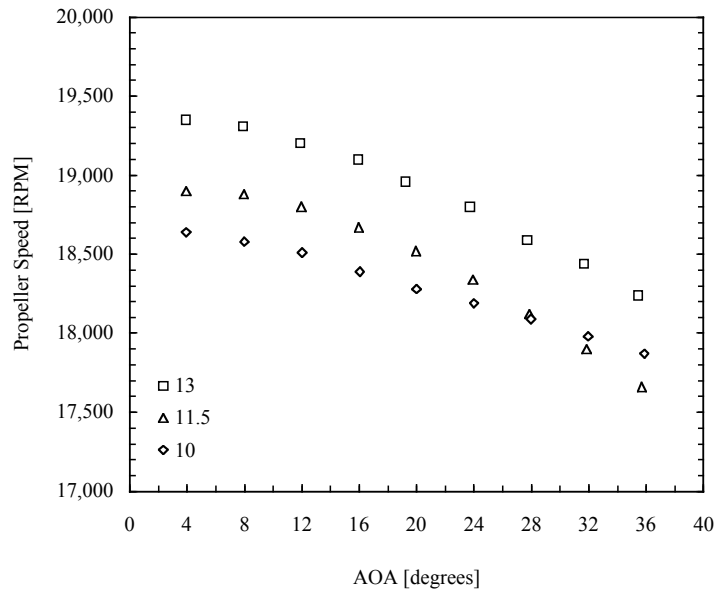


Figure 4-68. Propeller speed versus AOA, at three free stream velocities, for a motor's power setting of 7.0 Volt. The wing used on the MAV is the Rigid type.

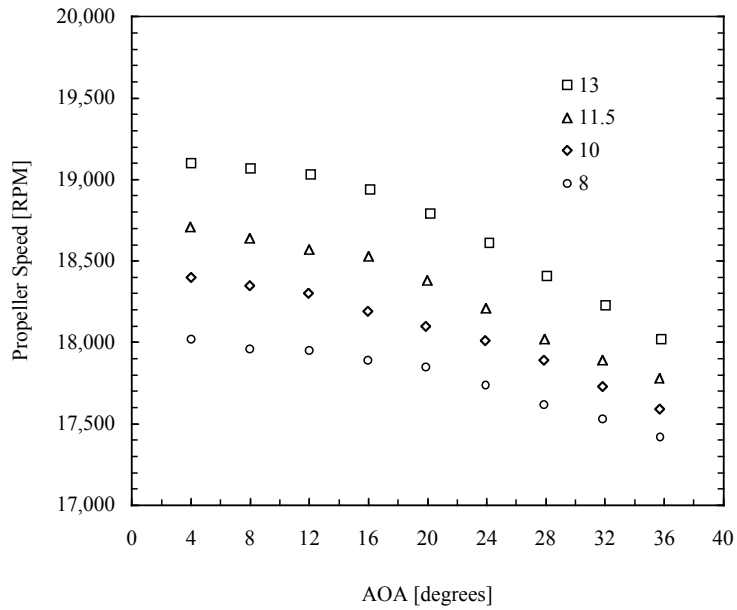


Figure 4-69. Propeller speed versus AOA, at four free stream velocities, for a motor's power setting of 7.0 Volt. The wing used on the MAV is the BR09 type.

Although there are no clear trends regarding the propeller speed with the different wing flexibilities, some observations can be made. The change in propeller speed, generally non-linear with AOA, is less steep for low AOA angles; a possible explanation is that the weaker lift at low angles of attack generates a smaller upwash in front of the wing thus having a weaker effect on the propeller.

The propeller speed curves, at constant motor voltage input, tend also to be linear at high voltage and higher velocity and increasingly non-linear at low motor voltage and at low free stream velocity. The propeller speed was recorded mainly with the purpose to define an analytical model that can be used to correlate the propulsion coefficients and the aerodynamic coefficients with the throttle setting in any flight conditions, as will be explained in Chapter 5.

4.5.5 Uninstalled Propeller Thrust and Power

A thorough experimental study of the propulsion characteristics was not the scope of this work, nevertheless several tests were conducted using the motor and propeller mounted on a special rig on the wind tunnel sting balance. In this way the propeller thrust and motor power were measured without the influence of the MAV's fuselage and the wing, using the motor voltage setting and free stream velocity as independent function.

A test matrix with a voltage setting sweep at different wind tunnel flow velocities was run with the same propeller at various diameter. Figures 4-70 and 4-71 shows a sample of plots with the thrust and power for motor voltage sweep tests at three values of wind tunnel free stream velocity for a propeller U-80, the same used in all the

experiments presented in this work. The propeller diameter was 64 mm. The AOA during all tests was constant at zero degrees.

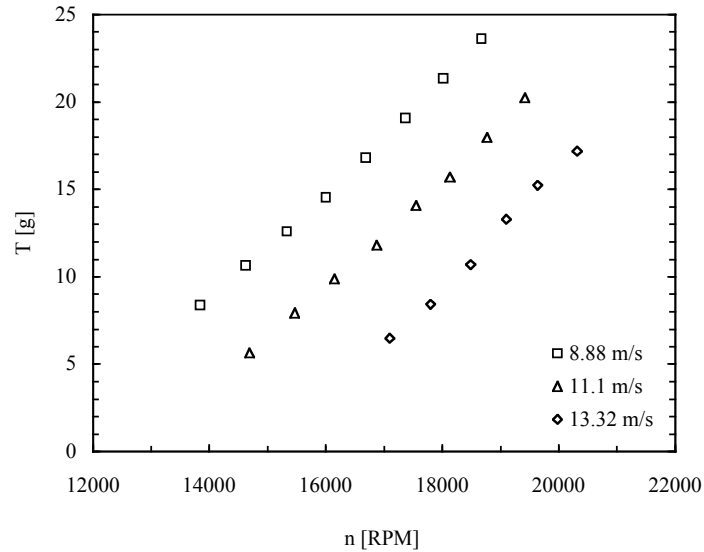


Figure 4-70. Isolated propeller thrust versus propeller speed for three wind tunnel flow velocities. The AOA is constant at zero degrees.

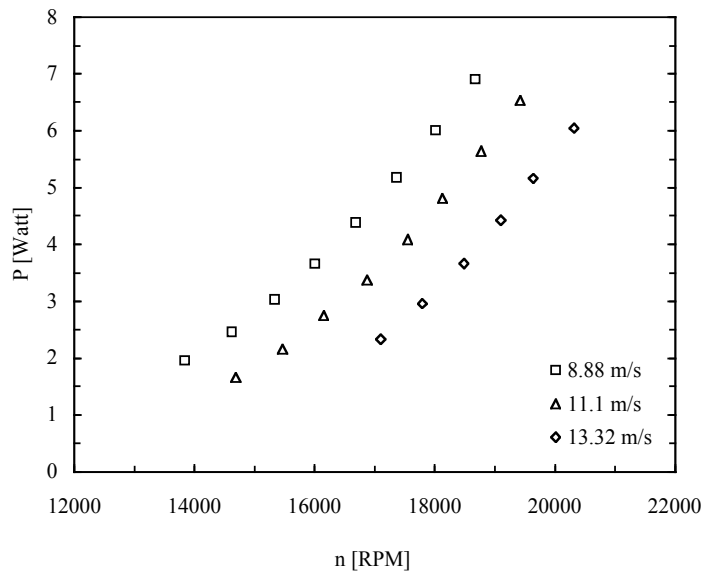


Figure 4-71. Isolated propeller power versus propeller speed for three wind tunnel flow velocities. The AOA is constant at zero degrees.

The plots of the thrust are linear and the power plots presents a mild non-linearity with the propeller speed; the constant value of the AOA is playing an important role in maintaining the linearity of the curves. Combining all the results at different propeller diameters, the values of the coefficient of thrust

$$C_T = \frac{T}{\rho n^2 D^4} \quad (4.10)$$

and the coefficient of power

$$C_P = \frac{P}{\rho n^3 D^5} \quad (4.11)$$

were computed and plotted in function of the advance ratio. The propeller advance ratio is defined as

$$J = \frac{V_\infty}{nD} \quad (4.12)$$

The resulting curves are presented in Figure 4-72 with the coefficient of thrust and in Figure 4-73 with the coefficient of power.

The following plots are useful for the computation of the propeller propulsion characteristics and to assess the propeller performance, including the efficiency, without the inevitable effects induced by the presence of the MAV and its lifting surfaces.

Isolated propeller tests in the wind tunnel are an indispensable step for propeller design and optimization of the propeller-motor.

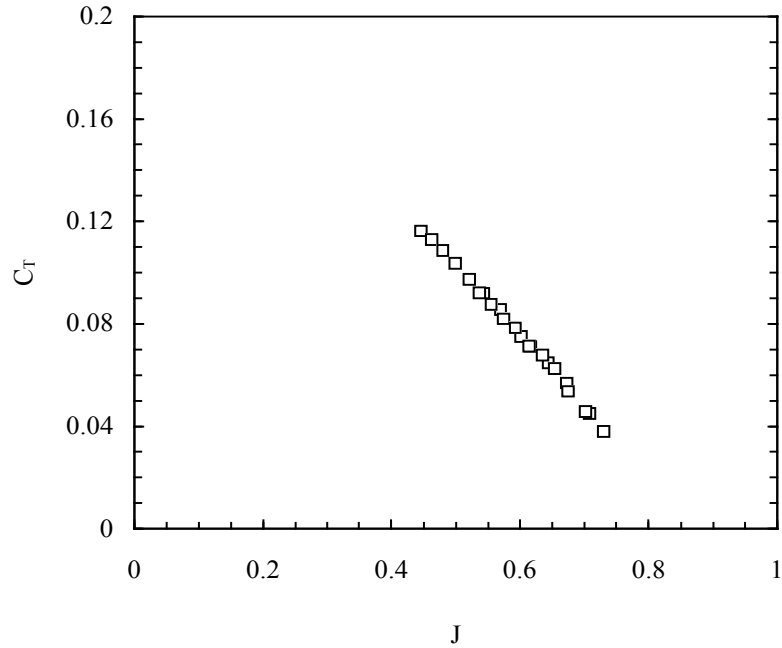


Figure 4-72. Coefficient of thrust versus advance ratio for the isolated propeller. The AOA is constant at zero degrees, propeller type U-80.

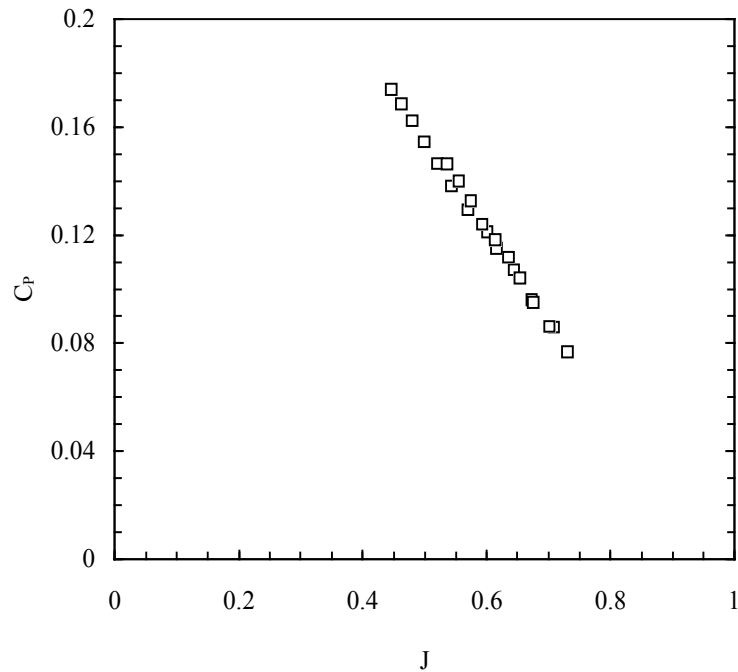


Figure 4-73. Coefficient of power versus advance ratio for the isolated propeller. The AOA is constant at zero degrees, propeller type U-80.

4.6 Summary Of Results

In this chapter the characteristics of LAR wings, as isolated wing and mounted on a MAV fuselage with and without a powered propeller, were studied by a modus operandi that included the use of two different experimental techniques in the low speed, low turbulence wind tunnel. The two test apparatuses consisted of a high sensitivity six components sting balance for aerodynamic and propulsion coefficients measurements, and a VIC system for static structural deformation measurements. In this section several aspects and conclusions presented in the previous paragraphs are listed.

4.6.1 Lift and Drag Characteristics of Wings

This section considers the aerodynamic characteristics of the isolated wings (without fuselage and propeller). The tests were conducted with AOA sweeps with the dynamic pressure as independent variable; the test matrix included the same wings with different structural design thus various flexibilities in amount of deformation and modes of deformation. A description of the structure of the wings is available in Table 3-2.

In terms of lift curve slope, a characteristic directly proportional to the sensitivity to gusts, by inspection of the Figures 4-28 and 4-29 is evident that the wings type BR02 and BR05 have the minimum value, lower than the reference value of the rigid wing. This is a confirmation that indeed the flexible wings, and in particular the wing, with very thin battens (BR02) or thick battens but a leading edge with low torsional stiffness (BR05), have a favorable gust alleviation capability. Wings type PR, due to the relatively rigid carbon fiber reinforced perimeter, are less compliant thus a value of the lift curve slope closer to the rigid type or, as the case for the wing PR12, even higher.

Regarding the amount of variation of the lift curve slope with the dynamic pressure, the rigid wing is practically insignificant whereas the flexible wings show a

moderate non-linear variation; as we could expect the wing type PR12 shows the highest non-linearity with the dynamic pressure due to the large area covered by latex.

The maximum lift coefficient, considering the R wing as reference, is significantly higher for the wings type PR04 and PR07, Figures 4-30 and 4-32, the two wings with the larger area covered with latex. The wing BR09 exhibits values close to the R wing and the wings PR07, BR02 and BR05 have lower values, another indication of a favorable reaction to vertical gusts. The variation of the maximum lift coefficient with the dynamic pressure is insignificant for all wings beside wing type BR09, which shows an important decrease of CL_{max} at a free stream velocity between 10 and 11.5 m/s. The stall is relatively smooth and clean for all wings; the wing type PR12 is the only wing displaying an obvious secondary stall, Figures C-21, C-25 and C-29, due perhaps to the relatively unstable big latex “bubble” with possible interactions with a laminar flow bubble reattaching the flow in certain high AOA conditions.

The value of the AOA for CL_{max} is very close for all wings at values between 22 and 25 degrees, Figures 4-31 and 4-33. The values show little variation with the flow velocity with the only exception, like the previous case for the CL_{max} , of wing BR09 that shows the same abrupt variation at the same range of velocity, Figure 4-30.

Considering the drag characteristics, an efficient way to compare the different wings consists of using the L/D ratio; observing the ratio $(L/D)_{max}$ in the Figures 4-34 and 4-35, the values for all wings are in the range between 6 and 10, with the exception of the wing type BR09 with higher values up to almost 12 at higher dynamic pressure. The values for each type of wing are relatively constant with the dynamic pressure, and the higher values are assigned to the rigid wing. This result should be generally expected due

to the fact that no energy from the airflow is transformed in elastic energy stored in the deformed wing structure.

4.6.2 Lift and Drag Characteristics of MAVs

Three wings from the group were selected for testing in the MAV configuration; the wings are R, PR07 and BR09. The first series of tests were conducted with the wing mounted on the same fuselage and with the same vertical stabilizer; the propeller was added in later tests. In general the fuselage, as expected, generate a decrease of lift at the same AOA; in the case of the wing BR09 only, the addition of the fuselage induced a smoother stall (Figure 4-45). The variation of lift due to the fuselage, always negative, is practically constant with the lowest absolute value, $-.04$, for wing PR07, Figure 4-47. The highest absolute value and most AOA dependent is assigned to the rigid wing, with values between $-.08$ and $-.16$; the BR09 wing has intermediate characteristics with a constant value of about $-.07$ up to an AOA of 16 degrees and increasing for higher AOA angles to a value of $-.10$. The trend is similar at different dynamic pressures.

The drag coefficient is plotted versus the coefficient of lift. In this way possible errors on the setting of the initial angle of the models won't be relevant and the contribution of the induced drag will not affect the results since it is practically identical for all wings at the same lift level. Figures 4-53 and 4-54 show the increase in drag by adding the fuselage and vertical stabilizer to the wing only configuration. Interestingly enough the increase in drag for the PR09 wing is the lowest, at a value of $.01$ constant with the AOA. The wings R and BR09 have similar drag increments and they are AOA dependent; the values are from $.02$ at low AOA to $.07$ at higher AOA. The trend is similar at for the entire range of dynamic pressure and Reynolds number. No explanation

can now be formulated on the favorably low drag increment of the PR wing in respect to the R and BR wings.

The case with the powered propeller was studied using the same three wings of the previous section; the new independent variable was the voltage setting to the DC motor driving the propeller however, differently than other larger motors, the resulting propeller velocity was strongly non-linearly dependent from AOA and wind tunnel dynamic pressure. This strong dependence is the cause of a strong coupling between aerodynamic coefficients and free stream velocity and, ultimately, the vehicle's flight speed. The abovementioned free stream velocity-aerodynamic coefficient dependence is unusual for regular subsonic flying vehicles in steady conditions.

Another obvious important effect of the propeller slipstream was the delay, or even cancellation of the stall. The noticeable wing buffet occurring without propeller at an AOA approximately between 16 and 18 degrees, in the case with the propeller on was visually undetectable. The linear part of the lift curve slope, at constant motor setting, extends 50% in respect to the case without propeller. The lift curve slope, for the rigid wing, remains roughly constant at different motor setting (Figure C-93) and different dynamic pressures (Figure C-96). However, in the cases of the flexible wings, a mild dependence of the lift derivative emerges with the motor setting (Figures C-99 and C-105) and with the dynamic pressure (Figure C-102 and C-108). Particularly an increase of the lift respect to AOA is observed for a decrease of free stream velocity.

The obviously non-linear intrinsic drag-lift characteristics make difficult to draw conclusions about trends with the different types of wing, crafting the case for further analysis by analytical models, obtained from wind tunnel data (Chapter 5). Two evident

features of the drag (or thrust for negative values) relation with lift is the strong dependence with the dynamic pressure at constant motor voltage setting, Figures C-97 and C-103 and the weak coupling with the motor voltage input at constant dynamic pressure, Figures C-100 and C-106, not including the large drag jump from the no propeller case to the powered propeller tests.

4.6.3 Pitching Moment Characteristics of Wings

Longitudinal characteristics are of paramount importance for MAVs flight. All the moment results reported in this work are measured about the 25% of the root chord. All wings exhibited favorable longitudinal static stability characteristics; trimmed flight can be achieved by the proper elevator setting.

All the flexible wings have generally a higher negative pitching moment with respect to the rigid wing; therefore the flexible wings have a nose down tendency, with respect to the rigid wing. This should not be a surprise giving that the reflex part is less effective in the flexible wing due to structural deformation. The numeric values of the derivative, always negative, are similar for the PR04 and the rigid wings, Figures 4-36 and 4-37. The values for the wing BR09 are approximately twice than the rigid and the PR07 and PR12 four times. This should not be a surprise due to the observed deformation of the latex membrane by the aerodynamic load and the subsequent shift downstream of the maximum camber.

The wing type BR05 has the most favorable trimming condition (Figure C-60) and the wings type PR have generally the linear part of the C_m curve extended towards higher AOAs, respect to the other wings, making the PR wings easier to control at higher AOAs.

4.6.4 Pitching Moment Characteristics of MAV

It is useful to remind the reader that the only wings selected for tests on vehicles were the R, PR07 and BR09. The first comments will be related to the cases without propeller.

In general the addition of the fuselage generates a nose down moment. The negative values of the longitudinal moment are higher for the flexible wings than the rigid wing but the increment of negative moment is substantial for the rigid wing and small for the flexible wings. In the case of the PR wings, the most stable, the value remains constant with the addition of the fuselage.

The values for the PR07 wing are the highest and remain constant with the fuselage addition (Figure C-88); the values for the BR09 wing are slightly and the function is linear for the least range of lift coefficient (Figure C-92). The case of the rigid wing demonstrates a substantial difference between the two configurations with and without fuselage, in terms of values (nose down with fuselage) and slope. The fuselage in general increases the stability.

The addition of the powered propeller has a significant effect on the longitudinal characteristics of the vehicles. As for the cases of the lift and drag, the dependence of the propeller speed with the AOA and dynamic pressure introduces a strong coupling of the dynamic pressure with the pitching moment, often with a significant amount of non-linearity. The coupling is generally less important for more traditional aircraft at subsonic speeds. In general the presence of the propeller creates a nose up moment and extends the linear part of the curve to higher lift coefficients but the trim lift does not change for the cases with and without propeller or at different propeller speed. A

possible explanation lies in the physics of a propeller operating at an AOA. The propeller generates an in-plane force with a magnitude directly proportional to the AOA, at constant velocity therefore, at low AOA, the in-plane force is small and the nose –up moment is also small causing the plots of $\delta C_L / \delta \alpha$ converging towards a common trim point.

The derivatives $\delta C_L / \delta \alpha$ for the rigid wing decrease with the increase of the motor voltage input at constant velocity, Figure C-98 and there is a significant decrease from the case without propeller to the case with propeller. The PR wing shows a constant value of the derivative in both cases at constant velocity (Figure C-101) and at constant motor voltage (Figure C-104); the BR wing exhibits an intermediate behavior with a constant $\delta C_L / \delta \alpha$ slope but the curves are more spread respect to the PR and less respect the rigid wing, Figure C-110.

4.6.5 Elastic Deformation Results of Wings

The three-dimensional geometry of the deformed structure of the wings was acquired using the VIC technique. The geometry of 10 wings and three wings mounted on the same MAV is available for a combination of values of AOAs, free stream velocities and propeller speed.

The two main parameters used to weight the deformation of the wings are the camber (value and position along the wing chord) and the geometric wing twist. The two parameters best describe the wings two main deformation modes: billowing (increase in camber) strongly present in the PR wings and moderately on BR wings and twist (change in the local angle of incidence), insignificant in the PR wings and predominant in the BR wings.

The section maximum camber increases linearly with the AOA up to a maximum value of 2% for the wing type BR05 (Figure 4-12) and increases linearly with the dynamic pressure up to 1.5% for the BR05 type wing, at a moderate AOA (Figure 4-13). The position along the chord of the section maximum camber increases linearly with the AOA up to a maximum value of 5% for the wing type BR05 (Figure 4-14) and increases linearly with the dynamic pressure up to 4% for the BR05 type wing, at a moderate AOA (Figure 4-15).

The wing twist is the product of the structural torsional deformation studied with the variation of the wing AOA. The wing twist was characterized using the distribution of the local angle of incidence i_w along the wingspan. The result of the twist is the washout effect, which has certain relevance on the gust alleviation characteristics of a wing. The wings type BR, as expected, exhibit a relevant amount of wing twist, Figure 4-21, absent on the PR type wings. The wing type BR05 presented the maximum amount of twist along the wingspan, Figure 4-17 and 4-18, as intended with its structural design. The value of the local i_w increases with the wingspan direction towards the tip, up to a maximum of approximately 7 degrees nose down, Figure 4-19.

The maximum value of i_w is linearly dependent with AOA in the range of linearity of the lift curve, Figure 4-20, and is inversely proportional to the AOA.

The complete model case was investigated only with the propeller on, with the objective of characterizing the propeller effects. It was found that the propeller slipstream has, in certain test conditions, enough energy to transmit to the wing skin causing a modification of the local shape and thus in the elastic energy stored. The most relevant case was found to be on the PR09 wing at high RPM and low free stream

velocity conditions. The asymmetry caused by the propeller was visualized by wing sections obtained at the same distance from the center line, Figure 4-25.

The new parameter R (Equations 4.1 and 4.2) was introduced to quantify the amount of asymmetry in the wing geometry introduced by the propeller slipstream; for a symmetric wing the value of R is one. For the wing PR09 the value of R is less than one at low AOA and goes to one for higher AOA, Figures 4-26 and 4-27, when the interaction of the propeller becomes less important than the effects of the free stream.

4.6.6 Combining the Aerodynamic Result with the Elastic Deformation Results

Several aerodynamic characteristics observed on the flexible wings, concurrently with their differences from the reference rigid wing, can be explained using the deformation of the wings caused by the static aerodynamic loads and measured by the VIC system. The decrease of the $\frac{dC_L}{d\alpha}$ derivative respect to the rigid wing was perhaps not so large as expected; a possible explanation is that the BR wings, which exhibited the lowest value when the AOA increases is subjected to the washout effect, as described in the previous section, and at the same time to an increase of camber, partially compensating for the decrease of the local AOA due to the washout.

The PR wings demonstrated the highest level of the $\frac{dC_L}{d\alpha}$ derivative and indeed have the highest $(t/c)_{max}$ measured in the deformed structure. For PR wings the $\frac{dC_L}{d\alpha}$ derivative is practically constant with AOA and dynamic pressure; the $(t/c)_{max}$ value is linearly dependent with AOA and dynamic pressure, for moderate levels of AOA.

The CL_{max} is the highest for the PR wings, particularly for wing PR12; those wings had also the maximum measured $(t/c)_{max}$. On the contrary CL_{min} is the lowest for

BR wings, and particularly for wings BR02 and BR05, which presented the same amount of increase of $(t/c)_{\max}$ than the other BR wings but have the highest washout values.

The flexible wings demonstrated higher absolute values of negative C_m (nose down) respect to the rigid wing and an important shift downstream of the X of $(t/c)_{\max}$ was measured. The PR wings presented the highest absolute values of negative C_m (nose down); indeed the largest shift downstream of X of $(t/c)_{\max}$ was measured for the PR wings.

4.6.7 Considerations on Propulsion

No clear trends regarding the propeller speed with the different wing flexibility were observed. In general the propeller speed at constant motor voltage and constant free stream velocity is AOA dependent in a non-linear fashion. Moreover the propeller speed tends to be more linear at high voltage and higher velocity and increasingly non-linear at low motor voltage and at high free stream velocity, Figures 4-66 and 4-69. The propeller speed, at constant motor voltage and AOA, increases with the increase of the free stream velocity. The local slope of the non-linear propeller speed versus AOA curve is smaller for low AOA and becomes steeper for high AOA.

The propeller thrust, at constant free stream velocity, is linearly dependent with the propeller speed (Figure 4-70); the power, in the same conditions, exhibits a mild non-linearity (Figure 4-71). The coefficients C_T and C_P are linearly dependent with the advance ratio J, Figures 4-72 and 4-73.

The couplings introduced by the propulsion parameters between the aerodynamic coefficients and the AOA and free stream dynamic pressure, often non-linear, introduce the necessity of an analytical modeling effort, presented in Chapter 5.

CHAPTER 5 ANALYTICAL MODELS FROM WIND TUNNEL RESULTS

5.1 Introduction

The class of MAVs subject of this work operates in flight regimes characterized by nonlinear propulsion characteristics and, in the case of extreme flight envelope conditions, by nonlinear aerodynamics. An important aspect of accurately modeling nonlinear characteristics is determining the mathematical form that relates the independent variables to the aerodynamic forces and moments operating on the vehicle, described in terms of non-dimensional coefficients.

The objective of this section is to devise analytical models to estimate propeller and aerodynamic parameters from data acquired in wind tunnel tests, in flying steady conditions, and to accurately characterize their mutual functional dependencies. These models can be implemented in an air vehicle model for flight simulation or flight parameters optimization.

The presentation of the results is organized in sections, with the propulsion models followed by the aerodynamic coefficients. The reliability of the models selected is verified from the values of residuals computed from wind tunnel check runs and the results presented in the third part of this chapter.

5.1.1 Model Structure Determination

With the experimental data collected and presented in the previous chapter, the typical task of modeling presented in this section consists of modeling the functional dependence of the output variables on the independent variables using polynomials in the

independent variables. In the proposed models the parameters are estimated from the measured data using least squares linear regression.

The task of which and how many polynomials terms should be included in the model, for a given set of data, is called model structure determination. Various modeling determination techniques can be used, usually in function of the number of independent variables, the ranges of the independent variable and level of complexity of the underlying functional dependency. Considering the case of global modeling with a larger number of independent variables, characterized by a large variation range and by complex mutual dependencies the formulation of nonlinear modeling technique using multivariate orthogonal functions [53, 56] is more appropriate and efficient.

In this work the number of independent variables is relatively small and the results contain several nonlinearities characterized by non-complex dependencies, therefore least squares linear regression techniques were used to model response surfaces from the wind tunnel data. The appropriate models structure is determined using predicted squared error criteria.

The technique will be demonstrated in details for the case of the model describing the lift coefficient C_L and applied to the following models determination. For the steady state tests carried out in the wind tunnel, at constant elevator angle, at constant rudder angle and not including terms associated with any AOA and pitch rates, the functional form for C_L can be described as

$$C_L = f(\alpha, E) = \sum_{i=1}^m a_i \hat{p}_i + e \quad (5.1)$$

The a_i are constant model parameters, \hat{p}_i are functions (linear and nonlinear) of the independent variables and m is the number of terms in the selected model. The choosing of the functions \hat{p}_i , which implicitly includes the determination of m in Equation (5.1), is a matter of determining how many functions are needed for a clearly specified squared-fit error. The value m and the forms of the functions \hat{p}_i are chosen based on a criterion that represents a tradeoff between reduction in squared fit error and the number of terms required in the final form of the model.

The mean squared error (MSE) is defined as [104]

$$MSE = \frac{1}{N-1} \sum_{i=1}^N (y - \hat{y})^2 \quad (5.2)$$

The MSE gives a merit for the model fit to the data, but does not consider the numbers of terms in the model. A decrease of the MSE is usually achieved by simply increase m , the number of terms in the model. The shortcoming in this simple procedure is that the MSE does not provide any safeguard from overfitting the modeling data set. We seek a model that fits the data well but also that has good predictive capabilities thus it needs to be compact [53]. To achieve the goal of a compact not overfitting model the predicted squared error [PSE] is introduced [105] as follows

$$PSE = MSE + 2\sigma_p^2(m/N) \quad (5.3)$$

The second term of Equation (5.3) is an overfit linear penalty (OP) to prevent to include too many terms in the model and therefore overfit the data. This term shows that

the expected performance depends on the degree of similarity between training data and future data. Assuming that we have a good notion of how future input data will be dispersed, in particular, if we know the variance of a large population of dependent variable by performing repeated wind tunnel runs at the same test conditions, we can assume that the maximum value of σ_p^2 is equal to σ_0^2 and

$$\sigma_0^2 = \frac{1}{N} \sum_{i=1}^N (y_i - \bar{y})^2 \quad (5.4)$$

The term in Equation (5.4) represents a constant model consisting of the average of the measured values. In this case the training input data can be chosen or generated to be representative of future data and the expected squared error simplifies to

$$PSE = MSE + 2\sigma_0^2(m/N) \quad (5.5)$$

The function PSE will always have a single global minimum, which corresponds to the optimum model structure [105].

For the sample case of the lift coefficient a model with variable number and type of terms was run and the MSE and PSE evaluated up to $m=10$. The initial model has the following form

$$C_L = a_0 + a_1\alpha + a_2E + a_3\alpha E + a_4\alpha^2 + a_5\alpha^3 + a_6\alpha^4 + a_7\alpha^5 + a_8E^2 + a_9\alpha^2 E + a_{10}E^2\alpha \quad (5.6)$$

A linear regression analysis of the equation (5.6) for m from three to ten was run for a population of approximately 50 experimental data points, obtaining the values of MSE and PSE according to Equations (5.2) and (5.5). The results are depicted in Figure 5-1.

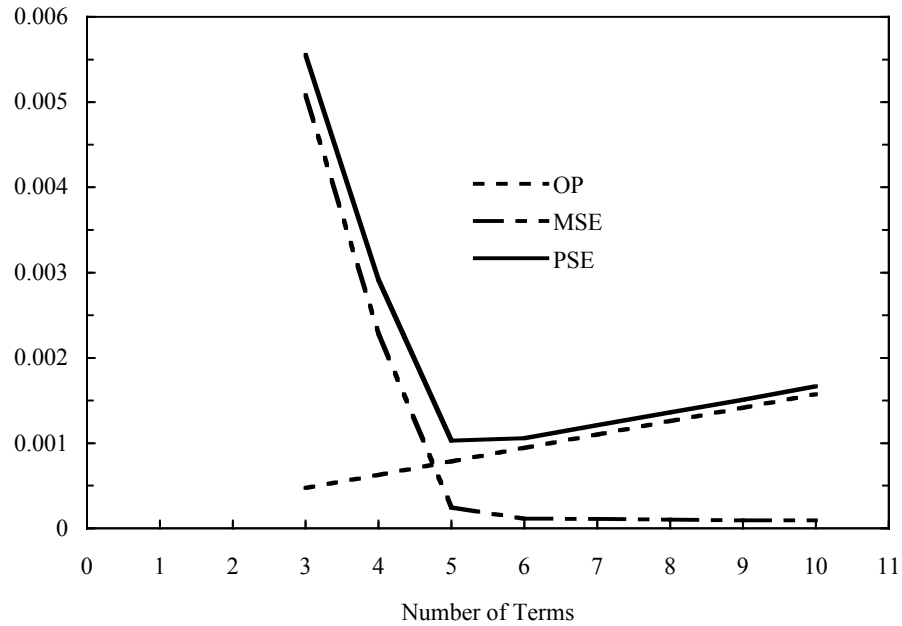


Figure 5-1. Overfit penalty, mean squared error and predicted squared error for the C_L model with various numbers of terms.

The minimum of the PSE function suggests the numbers of terms to keep in order to obtain the final form for the model. The resulting function for C_L is

$$C_L = a_0 + a_1\alpha + a_2E + a_3\alpha E + a_4\alpha^2 + a_5\alpha^3 + a_6\alpha^4 \quad (5.7)$$

The comparison of the model expressed by the equation (5.7) with the experimental data is illustrated in Figure 5-2.

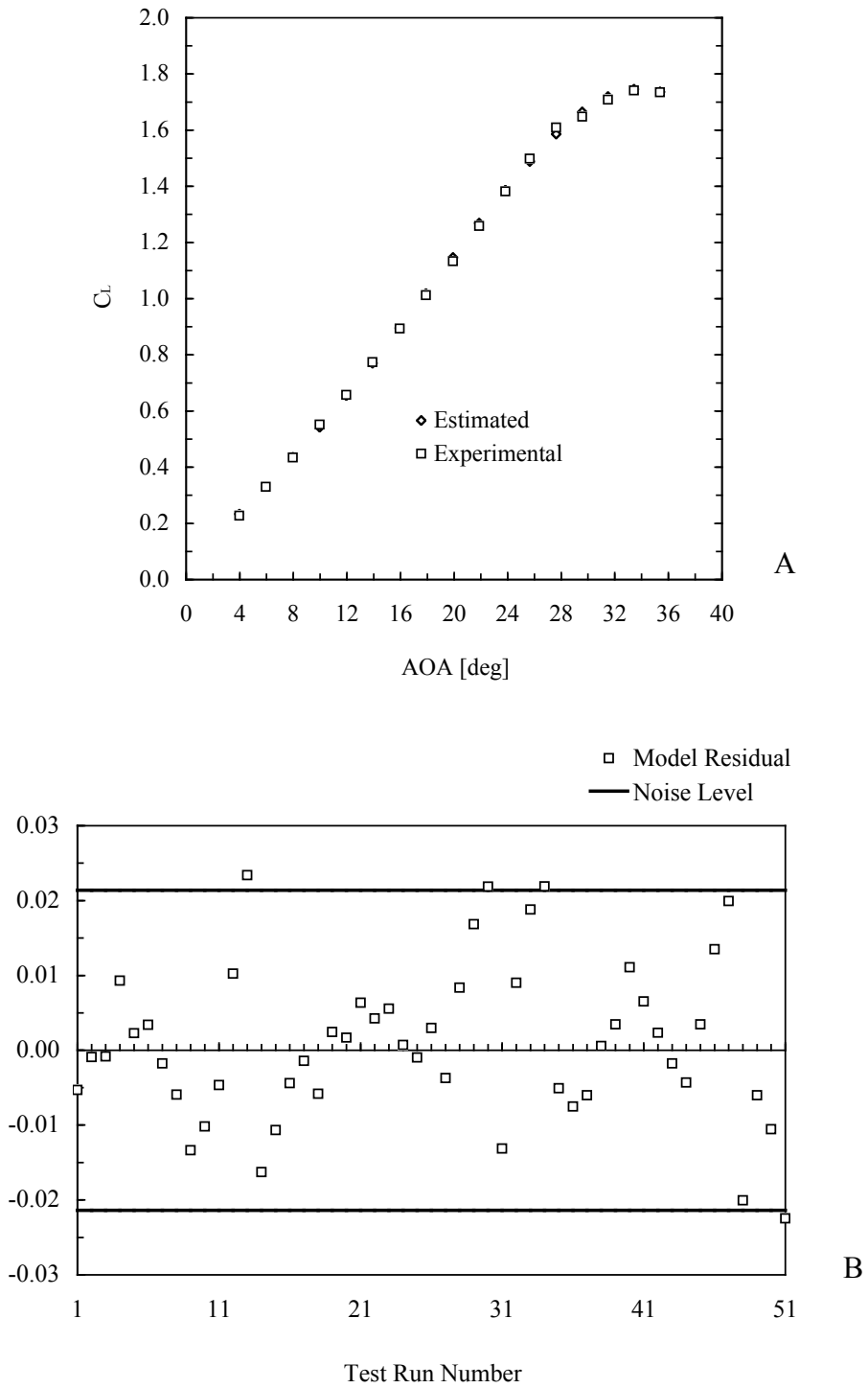


Figure 5-2. Comparison between experimental and estimated data. A) C_L versus AOA and B) model residual and noise level versus the test run number.

Similar procedure was carried out for the formulation of a model of the lift coefficient including the dynamic pressure as independent variable thus considering the following functional expression

$$C_L = f(\alpha, E, q) = \sum_{i=1}^m a_i \hat{p}_i + e \quad (5.8)$$

The minimum of PSE was found for $m=8$ and the final expression for C_L is

$$C_L = a_0 + a_1\alpha + a_2E + a_3\alpha E + a_4\alpha^2 + a_5\alpha^3 + a_6\alpha^4 + a_7q + a_8\alpha q \quad (5.9)$$

5.1.2 Propulsion Model

The work regarding the propulsion parameters of the MAV was divided in two parts; the first consisted in finding a model of the propeller rotating speed as a function of AOA, dynamic pressure and motor voltage setting. The target function is

$$n = f(\alpha, q, E) \quad (5.10)$$

The second part focused on modeling the coefficient of thrust C_T and coefficient of normal force C_Z as functions of propeller rpm, dynamic pressure and voltage motor setting. The target functions are:

$$C_T = f(n, q, E) \quad (5.11)$$

$$C_Z = f(n, q, E) \quad (5.12)$$

The fit functions for the relations 5.11 and 5.12 are obtained using experimental data in the linear range of the lift coefficient; the model of the propeller speed relation 5.10 is obtained from the entire range of AOAs, up to 38 degrees, thus in the non-linear range of the aerodynamics. The regression analysis was performed using a Maclaurin type expansion with linear coefficients as model structure and using a combination of linear and non-linear functions giving an adequate approximation of the experimental data. The model was considered acceptable for the minimum value of PSE.

The propeller rotating speed was measured at three motor settings, four levels of dynamic pressure and for various selected AOAs; the experimental data was checked using plots similar to the one depicted in Figure 5-3.

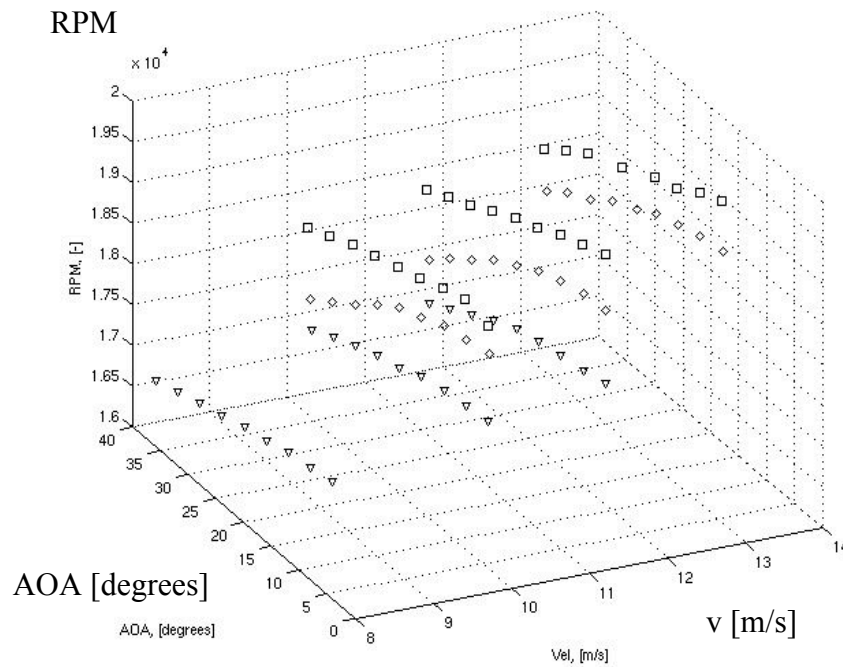


Figure 5-3. Plot of experimental data of propeller speeds versus AOA at three different levels of free stream dynamic pressure. The motor settings are 6.6, 7.0 and 7.4 Volt.

The best function to estimate the rpm was found to be

$$n = a_0 + a_1q + a_2\alpha + a_3\alpha^2 + a_4E + a_5E^2 + a_6E\alpha \quad (5.13)$$

The linear parameters are found by performing a classic least square procedure and solving the linear system

$$\{n_{\text{exp}}\} = \{A_0\} + [X]\{A\} \quad (5.14)$$

The Equation (5.13) represents a hyper-surface by which the propeller speed can be found for any desired flight condition. An example of the results from the model obtained by the fit functions is depicted in Figure 5-4, which shows the dependence of the propeller speed on AOA and dynamic pressure, at three different motor voltage inputs.

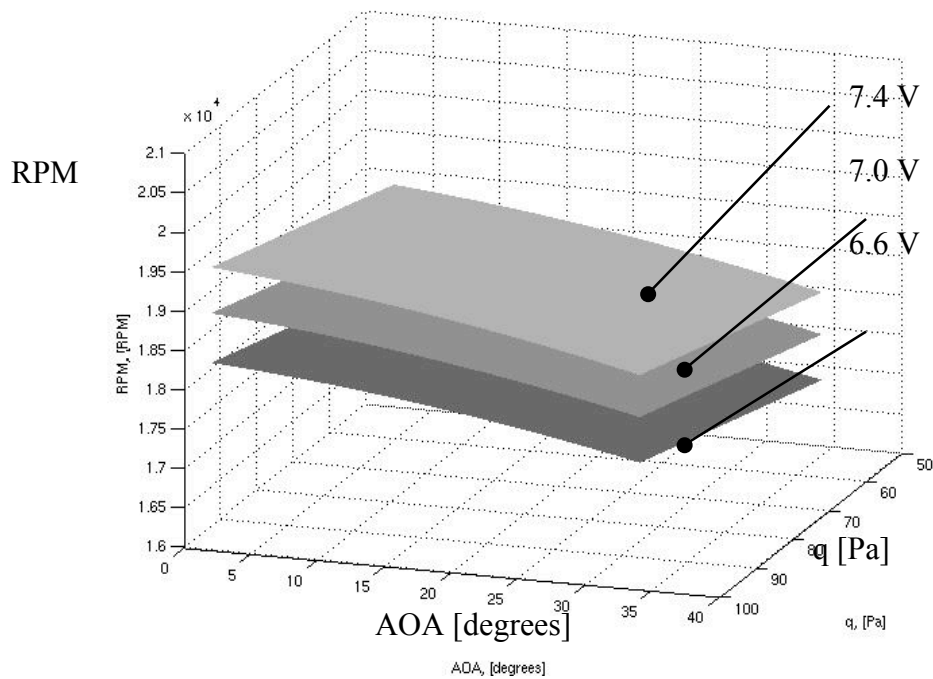


Figure 5-4. Plot of propeller speeds versus AOA and free stream dynamic pressure at three different levels of motor settings. The hyper-surfaces are obtained from the proposed model expressed by the Equation (5.13).

The propeller speed function (5.13) contains a linear term with dynamic pressure and linear and non-linear terms with voltage motor input and AOA in order to account for the non-linear dependence on those terms observed in the tests. The cross term between motor voltage and AOA was necessary to account for the wing's upwash effect on propeller rpm.

The other set of parameters necessary for the propulsion characterization are the thrust coefficient C_T and the propeller normal coefficient C_Z . Those coefficients are obtained from an analysis of the total aerodynamic coefficients by subtracting the results of the tests of the air vehicle without propeller from the results with the powered propeller and solving for the new coefficients in the body axes reference frame using the following linear system

$$\begin{cases} N \\ T \end{cases} = \begin{bmatrix} \Delta D & \Delta L \\ \Delta L & -\Delta D \end{bmatrix} \begin{cases} \cos \alpha \\ \sin \alpha \end{cases} \quad \begin{aligned} C_T &= T / qS \\ C_N &= N / qS \end{aligned} \quad (5.15)$$

The experimental coefficients were again fitted with specialized functions using a combination of parameters that describe the physics of the experiments; the functions for thrust and normal force coefficients respectively are:

$$\begin{aligned} C_T = f(q, n, E) &= a_1 + a_2 q + a_3 kn^3 + a_4 kn^2 + \\ &+ a_5 E + a_6 E^2 + a_7 (knE) + a_8 \left(\frac{kn}{E}\right) + a_9 \left(\frac{kn^2}{E}\right) \end{aligned} \quad (5.16)$$

$$\begin{aligned} C_N = f(q, \alpha, n, E) &= a_1 + a_2 q + a_3 \alpha + a_4 kn + a_5 E + \\ &+ a_6 (\alpha kn) + a_7 (\alpha E) + a_8 (qkn) + a_9 (kn^2) + a_{10} \frac{kn}{q} \end{aligned} \quad (5.17)$$

Even though the structure of equations (5.16) and (5.17) is not physically fully explained, the parameters were carefully chosen with respect to the experimental observations, data measurements and published material [32, 56]. The presence of the terms with AOA in Equation (5.17) is necessary to account for the substantial coupling between AOA and C_N . A plot of the thrust coefficient using Equation (5.16) is shown in Figure 5-5.

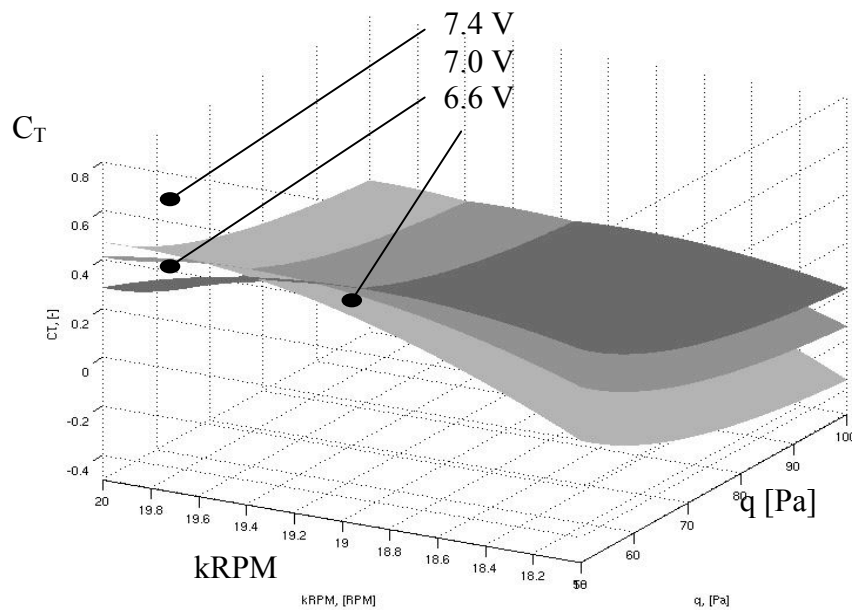


Figure 5-5. Plot of propeller coefficient of thrust versus propeller speed and free stream dynamic pressure, at three different levels of motor settings. The hyper-surfaces are obtained from the proposed model expressed by the Equation (5.16).

The non-linear dependence of C_T with the propeller speed and the dynamic pressure observed experimentally, at constant motor voltage input, is well captured by the proposed model. One explanation for the intersections of the surfaces could be that the angle of attack acts as a fifth variable embedded in the four dimensional space, enabling

the coefficient of thrust to have the same value for different motor voltages although at the same propeller speed.

5.1.3 Aerodynamic Model

The same procedure was used to generate models that estimate the dependence of aerodynamic forces and longitudinal pitching moment coefficients on propulsion coefficients, AOA and dynamic pressure. Lift and drag coefficients were found to be predominantly dependent on the thrust coefficient but, interestingly enough, was necessary to add, to the model of the pitching moment coefficient, the propulsion coefficient C_N . With the addition of the propeller coefficient, the contribution to the pitching moment of the propeller, when working at an AOA, was properly considered, as well as any coupling between AOA and wing up-wash effects on the propeller aerodynamics.

As previously described the propulsion coefficients were computed using the total aerodynamic coefficients in the linear region of lift that, in the case of the data with the powered propeller, could extend up to an AOA of 30 degrees or more. The same AOA range should be used for applications of the proposed aerodynamic models. The addition of data with powered propeller combined with control deflections, will made possible to account for the influence of the propeller speed on the aerodynamic coefficients with control deflections. Therefore, the related cross correlation terms between control deflections and lift, drag and moment coefficients are missing from the actual model.

Data analysis from a test campaign, specifically designed to investigate the propeller effects on the aerodynamic characteristics of a MAV with elevator deflections,

is under way and the terms with functional mutual dependencies with propeller speed and control deflections will be added to the analytical functions.

The results listed above and described in the Figures 5-3, 5-4 and 5-5 and from other publications [56], confirmed the need for dynamic pressure dependent terms in the proposed fitting functions for lift, drag and pitching moment coefficients. Experimental data were plotted and carefully checked for experimental noise or bad data. A least squares fit was performed with a similar procedure as previously described for the propeller speed using several candidates for expressions that would best describe both the experimental data and the expected physical behavior of the relevant quantities. The proposed best functions, and the corresponding linear parameters for total lift, total drag and total pitching moment coefficients are the following.

$$C_L = f(\alpha, C_T, q) = a_{C_L1} + a_{C_L2}\alpha + a_{C_L3}c_T + a_{C_L4}(\alpha c_T) + a_{C_L5}c_T^2 + a_{C_L6}q \quad (5.18)$$

$$C_D = f(\alpha, C_T, q) = a_{C_D1} + a_{C_D2}\alpha + a_{C_D3}\alpha^2 + a_{C_D4}c_T + a_{C_D5}c_T^2 + a_{C_D6}(\alpha c_T) + a_{C_D7}q + a_{C_D8}(qc_T) \quad (5.19)$$

$$C_m = f(\alpha, C_T, C_N, q) = a_{C_M1} + a_{C_M2}\alpha + a_{C_M3}c_T + a_{C_M4}c_N + a_{C_M5}(c_T c_N) + a_{C_M6}c_T^2 + a_{C_M7}\arctg(c_T) + a_{C_M8}q + a_{C_M9}(qc_T) \quad (5.20)$$

The above relations were structured using the physically relevant quantities AOA, C_T and C_N and by observing multiple dimensions plots of the experimental data and noting the general nature of the functions. The use of cross relation functions like $\alpha c_T, qc_T, c_T c_N$ account for geometrical twisting in planes or surfaces in the hyperspace, and the hyperbolic function \arctg , in the expression for C_m in Equation (5.20), introduces

a point of inflection in the dependence on C_T , observed in the experimental data. No further attempt was made to make a physical interpretation of the above equations.

The dependence of the aerodynamics of the vehicle with dynamic pressure is moderate for lift and stronger for drag, making the testing at different values of dynamic pressures, and the introduction of dynamic pressure dependent terms in the fitting functions, a necessity. Figure 5-6 shows a plot with the experimental and estimated lift coefficients using data from tests at a free stream velocity of 10 m/s. The estimated values were obtained using the model from Equation (5.18), without the term with the dynamic pressure. Figure 5-7 shows the lift coefficients measured at a flow velocity of 13 m/s using Equation (5.18) without the dynamic pressure terms and with the addition of the experimental coefficients at different dynamic pressures in the regression analysis, with the relative q dependent term included in the model.

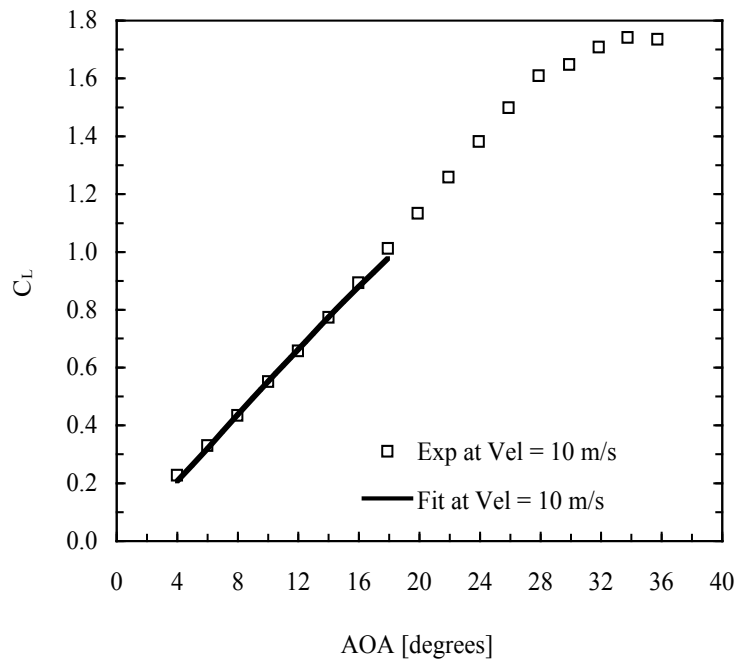


Figure 5-6. Total lift coefficient versus AOA at constant free stream dynamic pressure and motor setting. The analytical model matches the experimental points.

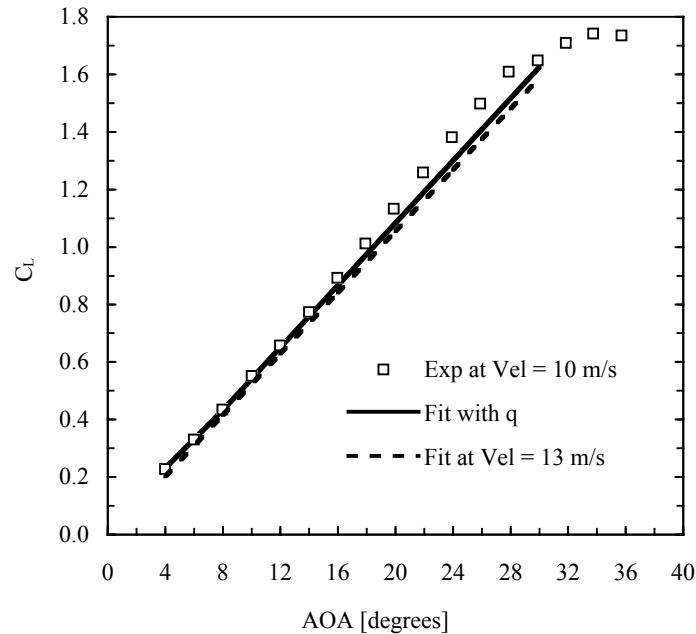


Figure 5-7. Total lift coefficient versus AOA at constant free stream dynamic pressure and motor setting. The two analytical models, one considering one velocity only and the other with terms with the dynamic pressure, are very close.

It is evident from Figure 5-7 that the model fits closely the experimental data, using a model for the specified value of dynamic pressure. Using two different models, one for a velocity of 10 m/s (Figure 5-7, dotted line), and the other with data at four different dynamic pressures using the full Equation (5.18), Figure 5-7 solid line, there is a close estimate of the experimental data at 13 m/s, with a slightly better result using the model that includes the dynamic pressure. Using the same procedure with the coefficient of drag and Equation (5.19), it is evident from Figure 5-8 and Figure 5-9 that the dependence of the drag coefficient, on the variations of dynamic pressure, cannot be ignored without an unacceptable error in the estimated values obtained by the application the aerodynamic model.

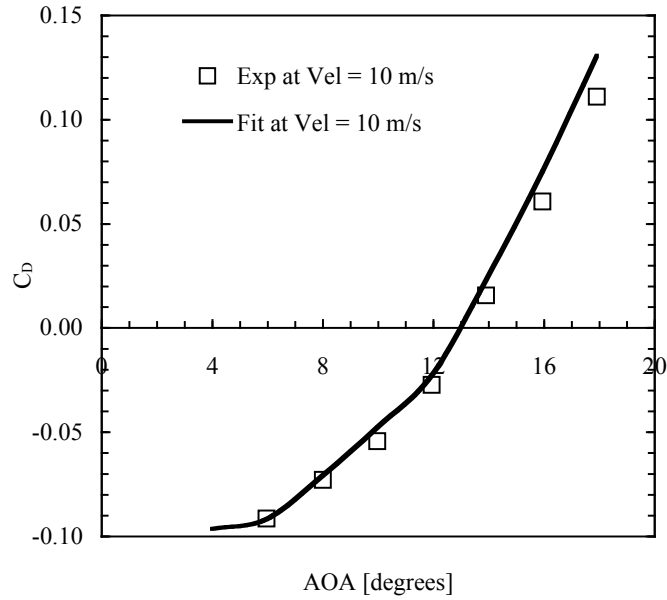


Figure 5-8. Drag coefficient versus AOA at constant motor setting. The line is obtained using the model at 10 m/s, without dependency terms with the dynamic pressure.

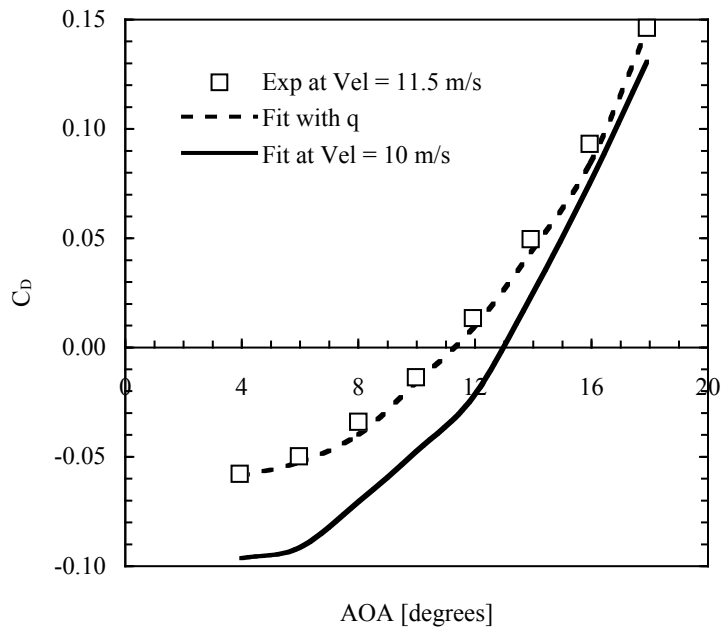


Figure 5-9. Drag coefficient versus AOA at constant motor setting. The experimental values are at 11.5 m/s. The solid line is obtained using the model for 10 m/s, without dependency terms with the dynamic pressure. The dotted line represents the model with dynamic pressure dependency terms.

5.1.4 A Sample Application of the Models.

The proposed analytical models for the aerodynamics and propulsion characteristics of a MAV, when integrated with the control deflection derivatives and eventually the dynamic derivatives terms, can be used for a variety of purposes: performance analysis, stability and control assessment, energy balance for battery life optimization and mission planning. The demonstration of the solution of the aforementioned cases is beyond the scope of this work, however a simple case with the objective to find trimmed flight conditions for a MAV will be demonstrate.

The total lift, drag and pitching moment coefficients were computed using a model with Equations (5.18-5.20) The estimated values are used in a simplified analytical trim model represented by the following linear system.

$$\begin{bmatrix} C_{L\alpha} & C_{L\delta} & 0 \\ C_{m\alpha} & C_{m\delta} & 0 \\ 0 & 0 & k \end{bmatrix} \begin{Bmatrix} \alpha \\ \delta \\ C_L^2 \end{Bmatrix} = \begin{Bmatrix} \frac{nW}{qS} - C_{L_0} \\ -C_{m_0} \\ -C_{D_0} \end{Bmatrix} \quad (5.21)$$

The terms with the controls deflections are estimated from tests without propeller and from other sources [28, 32]; elevator deflections are the subject of further specific wind tunnel tests, with the objective of characterize the terms for dependencies of angle of attack and thrust and coupling of control deflection with thrust, due to propeller slipstream effects [32].

The dynamic derivatives terms $\dot{\alpha}$ and \dot{q} are also omitted from the example for simplicity, but their estimated values can be obtained from other sources [32, 101]. The

third equation of the system (5.21) is the linearized total drag that will provide the trimmed propeller thrust via the propeller speed model.

A simple solution of the system (5.21), without performing any optimization for any parameter, is shown in Figure 5-10 and Figure 5-11, with the values of the trimmed angle of attack and elevator angles, respectively, at different values of the load factor n .

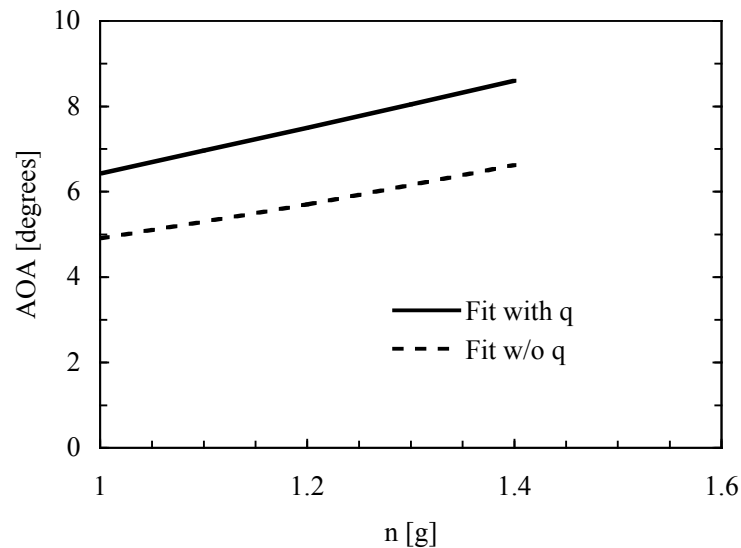


Figure 5-10. Trimmed flight angle of attack versus load factor at constant motor setting. The values are computed using the model with (solid line) and without (dotted line) dynamic pressure terms. The two models give similar results.

The difference in the computed values using the models with the dynamic pressure terms and without them is evident from the above plots, with more dramatic inconsistencies in the elevator angle, Figure 5-11. The main reason for the strong influence of the dynamic pressure terms is attributed to the propeller effects on the aerodynamics and flight mechanics of the MAV. Elevator angle values similar to those shown in Figure 5-9 were observed during flight tests [35] and in wind tunnel tests [32].

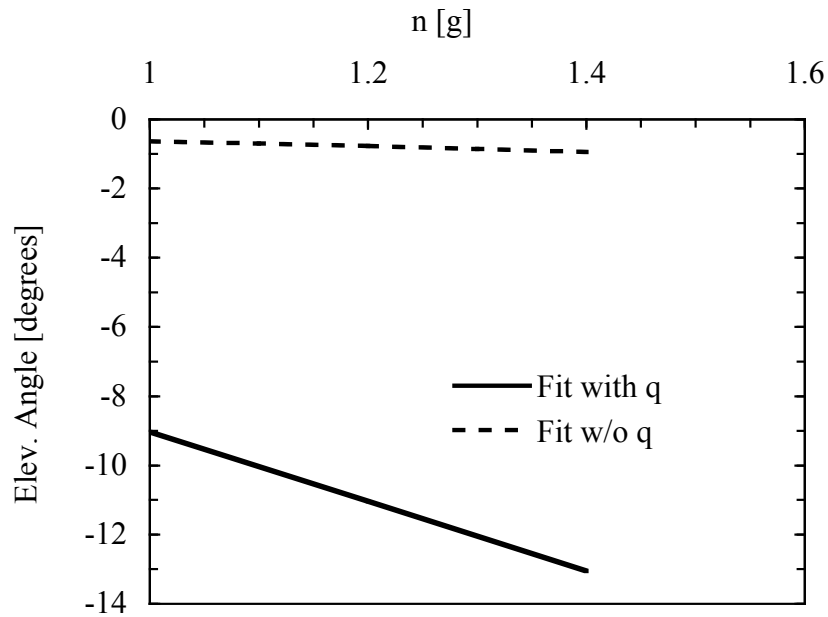


Figure 5-11. Trimmed elevator angle deflection versus load factor at constant motor setting. The values are computed using the model with (solid line) and without (dotted line) dynamic pressure terms. Only the first is acceptable.

5.2 Conclusions

The class of MAVs subject of this work operates in flight regimes characterized by nonlinear propulsion characteristics and nonlinear aerodynamics. The modeling technique described in this work is appropriate for the objective of obtaining a compact analytical representation of nonlinear aerodynamic and propulsion characteristics with good predictive capabilities, considering the relative small number and range of the independent variables considered.

The number of independent variables is relatively small and the results contain non-complex dependencies, therefore least squares linear regression techniques were used to model response surfaces from the wind tunnel data. The appropriate model's structure is determined using predicted squared error criteria.

The dependence of the aerodynamic and propulsion parameters on the free stream dynamic pressure is confirmed and evaluated. The lift coefficient resulted to be moderately affected by the flight dynamic pressure, while the drag and pitching moment coefficients are much more sensitive to changes in airflow velocity.

The model is based on a Micro Aerial Vehicle model developed at the University of Florida and currently flying. The model could be used for general trimmed flight parameters predictions, performance optimization, controls design, energy balance and therefore optimization of batteries usage, mission planning and flight simulations.

CHAPTER 6 SUMMARY AND RECOMMENDATIONS

A unique facility was developed at the University of Florida to implement a combination of a low speed wind tunnel and a visual image correlation system. The models tested in the wind tunnel in steady conditions, at a range of Reynolds number between 80,000 and 130,000, were fabricated at the University MAV lab and consisted of a series of ten models with an identical geometry, but differing on the structural design in order to differentiate the various levels of flexibility and deformation modes. The wing aspect ratio for all wings is 1.25.

Conspicuous differences were detected in the elastic static deformation characteristics between the batten reinforced (BR) wings and the perimeter reinforced (PR) wings. Accordingly, several variations in the aerodynamic characteristics were identified. The BR wings resulted to be potentially less sensitive to gusts due to the lower values of the lift curve slope and are better suited for high velocity flight conditions. The PR wings exhibited higher lift and higher maximum lift coefficients therefore they can be considered more appropriate for slower and more agile vehicles. The L/D values are in general slightly higher for the R wing and constant with the dynamic pressure. The PR wings have generally the lowest L/D values but their consistent higher longitudinal stability derivatives creates the most benevolent flight conditions for the aerial vehicle.

The propeller greatly enhances in all wings the maximum lift and the angle of attack for maximum lift, giving the vehicles a truly potential for agility. Furthermore the

propeller with the important longitudinal trim coupling could be considered as a good candidate for advanced control systems.

The rigid (R) wing proved that the aerodynamics effects caused by the variation of the Reynolds number are negligible within the range interested to the tests. The BR wings exhibited a moderate increase of the maximum camber, up to 2%, linearly dependent with the AOA and dynamic pressure; the PR wings otherwise presented a more important increase of the maximum camber, up to 5%. The static elastic twist of the wings under static aerodynamic loads is moderate insignificant for the PR wings, moderate for the BR09 wing and significant for wings BR02 and BR05.

Accordingly the aerodynamic coefficients present an insignificant increase of $C_{L_{max}}$ for the BR wings with a concurrent important increase of the AOA for $C_{L_{max}}$; in the case of the PR wings the increase of $C_{L_{max}}$ in respect to the R wing is relevant, showing a $C_{L_{max}}$ of 1.6; the AOA for $C_{L_{max}}$ remains similar to the R case. The maximum lift coefficient and the related AOA are constant with the free stream dynamic pressure.

The change of the position along the chord of the maximum camber is moderate for the BR wings, approximately 4% downstream, and more significant for the PR wings up to 15% downstream; the variation is linearly dependent with the AOA up to medium values of 18 or 20 degrees. Indeed the PR wings have the highest negative (nose down) pitching moment. The derivative of the pitching moment respect to the lift coefficient, an indication of the static stability margin, is lower for the BR wings in respect to the PR and R wings and in all cases constant with the dynamic pressure and moderate values of the AOA.

The addition of the same fuselage to the wings type R, BR and PR causes the expected decrease of lift and increase of drag. Interestingly enough the decrease in lift and the increase in drag are relevant for the R wing, decisively mild for the PR wing and at intermediate values for the BR wing. The explanation of this phenomenon is beyond the scope of this work. The addition of the fuselage causes a significant nose down moment for the R wing and a minor one for the BR and PR wings; the C_m versus C_L curve slope increases for the R wing and remains constant for the BR and PR wings.

The propeller speed at constant DC motor voltage input is non-linearly dependent with the AOA and the dynamic pressure. Furthermore the propeller slipstream effects introduce strong non-linear couplings between the propeller speed and the aerodynamic coefficients tested at different AOAs and dynamic pressures. In the aforementioned scenario was not possible to discern the possible effects of the flexibility of the wings because of the strong influence of the propeller on the aerodynamic characteristics of the vehicles. A significant asymmetry of shape between the right and the left wing was documented in several test cases for the PR wing.

Analytical nonlinear models for the propulsion parameters and the aerodynamic coefficients based on wind tunnel tests results are developed using least squares linear regression techniques to model response surfaces. The appropriate model's structure is determined using predicted squared error criteria. The AOA and free stream velocity demonstrated a significant nonlinear coupling with the propeller speed therefore to obtain reliable models, in spite of the fact that the effects of the change of the Reynolds number were proven irrelevant, it is suggested to include in the models terms with the dynamic pressure.

Several areas where further research would be justified by good potential for improvements in the MAV performance or an expansion of the flying envelope of the current models, have emerged as a result of this work. The BR wings exhibited potential beneficial characteristics for gust alleviation; this property should be proved in dynamic conditions. The top candidate would be to extend this experimental investigation to dynamic conditions obtained by pitching the models with selected frequencies and obtain the aerodynamic coefficients, propulsion characteristics and the deformation of the wings. The determination of the elastic energy stored by the structure and the skin would support the research on geometry control systems like morphing or structure tailoring in flapping wings systems.

Another area, related to the expansion of the analytical models would include tests, already partially performed, with the elevator set at different angles, and expand the experiments to higher AOAs, up to 90 degrees, to support global modeling; the objective could also include a study on the potential use of the propeller effects as an enhanced lift and control system. The tests should also be carried out at different rudder angles and yaw angles. Because of the tremendous number of tests required in the aforementioned case, the actual OFAT technique should be substituted with a more efficient MDOE technique. With the extension of the experimental subspaces and the increase of dependent variable more efficient statistical methods need to be considered for global non-linear analytical modeling involving the automatic determination of multivariate orthogonal functions.

A deeper experimental study of the propeller-flow-structure interactions would greatly support the design of a more agile micro aerial vehicle. A more comprehensive

post processing of the VIC data relative to the wings in the data base with a more efficient CAD oriented methodology would increase the efficiency of the manipulation of the three-dimensional geometry and better support the validation of CFD and FEM codes now in progress at the University.

In terms of experimental apparatus and procedures, further studies should be dedicated to further improve the response of the sting balance at very low axial forces, in the order of .01 N and the performance of the roll component, especially for low torque combined with relatively high lift. Furthermore, a dynamic VIC system will be required to support the aforementioned pitching tests or in the case of static tests at high AOAs, where structure and skin vibrations were observed.

APPENDIX A EXPERIMENTAL DATA CORRECTIONS

The wind tunnel tests data used and reported in this work have been corrected for a number of effects. Those effects can be divided in two main categories:

- wind tunnel corrections
- structure flexibility corrections

A.1 Wind Tunnel Corrections

The presence of the wind tunnel walls alters the measured values of the aerodynamic forces acting on the model. In particular the effects will be an increase in the measured lift, drag and pitching moment due to an increase of the velocity at the model. The wind tunnel corrections include three types: solid blockage, wake blockage and streamline curvature. The corrections procedure used are a combination of the methods reported by Torres [15], Pankhurst and Holder [88], Barlow, Rae and Pope [84] and Selig [102]. The buoyancy correction, the additional drag that arises from a decrease in static pressure in the test section due to the growing of the boundary layer on the wind tunnel walls, is considered insignificant for the test set-up used but its main effect will be taken into account in the corrections for the free stream velocity [102].

A.1.1 Solid Blockage

The solid blockage is an effect due to the physical presence of an object, the model, inside the test section that will produce a decrease in the test section effective area. From the equations of continuity and Bernoulli (Daniel Bernoulli, 1700-1782) follow that the velocity of the air in the model section must increase, increasing all the aerodynamic

forces and moments at a given angle of attack. The solid blockage effects are divided in wing effects and body (fuselage) effects.

The solid blockage correction factor for the wing is obtained by

$$\varepsilon_{sb,w} = \frac{k_1 \tau_1 (t \cdot b \cdot c)}{A^{3/2}} \quad (\text{A.1})$$

where A is the wind tunnel cross section area, and k_1 and τ_1 are coefficients from [84].

The solid blockage correction factor for the body (fuselage) is obtained by

$$\varepsilon_{sb,B} = \frac{k_3 \tau_1 (V_B)}{A^{3/2}} \quad (\text{A.2})$$

where k_3 and τ_1 are coefficients from [84] and V_B is the body (fuselage) volume considered as an ellipsoid with a circular cross sectional area equal to the maximum cross sectional area of the model and the same length (double the major axis) of the model.

The total solid blockage effect is the simple summation of (A.1) and (A.2)

$$\varepsilon_{sb,T} = \varepsilon_{sb,w} + \varepsilon_{sb,B} \quad (\text{A.3})$$

A.1.2 Wake Blockage

The wake blockage arises from the velocity within the airfoil wake that is lower than the free stream velocity. For closed tests sections, in order to satisfy the continuity equation, the velocity outside the model and outside of the wake must increase. In free flow conditions, the velocity outside the wake would be the same of the infinite free

stream velocity. The effect of wake blockage is proportional to the wake size and therefore proportional to the measured drag force on the model. The wake blockage correction factor proposed by Torres [15] is obtained by

$$\varepsilon_w = \frac{S_w}{4A} C_{D,u} \quad (\text{A.4})$$

where S_w is the wing reference area and $C_{D,u}$ is the uncorrected measured drag coefficient.

A.1.3 Streamline Curvature

The walls of the wind tunnel generate a modification in the streamlines of the airflow around the wing of the model. The curvature of the flow that passes on the model is altered, increasing the wing effective camber as the streamlines are “compressed” together. For closed wind tunnel test sections, the streamline curvature effects produce an increase in the measured lift, pitching moment and angle of attack. The drag is not influenced. The streamline curvature correction factor is obtained by

$$\sigma = \frac{\pi^2}{48} \left(\frac{c}{h} \right)^2 C_{L,u} \quad (\text{A.5})$$

where c is the reference chord length, h is the wind tunnel test section height and is the uncorrected measured lift coefficient.

A.1.4 Corrections to Measured Parameters

The measured parameters of interest are lift, drag, pitching moment and angle of attack and they were corrected in their nondimensional form to consider the solid

blockage, the wake blockage and streamline curvature. The corrected values for lift, drag, pitching moment and angle of attack are obtained as follows.

Lift

$$C_L = C_{L,u}(1 - \sigma - 2\varepsilon_T) \quad (\text{A.6})$$

where

$$\varepsilon_T = \varepsilon_{sb,T} + \varepsilon_w \quad (\text{A.7})$$

Drag

$$C_D = C_{D,u}(1 - 3\varepsilon_{sb,T} - 2\varepsilon_w) \quad (\text{A.8})$$

Pitching moment

$$C_M = C_{M,u}(1 - 2\varepsilon_T) + \frac{\sigma}{4.0} C_{L,u} \quad (\text{A.9})$$

Angle of attack

$$\alpha = \alpha_u + \frac{57.3\pi c^2}{\left(\frac{96}{h^2}\right)} C_{L,u} \quad (\text{A.10})$$

where α_u is the uncorrected measured angle of attack.

A.2 Structure Flexibility Corrections

In the general case, any change in the model position and shape during wind tunnel tests may be considered as the summation of the flexibility of the holding structure, of the sting balance (if an external balance is used) and the model itself. The above changes can cause differences between the acquired and the expected wind tunnel results if the expected results are based upon rigid body assumptions. Model deformation can be defined as the change in shape of a model under aerodynamic load in a wind tunnel. The measurement of model deformation has been of interest to the wind tunnel researchers for many years and various methods for detecting the model deformation were proposed and evaluated. A typical unwanted but inevitable deformation mode is the wing twisting of high speed, high aspect ratio swept wing aircraft and the relative wind tunnel models [100]. The three optical systems classically used for measuring model deformation are video model deformation or video photogrammetry (VMD), projection moiré interferometry (PMI) and Optotrak system [72]. Each system has advantages and disadvantages, depending on the nature of the test, but the VMD is enjoying an important revival due to the simplicity of its application and the relatively easy access to high capacity computing. The major drawback of a VMD system is the not great accuracy and the discrete nature of the sampled point on the model's surface. The system used in the present work to measure the shape of the wing is the VIC, previously described in Chapter 3. In our case, due to the specific design of the flexible wing's structure, the static deformation under aerodynamic loads is the principal subject of the research, therefore the change in wing shape won't be considered as a correction factor but a primary result. The effects of the flexibility of the model's holding structure, and the

flexibility of the sting balance will be evaluated and used to adjust the proper wind tunnel data. The high sensitivity of the sting balance was obtained, among other factors, by reducing the dimensions of its structural parts, inevitably introducing a relatively high deformation under static loads. The flexural deformation of the balance translates in a change of the effective AOA of the model during testing, respect to the AOA value commanded by the control software. The AOA feedback value recorded during the wind tunnel tests is measured at the shaft close to the gearbox, and can be considered a nominal value. The real value was detected by processing images of the model taken by the VIC system during the tests.

A.2.1 Test Procedure and Preliminary Data Reduction

The general procedure to perform the tests is the same already explained in the previous chapter regarding the VIC system description. In the case of the correction of the AOA during test, we are interested in the “rigid” part of the wing made by solid carbon fiber, instead of in the whole wing, including the flexible part. The AOI for image correlation will be set in the middle part of the wing, in order to detect rigid body translations and rotations. The test procedure is, as usual, based on detecting the differences of the wing in wind-on conditions from wind-off conditions (reference image). In this case the differences will be caused by rigid body translations and rotations of the wing, instead of elastic deformations. The test sequence is depicted in the block diagram in Figure A-1.

The images of the wing in the desired conditions of AOA and free stream velocity are stored in pairs, together with their reference image at the same nominal AOA but in wind-off conditions. Each pair will then be processed using the VIC software and

information about the geometry and deformation of the model can easily be extracted.

An example of the process is depicted in the following images. The reference image of the wing,

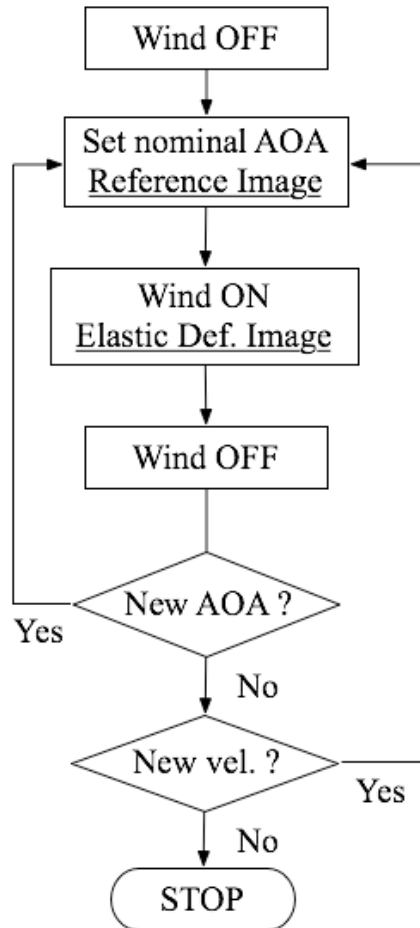


Figure A-1. Test sequence for AOA correction tests.

Figure A-2 (view from top) and Figure A-4 (3D view), captured at the nominal AOA and with airflow off, will be compared with the conditions at the same nominal AOA but with wind on, Figure A-3 (view from top) and Figure A-2 (3D view). All the figures represent a contour plot of the displacements w in the Z direction. The plots in Figures A-2 and A-4, with a solid uniform color in airflow off conditions (reference

state), show a pattern, Figures A2 and A5, at the same nominal AOA but with airflow on, which is evidence for the rotation of the model as a rigid body. The rigid body rotation of the model will be evaluated and interpreted as a change in the nominal AOA. Data from the processed image is stored in a file for late post processing.

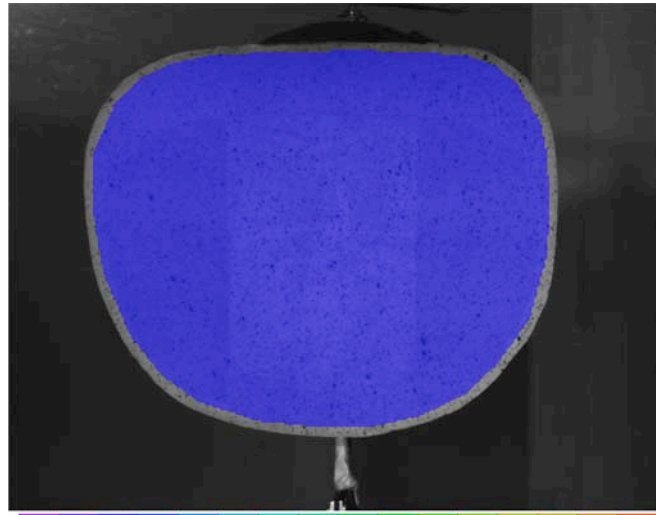


Figure A-2. Reference image, at nominal AOA and airflow off.

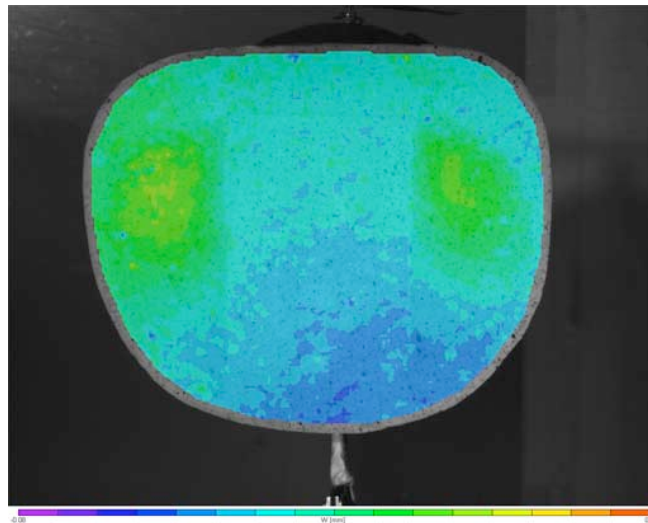


Figure A-3. Image with wing under loads, at nominal AOA and airflow on.

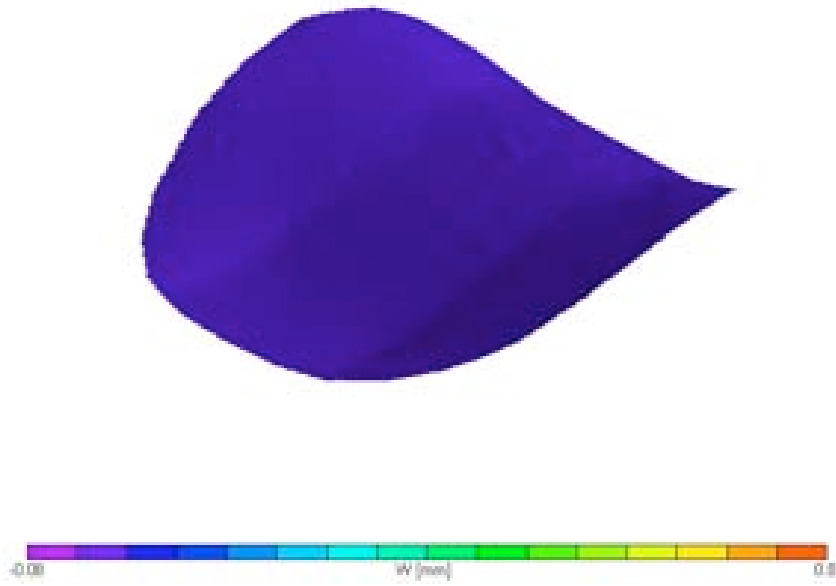


Figure A-4. Reference image, at nominal AOA and airflow off.

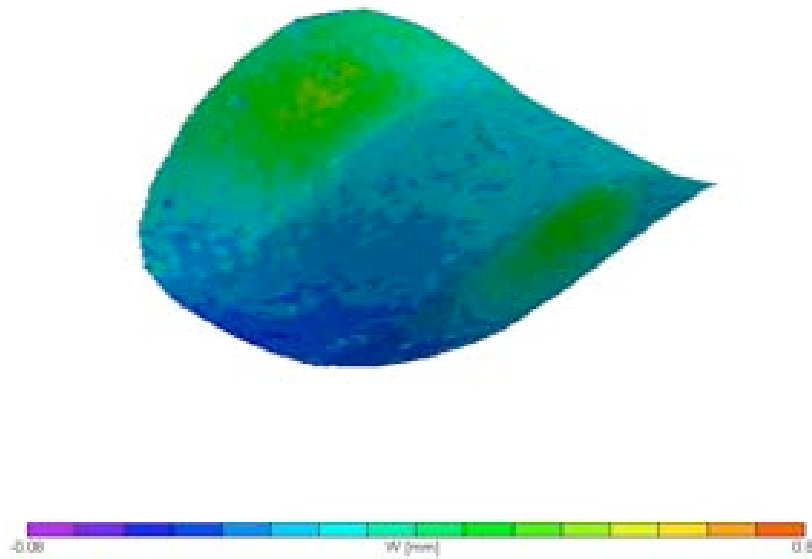


Figure A-5. Image with wing under loads, at nominal AOA and airflow on.

The rigid body rotation is also evident from the plot in Figure A-6, with the displacements along the chord of the wing section at the centerline of the model in the

reference conditions (airflow off, squares, all values are zero) and with airflow on (triangles). The values of the displacements given by the linear fit at the leading edge and at the trailing edge is an indication of the rigid body rotation of the wing and, in essence, of the change of the nominal AOA.

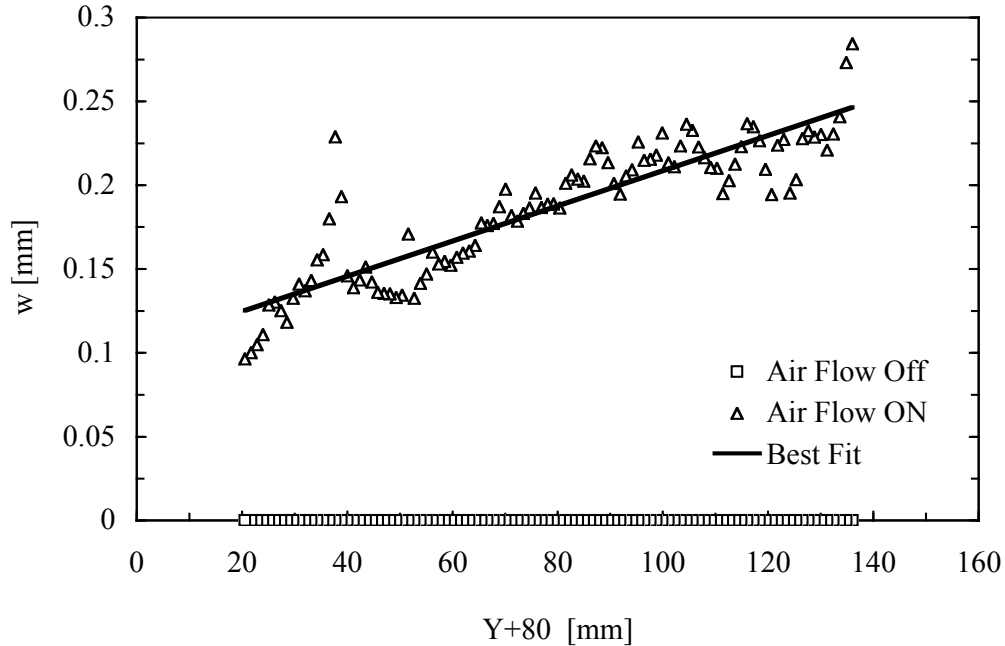


Figure A-6. Plot of the displacements w in the Z direction in two conditions: reference state with airflow off (squares, all zeros) and in loaded state (triangles).

A.2.2 Data Analysis and Results

Once the file with the coordinates of the geometry of the AOI in the displaced positions X_d , Y_d and Z_d is imported in a spreadsheet, with the corresponding displacements u , v and w , the rigid rotation of the portion of the wing was evaluated. The rotation of the part of the wing made of solid carbon fiber is assumed to represent the rigid body rotation (or translation when applies) of the whole wing. For each image, an

area 10 mm wide ($Y = \pm 5$ mm) was selected symmetrically placed alongside the wing's center line ($Y = 0$) and 20 sections in the Z-Y plane were selected at a distance of 0.5 mm from each other. The chord line at each section was established using the leading edge and trailing edge points and simple geometric relations between the reference image and the rotated image were used to evaluate the rotation angle of each section. Using the notations in Figure A-7.

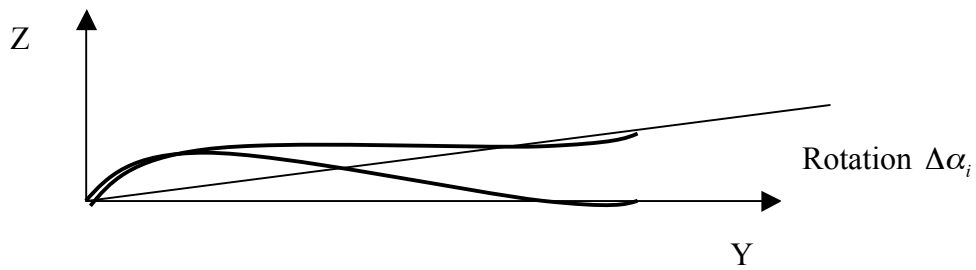


Figure A-7. Reference and rotated wing sections at a selected nominal AOA and dynamic pressure.

The rigid body rotation of the generic i_{th} section is

$$\Delta\alpha_i = \arctg \frac{(z_{TEi} - z_{LEi})}{(y_{TEi} - y_{LEi})} \quad (A.11)$$

The calculated value of the rotation angle in a single section from equation A.11 is repeated for N sections in the AOI area, and the average value is computed as

$$\Delta\alpha_{AV} = \frac{\sum_{i=1}^N \Delta\alpha_i}{N} \quad (A.12)$$

Where N in the proposed case is equal to 20. The sign of $\Delta\alpha_i$ will determine, in the conventional notation, if the rotation is nose up or nose down.

The result from equation A.12 is the value of the rigid body rotation for the selected AOA (or C_L) and free stream velocity in the wind tunnel. The smoothing result of using an average value for θ instead of the value of a single section is demonstrated in Figure A-8 at three different flow velocities for one of the PR wings (15004). Values averaged in N sections are solid while values for single section have no background.

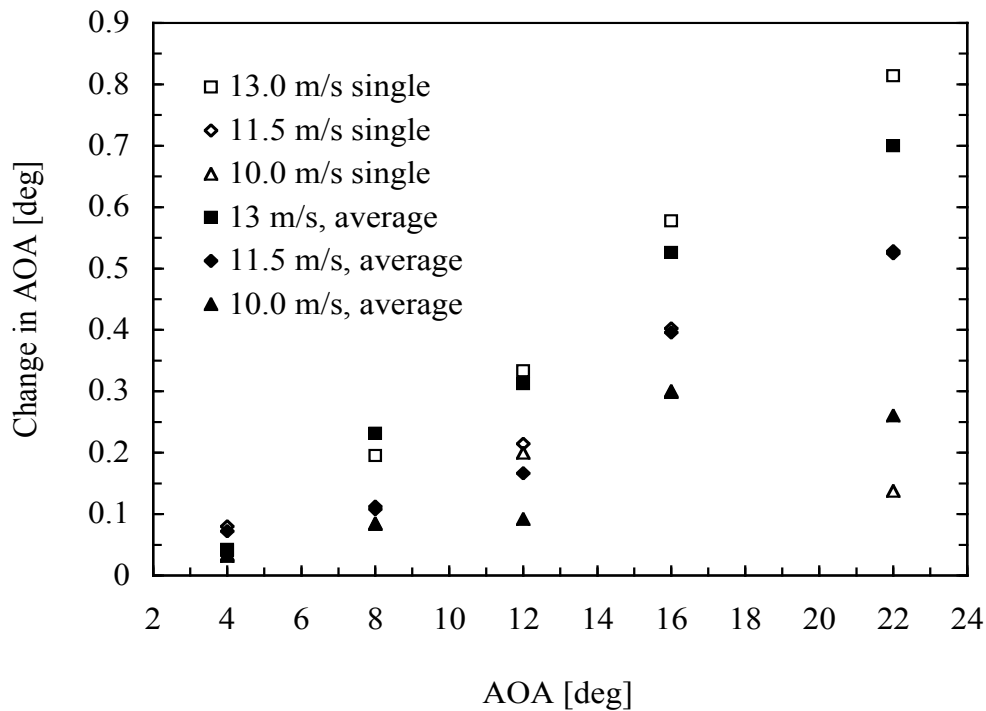


Figure A-8. Change of the AOA due to the flexibility of the holding structure versus the nominal testing AOA for one PR wing (15004), at three free stream velocities.

In order to avoid the unsteady post stall area, the measurement of the wing rigid displacements were acquired up to the limit of linear lift curve slope therefore, only results for a limited number of nominal AOAs were available. In spite of the above only

apparent limitation, a final corrected value for the AOA was extracted for the full range of the experimental nominal AOA, typically varying from 4 to 34 degrees.

A.2.3 Final Correction of the Nominal AOA

The values of α were plotted versus C_L (instead of AOA) at the available tested flow velocities for the two types of flexible wings, PR and BR. The plots are depicted in Figures A-9 and A-10.

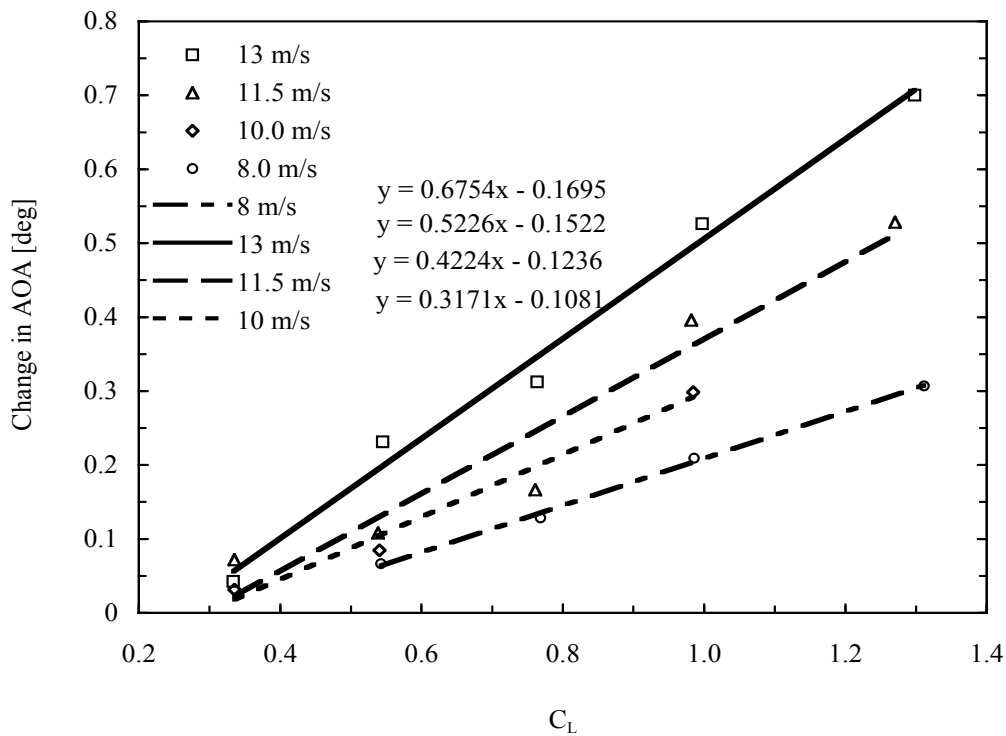


Figure A-9. Change of the AOA due to rigid body rotation versus C_L at four wind tunnel free stream velocities for a typical PR wing.

With the assumption that the wing rigid rotation is caused mainly by the lift component of the aerodynamic resultant, the corrections for the full range of AOA and velocities were estimated as function of the lift coefficient using the linear regressions depicted in the Figures A-8 and A-9.

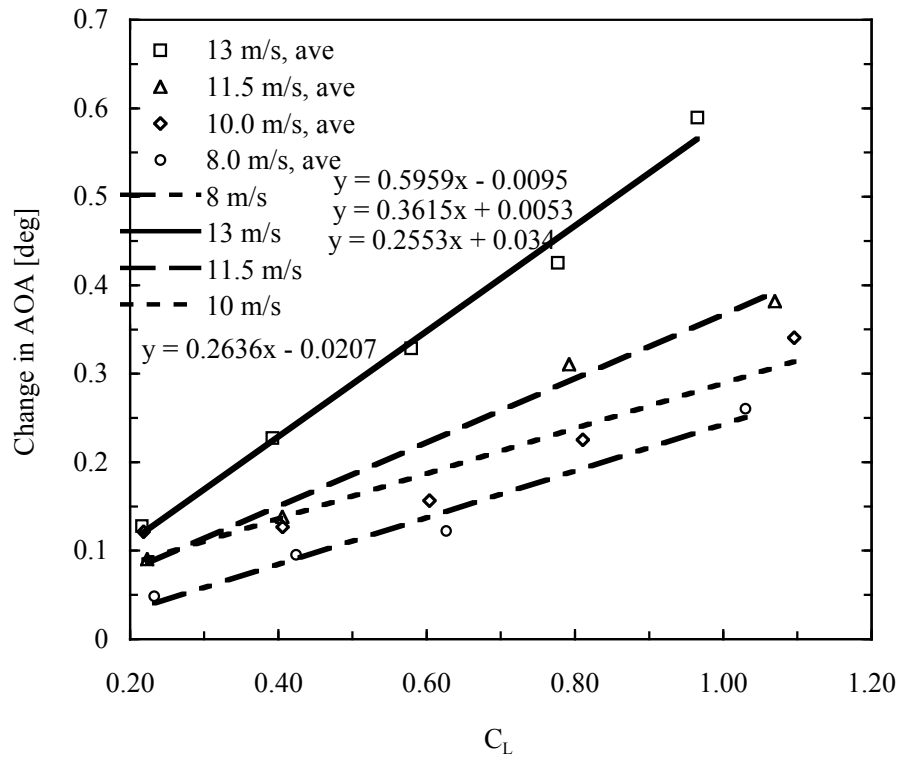


Figure A-10. Change of the AOA due to rigid body rotation versus C_L at four wind tunnel free stream velocities for a typical BR wing.

Using the linear equations we have the following expressions for the change of AOA for a particular flow velocity

$$\Delta\alpha = \frac{d(\Delta\alpha)}{d(C_L)}(C_L) + \Delta\alpha_{AOA=0} \quad (\text{A.13})$$

Where $\Delta\alpha = \Delta\alpha_{AV}$, $d(\Delta\alpha)/d(AOA)$ and $\Delta\alpha_{AOA=0}$ are respectively the slope and the constant of the linear regressions represented in the Figures A-8 and A-9. The effective value of the AOA finally is

$$\alpha_E = \alpha + \Delta\alpha \quad (\text{A.14})$$

APPENDIX B UNCERTAINTY ANALYSIS

This section will describe the methods used to estimate the level of reliability of the experimental results presented in this work. Because of the practical impossibility to estimate all the uncertainties of observation by repetition, the following methodology is derived from the single sample experiments techniques. The experimental systems used in this work were essentially two, the wind tunnel sting balance for forces measurements and the VIC for model structure deformations and rigid body rotations and translations. Because the nature and scope of the two systems were very different, two diverse uncertainties analysis were performed. By using both methodologies was possible to characterize the single experimental points by identifying an error bound associated with the experiments.

B.1 Wind Tunnel Measurements

Since very precise instrumentation were used but the balance was designed for loads in the order of 50 N maximum, much higher than the aerodynamic loads measured with MAVs, it is therefore reasonable to expect the main source of error to be the balance [28]. A preliminary estimate of accuracy was done by performing check runs, obtaining the necessary confidence in the results to go ahead and run the tests.

B.1.1 Wind Tunnel Check Runs

The check runs were conducted with flat plates, Clark-Y airfoil and sphere and the results compared with published data from very reliable known sources. As test case

results from a flat plate are presented at same test conditions for both the published [14] and the experimental data. Although the plates were not geometrically identical, as showed in Table B-1, the results were remarkably close.

Table B-1. Comparison of geometrical characteristics of flat plate models.

	Published	UFL
	Data	Experiment
LE	Elliptical	Elliptical
	Machined	Hand Made
t/C max %	2.0	1.2

A typical example from the runs with the flat plate is illustrated in Figure B-1 with the plots of C_L versus AOA for the published data and the wind tunnel runs at two different Re number.

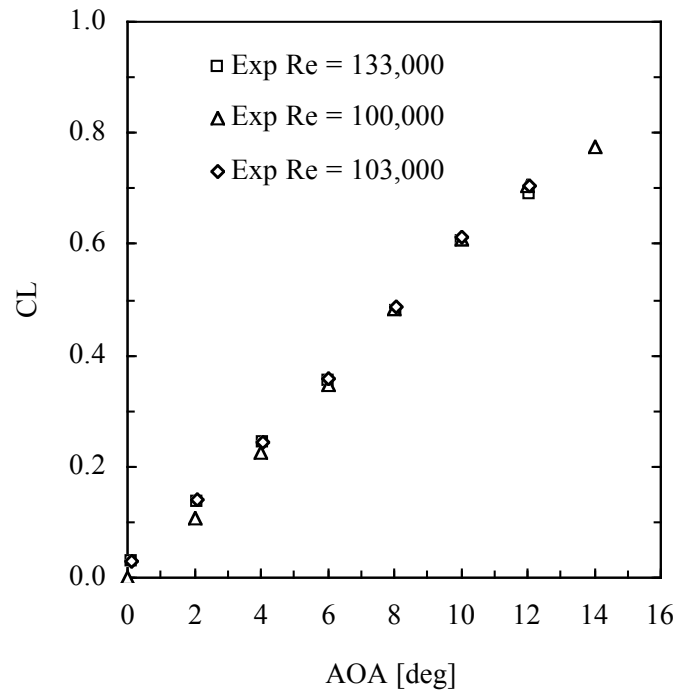


Figure B-1. Experimental lift coefficient versus AOA for flat plates.

Figure B-2 shows, for the same runs, the drag coefficient for the published case and the wind tunnel results. A lower drag for the University of Florida experimental case was observed which was attributed in part to the less maximum thickness of the tested flat plate in respect to the subject of the publication, as depicted in Table B-1 and in part to the intrinsic error of the sting balance at very low drag counts.

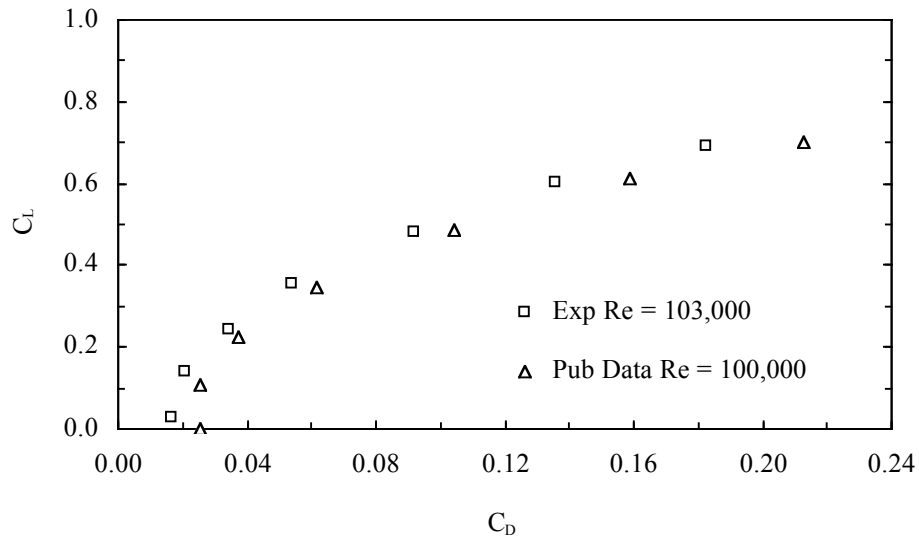


Figure B-2. Coefficient of lift versus coefficient of drag for flat plates.

The maximum difference in drag between the published data and the experimental data was found to be -36.95% at zero lift coefficient, a condition not very interesting for MAV flights. At typical flight lift coefficients the error was less than 15% , and at an average physical drag value of $.15\text{ N}$ the error was $-.02\text{ N}$. Figure B-3 shows the plot with the “error” in the coefficient of drag for different values of the lift coefficient. The “error”, in percent value, is defined as the difference of the published and the experimental value normalized with the published value times 100. The absolute error is

function of the value of the drag force with a threshold for errors less than 10 % at about .10 N of drag. Increasing the Re number this error tended to decrease due to the larger aerodynamic forces acting on the balance.

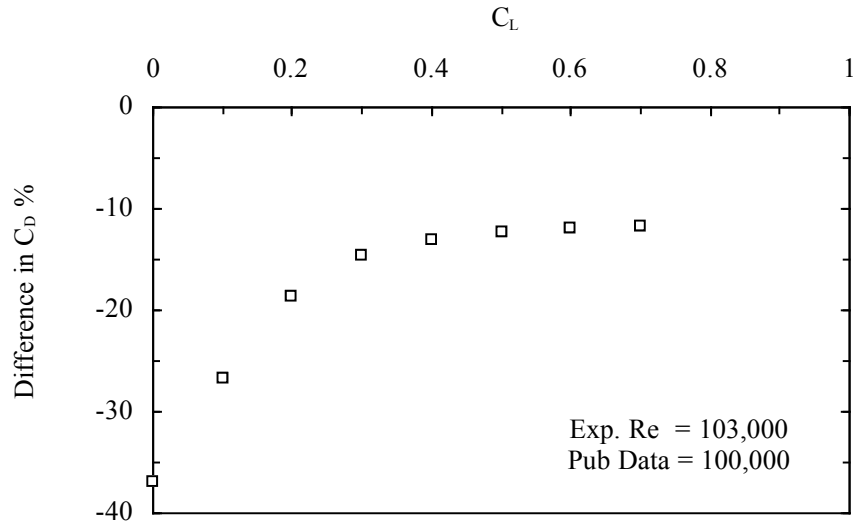


Figure B-3. Difference of coefficients of drag between the published data and the experimental data, in function of the coefficient of lift, for flat plates.

B.1.2 Uncertainty Analysis

The equations used to estimate the uncertainties and the propagation of error are derived from [87] and from standard uncertainties analysis methods [104].

The main sources of uncertainty were identified as the errors associated with solving the balance forces and moments and with the standard deviation of a mean output voltage for a given channel of the sting balance. The quantization error, due to the use of 16 bit DAQ cards, was assumed negligible [13]. Minor error factors were the uncertainties in the determination of model geometric quantities such as wing area and

measurements of physical quantities as ambient and dynamic pressures, dimensions of the models, AOA angle and ambient temperature.

The method consisted in a procedure involving the use of a sequence of equations enabling the systematic evaluation of single quantities, using variables based on a careful specification of the uncertainties in the various primary sensors or experimental measurements. Let X be a generic physical quantity with x_i variables, let V be the number of variables and N the number of measurements. The following equations were defined:

The sensitivity index

$$\theta_{x_i} = \frac{\partial X}{\partial x_i} \quad (\text{B.1})$$

The resolution error

$$R_{x_i} = .5 * \textit{leastcount} \quad (\text{B.2})$$

The resolution limit

$$R_X = \sqrt{\sum_{i=1}^V (\theta_{x_i} R_{x_i})^2} \quad (\text{B.3})$$

The standard deviation

$$P_{x_i} = \sqrt{\frac{\sum_{k=1}^N (x_{i_k} - \bar{x}_i)^2}{N-1}} \quad (\text{B.4})$$

The standard deviation of the means

$$P_{\bar{x}_i} = \frac{P_{x_i}}{\sqrt{N}} \quad (\text{B.5})$$

The precision index

$$P_X = \sqrt{\sum_{i=1}^V (\theta_{x_i} P_{x_i})^2} \quad (\text{B.6})$$

The degree of freedom using the Welch-Satterthwaite equation

$$v = \frac{\left[\sum_{i=1}^V (\theta_{x_i} P_{x_i})^2 \right]^2}{\sum_{i=1}^V \frac{(\theta_{x_i} P_{x_i})^4}{(N-1)_{x_i}}} \quad (\text{B.7})$$

Finally the uncertainty of the value of X was found as

$$u_x = \sqrt{R_X^2 + (t_{v,95} P_X)^2} \quad (\text{B.8})$$

The value given from equation (B8) represents, with a 95% confidence, the maximum possible difference between the calculated value X and the actual value. The previous procedure was implemented by writing a code in Labview and was carried out

for the experimental values of C_L , C_D and C_m with the objective to obtain the error bound for each experimental point.

An example of application of the theory proposed will be presented for the case of the calculation of the uncertainty for the lift coefficient, while was identically applied to the cases of drag and pitching moment coefficients. According to the previous section describing the wind tunnel sting balance the lift coefficient was obtained as

$$C_L = [(V_1 - V_1^T)C_{11} + (V_2 - V_2^T)C_{12} + (V_3 - V_3^T)C_{13} + (V_4 - V_4^T)C_{14} + (V_5 - V_5^T)C_{15} + (V_6 - V_6^T)C_{16}) \cos \alpha + -((V_1 - V_1^T)C_{21} + (V_2 - V_2^T)C_{22} + (V_3 - V_3^T)C_{23} + (V_4 - V_4^T)C_{24} + (V_5 - V_5^T)C_{25} + (V_6 - V_6^T)C_{26}) \sin \alpha] / (q * A) \quad (B.9)$$

The lift coefficient expressed by equation (B.9) is a linear equation in the 27 variables are V_j, V_j^T, C_{ij} where $i = 1, 6$ and $j = 1, 2, q$, and α , thus $V = 27$. The sensitivity indices, for each of the 27 variables, were evaluated using equation (B.1) giving the following 27 equations:

$$\partial C_L / \partial V_j = \theta_{V_j} = (C_{1j} \cos \alpha - C_{2j} \sin \alpha) / (q * A) \quad (B.10)$$

$$\partial C_L / \partial V_j^T = \theta_{V_j^T} = (-C_{1j} \cos \alpha + C_{2j} \sin \alpha) / (q * A) = -\theta_{V_j} \quad (B.11)$$

with $j = 1, 6$ and

$$\partial C_L / \partial C_{1j} = \theta_{C_{1j}} = (V_j - V_j^T) \cos \alpha / (q * A) \quad (B.12)$$

$$\partial C_L / \partial C_{2j} = \theta_{C_{2j}} = (V_j - V_j^T) \sin \alpha / (q * A) \quad (\text{B.13})$$

with $j = 1, 6$. The last 3 sensitivity indices are given by the following equations:

$$\partial C_L / \partial q = \theta_q = -1 / q * C_L \quad (\text{B.14})$$

$$\partial C_L / \partial A = \theta_A = -1 / A * C_L \quad (\text{B.15})$$

$$\partial C_L / \partial \alpha = \theta_\alpha = [-(V_j - V_j^T)C_{1j} \sin \alpha - (V_j - V_j^T)C_{2j} \cos \alpha] / (q * A) \quad (\text{B.16})$$

For a typical experiment with 500 measurements ($N = 500$) some assumptions for standard errors for single measurement devices were made.

By applying the above numerical values in the equations (B.10) to (B.16) first and, in order, from equation (B.2) to (B.8) the value of the uncertainty of C_L , named u_{C_L} was obtained. Using the uncertainty values the lift coefficient with the uncertainty bound was defined as follows

$$C_{L_u} = C_L \pm u_{C_L} \quad (\text{B.17})$$

The above procedure was repeated for every AOA in the same test obtaining plots as the sample depicted in Figure B-4, with the typical values of the uncertainty for C_L . By repeating the same procedure for C_D and C_m , the values of their uncertainties were obtained. Figures B-4 to B-9 show typical plots with the experimental values.

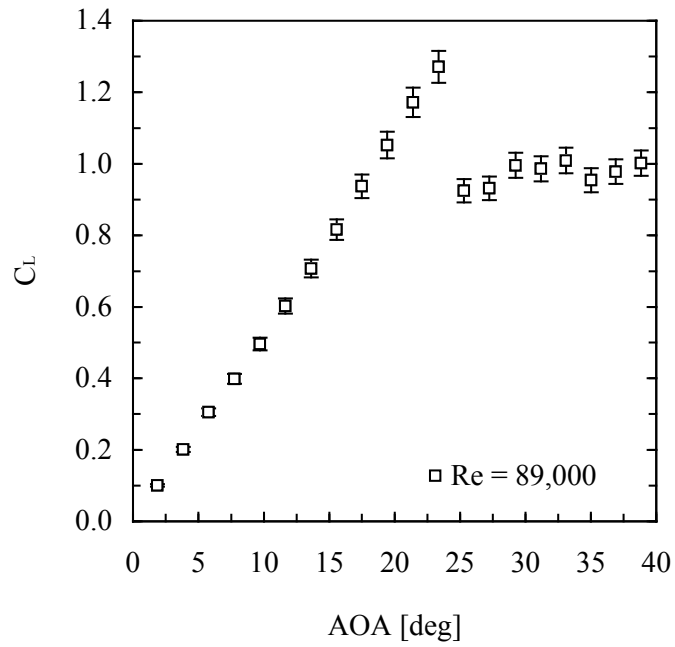


Figure B-4. Uncertainties bounds for the coefficient of lift at a Re number of 89,000.

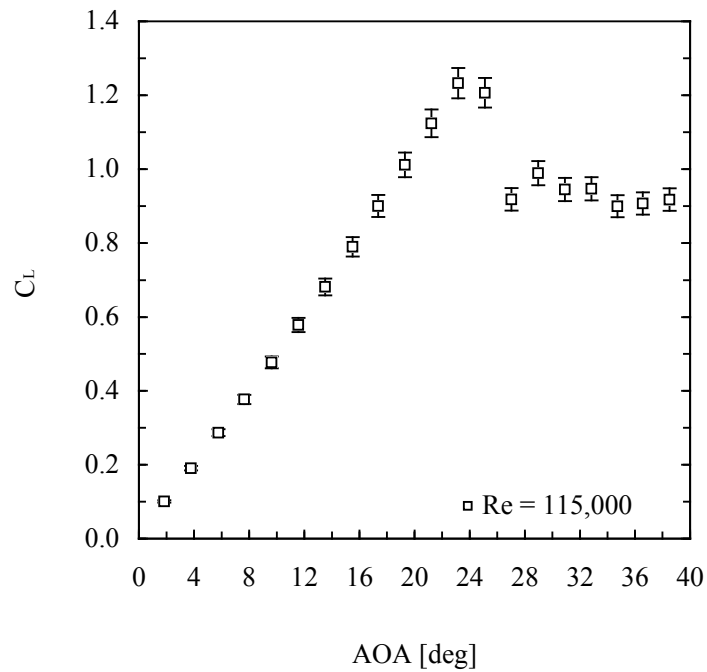


Figure B-5. Uncertainties bounds for the coefficient of lift at a Re number of 115,000.

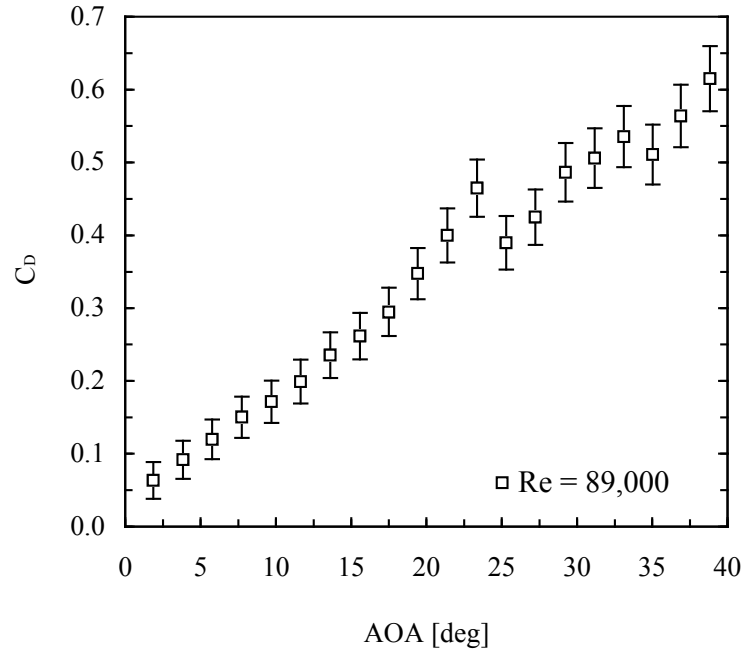


Figure B-6. Uncertainties bounds for the coefficient of drag at a Re number of 89,000.

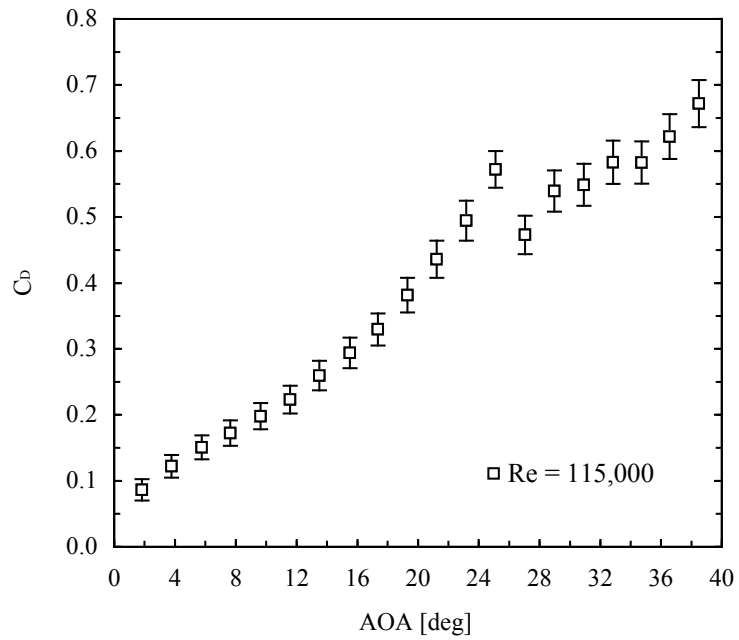


Figure B-7. Uncertainties bounds for the coefficient of drag at a Re number of 115,000.

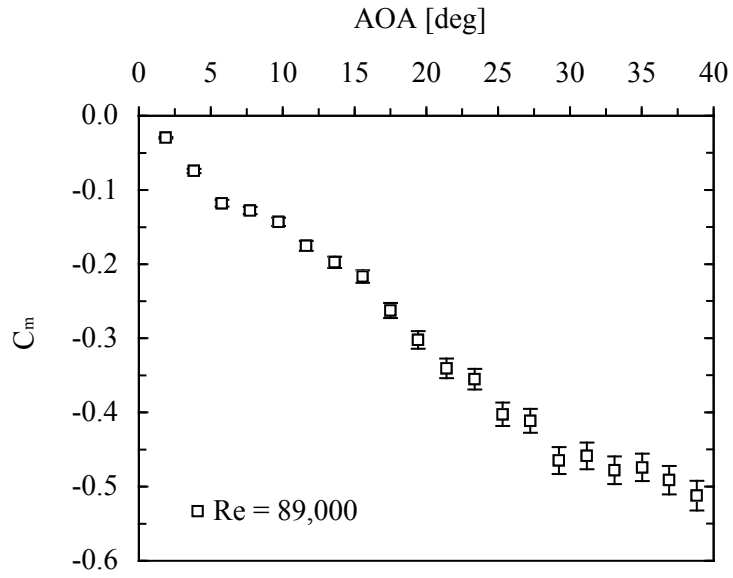


Figure B-8. Uncertainties bounds for the coefficient of pitching moment at a Re number of 89,000.

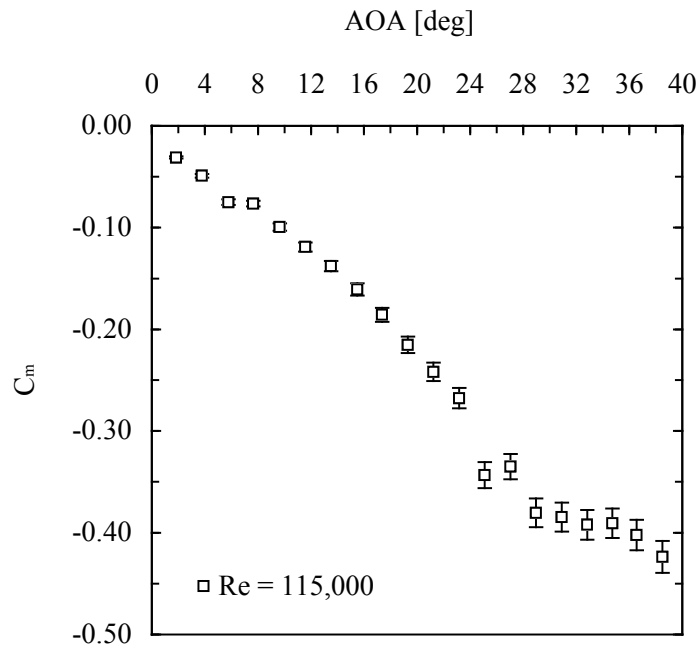


Figure B-9. Uncertainties bounds for the coefficient of pitching moment at a Re number of 115,000.

The resolution errors used in the above computations were estimated to be:

$$R_q = 1\%$$

$$R_A = .0005m^2$$

$$R_{Ch} = .002m$$

$$R_V = 1.2 * 10^{-7}V$$

$$R_\alpha = .05 \text{ degrees}$$

The larger values of the uncertainties obtained for large values of AOA, and depicted in the previous figures, is due to the relatively large standard deviation of the voltage signals from the six channels of the sting balance. Most of the models were also experiencing an important aerodynamic buffet at the same AOA values.

B.2 Visual Image Correlation

Because of the configuration of the wind tunnel sting balance instrumentation, basically an open source with in-house designed software for data acquisition and data analysis, it was possible to estimate the accuracy and the error of the single components, and apply the appropriate error propagation estimate techniques. The VIC system is a close system, with proprietary software not accessible to the operator. Nevertheless it was possible to perform a complete accuracy analysis and error assessment by carrying out an ad hoc set of experiments.

B.2.1 Theoretical Accuracy

The following imaging parameters need to be defined [94]:

Field of view (FOV): L by L (m²)

Recording resolution: N by N (pixels²)

Subset size (SS): m by m (pixels²)

Image displacement accuracy: β_1 (pixels)

Image speckle dimension: η_1 (pixels)

Object speckle dimension: η_0 (m)

With these definitions, we can determine parameters that are commonly used in computer vision:

Magnification factor, MT (pixels/m)

$$MT = L / N \quad (B.18)$$

Object displacement accuracy, β_0 (m):

$$\beta_0 = (\beta_1 * L) / N = \beta_1 * MT \quad (B.19)$$

Considering the typical values for the MAVs tested during this work, which had geometrically identical wings, we have a FOV of .0225 m² and N about 1000. Assuming [94] for the cameras used an image displacement accuracy of .01, using equation B.2 we obtain the best theoretical target displacement accuracy of .0015 mm.

The minimum object speckle size is obtained by using the minimum allowable image plane speckle size and the magnification factor

$$\eta_0 = \eta_1 / MT \quad (B.20)$$

Or by using the first “Rule of Thumb” [94], which states that speckles in the image should be sampled by at least 3 by 3 pixels to ensure over-sampling. In this case we have

$$\eta_0 \geq \frac{3L}{N} = .45(mm) \quad (B.21)$$

The minimum subset size is obtained using the second “Rule of Thumb” for the minimum subset size in terms of the minimum image speckle dimension. The rule states that the minimum image subset, $(N \times N)_{\min}$, should contain at least 3 X 3 speckles to maintain reasonable accuracy. In numerical terms we have

$$N \geq 3 * \eta_1 = 3 * 3 \text{ pixels} = 9 \text{ pixels} \quad (B.22)$$

$$(N * N)_{\min} = 9 * 9 = 81 \text{ pixels}^2 \quad (B.23)$$

The value given by equation (B.6) is generally considered too small. Reference use at least 15 X 15 pixels²)

B.2.2 Experimental Set-up

To check the theoretical figures and to obtain a physical estimate of the accuracy of the VIC system, a specific experimental set-up was designed and a special procedure was carried out. The test specimen consisted in a latex membrane, identical to the membrane used as wing skin on the MAVs, applied on the top of a rigid aluminum ring of the diameter of 100 mm with a thickness of 4 mm. The ring was held by a rigid steel structure at a certain distance from a table, on which the cameras of the VIC system were installed.

The experiments consisted by applying at the center of the membrane a known displacement by a steel bar with a spherical head of 8 mm diameter. The bar was moved against the latex membrane by a certified micrometer with minimum increments of .02

mm. The objective was to compare the readings from the VIC with the “true “ values impressed by the bar.

Figure B-10 shows the bar with the spherical head positioned close to the latex membrane (with speckles applied) and the aluminum ring. Figure B-11 shows the complete test apparatus with the micrometer, the ring with membrane and the VIC cameras.



Figure B-10. The bar with the spherical head positioned close to the latex membrane.

B.2.3 Experimental Results

A typical experiment was conducted by moving the shaft a certain amount in the vertical direction down using the micrometer. The latex membrane would accordingly deform and a picture was taken using the two cameras in the VIC system. The objective was to reach the maximum deflection position in several steps, recording the shape of the deformed membrane at every step.

After running the virtual image correlation for every displacement the entire AOI, for a surface of about $7,850 \text{ mm}^2$, was discretized with 13,500 points, giving a density of approximately 1.72 points per square millimeter. For any specific displacement was possible visualize the shape of the membrane and to plot any of the typical quantities in a contour plot style, as depicted in Figure B-12.



Figure B-11. The complete test apparatus with the micrometer, the ring with latex membrane and the VIC cameras.

The values in the contour plot in Figure B-12 represent the vertical displacements w for a maximum commanded displacement of 5.000 mm. The value detected by the system was 4.99896 mm with an error of -.00104 mm.

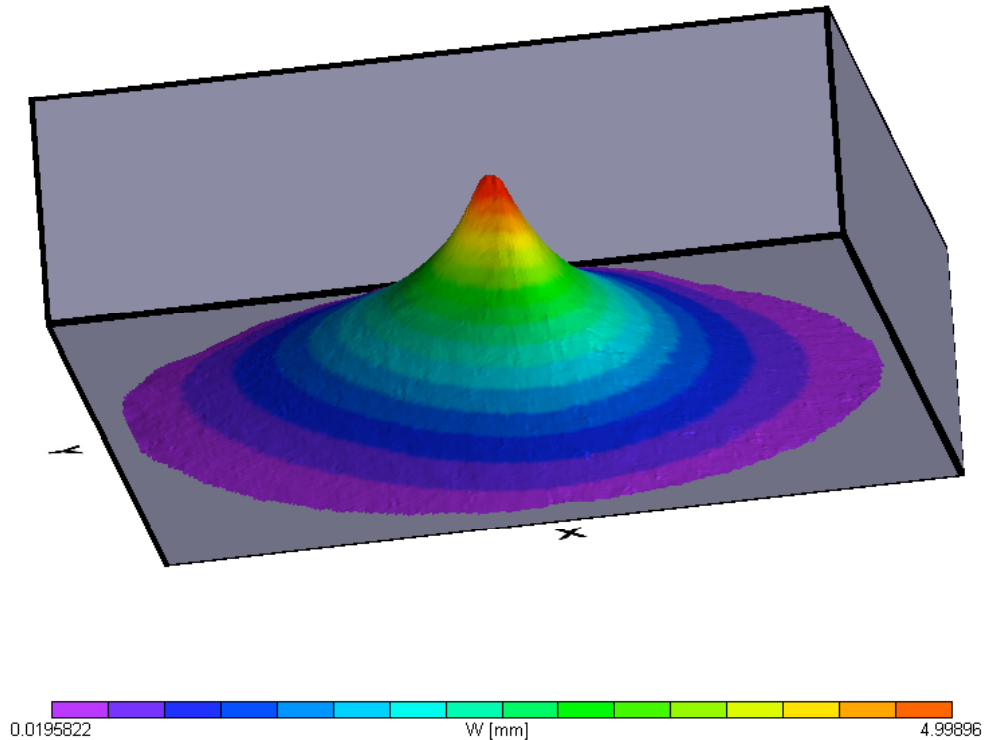


Figure B-12. Latex membrane shape as recorded and processed by the VIC system. The scale for w is from .0195822 mm to 4.99896 mm. The commanded displacement of the shaft was 5.0 mm.

B.2.4 Error Analyses

A preliminary estimate of the error was obtained by comparing the micrometer-imposed displacements of the latex membrane with the maximum values of w computed using the VIC system. Figure B-13 shows the results for a maximum commanded displacements of 5 mm, with steps of .25 mm in two configurations corresponding to the

two cameras in two different positions and both with the same speckle 's size (medium). It can be noted that with the cameras 25 % further away from each other, the accuracy was increased. Figure B-13 shows, for a maximum commanded displacement of .5 mm with steps of .05 mm, two cases with the cameras at the same position but with different speckle dimensions, fine and medium.

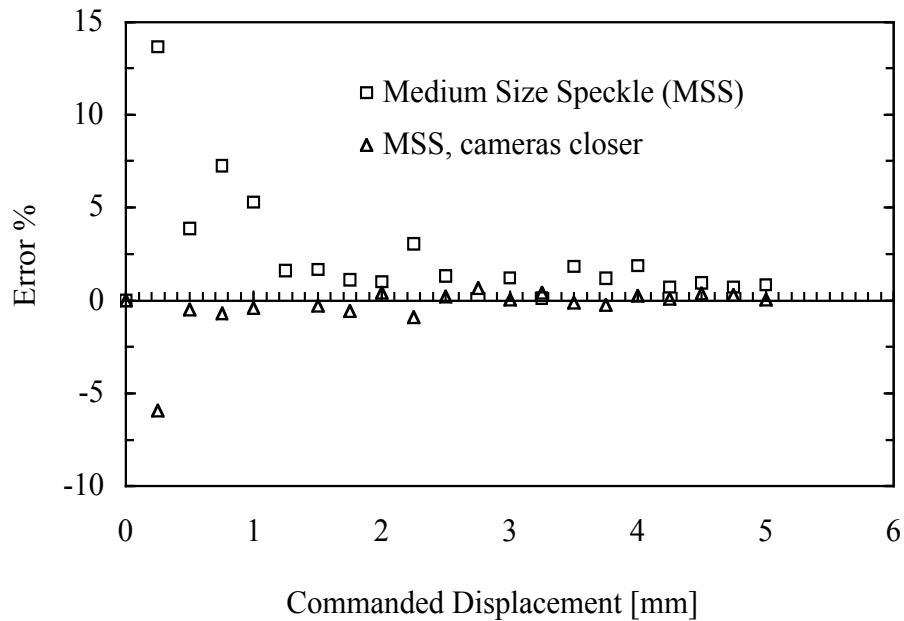


Figure B-13. Error in w_{max} for a specific commanded displacement for two cases with same speckle sizes but different cameras positions.

It was evident the low influence on accuracy of the speckle' s size for the physical dimensions proper of the experiments, in the order of few millimeters and with the smallest discrete steps in the order of .05 mm. The results depicted in Figure B-14 represent the peak error for each set of measurements of displacements; therefore it was affected by the inevitable experimental noise.

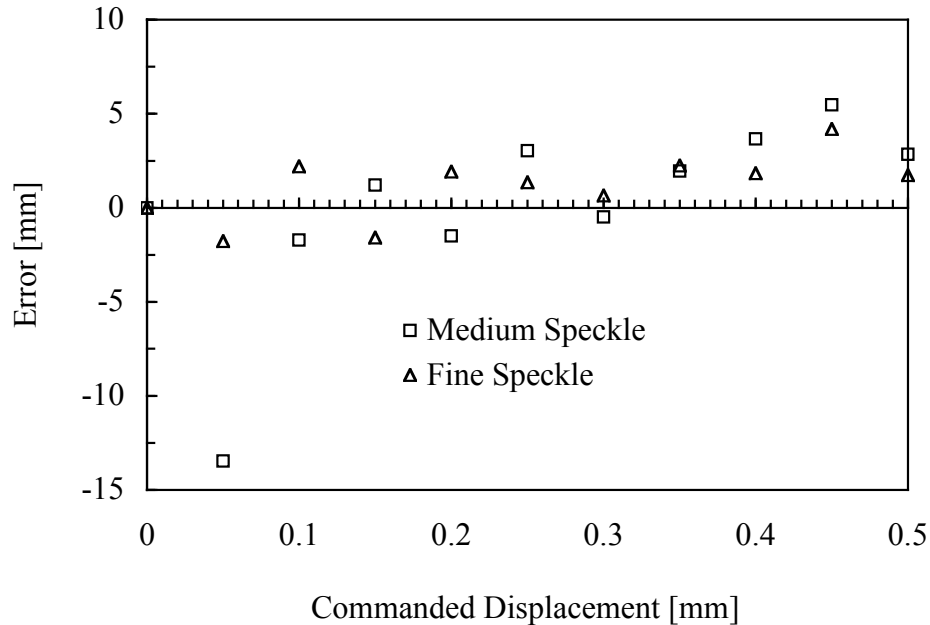


Figure B-14. Error in measured w_{max} versus commanded displacements for two cases with same cameras positions but different speckle sizes. The error value is the maximum value of the displacement in each experiment.

In order to have a more representative value of the VIC measurement, and thus of the error, a number of points around the maximum value were extracted from the data file for each experiment. The values, usually eleven including the maximum, were fitted with a least square regression using a second order polynomial function, with the objective to obtain a smooth measured latex membrane profile around the maximum. An experiment is depicted as example in Figure B-15, with the displacements in eleven locations on the latex membrane from a single experiment and the second order fit curve. In this case the commanded displacement was 0.1 mm, the maximum measured w_{max} was .1017 mm and maximum given from the curve fit was .0985 mm.

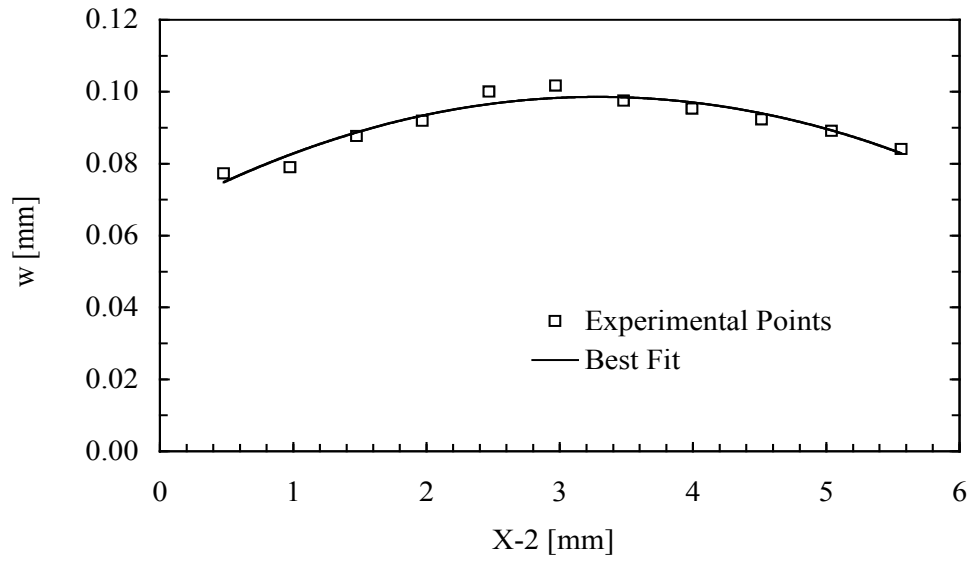


Figure B-15. Latex membrane profile versus X coordinate. The maximum measured w was .1017 mm with a commanded displacement of .100 mm.

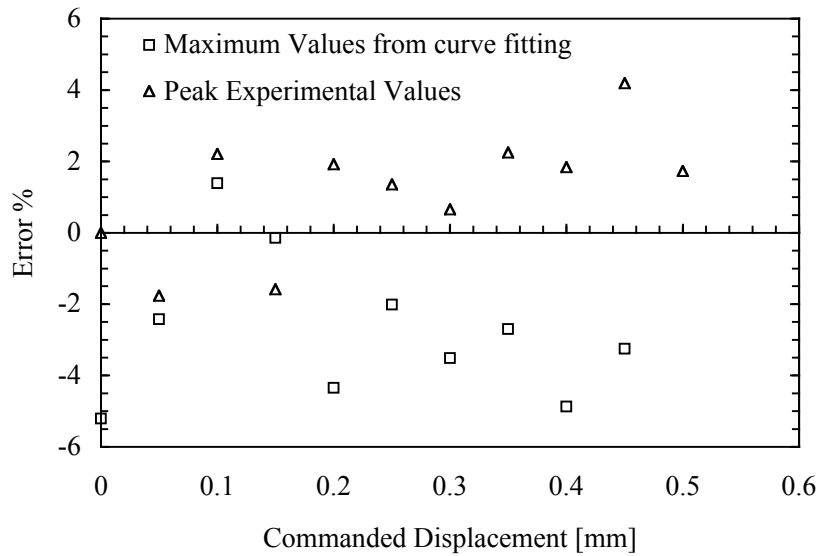


Figure B-16. Error in % measured w_{max} versus commanded displacements for the two cases of peak value from each experiment and the maximum of the fitted curve for the same experiments.

The maximum value of the fitted function was evaluated and considered as the experimental value corresponding to the imposed displacement. Figure B-16 represent the same experiment depicted in Figure B-14 but using the fitted smoothed values.

The maximum imposed displacement was 0.5 mm with steps of .05 mm. Figure B-13 shows the errors in the smoothed values with a maximum displacement of 5 mm with steps of .25 mm. These error values were compared with the peak values of Figure B-16.

The final values to be considered as error bound were obtained as the averages of the errors for the medium size speckle for both maximum displacements of 0.5 and 5 mm, depicted in the Figures B-13 and B-14, with its sign. The one more appropriate for the displacements in the experiments was used in the final results. The error bound is given by the following equation:

$$E_{VIC} = \frac{\sum_{i=1}^N e_{VIC_i}}{N} \quad (\text{B.24})$$

where N is the number of measurements for each experiment equal to the number of steps for the imposed displacements. The following values were obtained:

$E_{VIC} = -2.708 \%$ for a maximum displacement of 0.5 mm and

$E_{VIC} = -3.171 \%$ for a maximum displacement of 5 mm

The uncertainty bound was defined as the average error times two as following:

$$u_{VIC} = 2 * abs(E_{VIC})[mm] \quad (\text{B.25})$$

The membrane surface shape with the uncertainty bound is depicted in Figure B-17 for the commanded maximum displacement of 0.1 mm. The average error bound is less than $\pm .003$ mm.

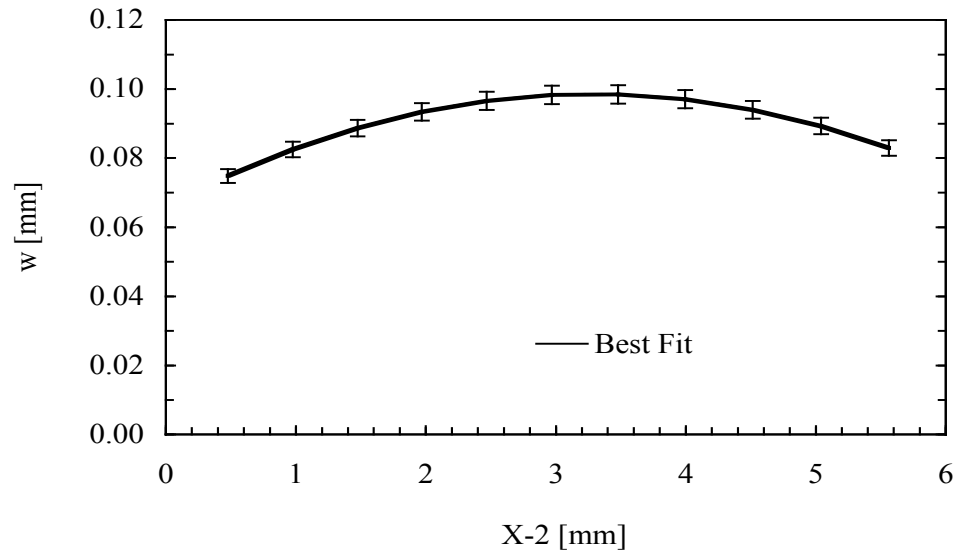


Figure B-17. Best fit of the experimental values of the latex membrane displacements versus X coordinates. The average error bound is less than $\pm .003$ mm.

APPENDIX C AERODYNAMIC AND PROPULSION RESULTS

This appendix presents a systematic list of plots with the main aerodynamic and propulsion experimental data for four different wings and three different aerial vehicles. It is useful to remind that the wings differ only for the structural design, which was chosen to achieve various levels of flexibility. A selected number of wings were mounted on the same vehicle, with the same motor and propeller, thus the only difference between different MAVs was the flexibility of the wing.

The presentation of the results has been organized in sections, with plots at different dynamic pressures and plots at different flexibility, keeping all the other factors constant. In the tests of vehicles, another dependent variable was introduced, the propeller speed via the DC motor setting at pre-determined voltage levels.

A complete description of the differences of the models can be found in the section 3.1.1.1. Table 3-1 and Table 3-2 show the main characteristics of the models in a table form, Figure 3-2 shows schematically the characteristics of the wings' structures. The wings selected for the following plots represent a complete range of flexibilities; table C-1 shows the wings and the vehicles main characteristics with their designation. When the model designation starts with MAV, is referring to a complete vehicle.

Table C-1. Table with summary of wings' characteristics and their designation.

Model	Type	Description	Design.
15001	R	Wing made by Solid Carbon Fiber (Rigid)	Rigid
15007	PR	As 15004 with middle part 60 mm wide	PR07
15009	BR	Thick battens (two plies 0/0), 2.5 mm wide, LE +/- 45	BR09
15012	PR	Rigid thin perimeter, no middle part, LE +/- 45	PR12
MAV15001	R	Vehicle with wing 15001	MAVR
MAV15007	PR	Vehicle with wing 15007	MAVPR07
MAV15009	BR	Vehicle with wing 15009	MAVBR09

C.1 Aerodynamic Results: Wings at Constant Flexibility

The section presents corrected experimental results for constant flexibility. Each plot shows the aerodynamic coefficients of one type of wing, with the distinctive structural design thus flexibility, at four different free stream dynamic pressures (velocities). The graphs can be used to compare how the aerodynamic characteristics of a particular wing design changes with the dynamic pressure, while holding the flexibility constant. Those results will be also used to estimate the aerodynamic derivatives of the wings.

The four plots presented, for each wing, are:

- 1 - C_L versus α at $V_\infty = 8.0, 10.0, 11.5$ and 13.0 m/s
- 2 - C_L versus C_D at $V_\infty = 8.0, 10.0, 11.5$ and 13.0 m/s
- 3 - L/D versus C_L at $V_\infty = 8.0, 10.0, 11.5$ and 13.0 m/s
- 4 - C_m versus C_L at $V_\infty = 8.0, 10.0, 11.5$ and 13.0 m/s

It possible by inspecting the following plots to verify the logic behind the structural design of the different wings; the correlation between the BR wings and geometric twist and between the PR wings and aerodynamic twist is an example.

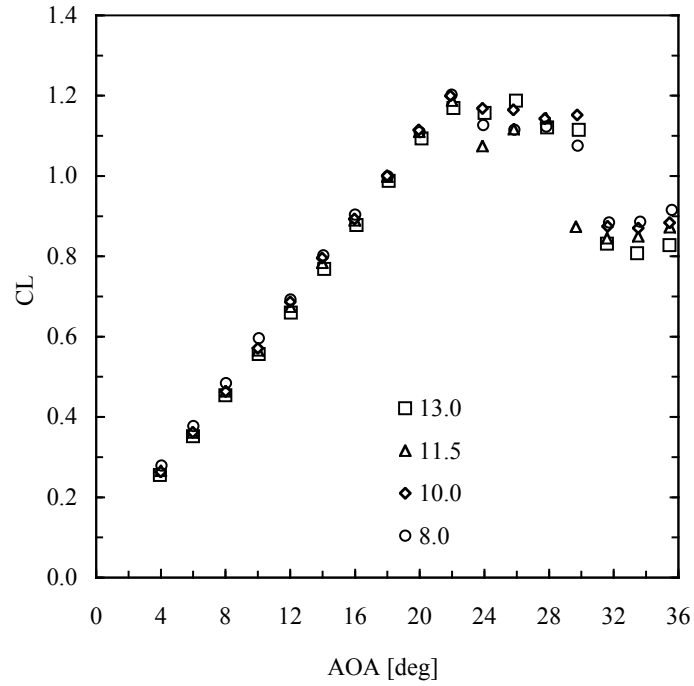


Figure C-1. C_L versus α for R01 (Rigid) wing at $V_\infty = 8, 10, 11.5$ and 13 m/s.

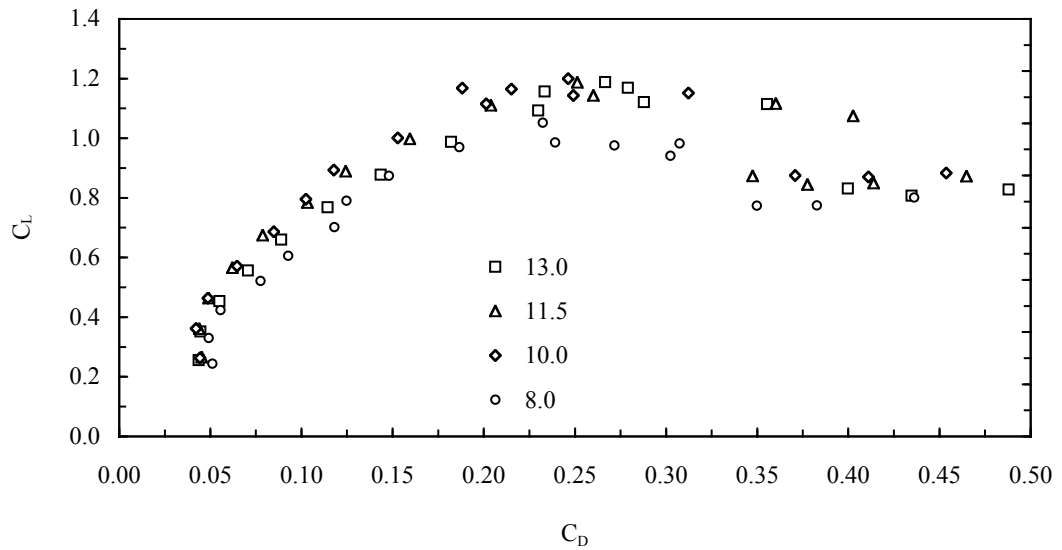


Figure C-2. C_L versus C_D for R01 (Rigid) wing at $V_\infty = 8, 10, 11.5$ and 13 m/s.

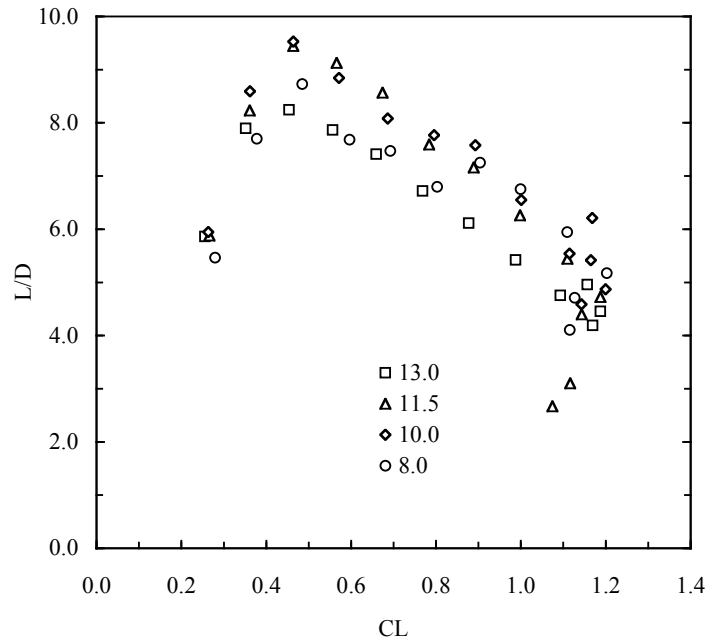


Figure C-3. L/D versus C_L for R01 (Rigid) wing at $V_\infty = 8, 10, 11.5$ and 13 m/s.

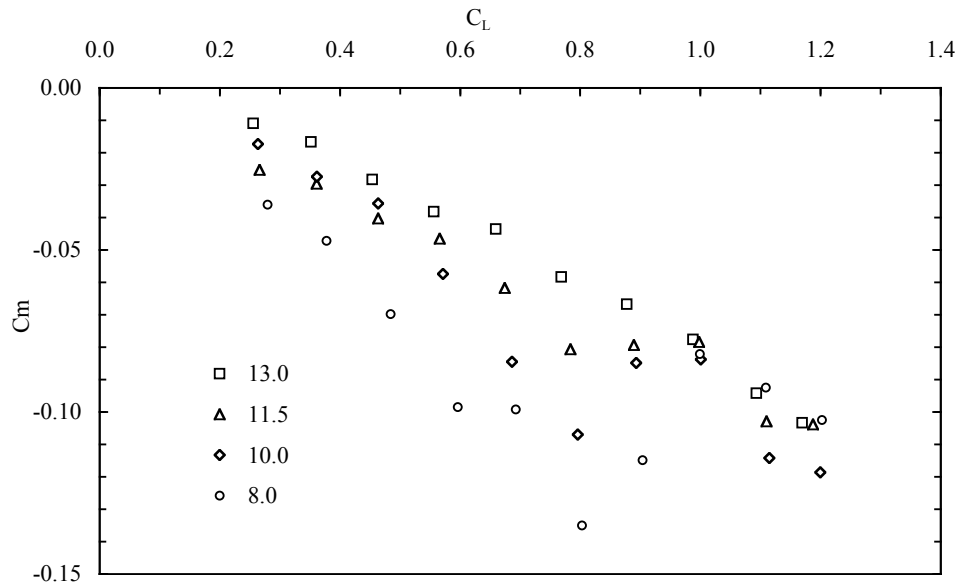


Figure C-4. C_m versus C_L for R01 (Rigid) wing at $V_\infty = 8, 10, 11.5$ and 13 m/s.

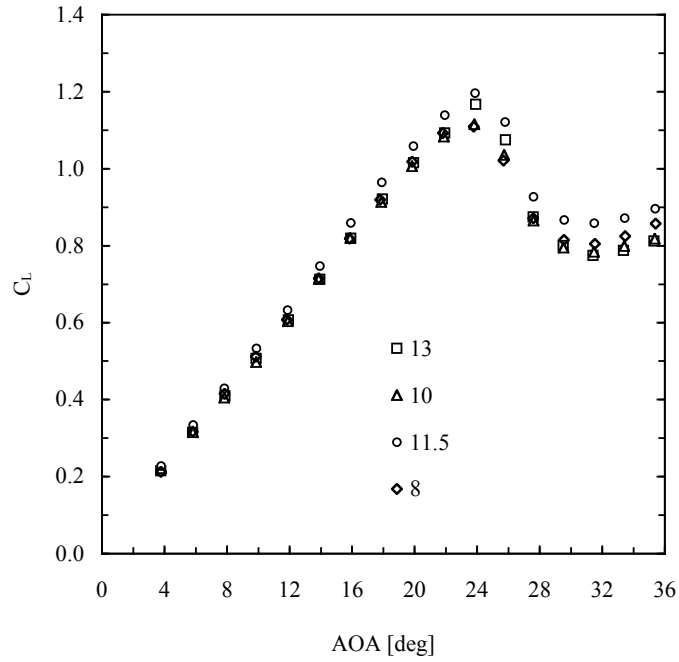


Figure C-5. C_L versus α for wing PR07 at $V_\infty = 8, 10, 11.5$ and 11.5 m/s.

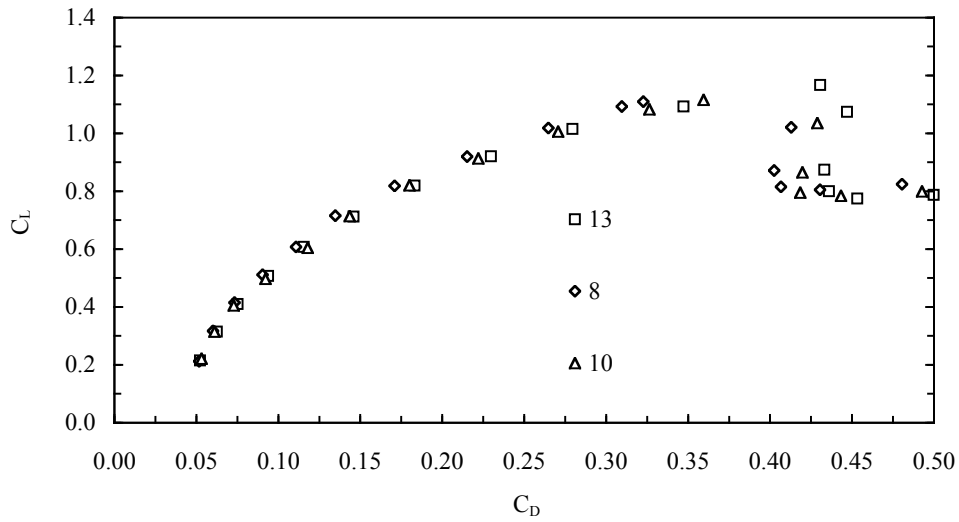


Figure C-6. C_L versus C_D for wing PR07 at $V_\infty = 8, 10, 11.5$ and 11.5 m/s.

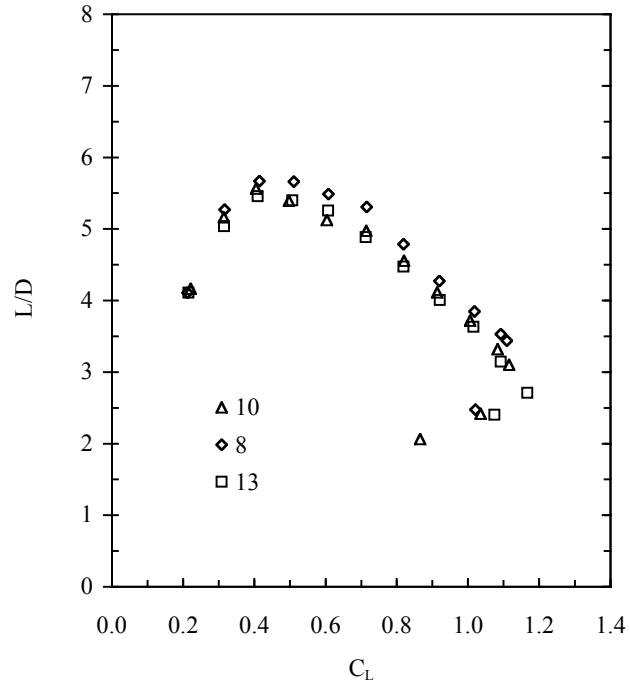


Figure C-7. L/D versus C_L for wing PR07 at $V_\infty = 8, 10, 11.5$ and 11.5 m/s.

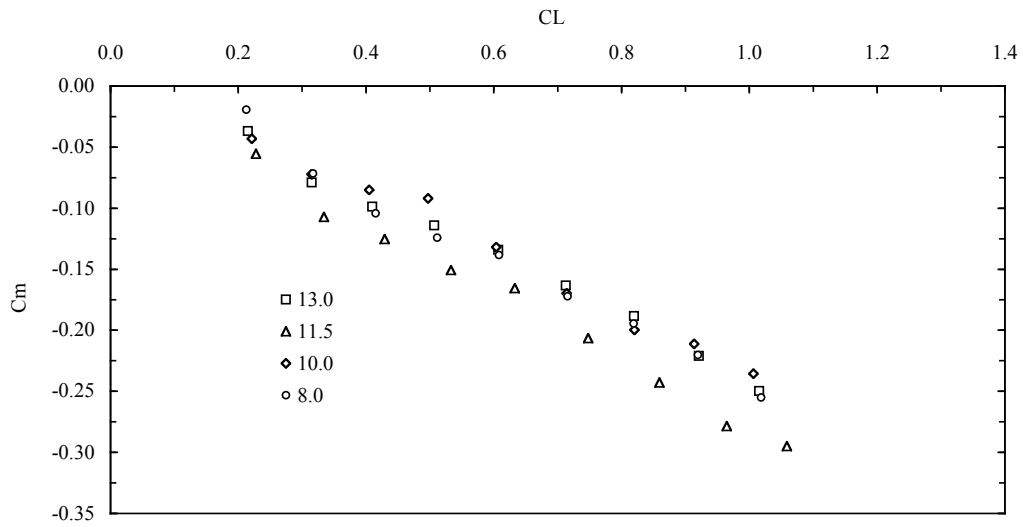


Figure C-8. C_m versus C_L for wing PR07 at $V_\infty = 8, 10, 11.5$ and 11.5 m/s.

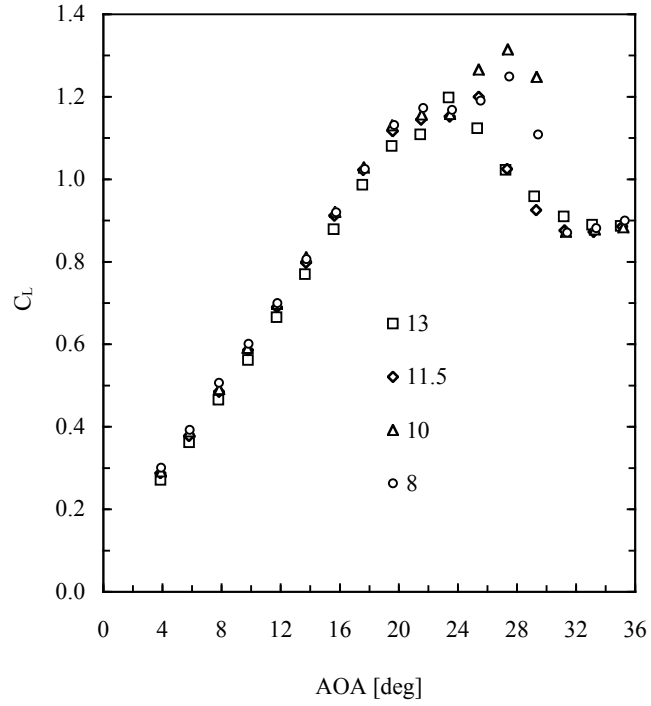


Figure C-9. C_L versus α for wing BR09 at $V_\infty = 8, 10, 11.5$ and 10 m/s.

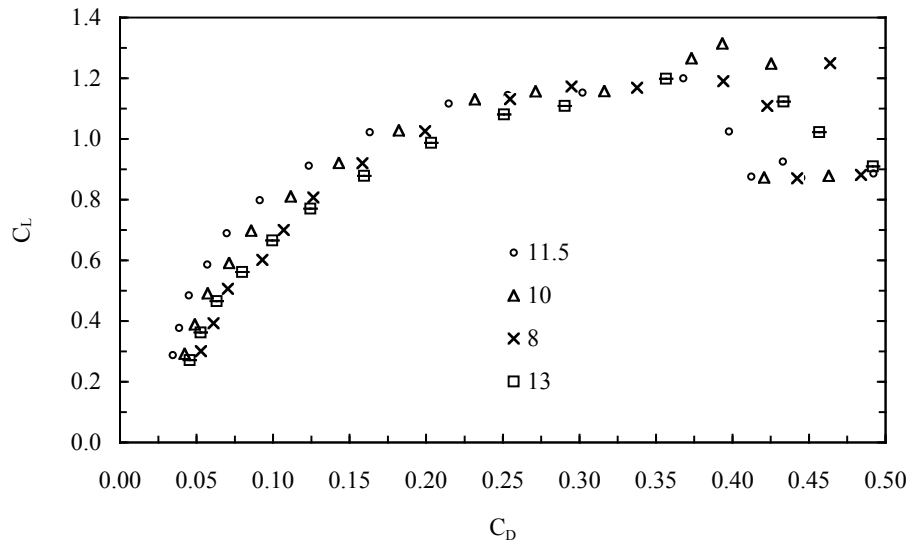


Figure C-10. C_L versus C_D for wing BR09 at $V_\infty = 8, 10, 11.5$ and 10 m/s.

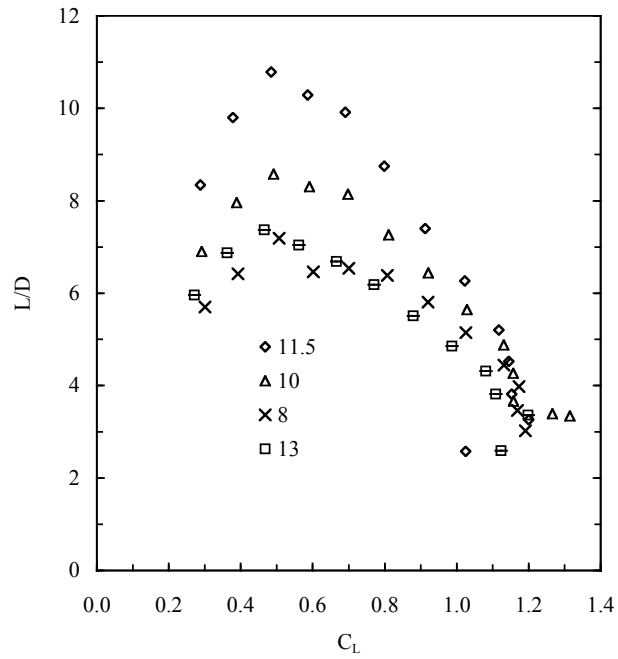


Figure C-11. L/D versus C_L for wing BR09 at $V_\infty = 8, 10, 11.5$ and 10 m/s.

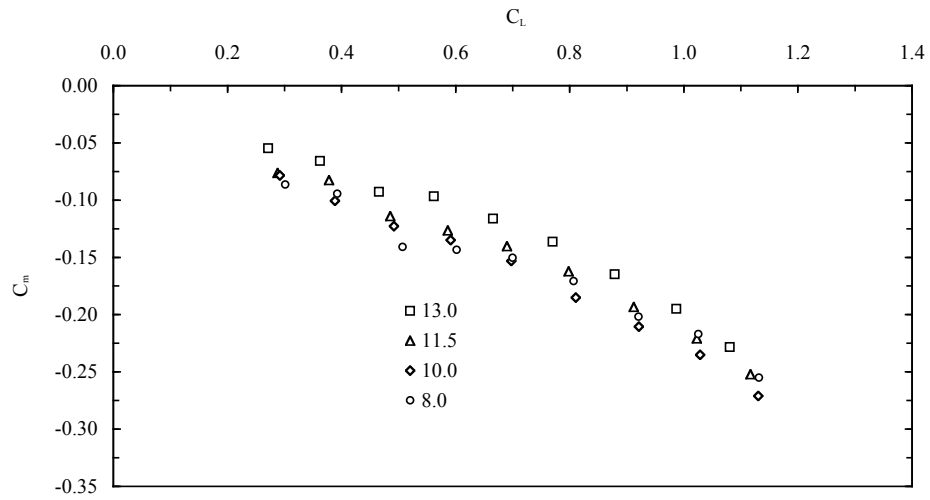


Figure C-12. C_m versus C_L for wing BR09 at $V_\infty = 8, 10, 11.5$ and 10 m/s.

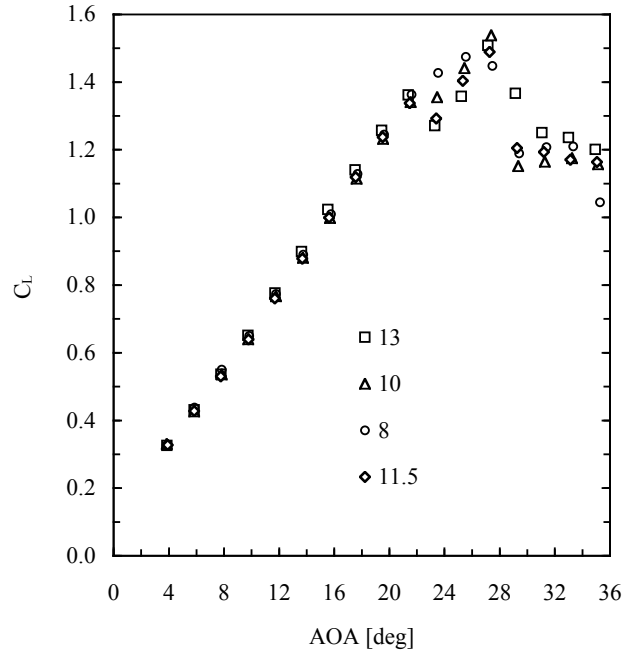


Figure C-13. C_L versus α for wing PR12 at $V_\infty = 8, 10, 11.5$ and 13 m/s.

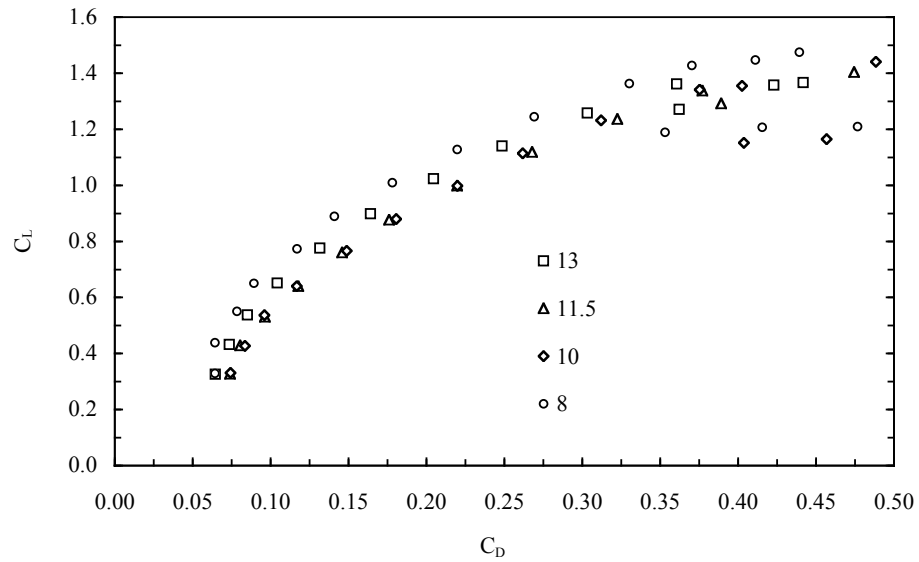


Figure C-14. C_L versus C_D for wing PR12 at $V_\infty = 8, 10, 11.5$ and 13 m/s.

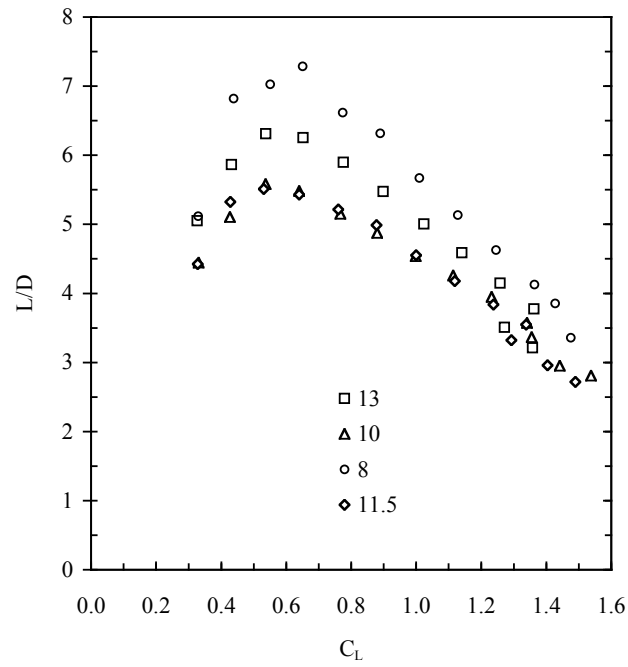


Figure C-15. L/D versus C_L for wing PR12 at $V_\infty = 8, 10, 11.5$ and 10 m/s.

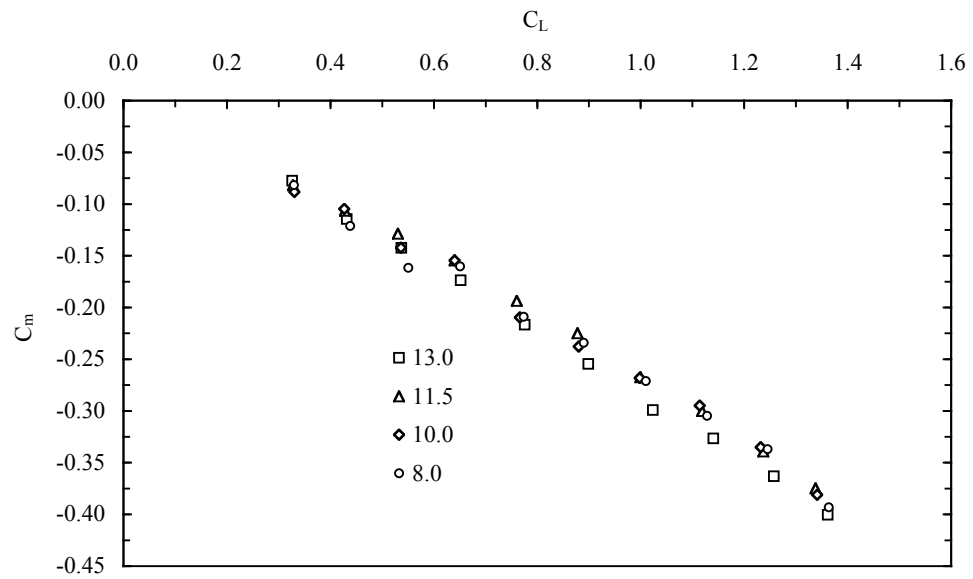


Figure C-16. C_m versus C_L for wing PR12 at $V_\infty = 8, 10, 11.5$ and 10 m/s.

C.2 Aerodynamic Results: Wings at Constant Dynamic Pressure

The section presents corrected experimental results for constant dynamic pressure. Each plot shows the aerodynamic force and moment coefficients of the four different types of wing, with the distinctive structural design thus flexibility, at constant free stream dynamic pressure (velocity). The graphs can be used to compare how the aerodynamic characteristics of the wings change with the flexibility, while holding the dynamic pressure (velocity) constant. Those results will be used also to estimate the aerodynamic derivatives of the wings.

The four plots presented, for each dynamic pressure (velocity), are:

- 1 - C_L versus α for wings Rigid, PR07, BR09 and PR12
- 2 - C_L versus C_D for wings Rigid, PR07, BR09 and PR12
- 3 - L/D versus C_L for wings Rigid, PR07, BR09 and PR12
- 4 - C_m versus C_L for wings Rigid, PR07, BR09 and PR12

Please see Table C-1 for the design characteristics of the wings and their designations and Figure 3-2 for an overall view of the different structural configurations.

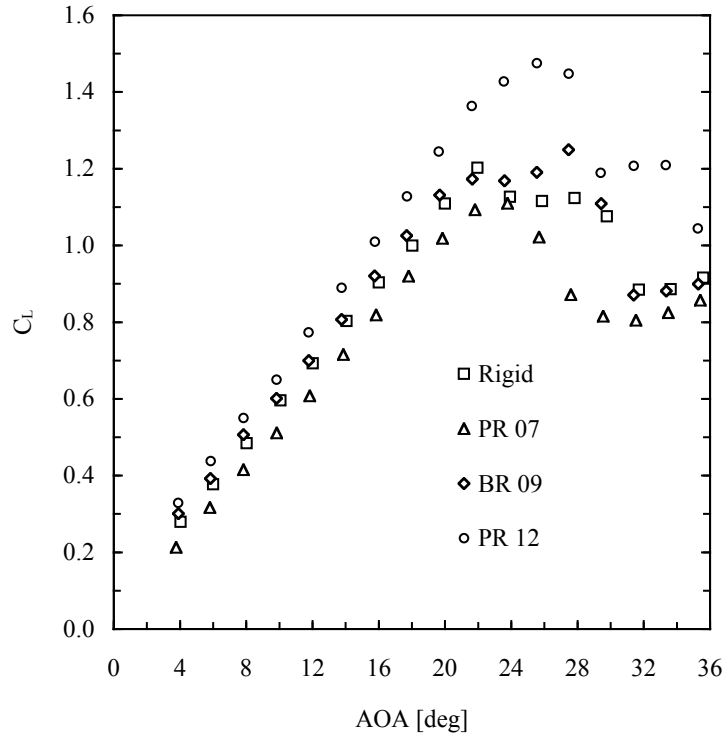


Figure C-17. C_L versus α for wings Rigid (01), PR07, BR09 and PR12 at $V_\infty = 8.0$ m/s.

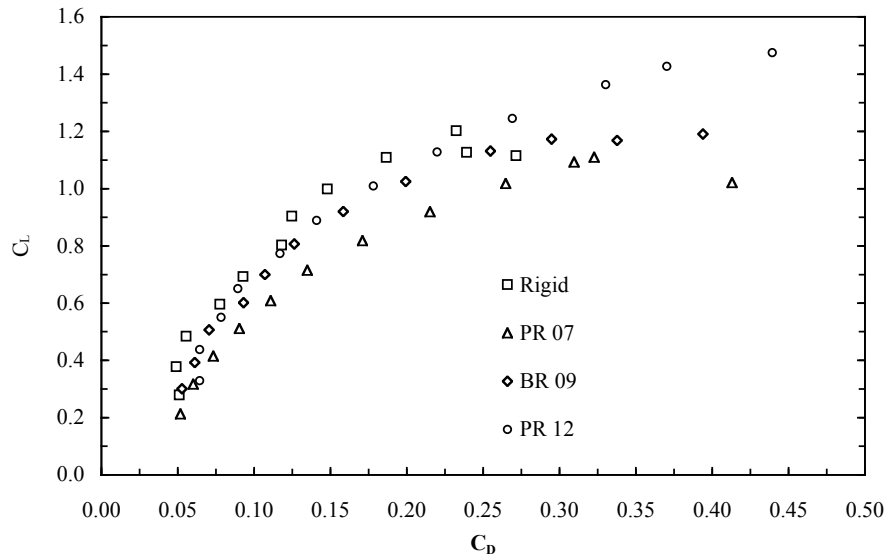


Figure C-18. C_L versus C_D for wings Rigid (01), PR07, BR09 and PR12 at $V_\infty = 8.0$ m/s.

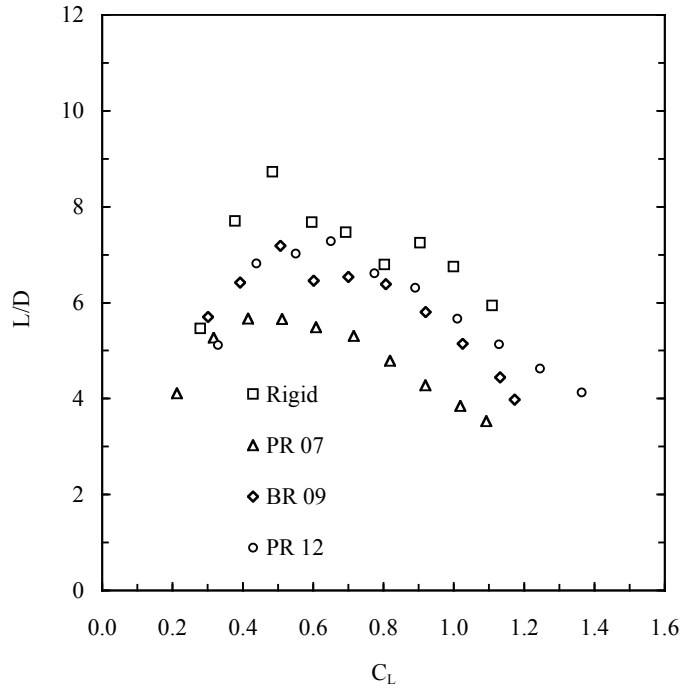


Figure C-19. L/D versus C_L for wings Rigid (01), PR07, BR09 and PR12 at V_∞ = 8.0 m/s.

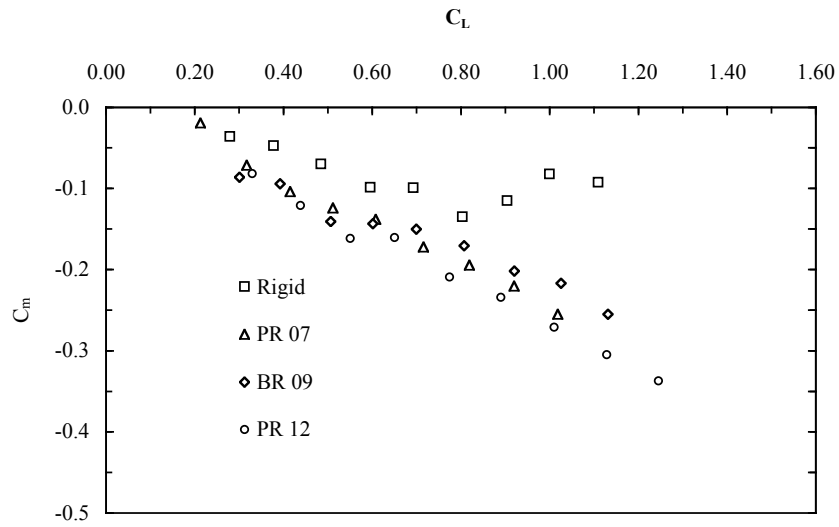


Figure C-20. C_m versus C_L for wings Rigid (01), PR07, BR09 and PR12 at V_∞ = 8.0 m/s.

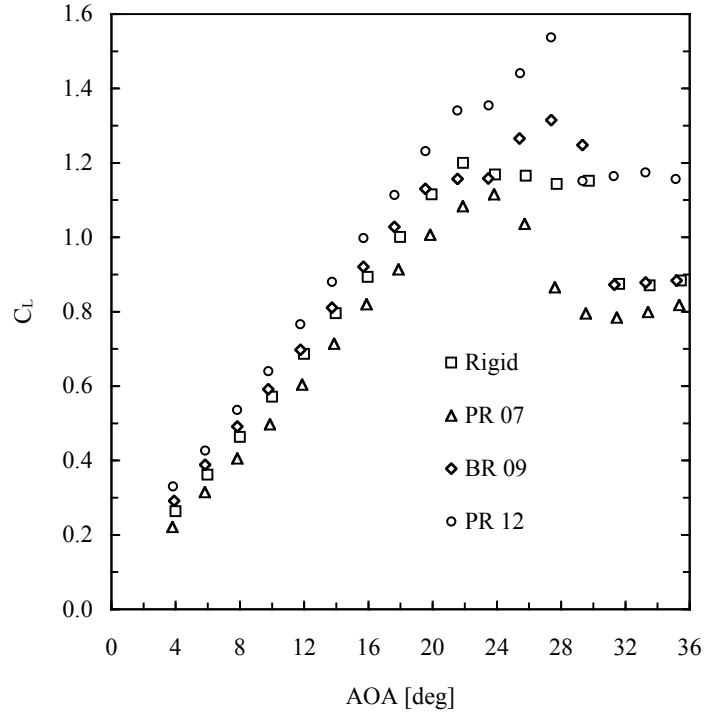


Figure C-21. C_L versus α for wings Rigid (01), PR07, BR09 and PR12 at $V_\infty = 10.0$ m/s.

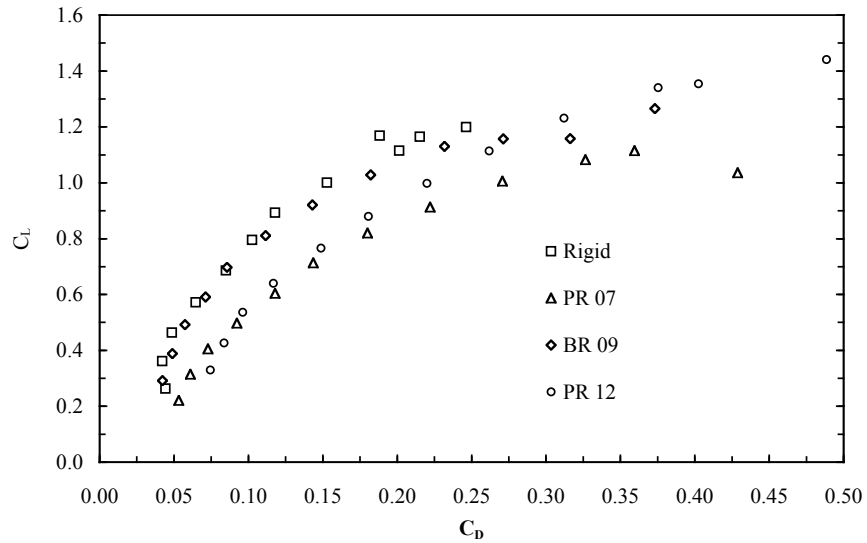


Figure C-22. C_L versus C_D for wings Rigid (01), PR07, BR09 and PR12 at $V_\infty = 10.0$ m/s.

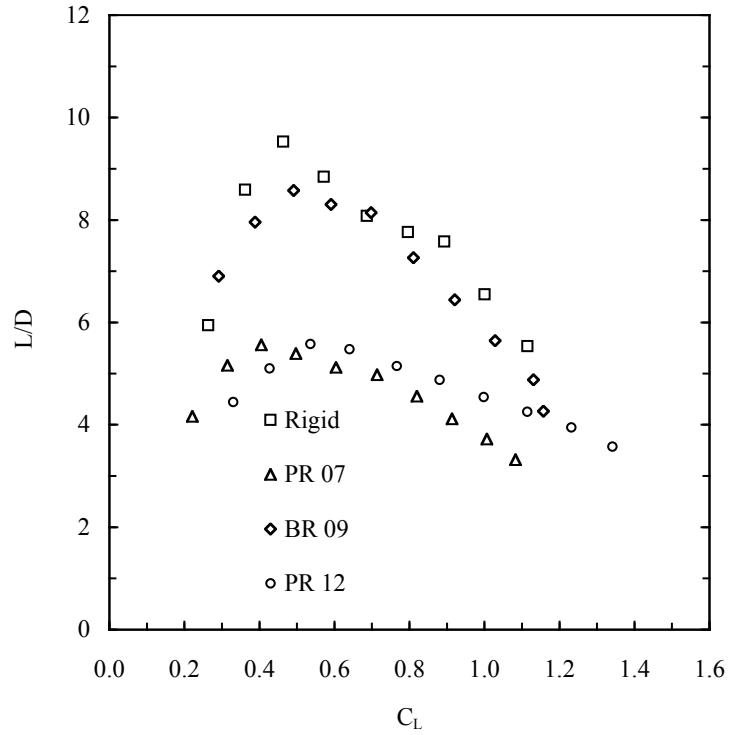


Figure C-23. L/D versus C_L for wings Rigid (01), PR07, BR09 and PR12 at $V_\infty = 10.0$ m/s.

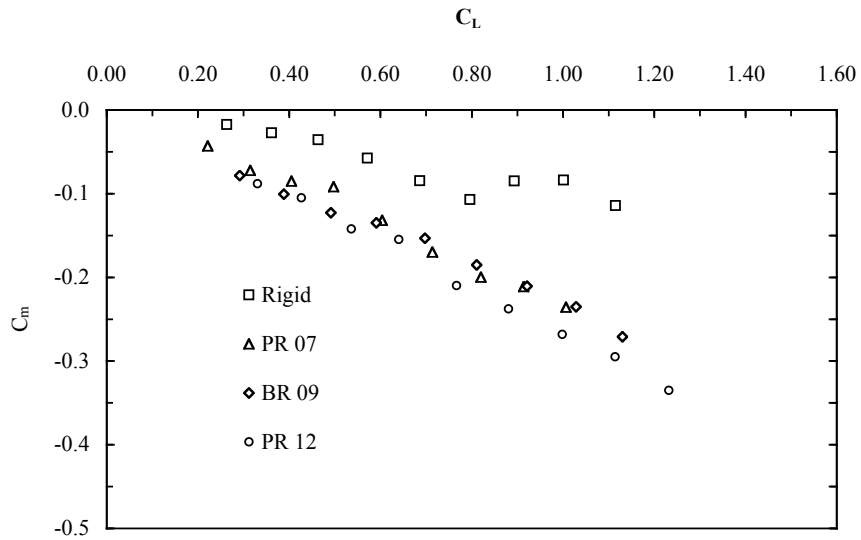


Figure C-24. C_m versus C_L for wings Rigid (01), PR07, BR09 and PR12 at $V_\infty = 10.0$ m/s.

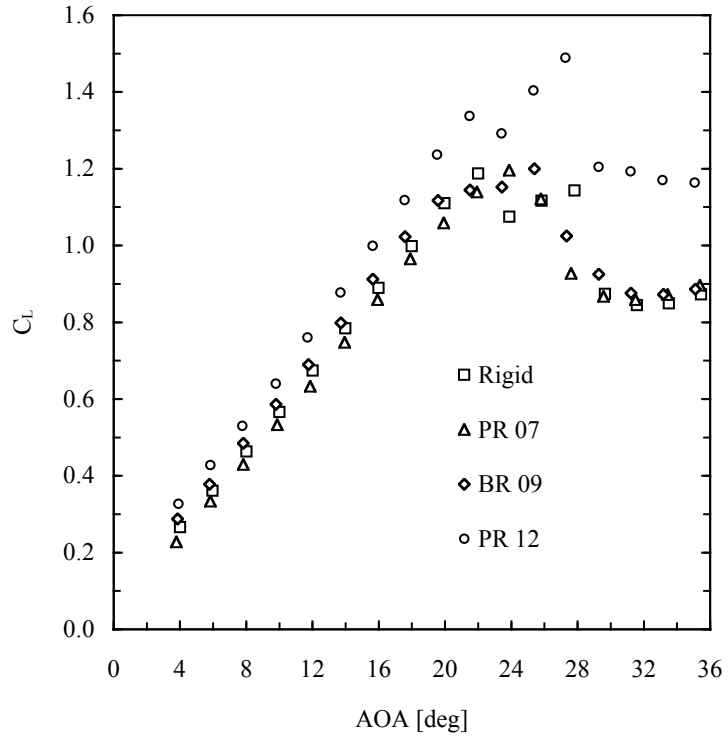


Figure C-25. C_L versus α for wings Rigid (01), PR07, BR09 and PR12 at $V_\infty = 11.5$

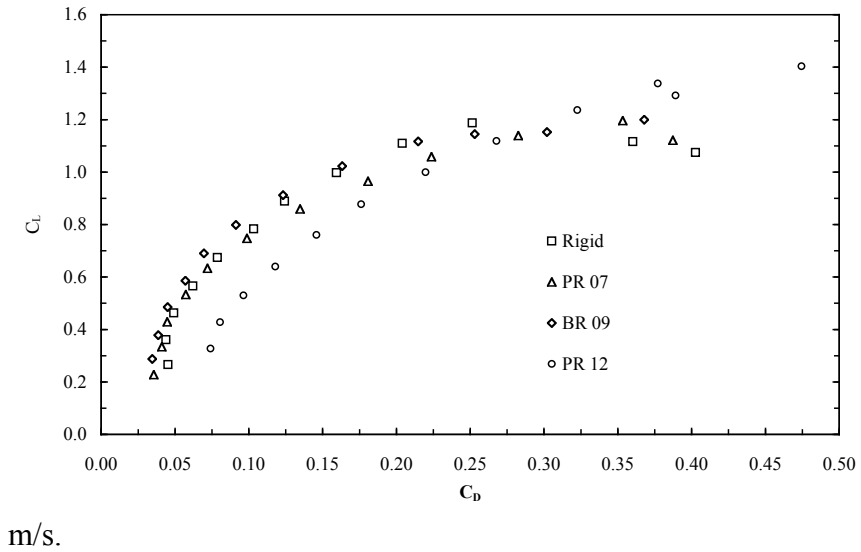


Figure C-26. C_L versus C_D for wings Rigid (01), PR07, BR09 and PR12 at $V_\infty = 11.5$ m/s.

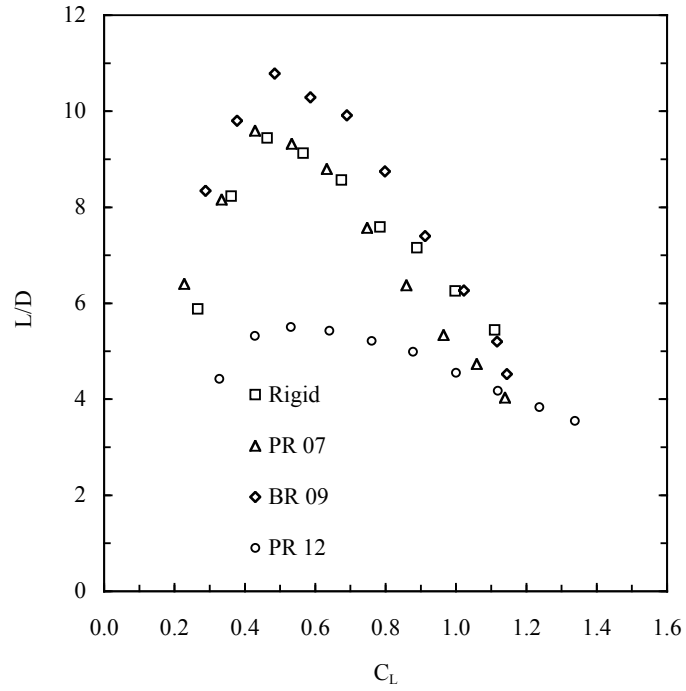


Figure C-27. L/D versus C_L for wings Rigid (01), PR07, BR09 and PR12 at $V_\infty = 11.5$

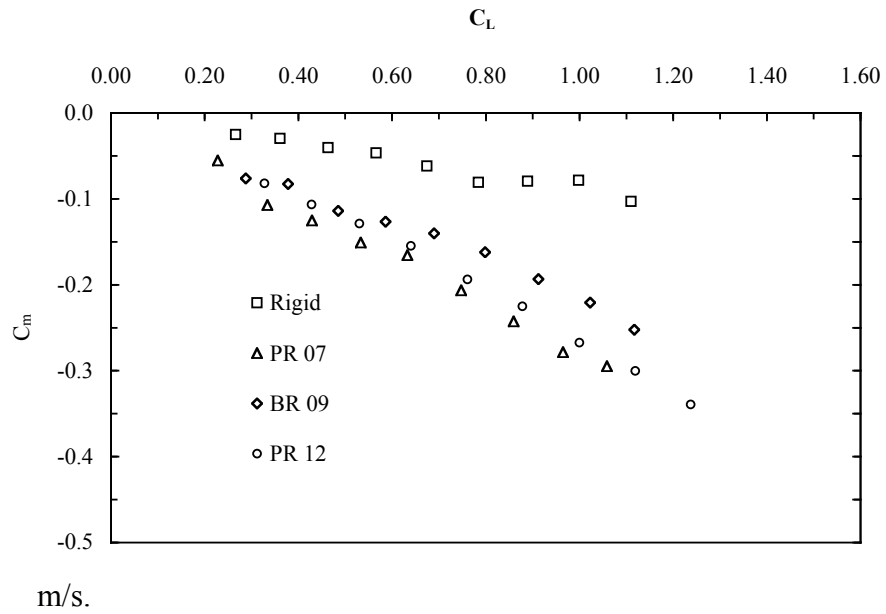


Figure C-28. C_m versus C_L for wings Rigid (01), PR07, BR09 and PR12 at $V_\infty = 11.5$ m/s.

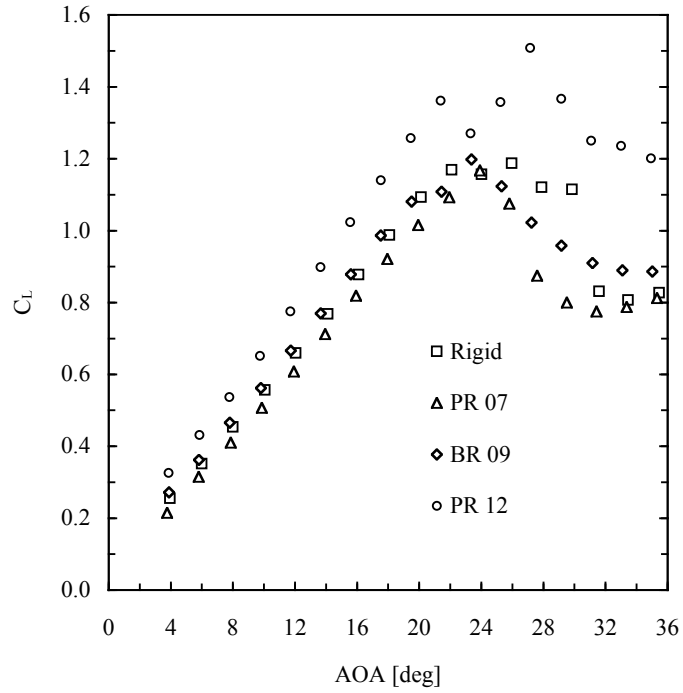


Figure C-29. C_L versus α for wings Rigid (01), PR07, BR09 and PR12 at $V_\infty = 13.0$ m/s.

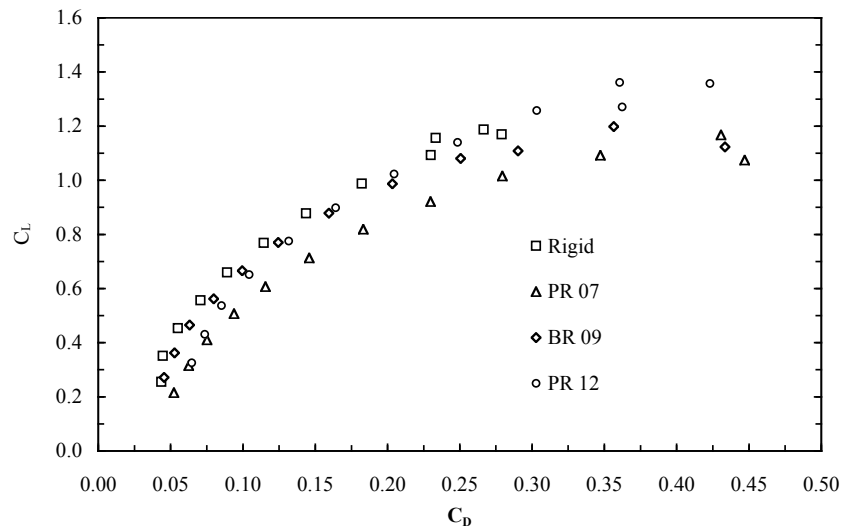


Figure C-30. C_L versus C_D for wings Rigid (01), PR07, BR09 and PR12 at $V_\infty = 13.0$ m/s.

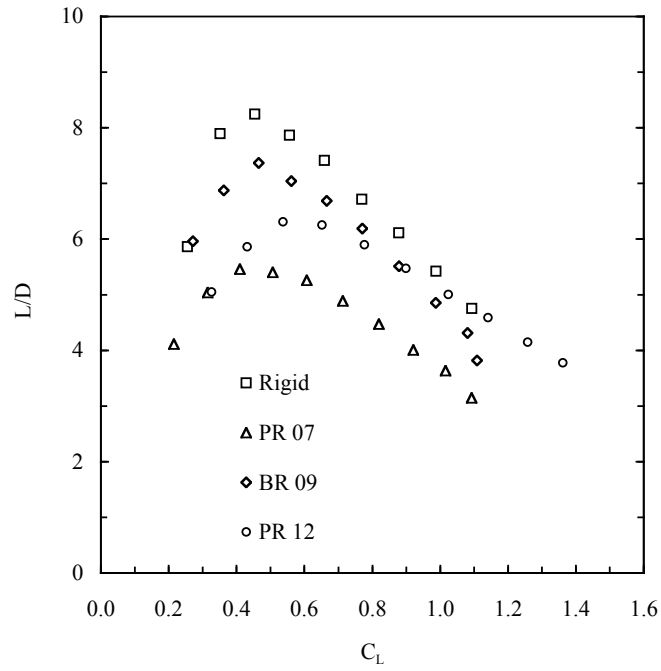


Figure C-31. L/D versus C_L for wings Rigid (01), PR07, BR09 and PR12 at $V_\infty = 13.0$ m/s.

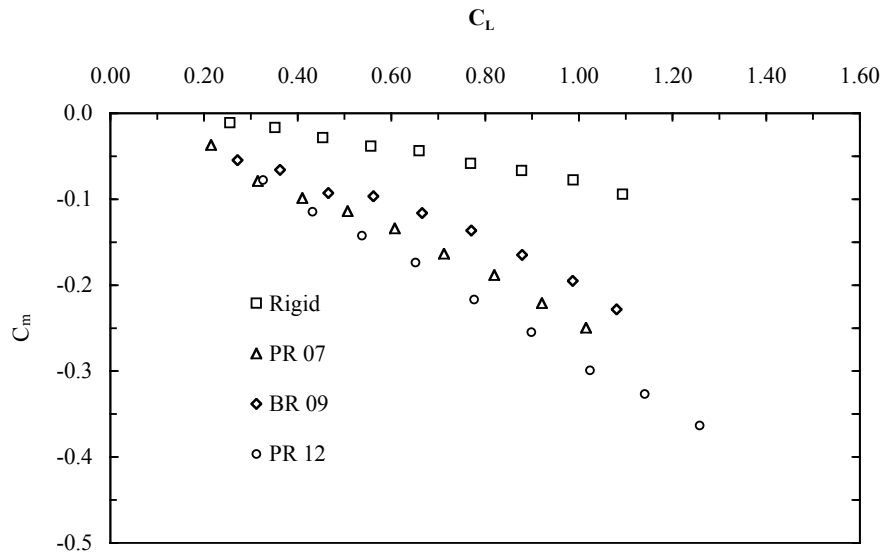


Figure C-32. C_m versus C_L for wings Rigid (01), PR07, BR09 and PR12 at $V_\infty = 13.0$ m/s.

C.3 Propeller Speed

The section presents the experimental measurements of the propeller speed versus the AOA. The data for two types of wing, the PR and BR, are organized in two series of three plots. The first group is plotted at three different values of the free stream velocity at the same power setting. The second group is plotted at three different values of power settings at the same free stream velocity.

Each plot shows the propeller speed versus the corrected AOA of one type of wing with the distinctive structural design thus flexibility. The graphs can be used to compare how the propeller speed changes with the AOA are influenced by the combination of power settings and free stream velocity. The results will be also used to estimate if the flexibility of the wing exert any influence in the propeller speed.

The two groups of three plots presented, for the Rigid wing, are:

1 - propeller speed versus α at $V_\infty = 10, 11.5$ and 13 m/s for $E = 7.4$ Volt

2 - propeller speed versus v at $V_\infty = 10, 11.5$ and 13 m/s for $E = 7.0$ Volt

3 - propeller speed versus v at $V_\infty = 11.5$ and 13 m/s for $E = 6.6$ Volt

4 - propeller speed versus α at $E = 6.6, 7.0$ and 7.4 Volt for $V_\infty = 13.0$ m/s

5 - propeller speed versus α at $E = 6.6, 7.0$ and 7.4 Volt for $V_\infty = 11.5$ m/s

6 - propeller speed versus α at $E = 7.0$ and 7.4 Volt for $V_\infty = 10.0$ m/s

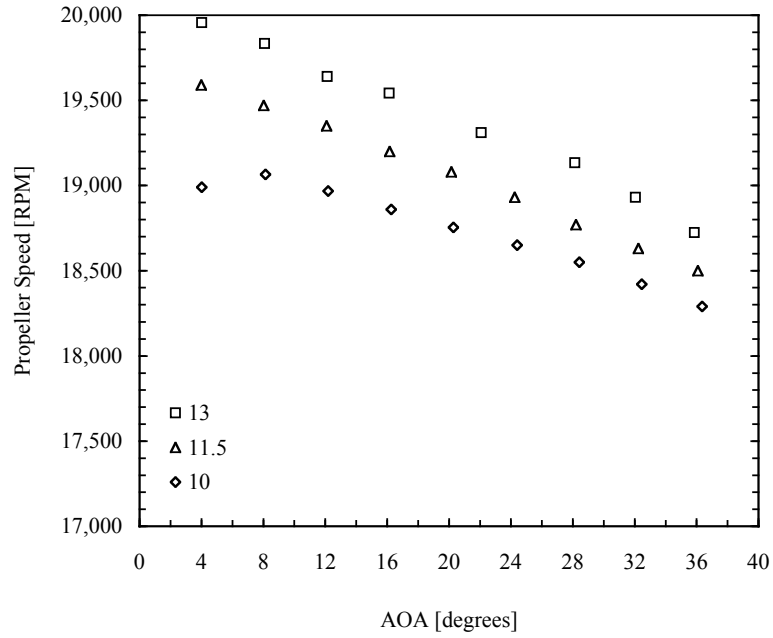


Figure C-33. Propeller speed versus AOA, at three free stream velocities, for a motor's power setting of 7.4 Volt. The wing used on the MAV is the Rigid type.

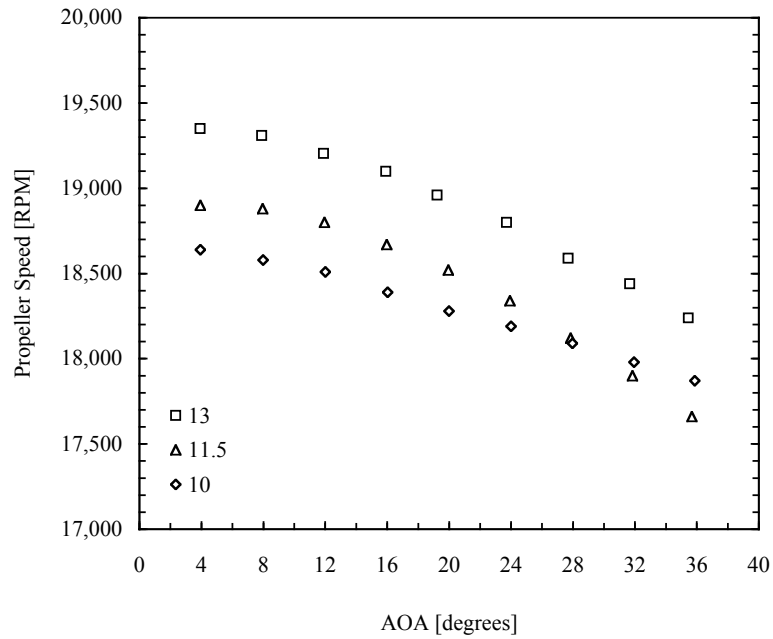


Figure C-34. Propeller speed versus AOA, at three free stream velocities, for a motor's power setting of 7.0 Volt. The wing used on the MAV is the Rigid type.

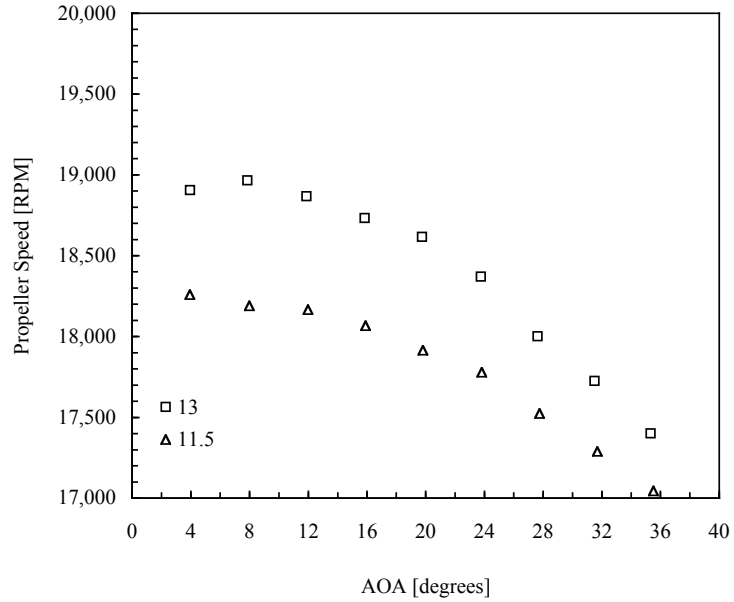


Figure C-35. Propeller speed versus AOA, at two free stream velocities, for a motor's power setting of 6.6 Volt. The wing used on the MAV is the Rigid type.

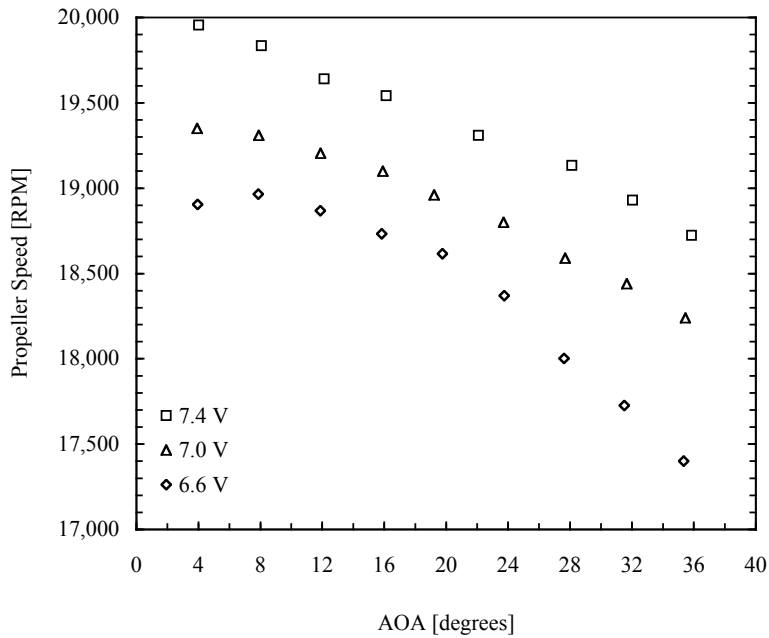


Figure C-36. Propeller speed versus AOA, for three motor's power settings, at a free stream velocity of 13.0 m/s. The wing used on the MAV is the Rigid type.

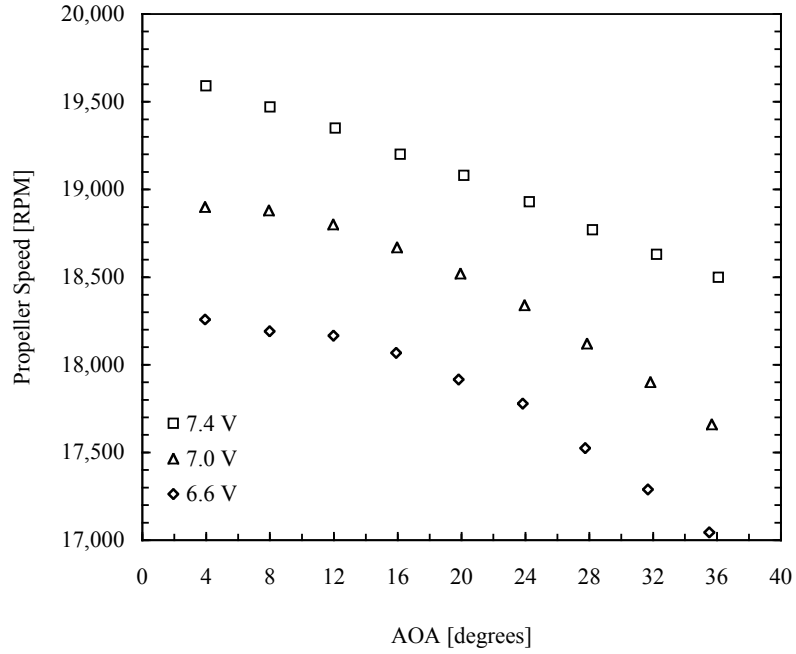


Figure C-37. Propeller speed versus AOA, for two motor’s power settings, at a free stream velocity of 11.5 m/s. The wing used on the MAV is the Rigid type.

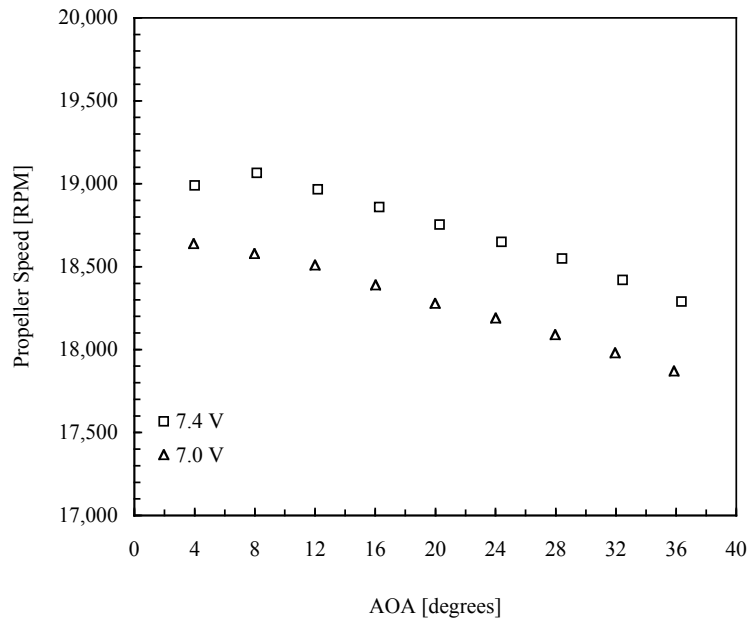


Figure C-38. Propeller speed versus AOA, for two motor’s power settings, at a free stream velocity of 10.0 m/s. The wing used on the MAV is the Rigid type.

The two groups of plots presented, for the wing type BR09, are:

- 1 - propeller speed versus v at $V_\infty = 8, 10, 11.5$ and 13 m/s for $E = 7.4$ Volt
- 2 - propeller speed versus α at $V_\infty = 8, 10, 11.5$ and 13 m/s for $E = 7.0$ Volt
- 3 - propeller speed versus α at $V_\infty = 8, 10$ and 11.5 m/s for $E = 6.6$ Volt
- 4 - propeller speed versus α at $E = 6.6, 7.0$ and 7.4 Volt for $V_\infty = 13.0$ m/s
- 5 - propeller speed versus α at $E = 6.6, 7.0$ and 7.4 Volt for $V_\infty = 11.5$ m/s
- 6 - propeller speed versus α at $E = 7.0$ and 7.4 Volt for $V_\infty = 10.0$ m/s

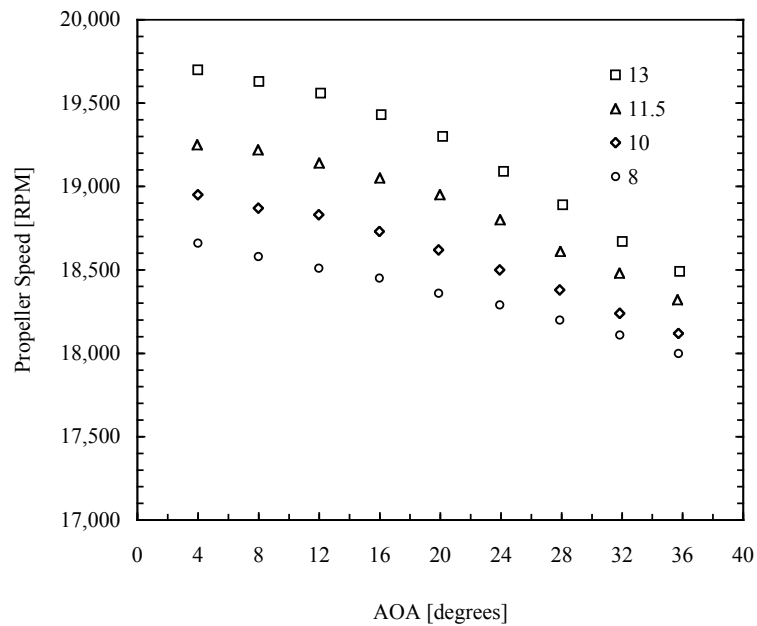


Figure C-39. Propeller speed versus AOA, at four free stream velocities, for a motor's power setting of 7.4 Volt. The wing used on the MAV is the BR09 type.

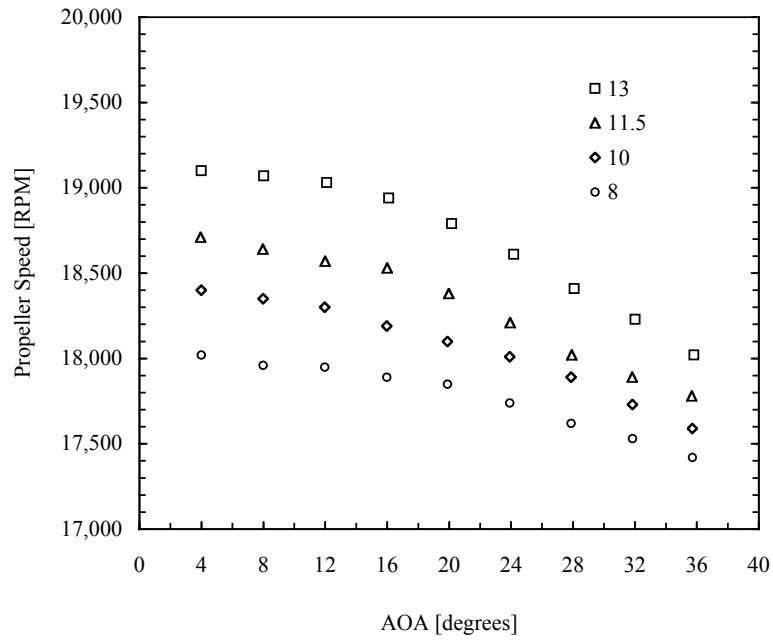


Figure C-40. Propeller speed versus AOA, at four free stream velocities, for a motor's power setting of 7.0 Volt. The wing used on the MAV is the BR09 type.

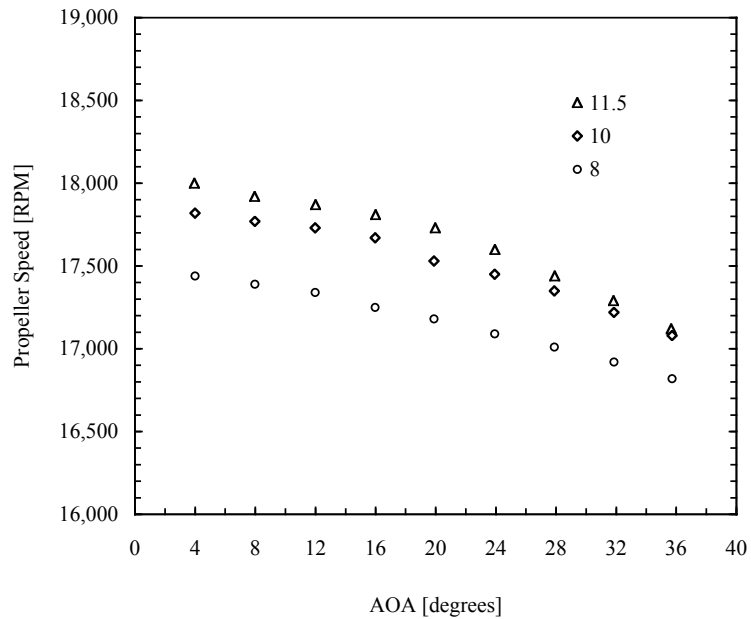


Figure C-41. Propeller speed versus AOA, at three free stream velocities, for a motor's power setting of 6.6 Volt. The wing used on the MAV is the BR09 type.

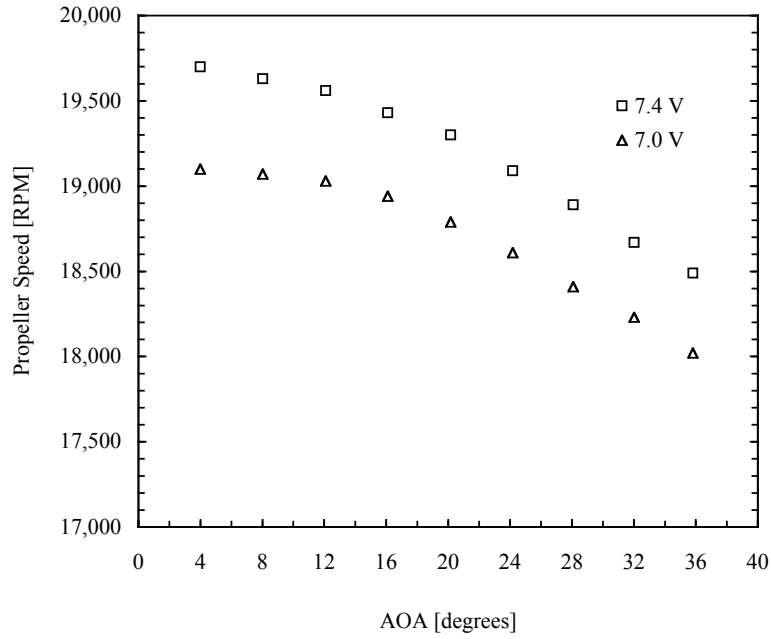


Figure C-42. Propeller speed versus AOA, for two motor's power settings, at a free stream velocity of 13 m/s. The wing used on the MAV is the BR09 type.

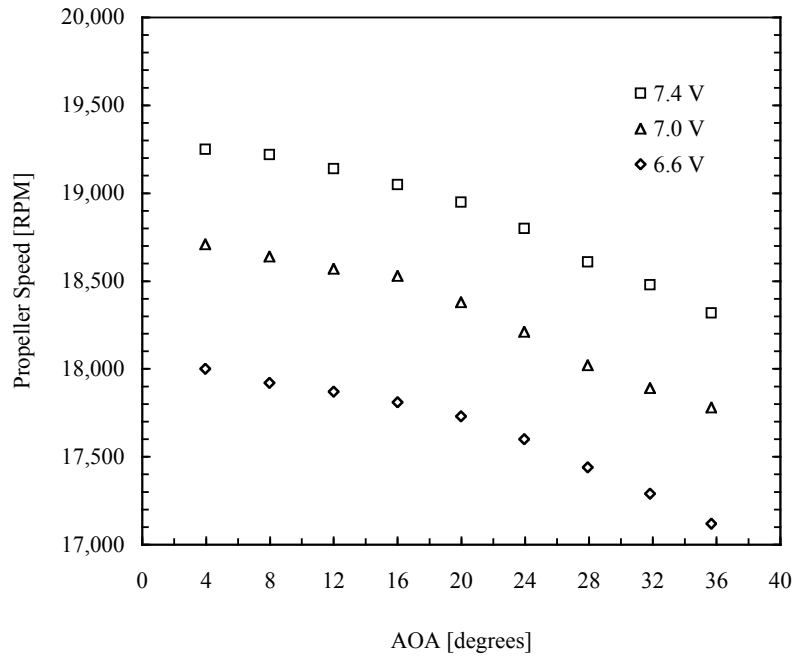


Figure C-43. Propeller speed versus AOA, for three motor's power settings, at a free stream velocity of 11.5 m/s. The wing used on the MAV is the BR09 type.

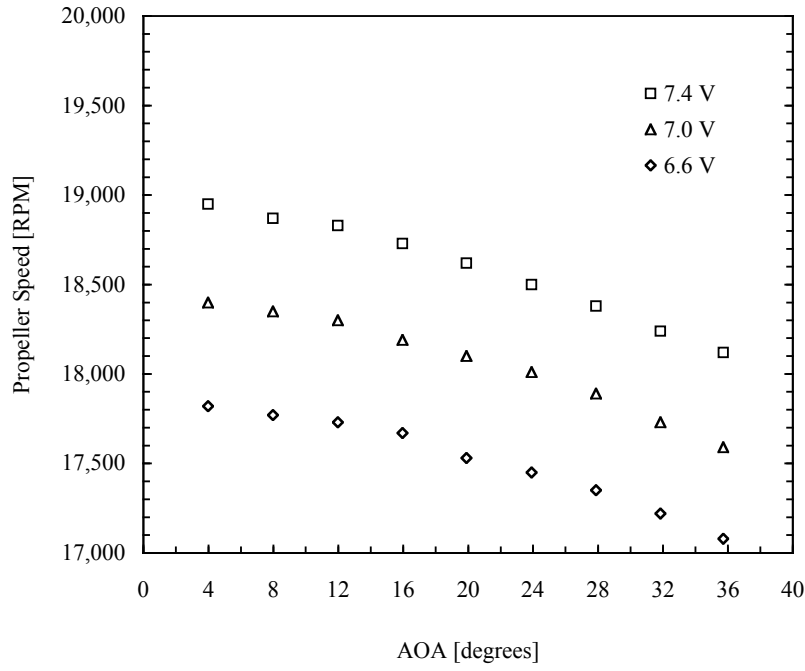


Figure C-44. Propeller speed versus AOA, for three motor’s power settings, at a free stream velocity of 10 m/s. The wing used on the MAV is the BR09 type.

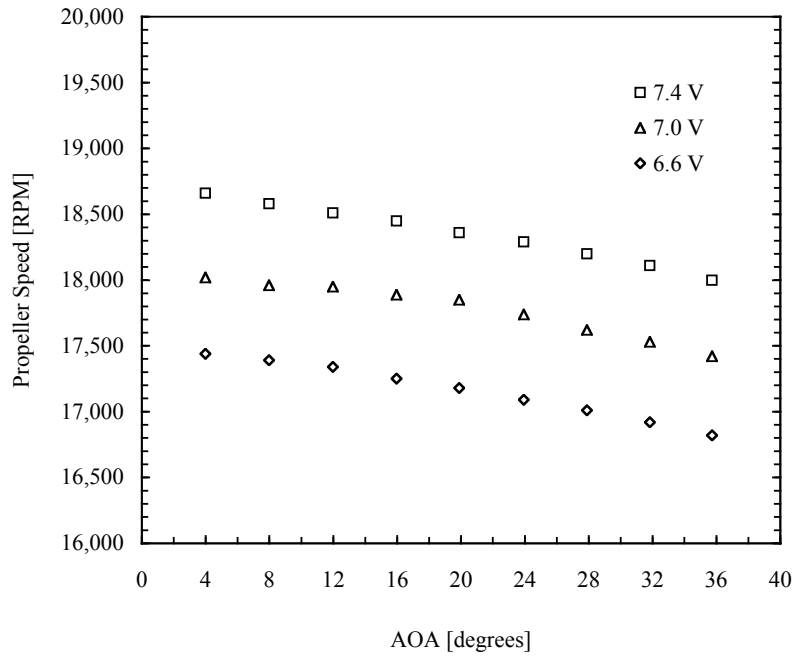


Figure C-45. Propeller speed versus AOA, for three motor’s power settings, at a free stream velocity of 8 m/s. The wing used on the MAV is the BR09 type.

C.4 MAV without Propeller

An interesting insight of the characteristics of a complete MAV is offered from tests with a selected number of the wings, subject of the aforementioned tests, mounted on a standard fuselage and vertical stabilizer (the MAV design is a horizontal tailless design). Three wings were selected for those tests; one is the rigid wing, which was selected as the standard reference to test flexible wings. The flexible wings selected are the BR09 and PR07 for their relevance for the use on flying vehicles. All MAVs were tested at the four standard wind tunnel free stream velocity of 8, 10, 11.5 and 13 m/s.

The section presents corrected experimental results for constant dynamic pressure. Each plot shows the aerodynamic force and moment coefficients of the same wing with and without fuselage and vertical stabilizer, at constant free stream dynamic pressure (velocity). The graphs can be used to compare how the aerodynamic characteristics of the vehicles change while holding the dynamic pressure (velocity) constant. Those results will be used also to estimate the effects of adding the fuselage to the basic wings. The cross-correlation of the results with different wings structure can give more information on the effects of the flexible structure-fuselage flow interactions. Particular attention will be devoted to the changes in the longitudinal moment characteristics.

The four plots presented, selected as a sample, are the results for the three different wings mounted on the same fuselage and with the same vertical stabilizer, obtained at a free stream velocity of 13 m/s, are:

1 - C_L versus α for wings only and wings with fuselage and vertical stab, for Rigid, PR07 and BR09 wings

2 - C_L versus C_D for wings only and wings with fuselage and vertical stab, for Rigid, PR07 and BR09 wings

3 - L/D versus C_L for wings only and wings with fuselage and vertical stab, for Rigid, PR07 and BR09 wings

4 - C_m versus C_L for wings only and wings with fuselage and vertical stab, for Rigid, PR07 and BR09 wings

Please see Table C-1 for the design characteristics of the wings and their designations

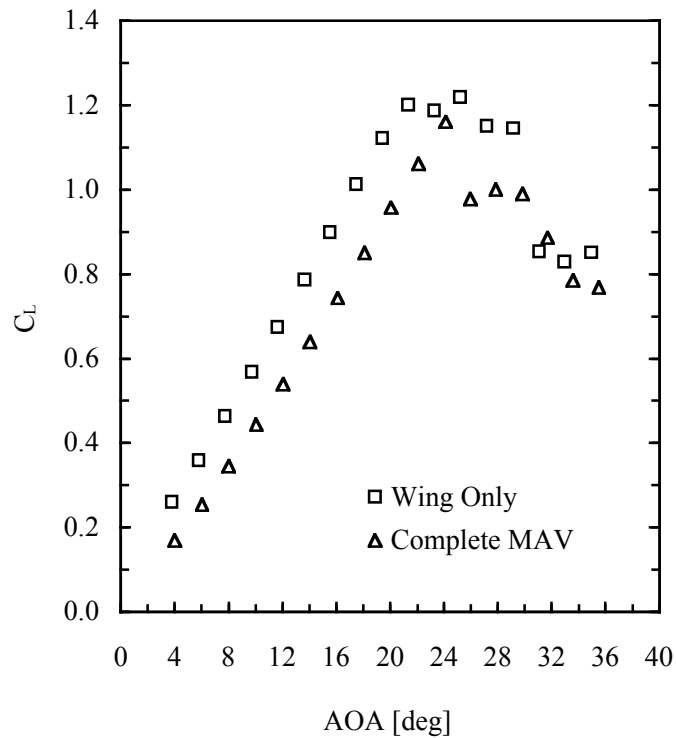


Figure C-46. C_L versus α for Rigid wing and MAVR at $V_\infty = 13$ m/s.

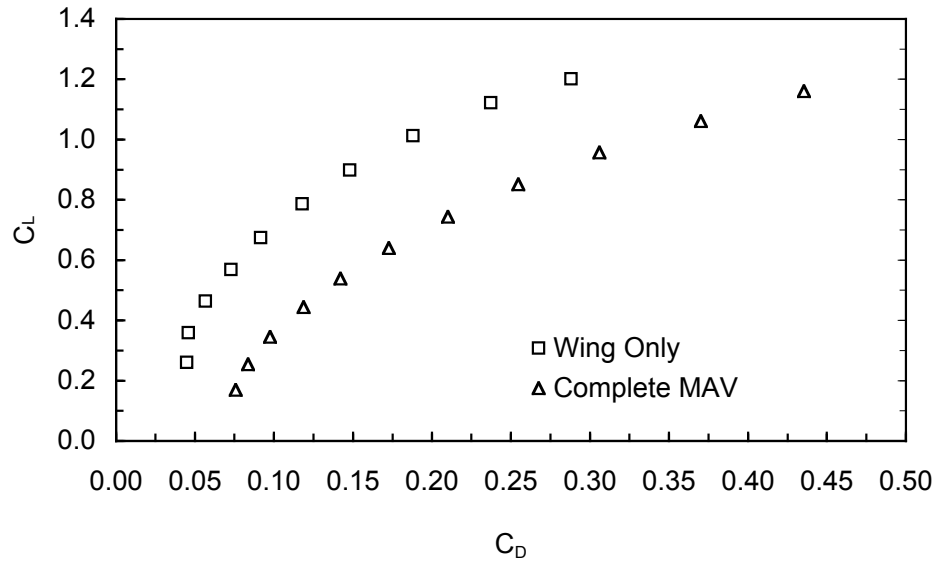


Figure C-47. C_L versus C_D for Rigid wing and MAVR at $V_\infty = 13$ m/s.

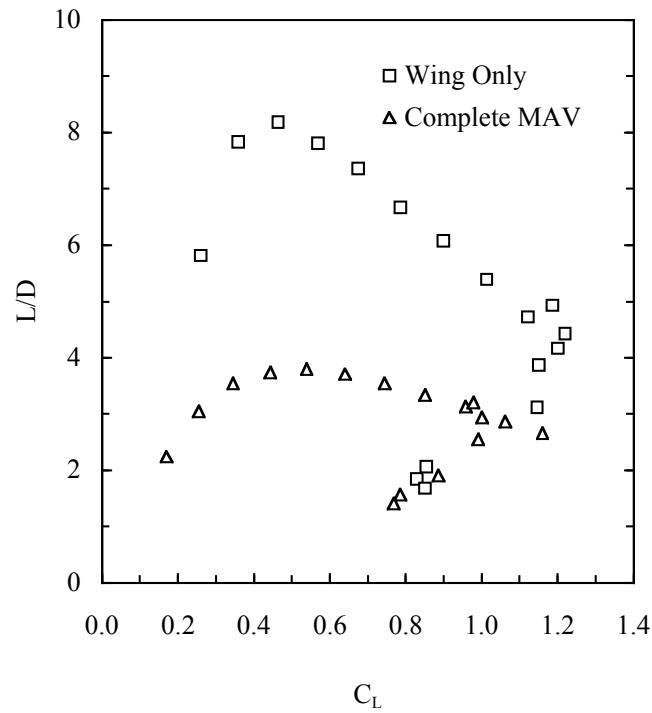


Figure C-48. L/D versus C_L for Rigid wing and MAVR at $V_\infty = 13$ m/s.

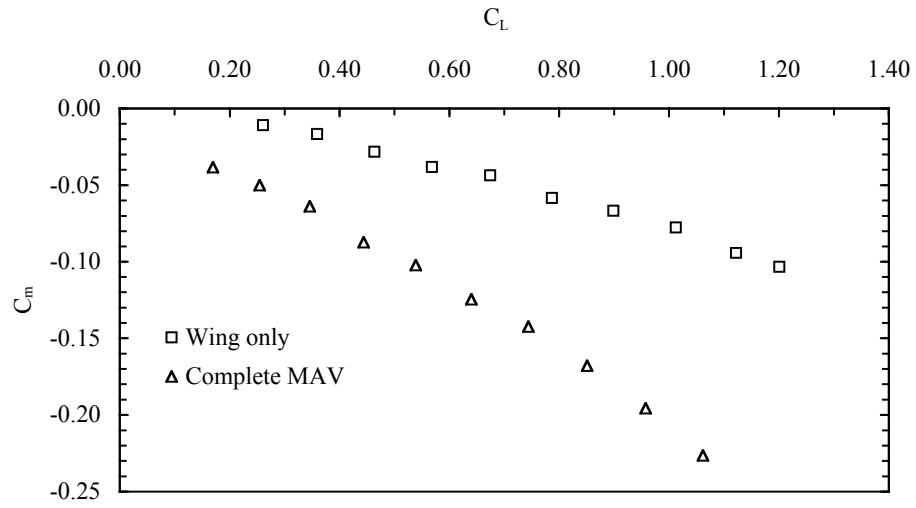


Figure C-49. C_m versus C_L for Rigid wing and MAVR at $V_\infty = 13$ m/s.

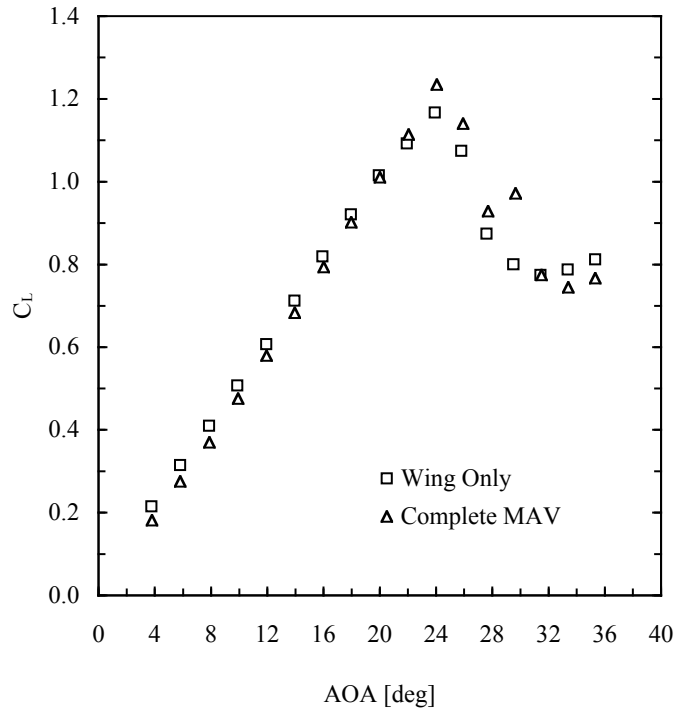


Figure C-50. C_L versus α for PR07 wing and MAVPR07 at $V_\infty = 13$ m/s.

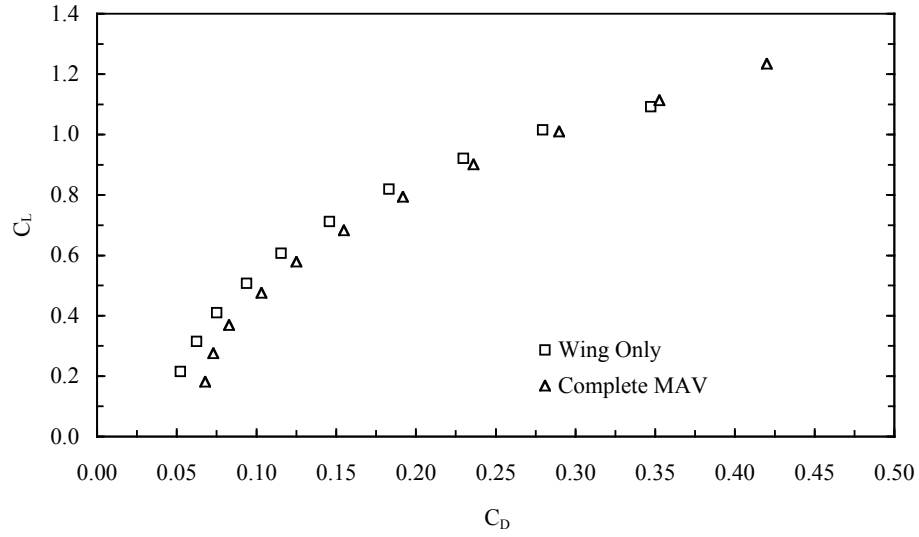


Figure C-51. C_L versus C_D for PR07 wing and MAVPR07 at $V_\infty = 13$ m/s.

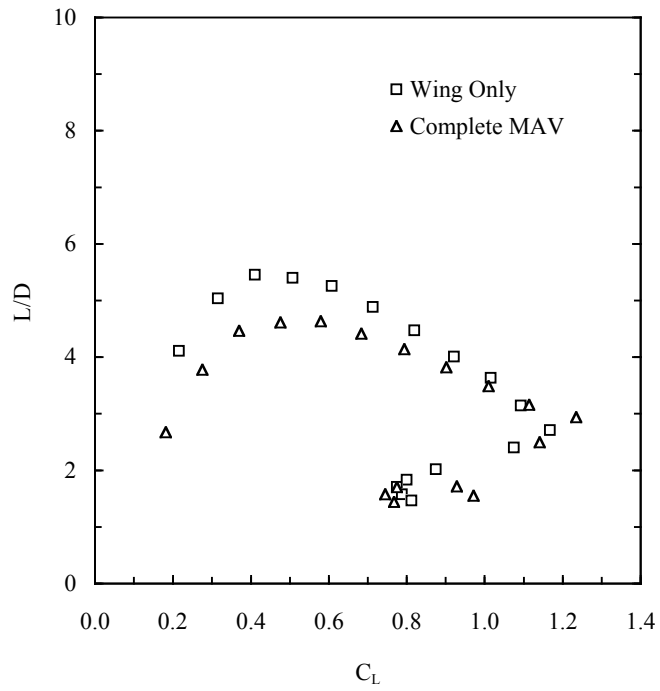


Figure C-52. L/D versus C_L for PR07 wing and MAVPR07 at $V_\infty = 13$ m/s.

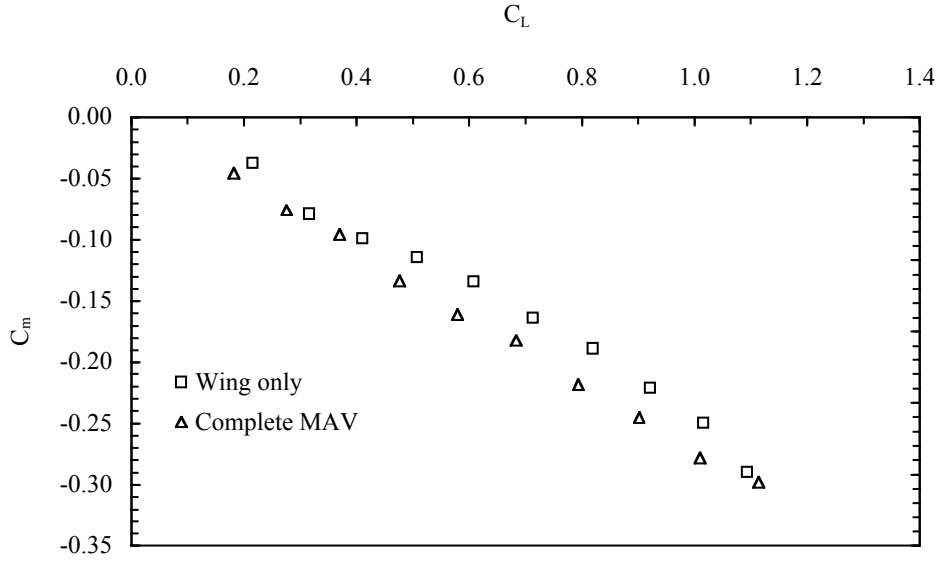


Figure C-53. C_m versus C_L for PR07 wing and MAVPR07 at $V_\infty = 13$ m/s.

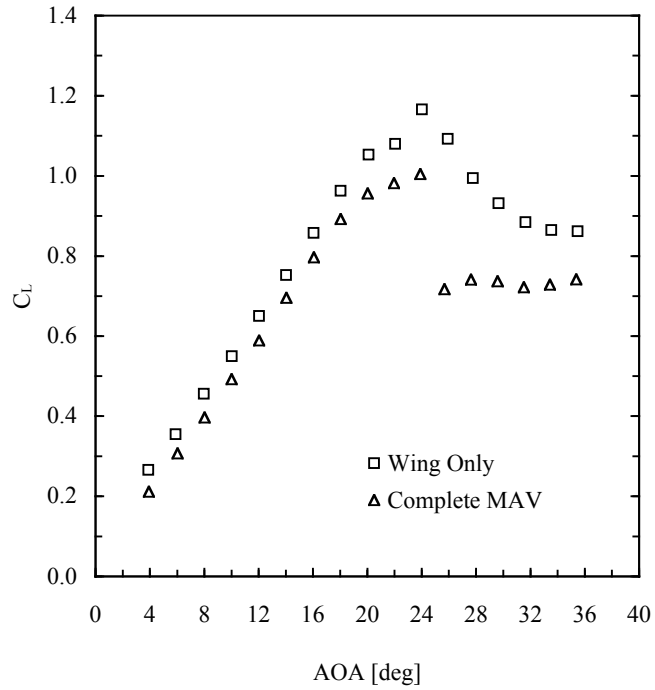


Figure C-54. C_L versus AOA for BR09 wing and MAVBR09 at $V_\infty = 13$ m/s.

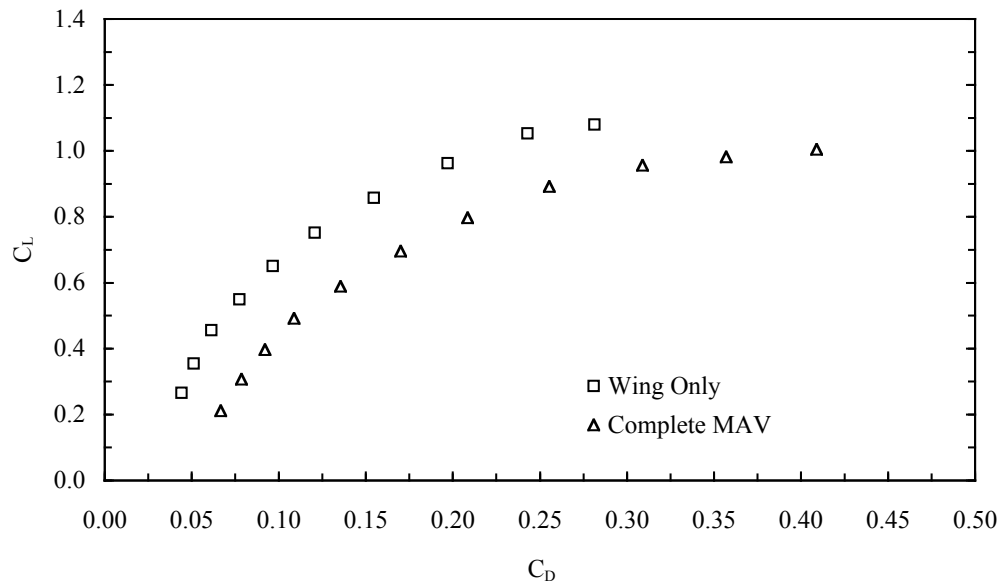


Figure C-55. C_L versus C_D for BR09 wing and MAVBR09 at $V_\infty = 13$ m/s.

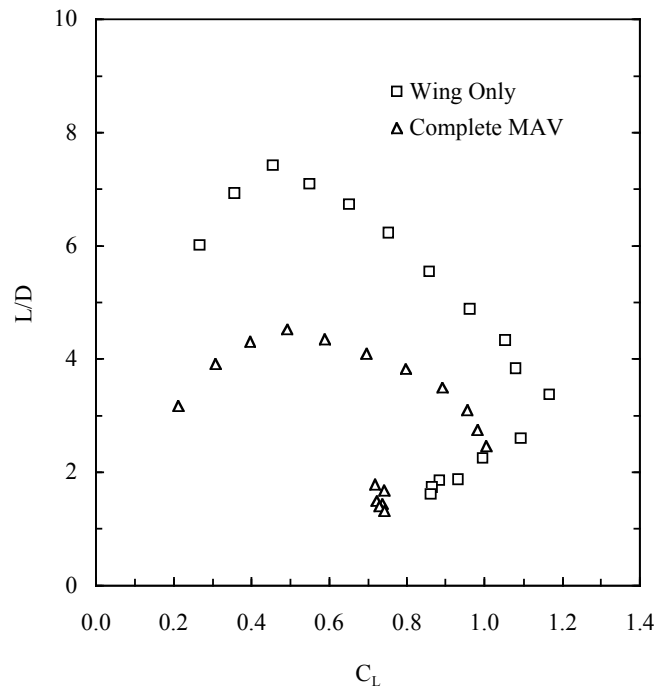


Figure C-56. L/D versus C_L for BR09 wing and MAVBR09 at $V_\infty = 13$ m/s.

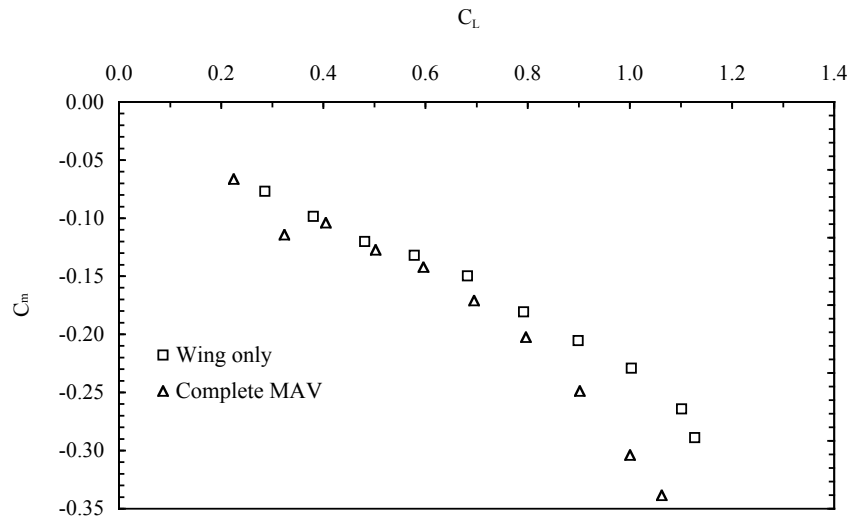


Figure C-57. C_m versus C_L for BR09 wing and MAVBR09 at $V_\infty = 13$ m/s.

C.5 MAV with Propeller

The ultimate description of the characteristics of a complete MAV was obtained from tests using the same vehicles used in the aforementioned tests but with the powered propeller. Chapter three gives a complete description of the models and the propulsion specifications.

The test matrix was populated, for each of the three vehicles, with three independent variables namely the angle of attack, the free stream velocity and the motor voltage setting. The tests were performed with the usual AOA sweeps with 17 values, at the four standard wind tunnel free stream velocities of 8, 10, 11.5 and 13 m/s and at three voltage motor settings of 7.4, 7.0 and 6.6 Volt. The total number of test points is 204 for each wing.

The section presents corrected experimental total aerodynamic force and moment coefficients for constant dynamic pressure and constant voltage motor setting. The

graphs can be used to compare how the aerodynamic characteristics of the vehicles change while holding the dynamic pressure (velocity) constant and varying the propeller speed or at constant voltage motor input and changing the free stream dynamic pressure. The cross-correlation of the results with different wings structure can give more information on the effects of the flexible wing structure and propeller interactions. Particular attention will be devoted to the changes in the longitudinal moment characteristics.

The four plots presented, selected as a sample of the entire test matrix, are the results for the three different wings mounted on the same vehicle are:

1 - C_L versus α for MAV with and without propeller for Rigid, PR07 and BR09 wings

2 - C_L versus C_D for MAV with and without propeller for Rigid, PR07 and BR09 wings

3 - C_m versus C_L for MAV with and without propeller for Rigid, PR07 and BR09 wings

The negative values of C_d represent a total net thrust. The reader can refer to Table C-1 for the design characteristics of the wings and their designations and to Figure 3-2 for a schematic view of the structural characteristics of each wing.

The propeller speed was measured by using a laser tachometer and only one time for every set of conditions with a combination of AOA, free stream velocity and voltage motor input. The voltage was hold constant for the entire AOA sweep and monitored by the power supply display.

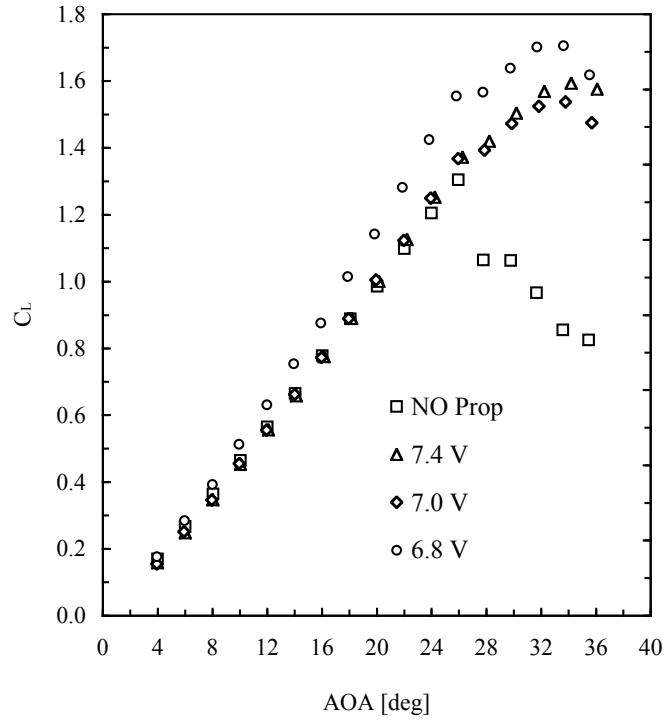


Figure C-58. C_L versus α for MAVR at $V_\infty = 11.5$ m/s and $E = 7.4, 7.0$ and 6.6 Volt.

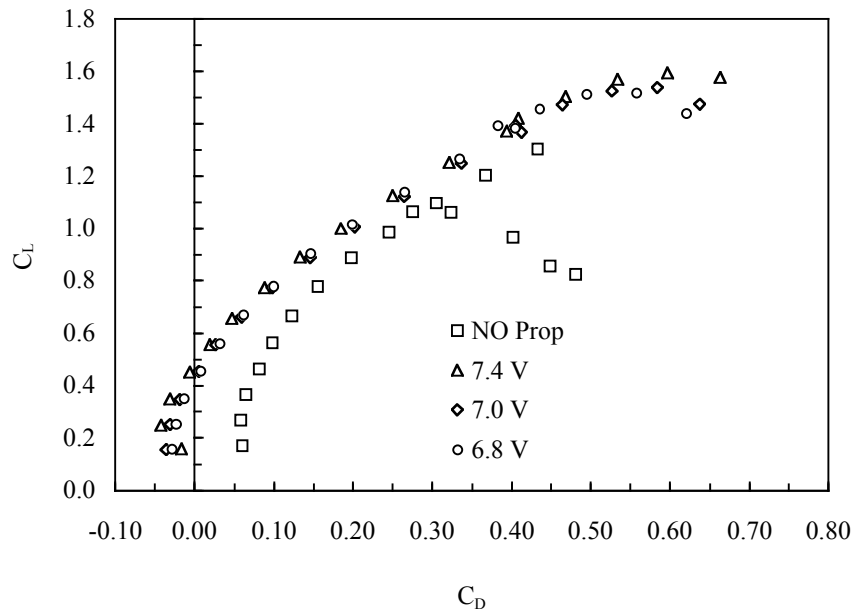


Figure C-59. C_L versus C_D for MAVR at $V_\infty = 11.5$ m/s and $E = 7.4, 7.0$ and 6.6 Volt.

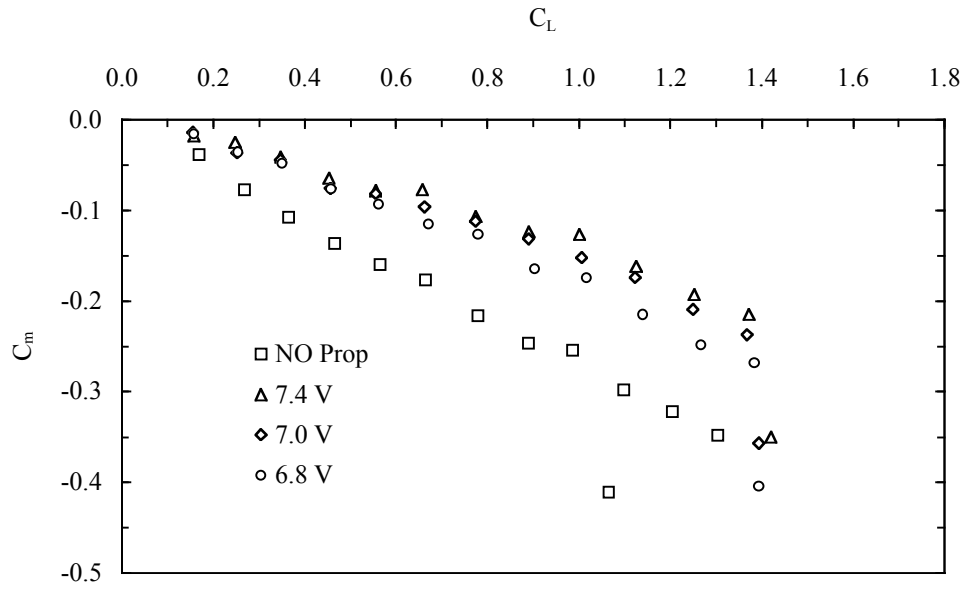


Figure C-60. C_m versus C_L for MAVR at $V_\infty = 11.5$ m/s and $E = 7.4, 7.0$ and 6.6 Volt Volt.

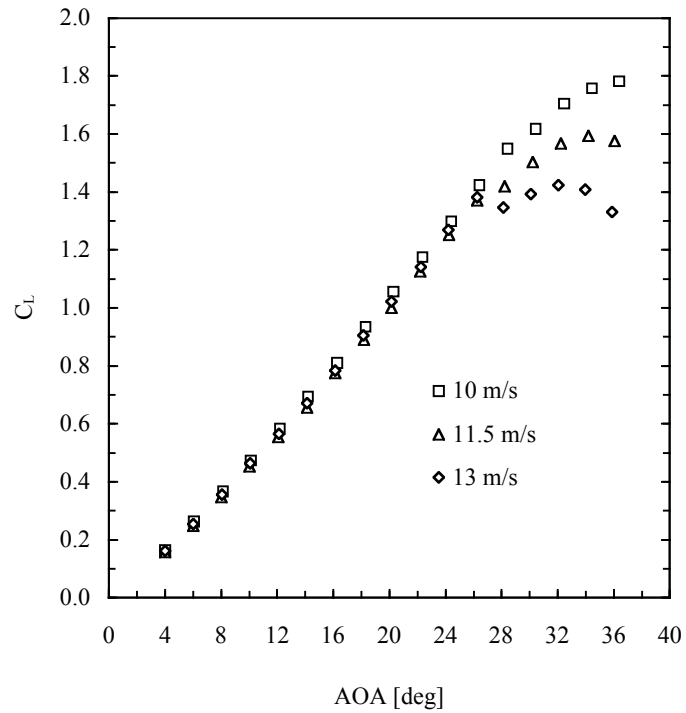


Figure C-61. C_L versus α for MAVR at $E = 7.4$ Volt and $V_\infty = 13, 11.5, 10$ and 8 m/s.

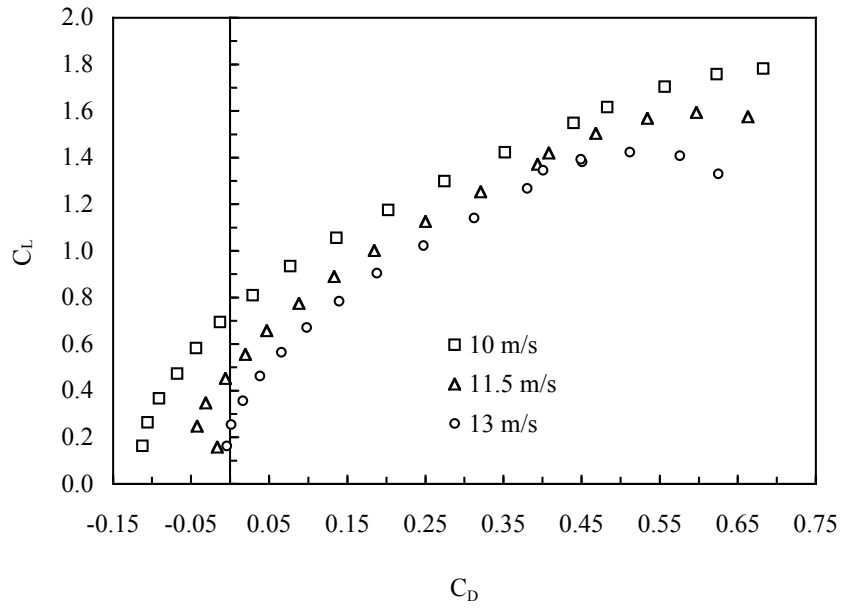


Figure C-62. C_L versus C_D for MAVR at $E = 7.4$ Volt and $V_\infty = 13, 11.5, 10$ and 8 m/s.

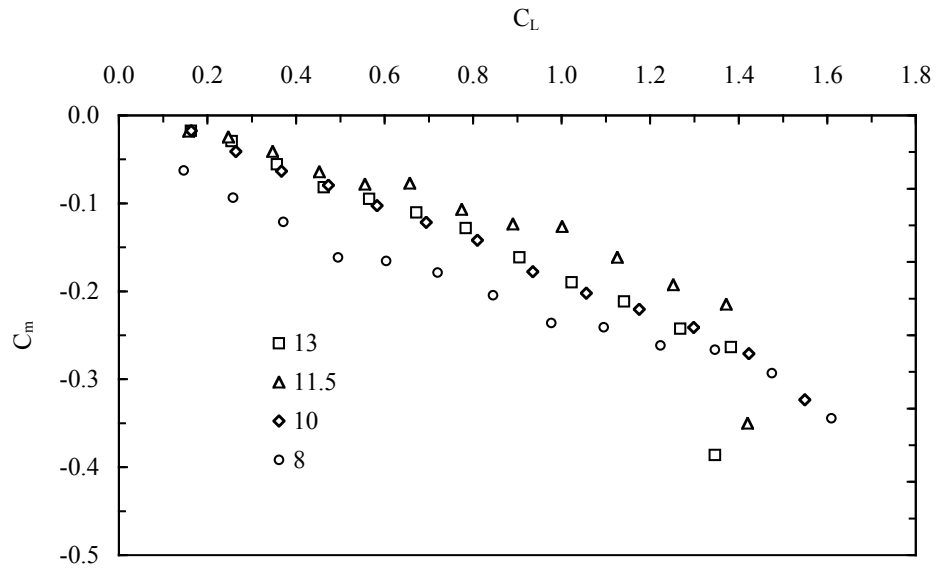


Figure C-63. C_m versus C_L for MAVR at $E = 7.4$ Volt and $V_\infty = 13, 11.5, 10$ and 8 m/s.

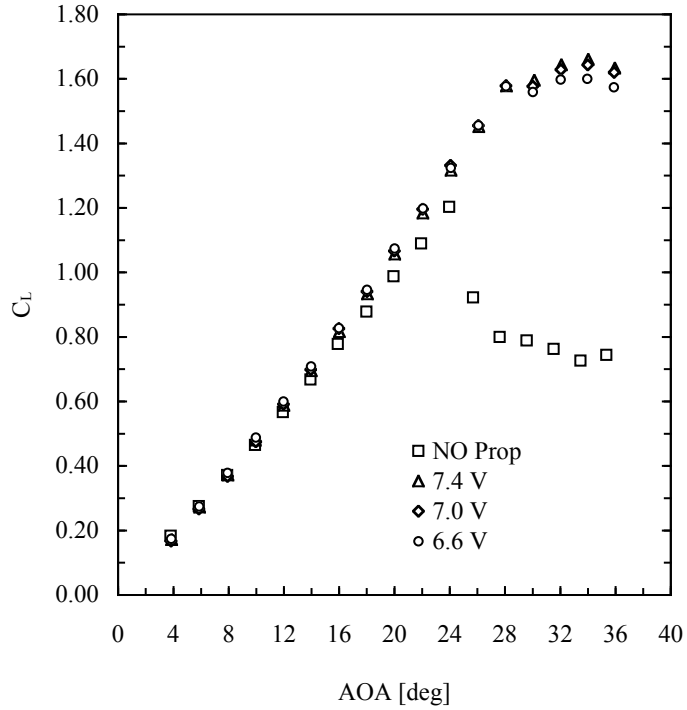


Figure C-64. C_L versus α for MAVPR07 at $V_\infty = 11.5$ m/s and $E = 7.4, 7.0$ and 6.6 Volt.

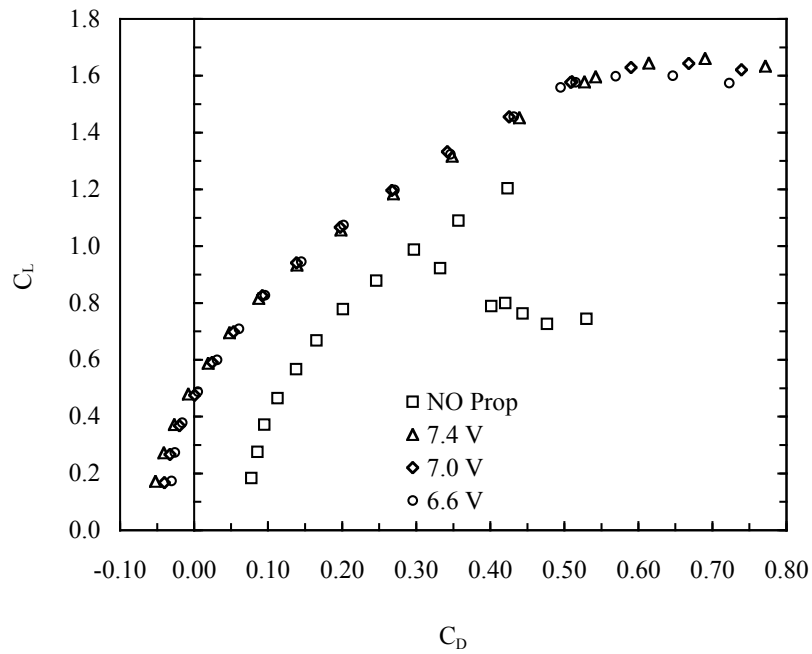


Figure C-65. C_L versus C_D for MAVPR07 at $V_\infty = 11.5$ m/s and $E = 7.4, 7.0$ and 6.6 Volt.

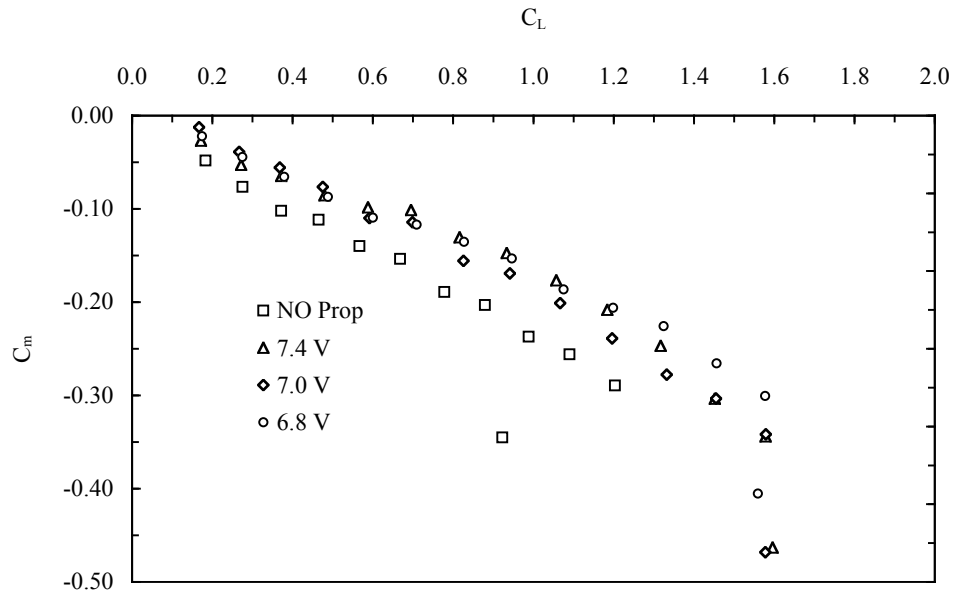


Figure C-66. C_m versus C_L for MAVPR07 at $V_\infty = 11.5$ m/s and $E = 7.4, 7.0$ and 6.6 Volt.

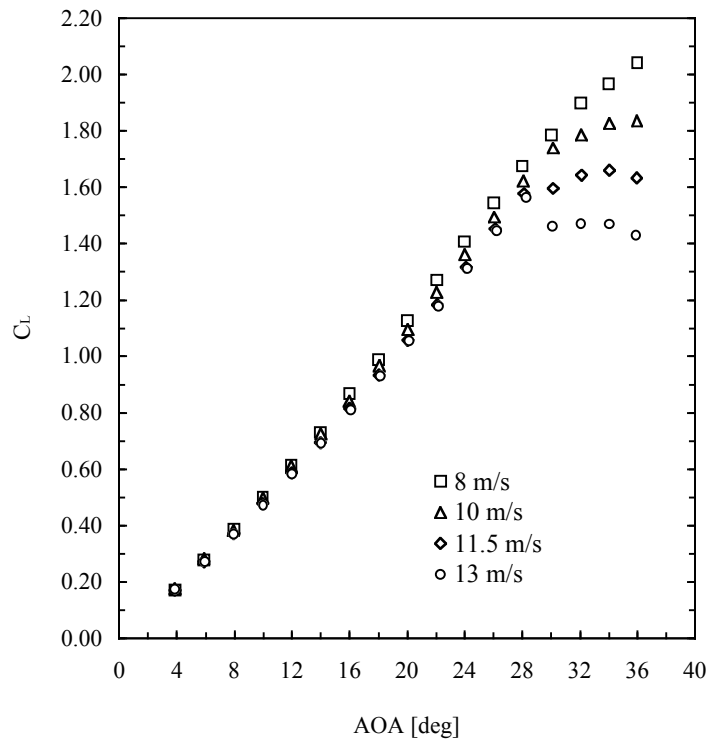


Figure C-67. C_L versus α for MAVPR07 at $E = 7.4$ Volt and $V_\infty = 13, 11.5, 10$ and 8 m/s.

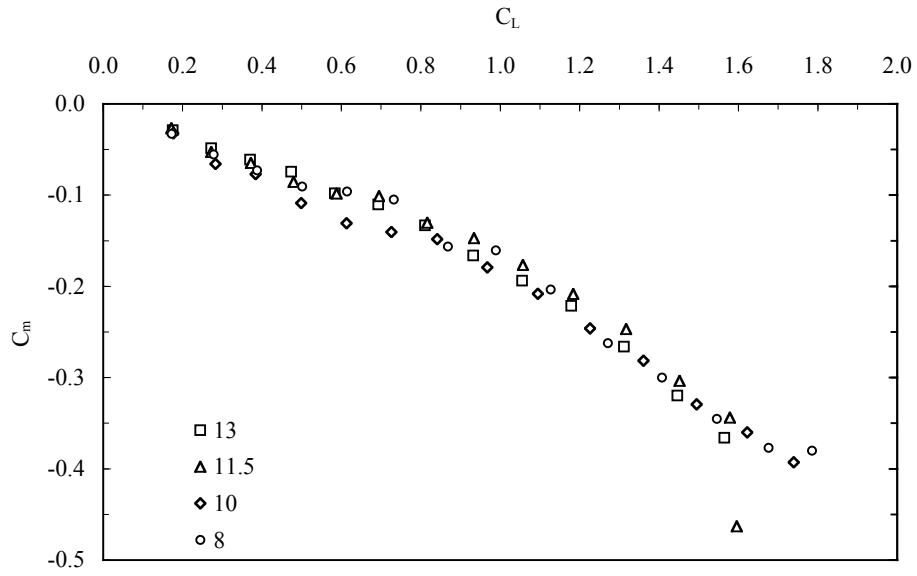


Figure C-68. C_m versus C_L for MAVPR07 at $E = 7.4$ Volt and $V_\infty = 13, 11.5, 10$ and 8 m/s.

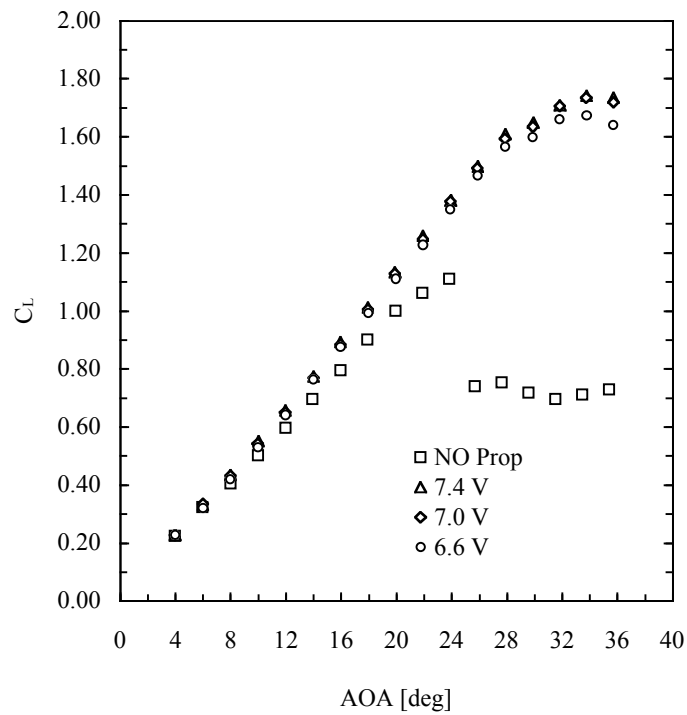


Figure C-69. C_L versus α for MAVBR09 at $V_\infty = 10$ m/s and $E = 7.4, 7.0$ and 6.6 Volt.

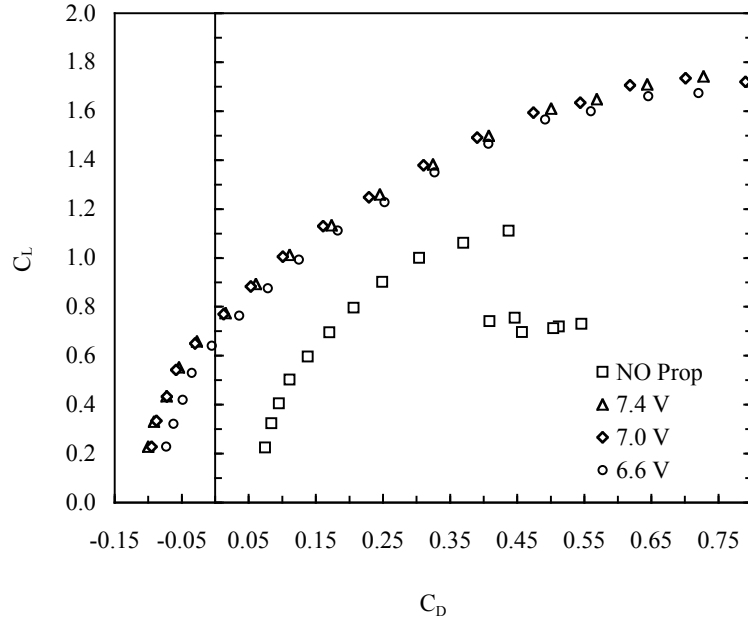


Figure C-70. C_L versus C_D for MAVBR09 at $V_\infty = 10$ m/s and $E = 7.4, 7.0$ and 6.6 Volt.

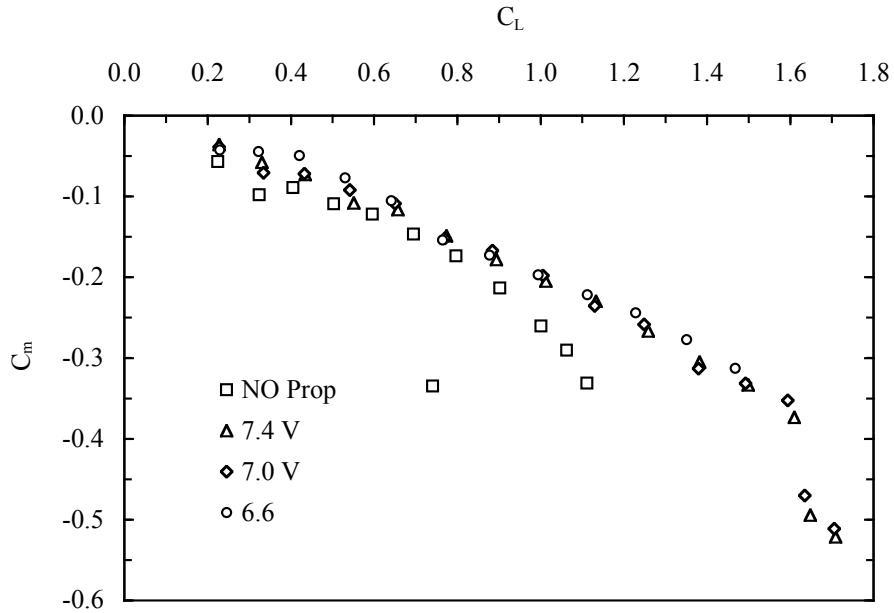


Figure C-71. C_m versus C_L for MAVBR09 at $V_\infty = 10$ m/s and $E = 7.4, 7.0$ and 6.6 Volt.

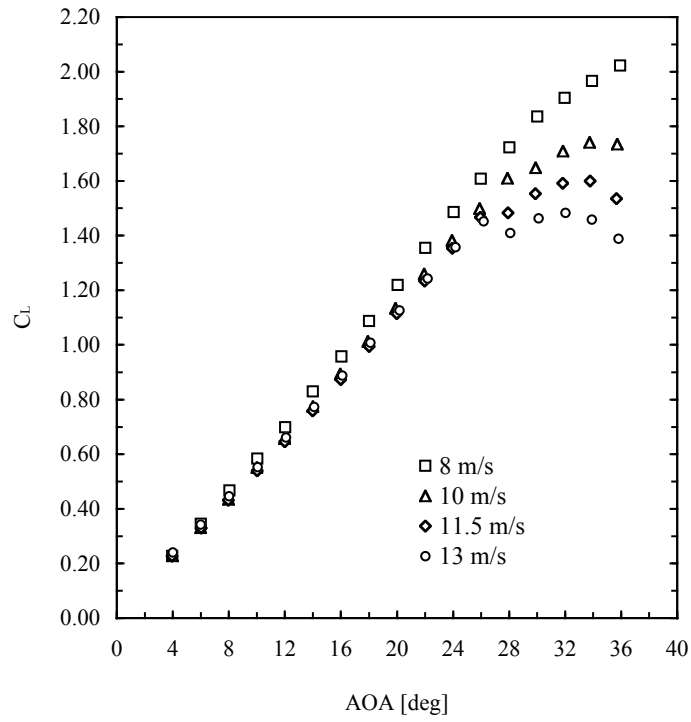


Figure C-72. C_L versus α for MAVBR09 at $E = 7.4$ Volt and $V_\infty = 13, 11.5, 10$ and 8 m/s.

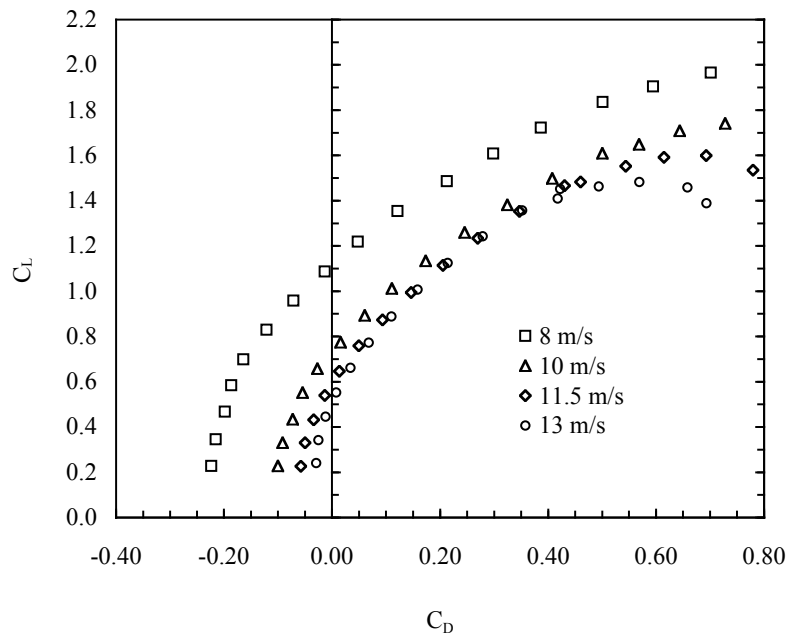


Figure C-73. C_L versus C_D for MAVBR09 at $E = 7.4$ Volt and $V_\infty = 13, 11.5, 10$ and 8 m/s.

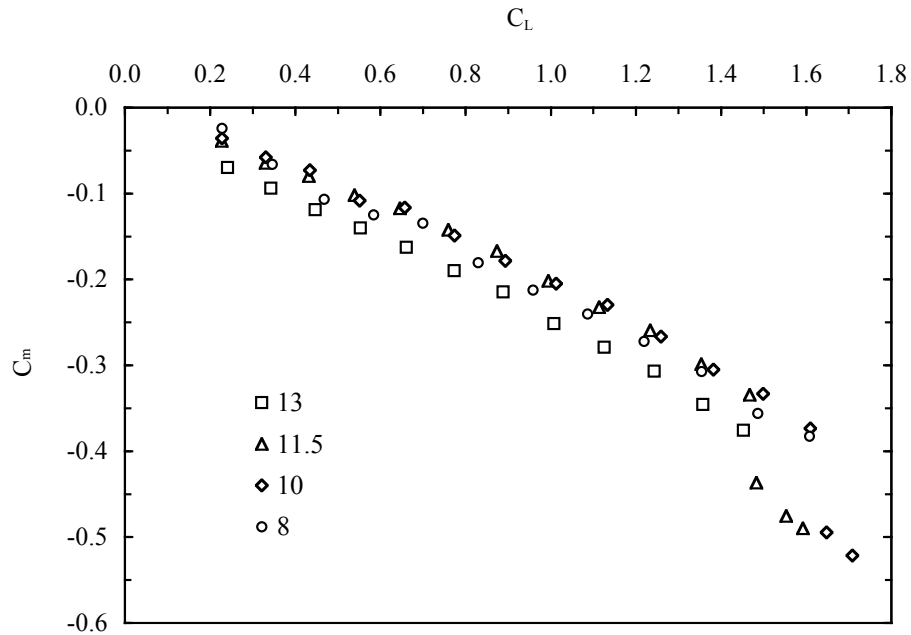


Figure C-74. C_m versus C_L for MAVBR09 at $E = 7.4$ Volt and $V_\infty = 13, 11.5, 10$ and 8 m/s.

C.6 Wings Arranged by Structural Design

The aerodynamic results organized with plots with different wing flexibility at the same dynamic pressure, will be presented in two sets with the two main structural designs, the BR and the PR types, grouped together. The graphs can be used to compare how the aerodynamic characteristics of a particular wing design changes with the dynamic pressure, while holding the structural design group, BR or PR, constant.

C.6.1 Batten Reinforced Wings

In reference to the BR type wing the two groups of four plots presented, for each dynamic pressure (velocity), are:

- 1 - C_L versus α for wings Rigid, BR02, BR03 and BR05
- 2 - C_L versus C_D for wings Rigid, BR02, BR03 and BR05
- 3 - L/D versus C_L for wings Rigid, BR02, BR03 and BR05
- 4 - C_m versus C_L for wings Rigid, BR02, BR03 and BR05

The results for each group are presented at two dynamic pressures, corresponding to the free stream velocities of 8 and 13 m/s.

Please see Table 3-2 for the design characteristics of the wings and their designations.

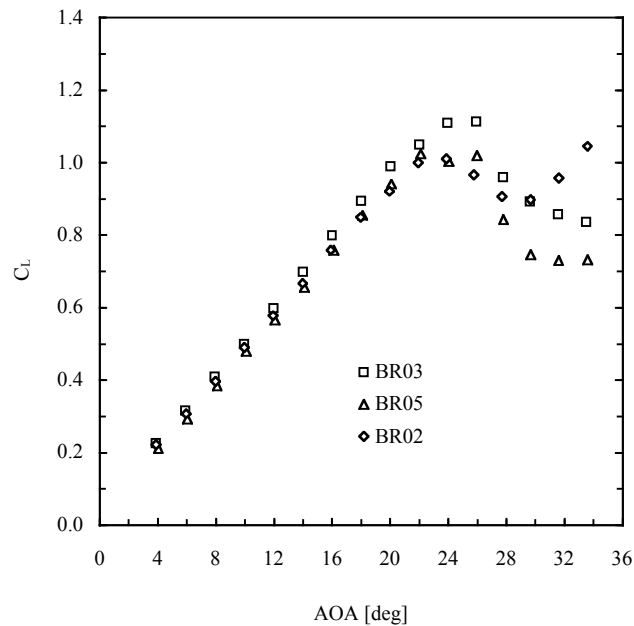


Figure C-75. C_L versus α for wings BR03, BR05 and BR02 at $V_\infty = 8$ m/s.

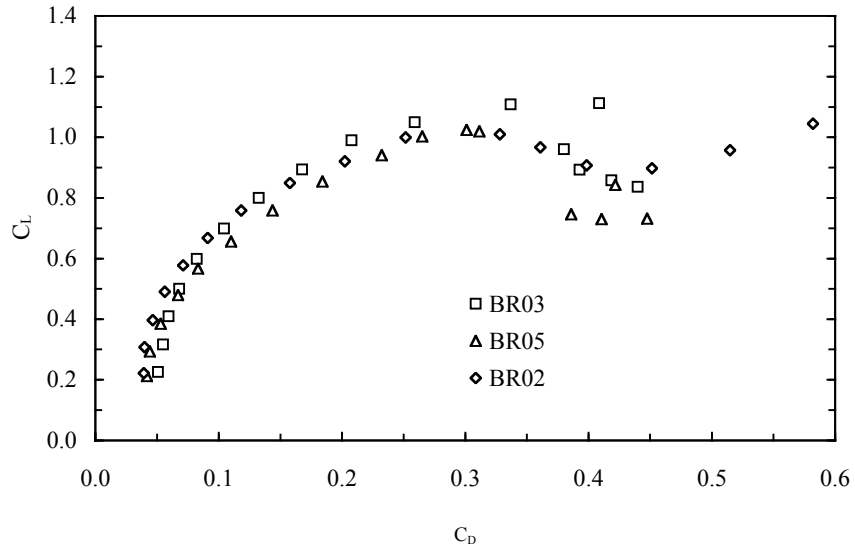


Figure C-76. C_L versus C_D for wings BR03, BR05 and BR02 at $V_\infty = 8$ m/s.

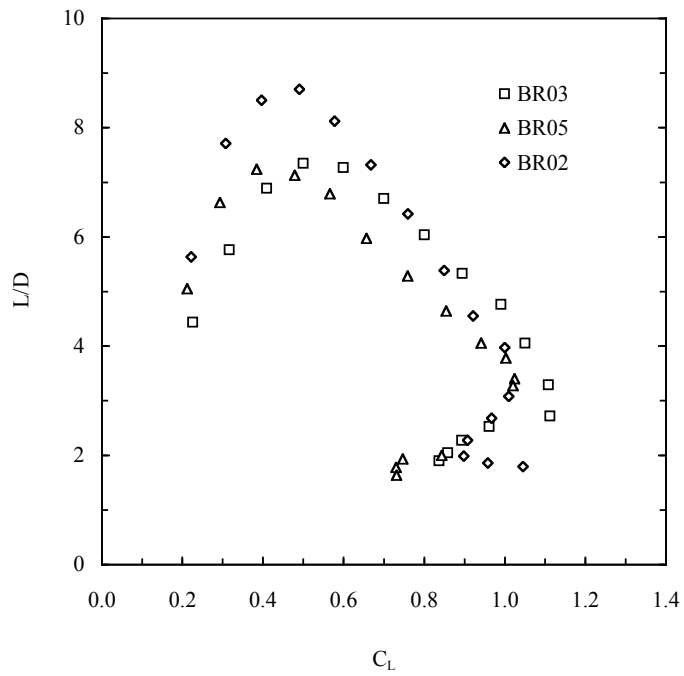


Figure C-77. L/D versus C_L for wings BR03, BR05 and BR02 at $V_\infty = 8$ m/s.

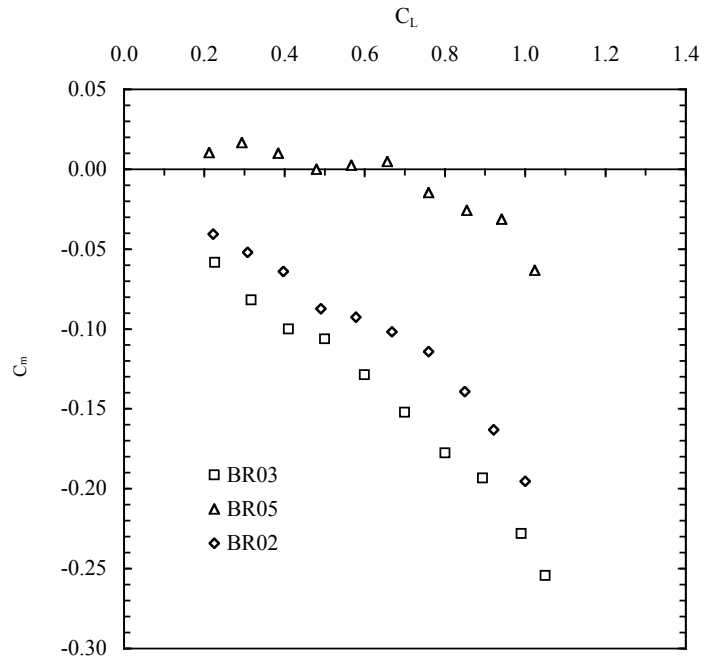


Figure C-78. C_m versus C_L for wings BR03, BR05 and BR02 at $V_\infty = 8$ m/s.

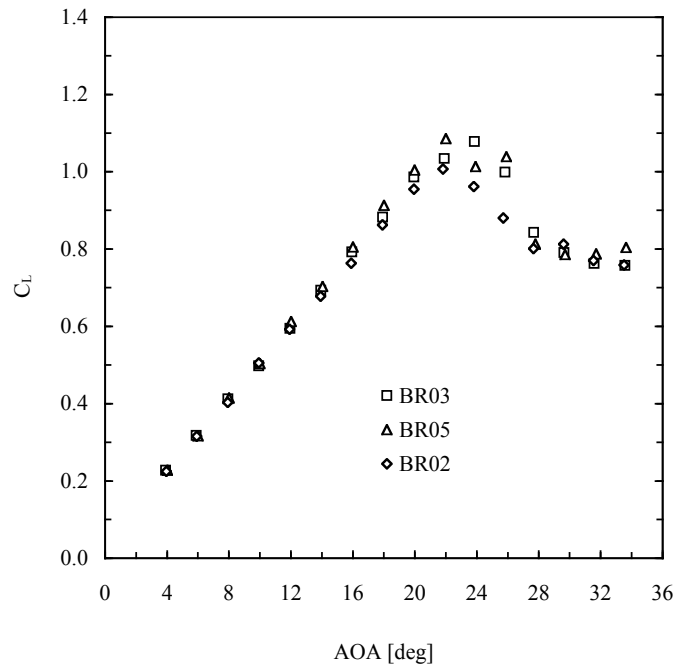


Figure C-79. C_L versus α for wings BR03, BR05 and BR02 at $V_\infty = 13$ m/s.

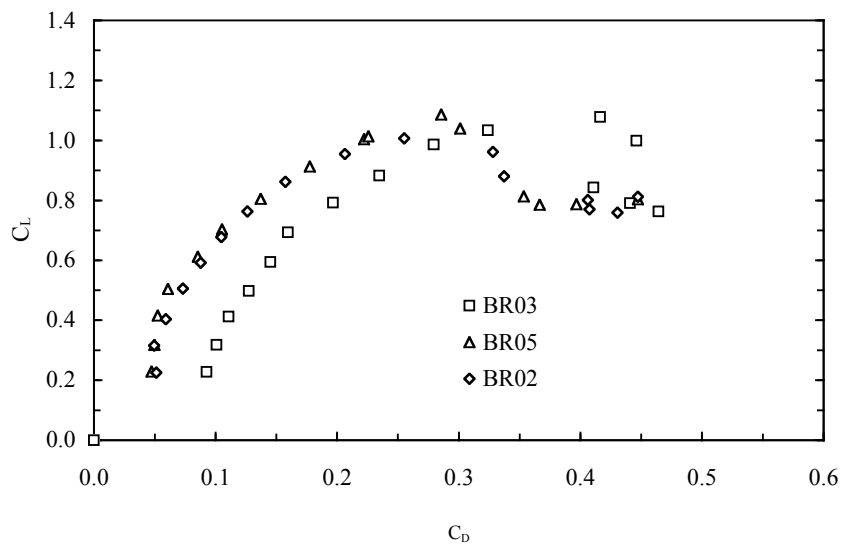


Figure C-80. C_L versus C_D for wings BR03, BR05 and BR02 at $V_\infty = 13$ m/s.

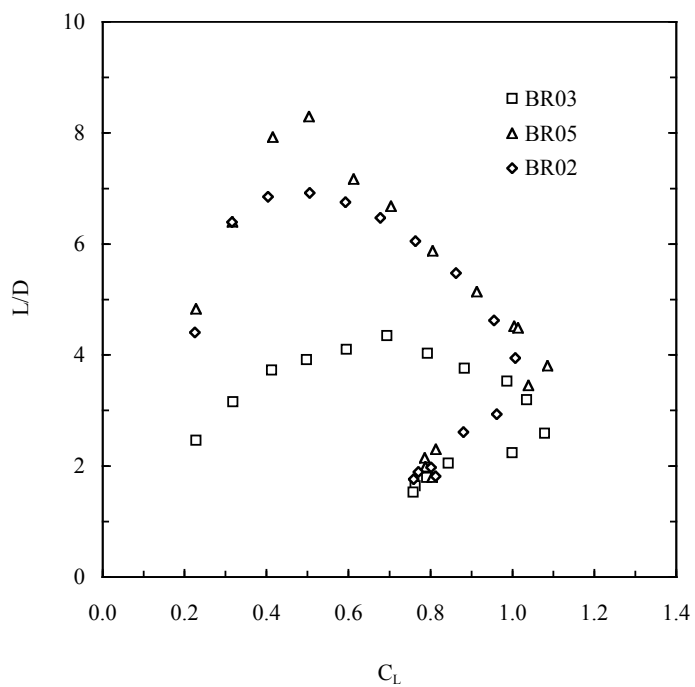


Figure C-81. L/D versus C_L for wings BR03, BR05 and BR02 at $V_\infty = 13$ m/s.

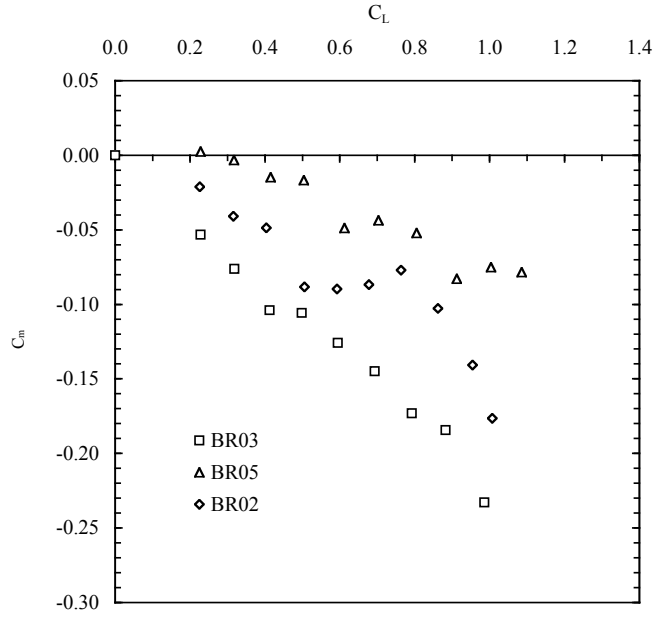


Figure C-82. C_m versus C_L for wings BR03, BR05 and BR02 at $V_\infty = 13$ m/s.

C.6.2 Perimeter Reinforced Wings

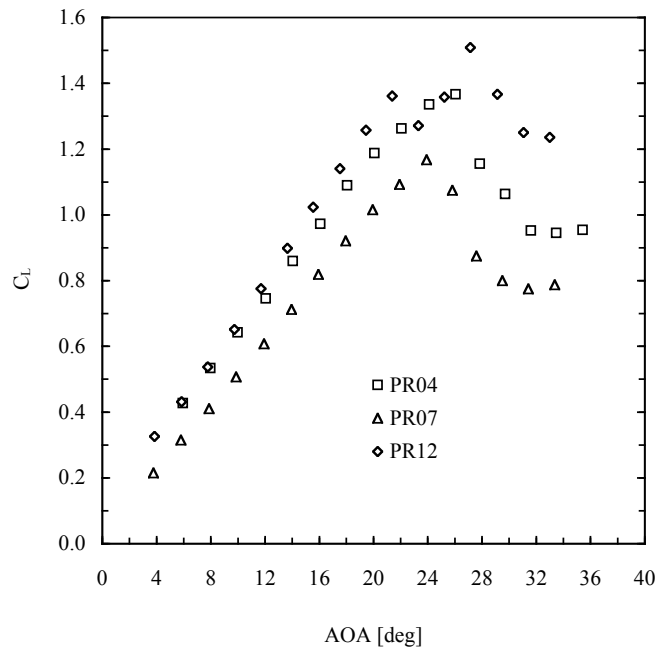


Figure C-83. C_L versus α for wings PR04, PR07 and PR12 at $V_\infty = 8$ m/s.

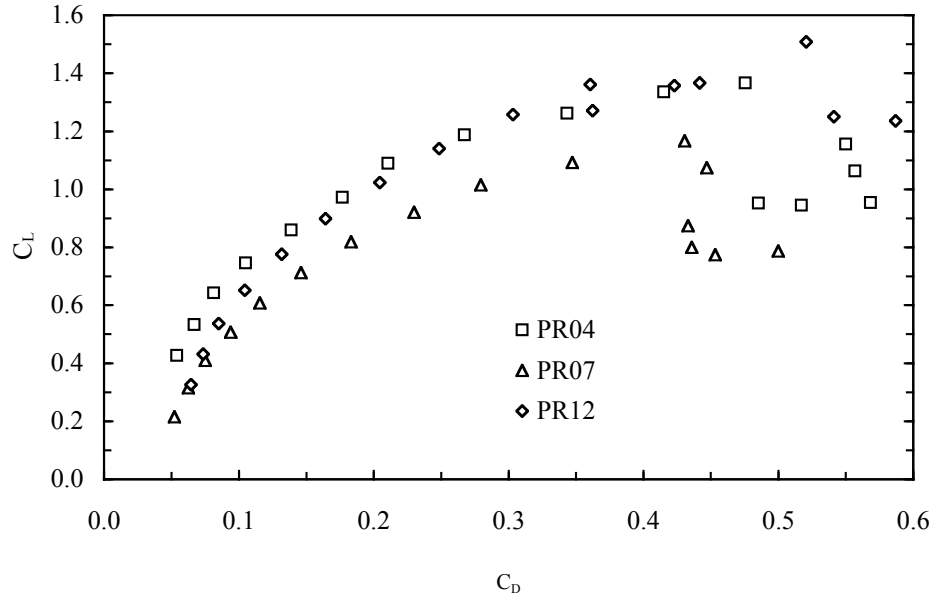


Figure C-84. C_L versus C_D for wings PR04, PR07 and PR12 at $V_\infty = 8$ m/s.

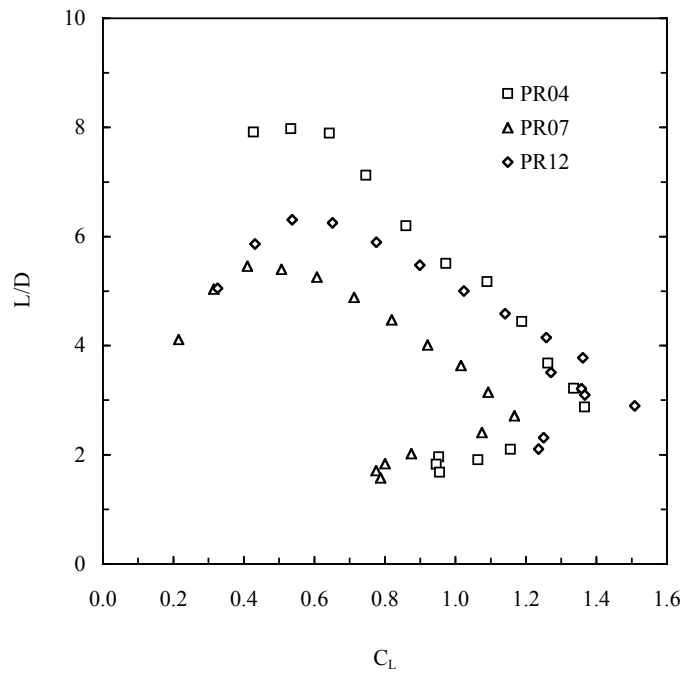


Figure C-85. L/D versus C_L for wings PR04, PR07 and PR12 at $V_\infty = 8$ m/s.

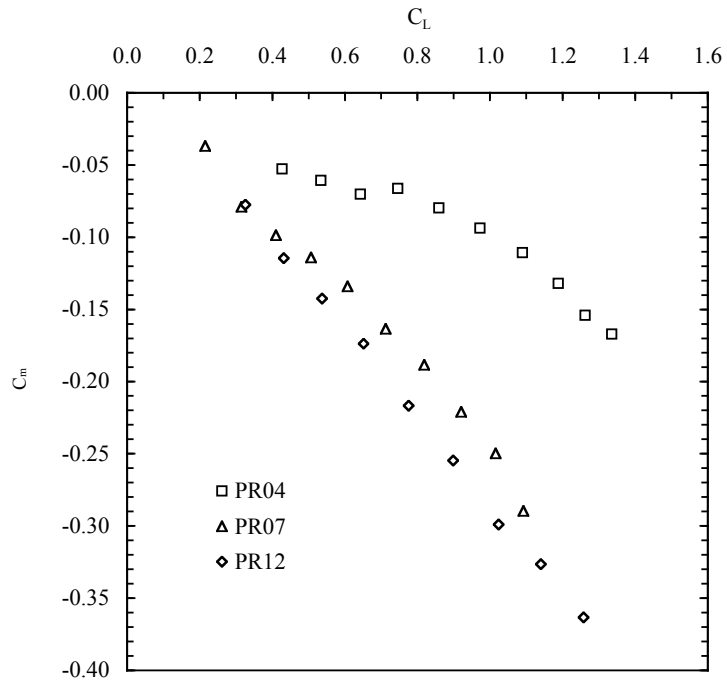


Figure C-86. C_m versus C_L for wings PR04, PR07 and PR12 at $V_\infty = 8$ m/s.

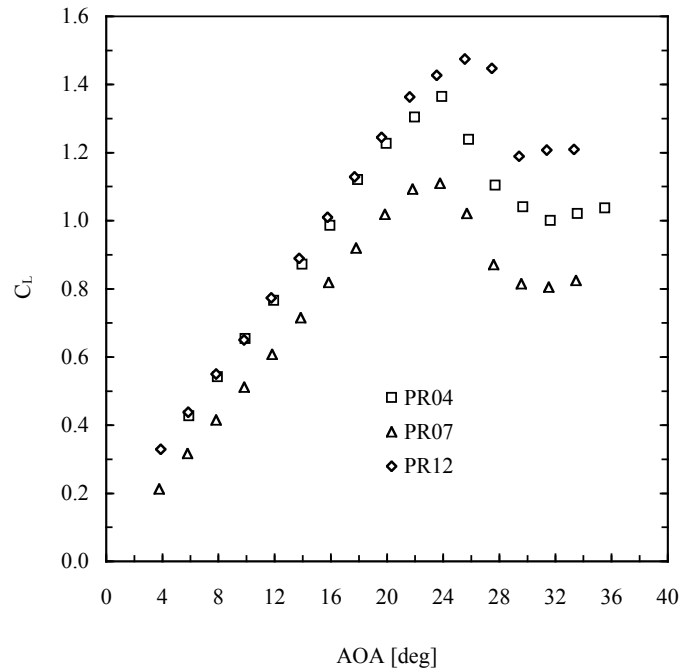


Figure C-87. C_L versus α for wings PR04, PR07 and PR12 at $V_\infty = 13$ m/s.

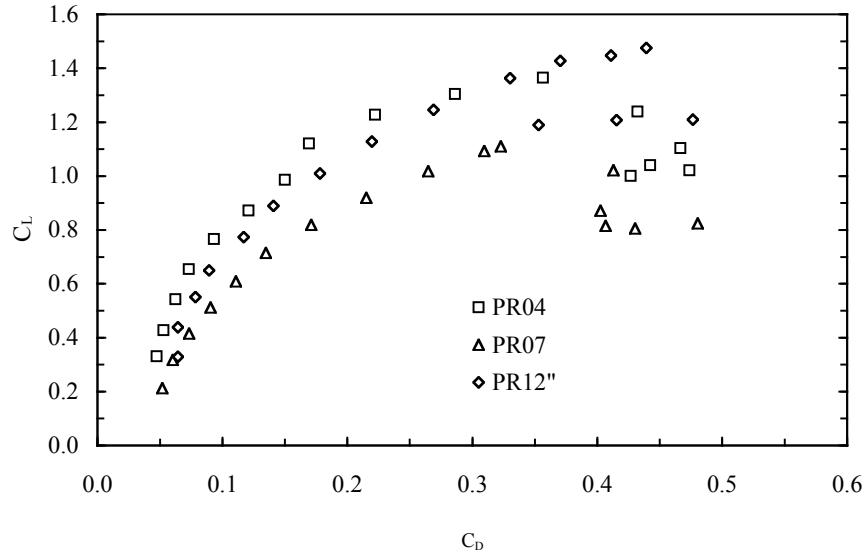


Figure C-88. C_L versus C_D for wings PR04, PR07 and PR12 at $V_\infty = 13$ m/s.

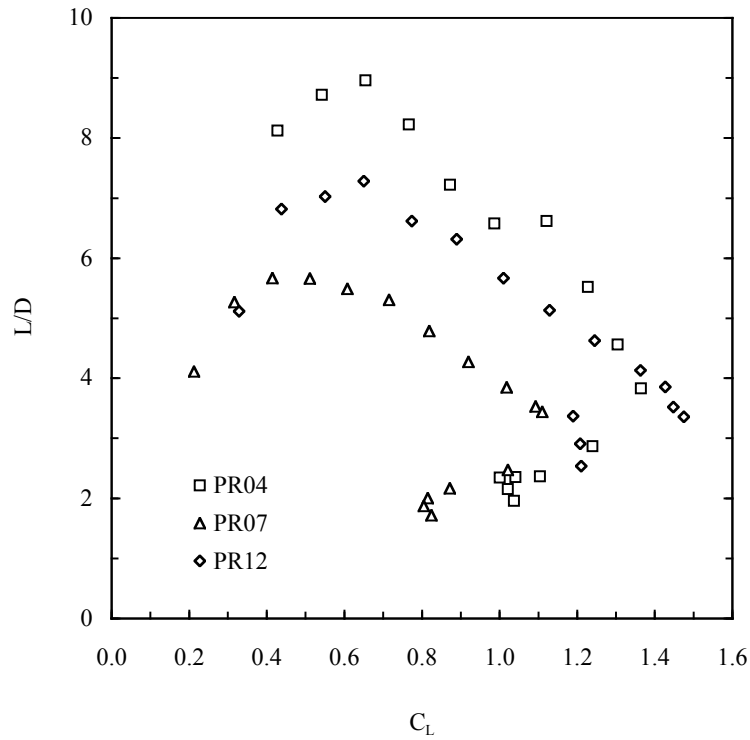


Figure C-89. L/D versus C_L for wings PR04, PR07 and PR12 at $V_\infty = 13$ m/s.

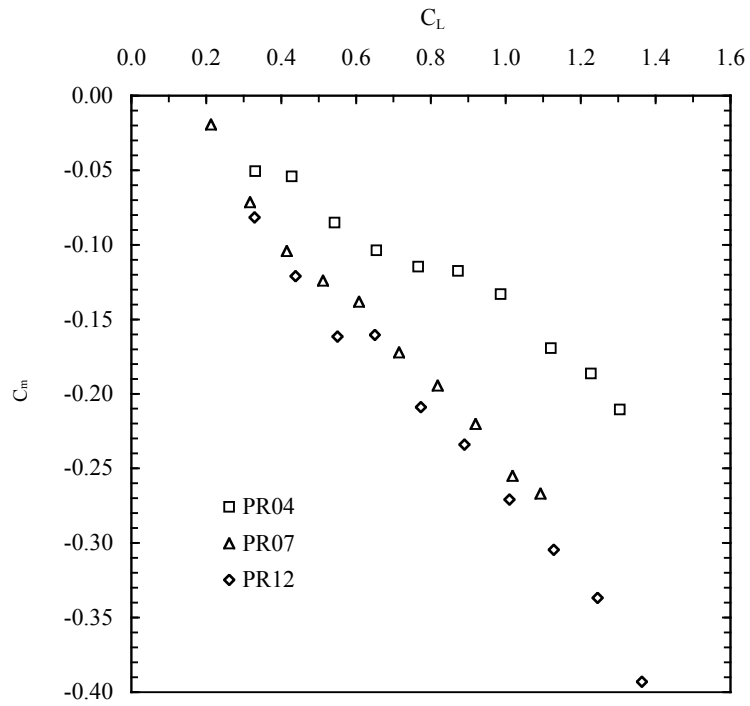


Figure C-90. C_m versus C_L for wings PR04, PR07 and PR12 at $V_\infty = 13$ m/s.

APPENDIX D WINGS' STATIC ELASTIC DEFORMATION RESULTS

This appendix presents a selection of results in terms of plots with the geometry and elastic experimental data for four different wings. Data from the collection of all structural tests using the VIC technique were used throughout this work to present geometry analysis of the deformed wings, elastic deformation analysis and strain investigation.

The data base collected during the entire tests campaign includes 13 isolated wings and three wings mounted on vehicles, thus tested with the propeller on with the purpose to investigate on the propeller slipstream effects. The description of the tests procedure is reported in Chapter 3; a typical test matrix for a single wing consists of 4 files (8 original VIC pictures converted in four files with geometry, displacements and strains) per test point; the test points in the matrix are formed with a sweep of five AOAs at four free stream velocities (8, 10, 11.5 and 13 m/s), for a total of approximately 80 files per wing.

The case for the MAV is more complex due to the addition of one more independent variables, the motor setting, thus a typical test matrix includes a sweep of five AOAs at three free stream velocities at three motor voltage inputs, for a total of approximately 120 files per vehicle. The rigid wing and the correspondent vehicle are related to smaller test matrices because only few conditions were examined for system calibration and corrections purposes. During the general test procedure the eight pictures per test point, generating four VIC files, were set including the wind off conditions (first two pictures and first file) and three wind on in the same state for redundancy.

The total number of geometry files and the information contained are vast, therefore only four wings, type BR05, BR09, PR07 and PR12 were selected for presentation in this section, relative to a small number of test conditions.

The exhibit of the results has been organized in two sections, with plots at different dynamic pressures and plots at different flexibility, keeping all the other factors constant. A complete description of the wings can be found in Chapter 3, Table 3-1 and Table 3-2 show the main characteristics of the models in a table form. The wings selected for the following plots represent a range of flexibilities; table C-1 shows the wings and the vehicles main characteristics with their designation.

For the purpose of this Appendix the sections of the wings are cut always on the same plane at 50 mm from the centerline of the wing or the vehicle. All data have been corrected for rigid body translations and rotations.

D.1 Batten Reinforced Wings

The section presents results for the wings type BR05 and BR09. The plots show the elastic deformation of one type of wing with the distinctive structural design thus flexibility, at two different free stream dynamic pressures (velocities) or AOAs. The graphs can be used to compare how the shape and other geometric characteristics of a particular wing design change with the dynamic pressure and AOA, while holding the flexibility constant.

The two series of three plots presented are:

- 1- i_c , sections and w for $\alpha = 18$ degrees at $V_\infty = 8$ and 13 m/s for wing type BR09
- 2 - i_c , sections and w for $\alpha = 4$ and 20 degrees at $V_\infty = 13$ m/s for wing type BR05

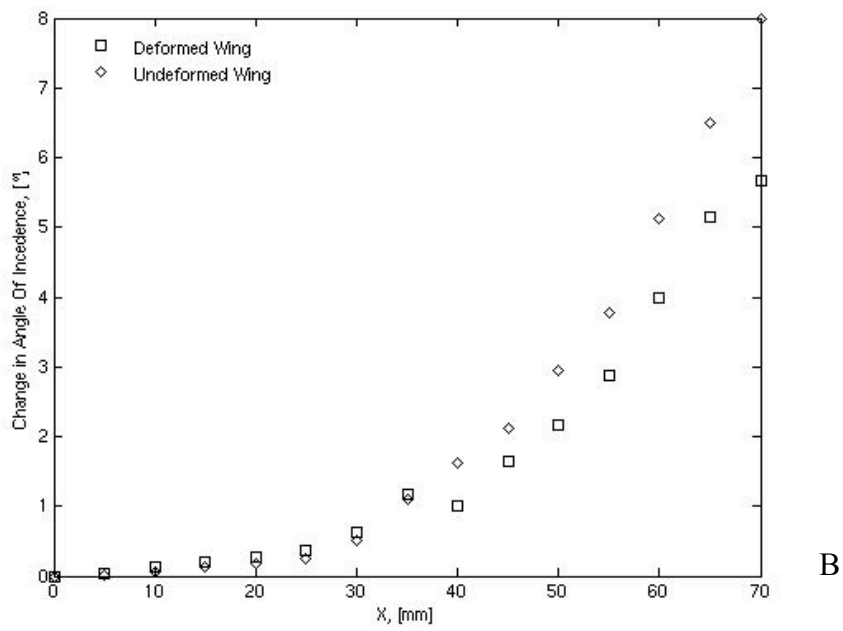
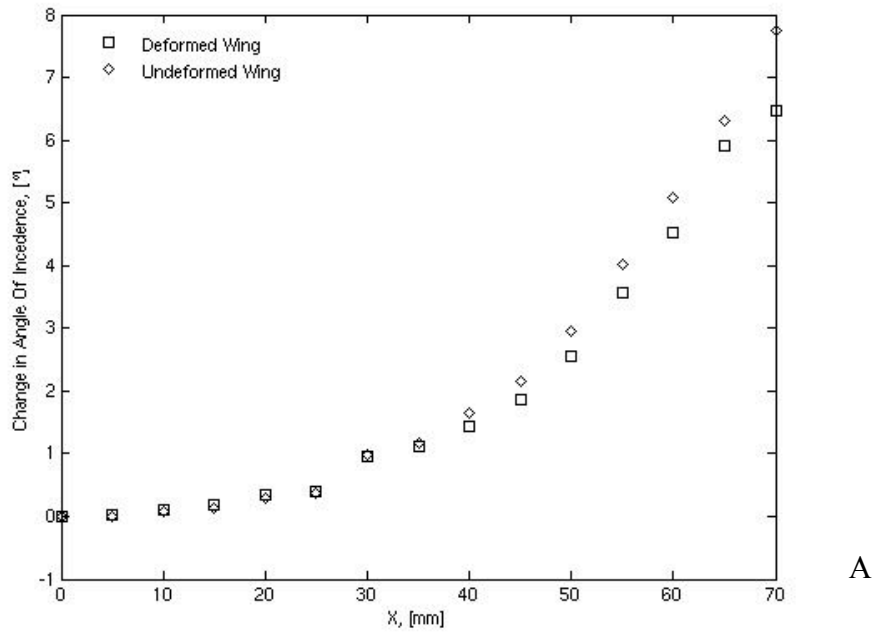


Figure D-1. Local angle of incidence distribution in the X direction from centerline for wing BR09 at $\alpha = 18$ degrees. A) $V_\infty = 8$ m/s and B) $V_\infty = 13$ m/s.

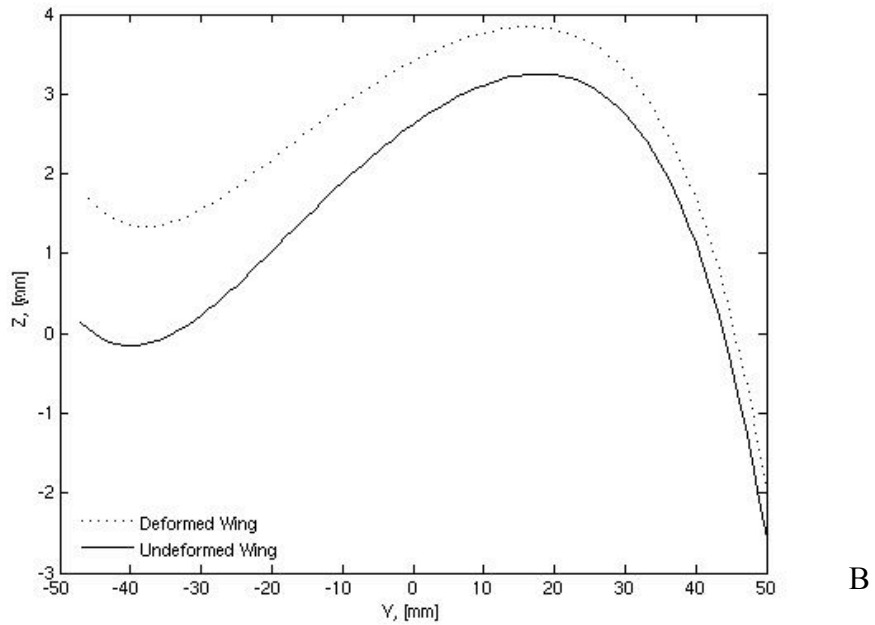
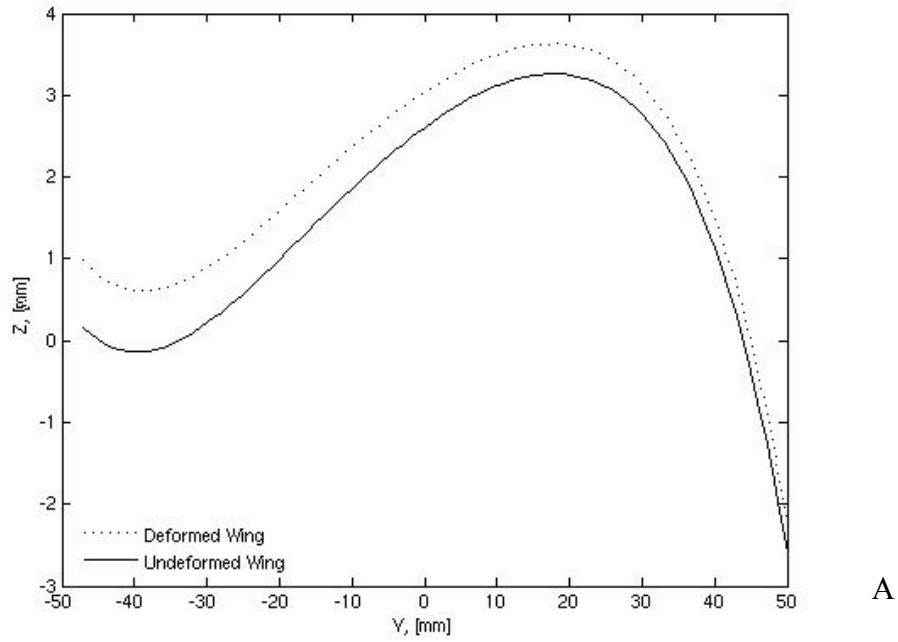


Figure D-2. Undeformed (flow off) and deformed (flow on) wing sections for wing BR09 at $\alpha = 18$ degrees. A) $V_\infty = 8$ m/s and B) $V_\infty = 13$ m/s.

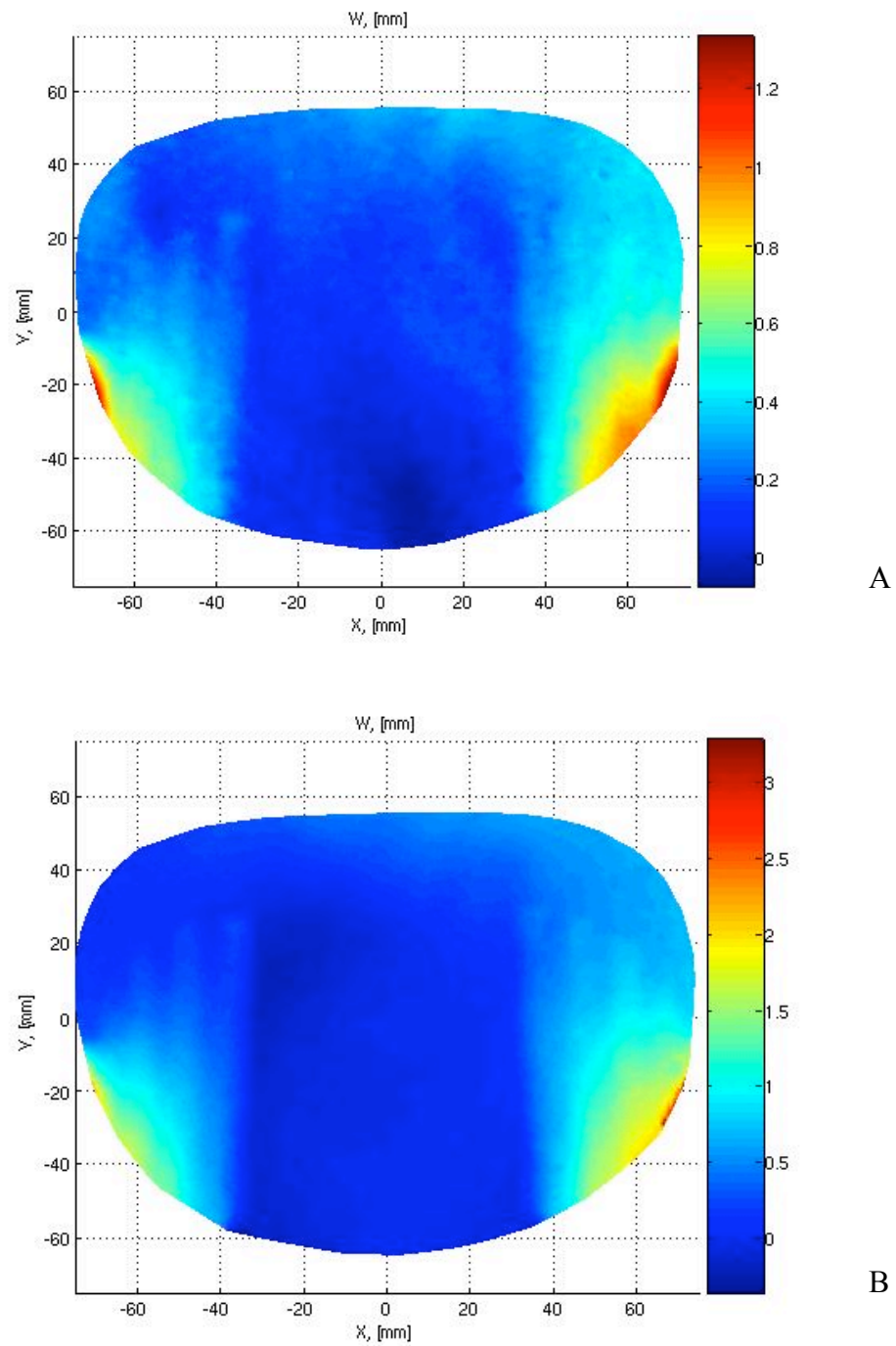
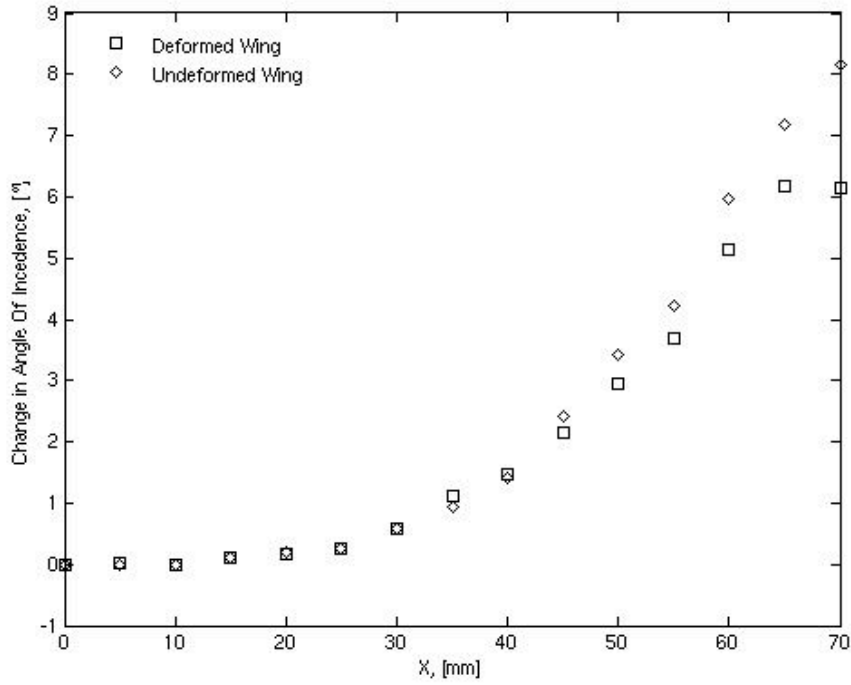
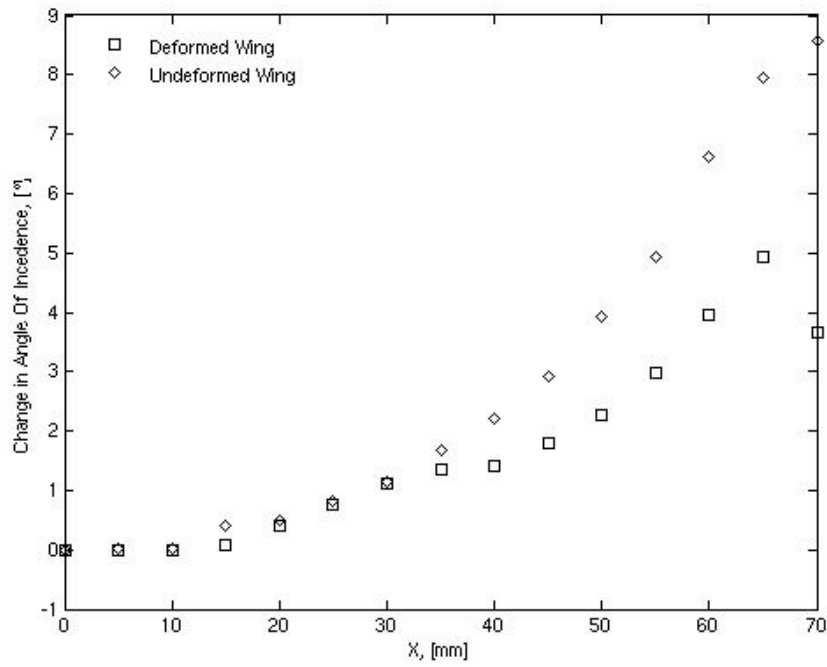


Figure D-3. w contour plots for wing BR09 at $\alpha = 18$ degrees. A) $V_\infty = 8$ m/s and B) $V_\infty = 13$ m/s.

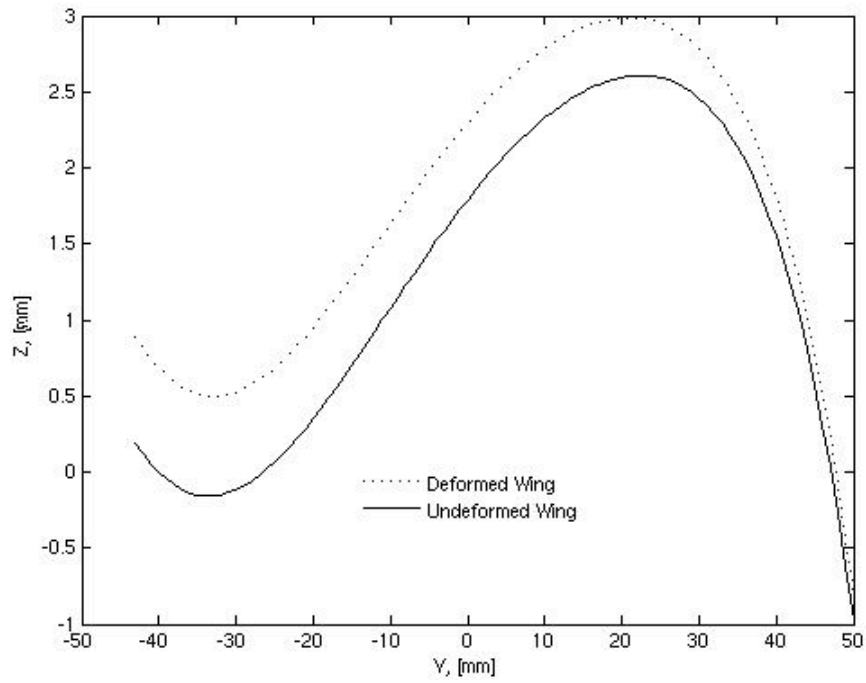


A

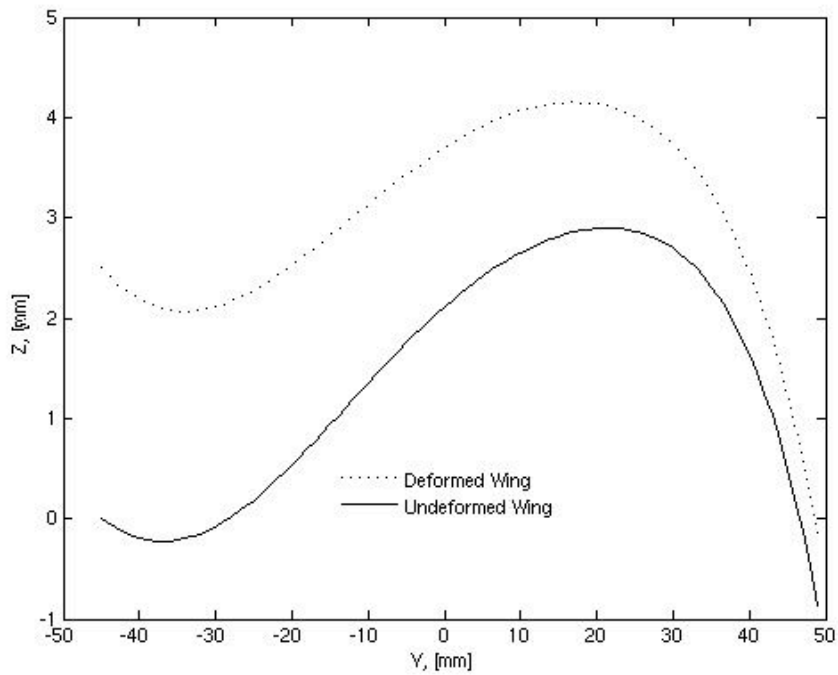


B

Figure D-4. Local angle of incidence distribution in the X direction from centerline for wing BR05 at $V_\infty = 13$ m/s. A) $\alpha = 4$ degrees and B) $\alpha = 20$ degrees.



A



B

Figure D-5. Undeformed (flow off) and deformed (flow on) wing sections for wing BR05 at $V_\infty = 13$ m/s. A) $\alpha = 4$ degrees and B) $\alpha = 20$ degrees.

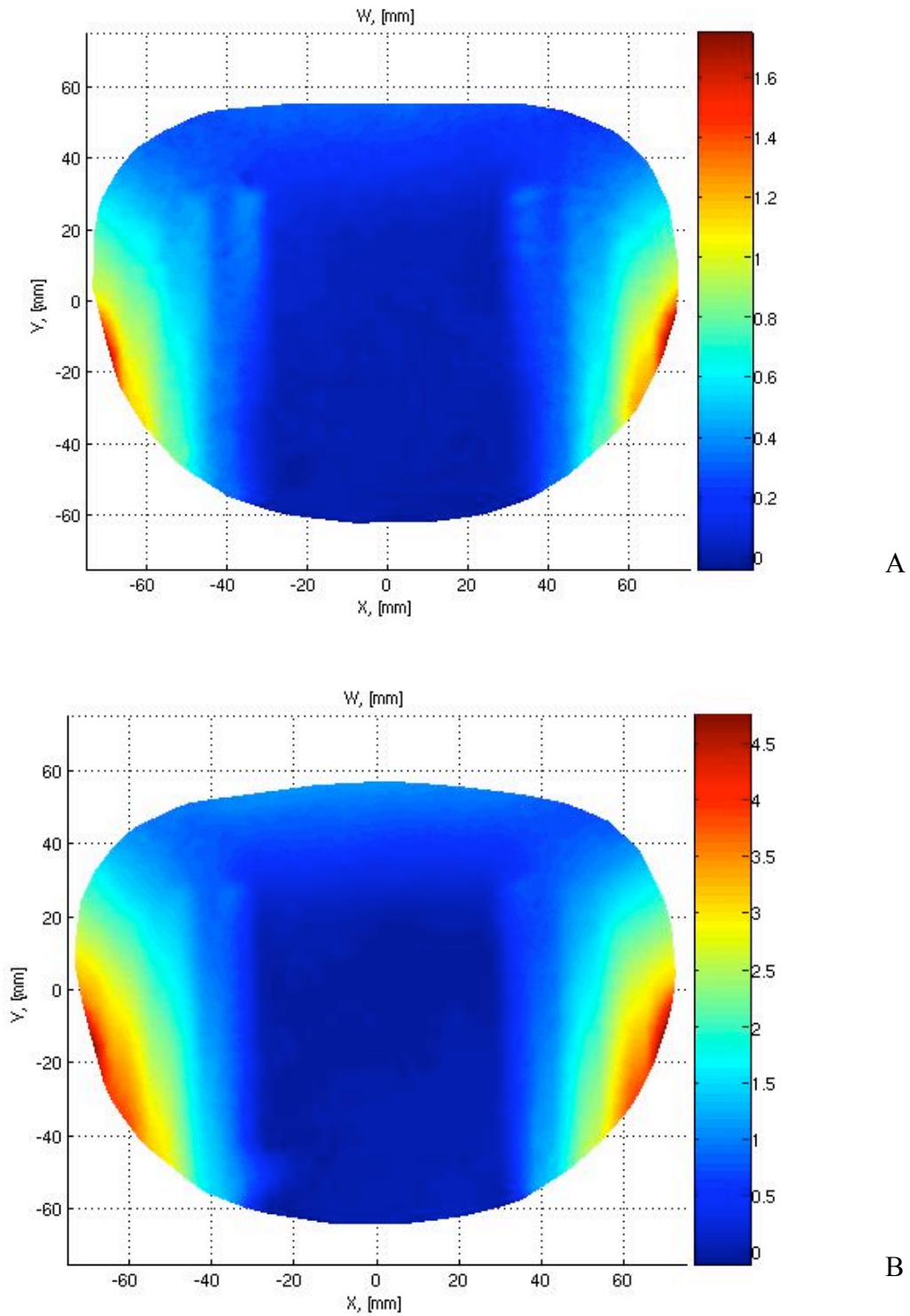


Figure D-6. w contour plots for wing BR05 at $V_\infty = 13$ m/s. A) $\alpha = 4$ degrees and B) $\alpha = 20$ degrees.

D.2 Perimeter Reinforced Wings

The section presents results for the wings type PR07 and PR12. The plots show the elastic deformation of one type of wing with the distinctive structural design thus flexibility, at two different free stream dynamic pressures (velocities) or AOAs. The graphs can be used to compare how the shape and other geometric characteristics of a particular wing design change with the dynamic pressure and AOA, while holding the flexibility constant.

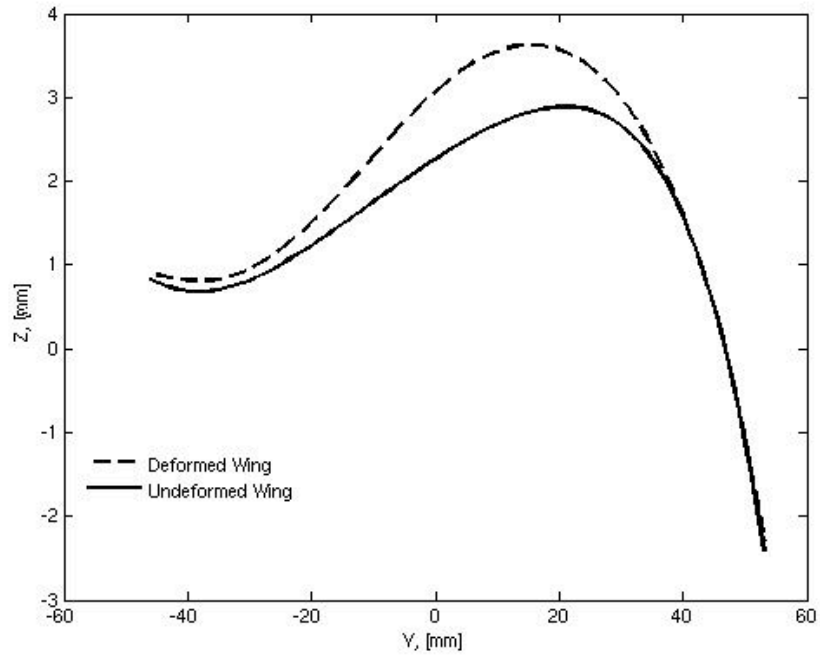
The two series of three plots presented are:

1- sections and w for $\alpha = 4$ and 22 degrees at $V_\infty = 13$ m/s for wing type PR07

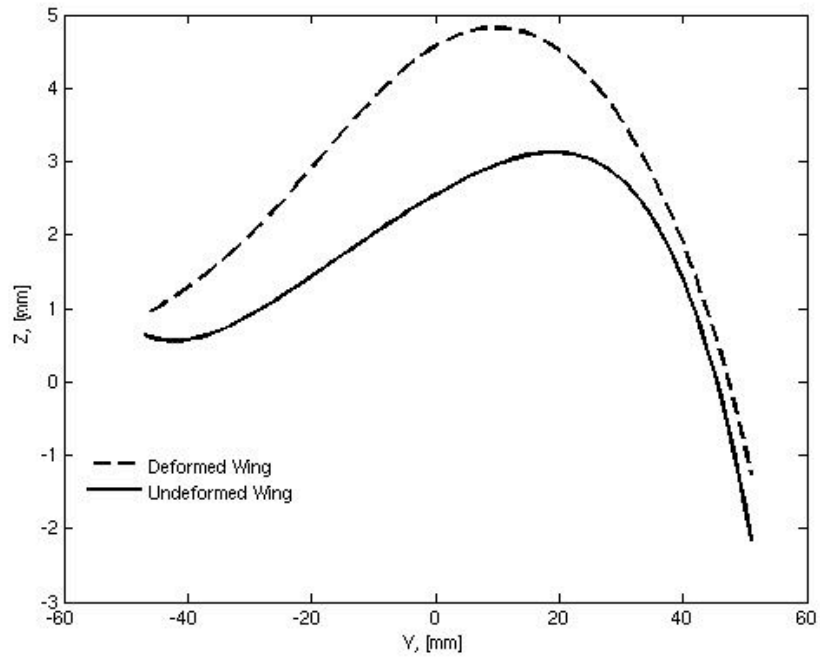
2- sections and w for $\alpha = 4$ and 20 degrees at $V_\infty = 13$ m/s for wing type PR12

Because of the particular design of the PR wing, with a stiff carbon fiber perimeter around the all wing, the local angle of incidence was practically constant with the change of AOA or dynamic pressure. In addition several plots with the strain field will be proposed.

The wing type PR07 is particularly interesting because it represents the last generation of wings used in flight tests and MAV competitions. The wings type PR established the new flight line of the University of Florida MAV flying fleet. The MAV equipped with wing PR07 exhibited a significantly better maneuverability at low speeds and a decisively improvement to reach trimmed flight characteristics respect to the BR type wings.



A



B

Figure D-7. Undeformed (flow off) and deformed (flow on) wing sections for wing PR07 at $V_\infty = 13$ m/s. A) $\alpha = 4$ degrees and B) $\alpha = 22$ degrees.

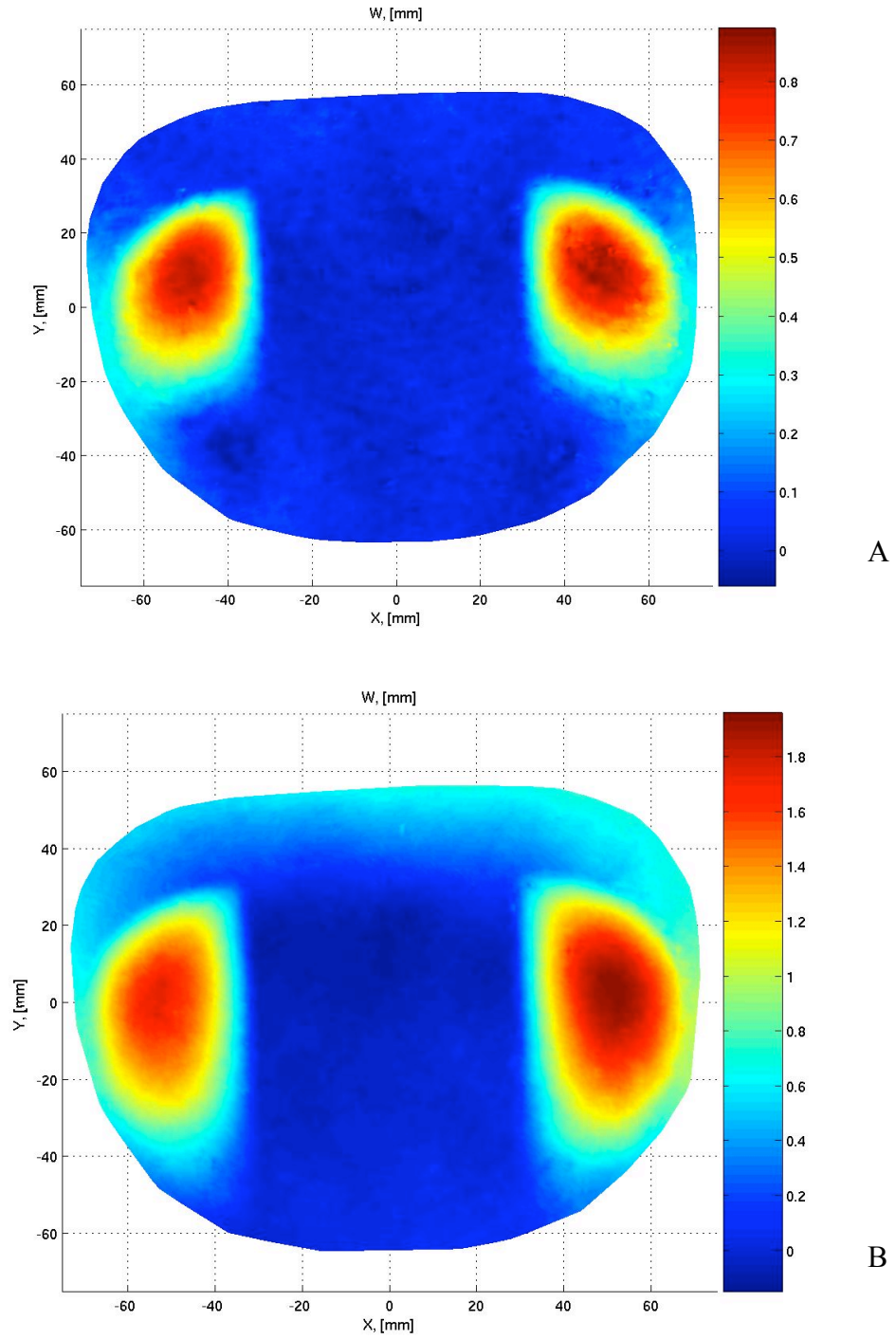


Figure D-8. w contour plots for wing PR07 at $V_\infty = 13$ m/s. A) $\alpha = 4$ degrees and B) $\alpha = 22$ degrees.

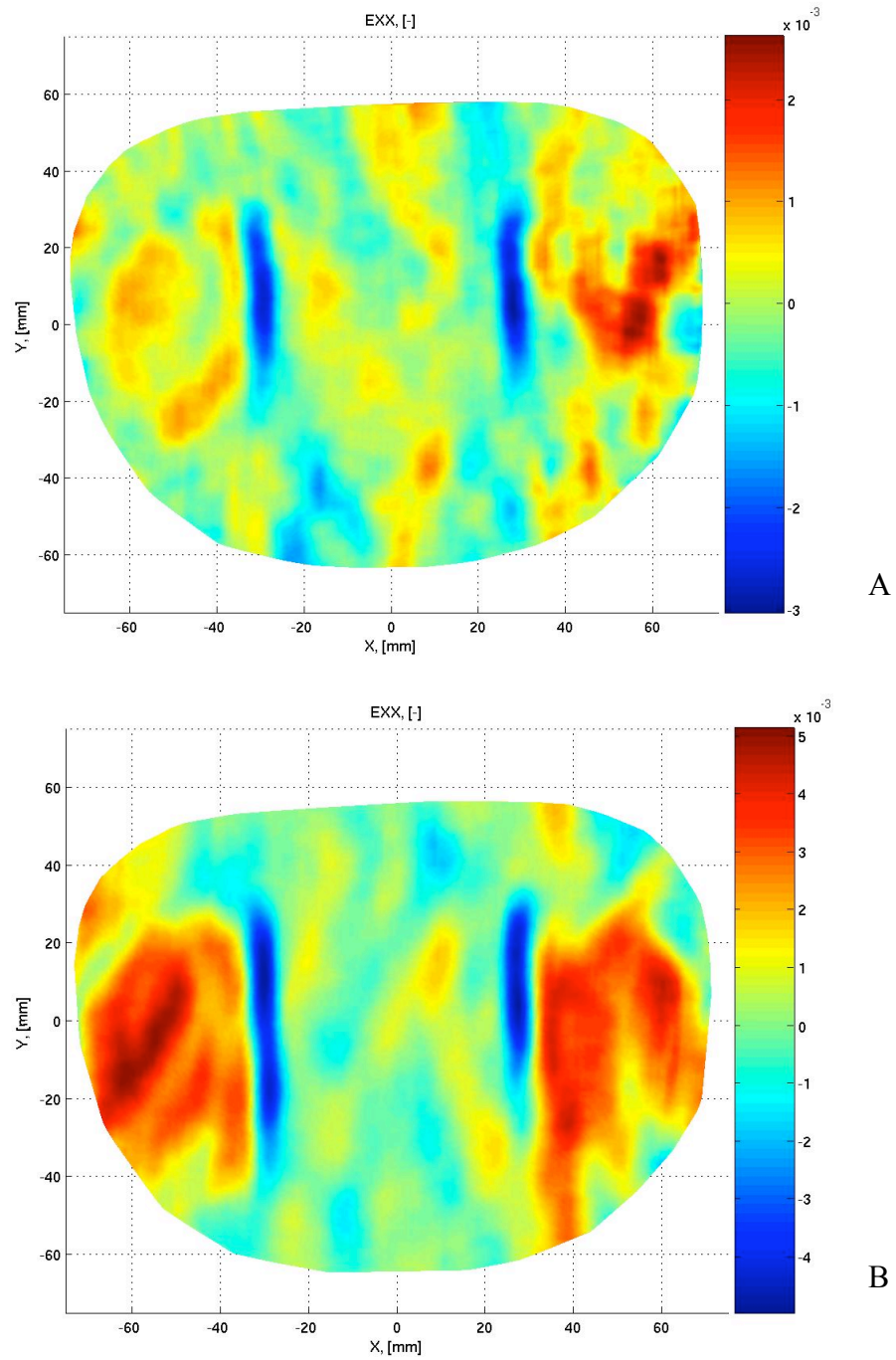


Figure D-9. Contour plots with the strain in the X direction for wing PR07 at $V_\infty = 13$ m/s. A) $\alpha = 4$ degrees and B) $\alpha = 22$ degrees.

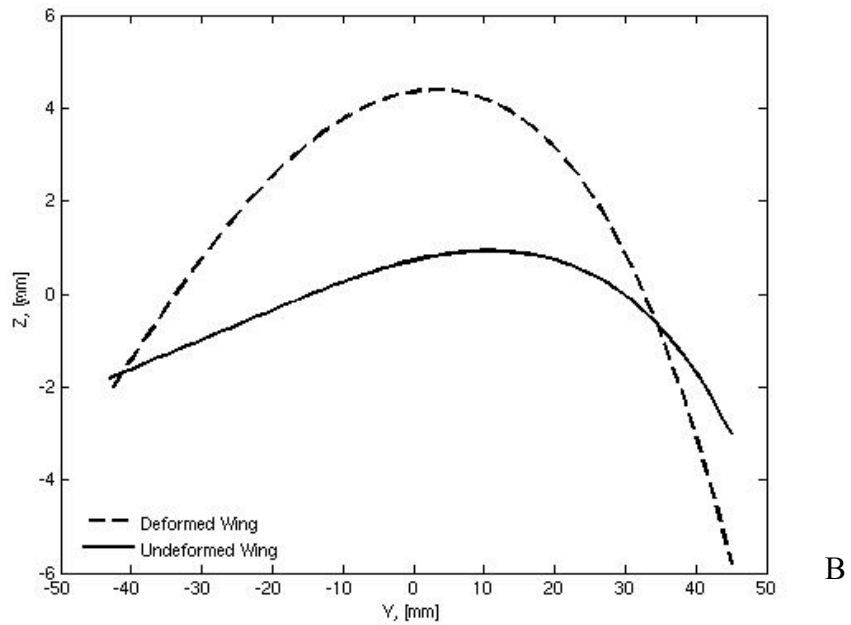
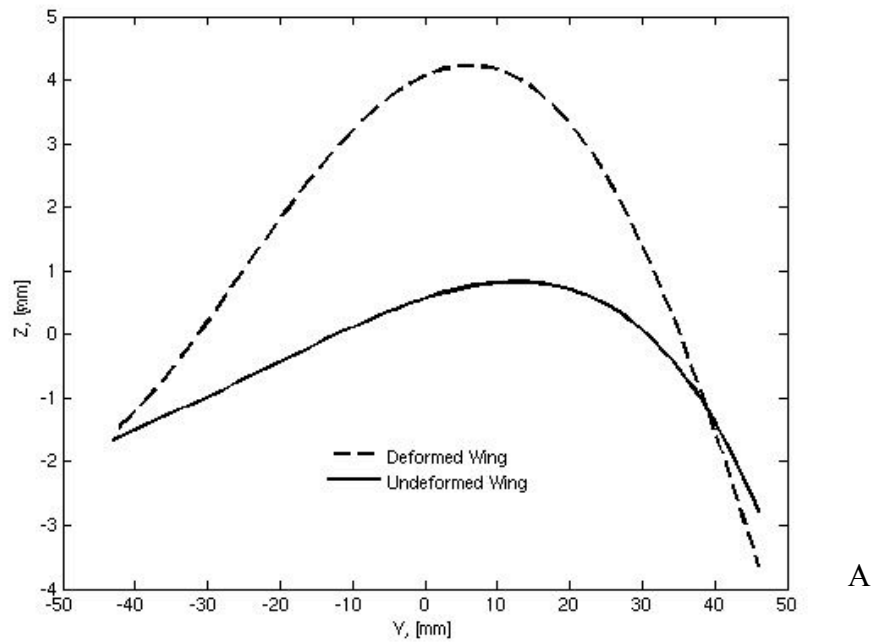


Figure D-10. Undeformed (flow off) and deformed (flow on) wing sections for wing PR12 at $V_\infty = 13$ m/s. A) $\alpha = 4$ degrees and B) $\alpha = 22$ degrees.

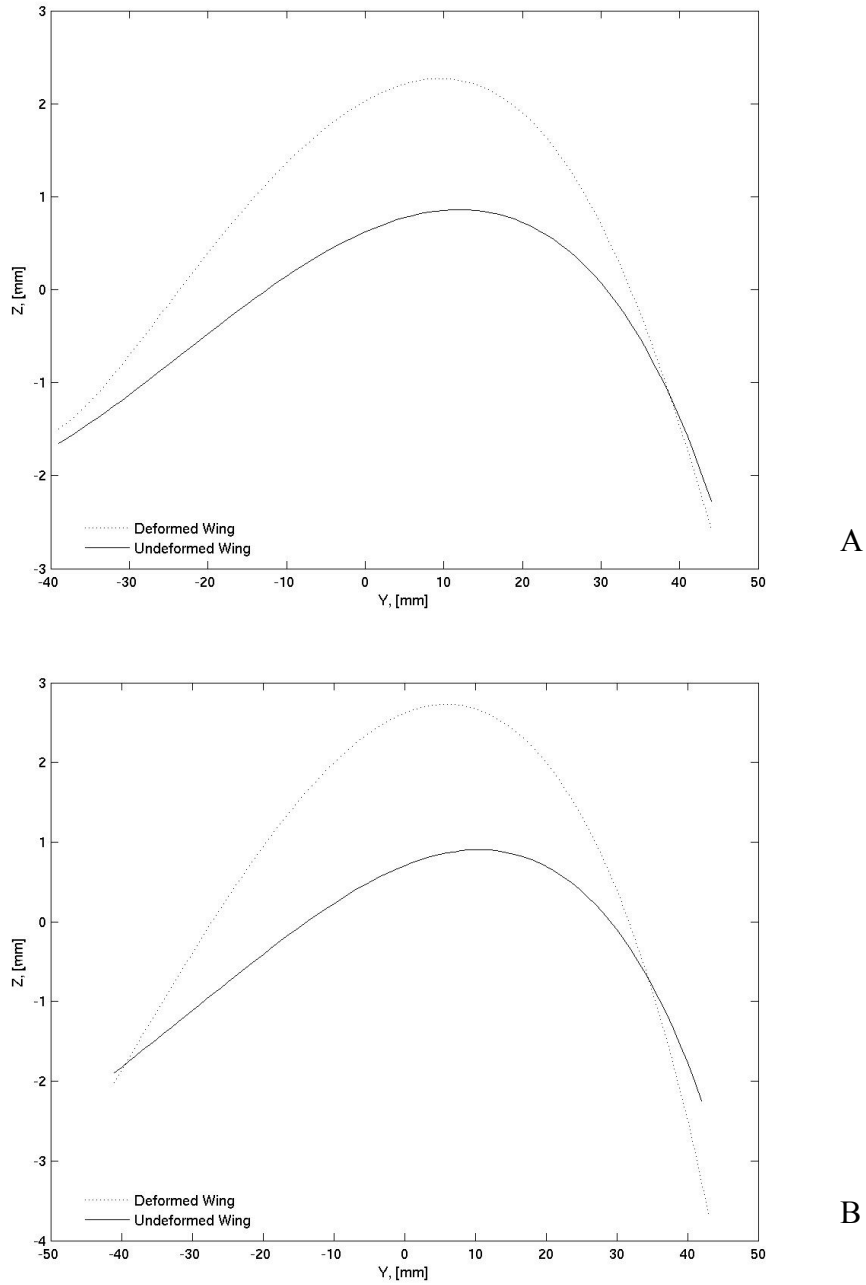


Figure D-11. Undeformed (flow off) and deformed (flow on) wing sections for wing PR12 at $V_\infty = 8$ m/s. A) $\alpha = 4$ degrees and B) $\alpha = 22$ degrees.

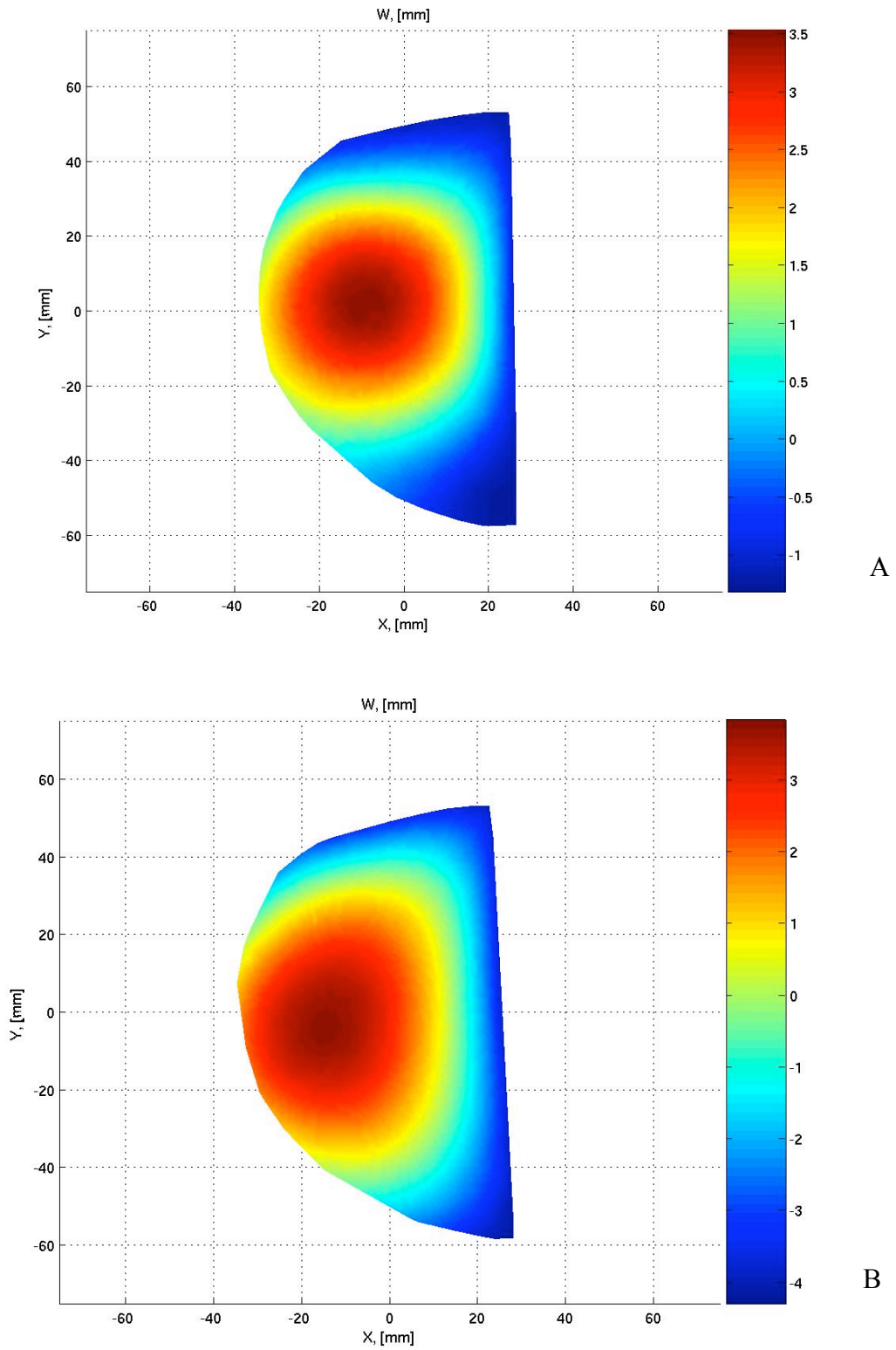


Figure D-12. w contour plots for wing PR12 at $V_\infty = 13$ m/s. A) $\alpha = 4$ degrees and B) $\alpha = 22$ degrees.

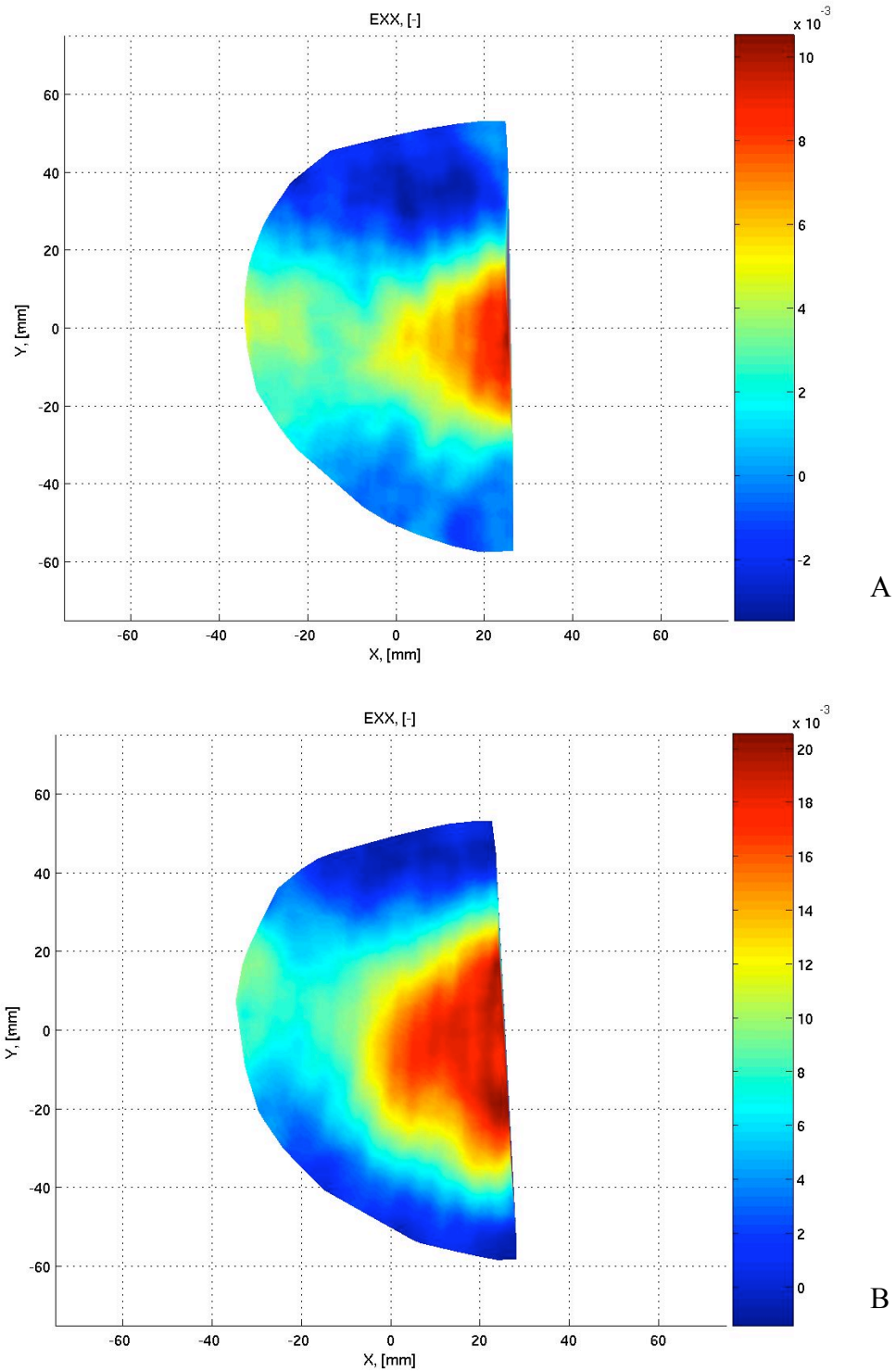


Figure D-13. Contour plots with strain in the X direction for wing PR12 at $V_\infty = 13$ m/s.
A) $\alpha = 4$ degrees and B) $\alpha = 22$ degrees.

Figure D-14 shows that indeed for the PR wings the wing twist, thus the washout effect, was negligible.

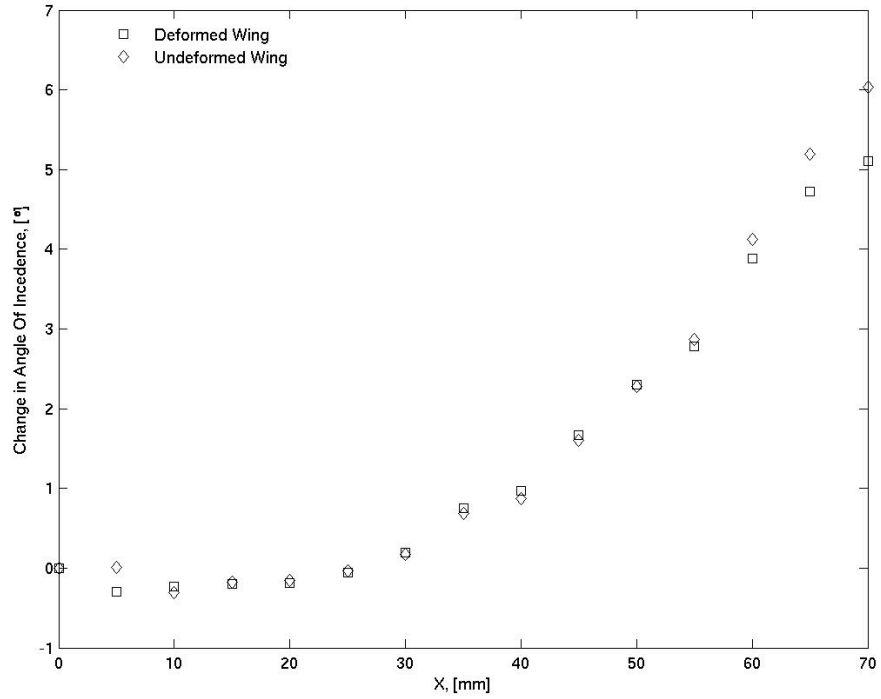


Figure D-14. Local angle of incidence distribution in the X direction from centerline for wing PR07 at $\alpha = 20$ degrees and at $V_\infty = 13$ m/s.

APPENDIX E
SYMBOLS

E.1 English Symbols

A	Wind tunnel cross section area [m ²]
a_i	Constant model parameters
A_{ij}	Sting balance calibration curve slope [V/N]
AR	Wing aspect ratio
b	Wing span [m]
c	Wing chord [m]
\bar{C}	Mean aerodynamic chord [m]
C_r	Root chord [m]
C_D	Drag coefficient
C_{dc}	Cross flow coefficient
$C_{D,u}$	Uncorrected measured drag coefficient
C_{D_0}	Drag coefficient at zero lift
$C_{l,u}$	Rolling moment coefficient
C_L	Lift coefficient
$C_{L\alpha}$	Lift curve derivative respect to angle of attack or slope [1/deg]
$C_{L\delta}$	Lift curve derivative respect to elevator deflection [1/deg]
$C_{L,u}$	Uncorrected measured lift coefficient
C_{L_0}	Lift coefficient at zero angle of attack

C_m	Pitching moment coefficient
$C_{m\alpha}$	Pitching moment coefficient derivative respect to angle of attack [1-deg]
$C_{m\delta}$	Pitching moment coefficient derivative respect to elevator angle [1-deg]
$C_{m,u}$	Uncorrected measured pitching moment coefficient
C_{m_0}	Pitching moment coefficient at zero lift
$C_{n,u}$	Yawing moment coefficient
C_p	Propeller power coefficient
C_T	Propeller thrust coefficient
C_X	Force coefficient in the X direction
$C_{y,u}$	Side force coefficient
C_Z	Propeller force coefficient in the Z direction
D	Drag [N], Propeller diameter [m]
ΔD	Difference between drag with and without propeller
e	Modeling error
E	voltage motor setting [Volt]
E	Strain tensor
E_{VIC}	VIC experimental displacement error [mm]
ΔL	Difference between lift with and without propeller [N]
F_i	Force applied on the i th channel of the sting balance [N]
h	Wind tunnel test section height [m]
H	Modulus characterizing asymmetry of reciprocal deformations
i_w	Wing's angle of incidence [deg]
$(i_w)_{max}$	Wing's maximum angle of incidence [deg]

J	Propeller advance ratio
k	Induced drag factor
k_1	Body shape factor for wind tunnel corrections
k_3	Streamline body factor for wind tunnel corrections
L	Lift [N]
\mathcal{L}	Rolling moment [Nm]
M	Pitching moment [Nm]
m	Number of terms in the model
MT	VIC magnification factor
n	Propeller speed [rounds per minute], load factor [g]
N	Force in the Z axis [N], population of experimental results
\mathcal{N}	Yawing moment [Nm]
P	Propeller power [W]
\hat{p}_i	Functions of the independent variables
q	Dynamic pressure [N/m ²]
R_i	Signal of ith channel of the sting balance with no airflow [Volt]
S_i	Signal of ith channel of the sting balance [Volt]
S_w	Wing reference area [m ²]
t	Airfoil camber [m]
t/c	Airfoil camber to chord ratio
T	Propeller thrust [N]
T_r	Resultant propeller thrust [N]
u	Displacement in the X direction [mm]

v	Displacement in the Y direction [mm], experimental dependent variable
\hat{y}	Estimated dependent variables
\bar{y}	Average value of the dependent variables
V_B	Body volume [m ³]
V	Sting balance signal with load [Volt]
VT	Tare balance signal [Volt]
V_∞	Free stream velocity [m/s]
w	Displacement in the Z direction [mm]
\mathcal{X}	Force in the X axis [N]
X_{ac}	Location of ac normalized with c
\bar{X}_{ac}	Location of ac normalized to c/4
X, Y, Z	body coordinates [m]
x, y, z	wind coordinates [m]
X_d, Y_d, Z_d	deformed or translated body coordinates [m]
Υ	Side force [N]

E.2 Greek Symbols

α	Angle of attack
α_E	Actual of final corrected angle of attack
α_u	Uncorrected measured angle of attack
β_0	VIC object displacement accuracy [m]
β_1	VIC image displacement accuracy
δ	Elevator deflection angle [degrees]

ε	Strain
$\varepsilon_{sb,B}$	Solid blockage correction factor for the body
$\varepsilon_{sb,T}$	Total solid blockage effect
$\varepsilon_{sb,w}$	Solid blockage correction factor for the wing
ε_T	Sum of total solid blockage effect and wake blockage correction factor
ε_w	Wake blockage correction factor
η_c	Combined propeller efficiency
η_0	VIC object speckle dimension [m]
η_1	VIC image speckle dimension [pixels]
λ_i	Principal stretch
ρ	Air density
σ	Streamline curvature correction factor
σ_p^2	Upper-bound estimate of prediction mean squared error
σ_0^2	Maximum prediction mean squared error
τ_1	Wind tunnel correction factor

E.3 Acronyms

ac	Aerodynamic Center
AFIT	Air Force Institute of Technology
AOA	Angle of Attack
AOI	Area of Interest (for visual image correlation)
BR	Batten reinforced wing
CFD	Computational fluid dynamics

CG	Center of gravity
DAQ	Data acquisition
DC	Direct current
FEA	Finite element analysis
FOV	VIC field of view
HAARV	High angle of attack research vehicle
HIL	Hardware in the loop
LAD	Least absolute deviations
LAR	Low Aspect Ratio
LARC	Langley Research Center
LRN	Low Reynolds Number
LS	Least squares
LSE	Linear stochastic estimation
LSWT	Low speed wind tunnel
MDOE	Modern design of experiment
MSE	Mean squared error
OFAT	One factor at a time
PMI	Projection moire' interferometry
POD	Proper orthogonal decomposition
PR	Perimeter reinforced wing
PSE	Predicted squared error
R	Rigid wing
RSM	Response surface modeling

SS	VIC subset size [pixels ²]
TLS	Trimmed least squares
UCAV	Unmanned combat aerial vehicle
VIC	Visual image correlation
V/STOL	Vertical/short takeoff and landing

E.4 Subscripts and superscripts

AV	average value
i	i th element of an array

LIST OF REFERENCES

1. Prandtl, L., Tietjens, O.G., and Hartjog, J. Applied Hydro and Aeromechanics, McGraw-Hill Book Company, Inc., London, England, 1934.
2. Zimmerman, C. H., "Aerodynamic Characteristics of Several Airfoils of Low Aspect Ratio," NACA Technical Report TN 539, 1935.
3. Winter, H., "Flow Phenomena on Plates and Airfoils of Short Span," NACA Technical Report TN 798, 1932.
4. Hoerner, S. F., Fluid Dynamic Drag, published by the Author, Brick Town, NJ, 1975.
5. Hoerner, S. F., Fluid Dynamic Lift, published by Mrs. Liselotte A. Hoerner, Brick Town, NJ, 1975.
6. Bartlett, G. E., Vidal, R. J., "Experimental Investigation of Influence of Edge Shape on the Aerodynamic Characteristics of Low Aspect Ratio Wings at Low Speeds," Journal of Aeronautical Sciences, Volume 22(8), 1955, pp. 517-533.
7. Jacobs, E. N., "Airfoil Section Characteristics," NACA Technical Report TN 586
8. Schmitz, F., "Aerodynamics of the Model Airplane, part 1, Airfoil Measurements," N70-39001.
9. Riegels, F. W., Aerofoil Sections, Butterworths, London, 1961.
10. Selig, M. S., Summary of Low Speed Airfoil Data, Volume 1, 2 and 3, SoarTech Publications, Virginia Beach, VA.
11. Carmichael, B. H. "Low Reynolds Number Airfoil Survey": Volume 1, NASA CR165803, Nov, 1981.
12. Pellettier, A., Mueller. T. J., "Low Reynolds Number Aerodynamics of Low-Aspect Ratio, Thin/flat/cambered-plate Wings," Journal of Aircraft, Volume 37(5), 2000, pp. 825-832.
13. Mueller, T. J., " Aerodynamic Measurements at Low Reynolds Numbers for Fixed Wing MAVs," RTO/VKI Special Course, VKI, Belgium, 1999.

14. Torres, G.E., and Mueller, T.J., "Aerodynamic Characteristics of Low Aspect Ratio Wings at Low Reynolds Numbers," MAE Department, University of Notre Dame 2000.
15. Torres, G. E., "Aerodynamics of Low Aspect Ratio Wings at Low Reynolds Numbers With Applications to Micro Air Vehicle Design," Ph.D. Dissertation, Department of Aerospace and Mechanical Engineering, University of Notre Dame, Indiana, April 2002.
16. Laitone, E. V., "Wind Tunnel Tests of Wings and Rings at Low Reynolds Numbers," Fixed and Flapping Wing Aerodynamics for Micro Air Vehicle Applications, Volume 195, Progress in Astronautics and Aeronautics, Edited by Mueller, T. J, Published by AIAA, Reston, VA, pp. 83-90.
17. Lian, Y., and Shyy, W., "Three Dimensional Fluid Structure Interactions of a Membrane Wing for MAV Applications", AIAA 2003-1726.
18. Viieru, D., Lian, Y., Shyy, W., and Ifju, P., " Investigation of Tip Vortex on Aerodynamic Performance of a Micro Air Vehicle," AIAA Paper 2003-3597.
19. Viieru, D., Albertani, R., Shyy, W., and Ifju, P., "Effect of Tip Vortex on Wing Aerodynamics of Micro Aerial Vehicles," 22nd AIAA Applied Aerodynamics Conference and Exhibit, Paper 2004-4971, Aug. 2004.
20. Kellogg, M. I., Bowman, W. J., "Parametric Design Study of the Thickness of Airfoils at Reynolds Numbers from 60,000 – 150,000," 42nd AIAA Aerospace Sciences Meeting and Exhibit, Paper 2004-1054, 5-8 January 2004, Reno, NV.
21. Boughton, S. E., Attari, T., Kozak, J., "Comparison and Validation of Micro Air Vehicle Design Methods," 42nd AIAA Aerospace Sciences Meeting and Exhibit, Paper 2004-0406, 5-8 January 2004, Reno, NV.
22. Igreeley, D. S., Kirkman, K. L., Drew, A. L., and Cross-Whiter, J., "Scientific Sail Shape Design," Proceedings for The Ninth Chesapeake Sailing Yacht Symposium, Annapolis, MD, March 11, 1989.
23. Shyy, W., Smith, R., "A Study of Flexible Airfoil Aerodynamics with Application to Micro Air Vehicles," AIAA Paper 97-1933.
24. Sugimoto, T., and J. Sato, "Aerodynamic Characteristics of Two-Dimensional Membrane Airfoils," Transactions of the Japan Society of Space Sciences, Volume 34, pp. 88-100, 1991.
25. Shyy, W., Klevebring, F., Nilsson, M., Sloan, J., Carroll, B., Fuentes, C., "Rigid and Flexible Low Reynolds Number Airfoils," Journal of Aircraft, Volume 36, No. 3, May-June 1999.

26. Lian, Y., Shyy, W., and Ifju, P. G., "Membrane Wing Model for Micro Air Vehicles," *AIAA Journal*, Volume 41, No. 12, Dec. 2003, pp.2492-2494.
27. Lian, Y., and Shyy, W., "Three Dimensional Fluid Structure Interactions Of A Membrane Wing For MAV Applications", AIAA 2003-1726.
28. Waszak, M., Jenkins, L., and Ifju, P., "Stability and Control Properties of an Aeroelastic Fixed Wing Micro Aerial Vehicle," AIAA Atmospheric Flight Mechanics Conference, Paper 2001-4005, August 2001.
29. Marchaj, C., A., *Sailing: Theory and Practice*, Dodd Mead & Co., New York, 1964.
30. Fink, M., P., "Full-Scale Investigation of the Aerodynamic Characteristics of a Model Employing a Sailwing Concept," NASA TN D-4062, Langley Research Center, Langley Station, Hampton, Va., July 1967.
31. Sneyd, A. D., "Aerodynamic Coefficients and Longitudinal Stability of Sail Airfoils," *Journal of Fluid Mechanics*, Volume 149, pp. 127-146, 1984.
32. Waszak M. R., and John B. Davidson J. B., and Ifju P., "Simulation and Flight Control of an Aeroelastic Fixed Wing MAV" AIAA Paper 2002-4875.
33. DeLuca, E., M., "Experimental Investigation into the Aerodynamic Performance of both Rigid and Flexible Wing Structured MAVs", MS Thesis, A.F. Institute of Technology.
34. Ettinger, S. M., Nechyba, M. C., Ifju, P. G., and Waszak, M. "Vision-Guided Flight Stability and Control for Micro Air Vehicles," *IEEE Int. Conf. on Intelligent Robots and Systems*, Volume 3, 2002, pp. 2134-40.
35. Jenkins, D. A., Ifju., P. J., Abdulrahim, M., and Olipra, S. "Assessment of Controllability of Micro Air Vehicles," MAV Conference, Bristol, UK, April 2001.
36. Abdulrahim, M., Garcia, H., Lind, R., "Flight Characteristics of Shaping the Membrane Wing of a Micro Air Vehicle," *Journal of Aircraft*, Volume 42, No. 1, January-February 2005.
37. Prandtl, L., "Mutual Influence of Wings and Propeller," NACA Technical Notes No. 74, Extract from The First of the Gottingen Aerodynamic Laboratory, Chapter IV, Sec. 6, December 1921.
38. Von Mises. R., *Theory of Flight*, Dover Publications Inc., New York, New York, 1959.
39. McCormick, B. W., *Aerodynamics, Aeronautics, and Flight Mechanics*, John Wiley & Sons, New York, 1979.

40. Perkins, C., and Hage, R. Airplane Performance Stability and Control, John Wiley & Sons, New York, 1950.
41. Kuhn, R. E., Draper, J. W., "Investigation of the Aerodynamic Characteristics of a Model Wing-propelled Combination and of the Wing and Propeller Separately at Angles of Attack up to 90 Degrees" NACA Report 1263.
42. Pendley, R., E., "Effect of Propeller- Axis Angle of Attack on Thrust Distribution over the Propeller Disk in Relation to Wake-Survey Measurement of Thrust," NACA Wartime Report, ARR No. L5J02b.
43. Trebble, W. J. G., "Techniques for the Aerodynamic Testing of V/STOL Models," The Aerodynamic of V/STOL Aircraft Lecture Series, Advisory Group for Aerospace Research and Development, Organisation du Traite de l' Atlantique Nord, AD 688 921, Published by AGARD and von Karman Institute, Rhode-Saint-Genese, Belgium, May 1968.
44. Crowther, W., J., "Perched Landing and Takeoff for Fixed Wing UAVs," Paper RTO-MP-052, AC/323(AVT-049)TP/37, RTO AVT Symposium on "Unmanned Vehicles (UV) for Aerial, Ground and Naval Military Operations, Ankara, Turkey, October 9-13, 2000.
45. Polhamus, E., C., "A concept of the Vortex Lift of Sharp-Edge Delta Wings based on a Leading-Edge-Suction Analogy," NASA Technical Report TN D-3767, 1966.
46. Polhamus, E., C., "Prediction of Vortex-Lift Characteristics by a Leading-Edge-Suction Analogy," Journal of Aircraft, Volume 8(4): 193-199, 1971.
47. Raymer, D., P., Aircraft Design: A Conceptual Approach, AIAA Education Series, Washington, D.C., 1992.
48. Hoak, D., E., Finck, R., D., U.S.A.F Stability and Control DATCOM, McDonnell Douglas Corporation, 1978.
49. Draper, N., R., Applied Regression Analysis, John Wiley & Sons, New York, 1966.
50. Dodge, Y., Jureckova, J., Adaptive Regression, Springer-Verlag, New York, 2000.
51. Steffen, J., "Response Surface Modeling of Combined-Cycle Propulsion Components Using Computational Fluid Dynamics," NASA TM-2002-211379, AIAA Paper 2002-0542, Glenn Research Center, Cleveland, Ohio, March 2002.
52. Giunta, A., A., Watson, L., T., "A Comparison of Approximation Modeling Techniques: Polynomial Versus Interpolating Models," AIAA Paper 98-4758.
53. Morelli, E., A., "Global Nonlinear Aerodynamic Modeling Using Multivariate Orthogonal Functions," Journal of Aircraft, Volume 32, No. 2, March-April 1995.

54. Morelli, E., A., "Global Nonlinear Parametric Modeling with Application to F-16 Aerodynamics," NASA Langley Research Center, Hampton, Virginia.
55. DeLoach, R., "Applications of Modern Experiment Design to Wind Tunnel Testing at NASA Langley Research Center," AIAA Paper 98-0713, January 1998.
56. Morelli, E., A., DeLoach, R., "Wind Tunnel Database Development using Modern Experiment Design and Multivariate Orthogonal Functions," AIAA Paper 2003-0653, 41st AIAA Aerospace Sciences Meeting and Exhibit, Reno, NV, January 6-9, 2003.
57. Wainwright, S. A., Biggs, W. D., Currey, J. D., and Gosline J. M., *Mechanical Design in Organisms*, Princeton University Press, Princeton, N, J., 1976.
58. Pawlowski, K. J., Belvin, H. L., Raney, D. L., Su, J., Harrison, J. S., Siochi, E. J., "Electrospinning of a Micro Air Vehicle wing skin," *Polymer Communication*, Volume 44 (2003), pp. 1309-1314, Elsevier Publishing, November 2002.
59. Schmit R.F. , Glauser M. N., and Gorton S. A., "Low Dimensional Tools For Flow-Structure Interaction Problems: Application To Mavs", AIAA 2003-06.
60. Zheng, L., Ramaprian, B.R., "A Piezo-Electrically Actuated Wing for a Micro Air Vehicle," AIAA Fluids 2000, AIAA 2000-2302, Denver, CO, 19-22 June 2000.
61. Combes, S. A., Daniel, T. L., "Flexural stiffness in insect wings II. Spatial distribution and dynamic wing bending," *The Journal of Experimental Biology*, Volume 206, pp. 2989-2997, The Company of Biologist Ltd, 2003.
62. Daniel, T. L., Combes, S. A., "Flexible Wings and Fins: Bending by Inertial or Fluid-dynamic Forces?," Annual Meeting of the Society for Integrative and Comparative Biology, Symposium Dynamics and Energetics of Animal Swimming and Flying, Paper 42, pp. 1044-1049, Anaheim, CA, 2-6 January 2002.
63. Combes, S. A., Daniel, T. L., "Into Thin Air: Contributions of Aerodynamic and Inertial-elastic Forces to Wing Bending in the Hawkmoth *Manduca Sexta*," *The Journal of Experiment Biology*, Volume 206, pp. 2989-2997, The Company of Biologist Ltd., 2003.
64. Stepan, S. J., "Flexural stiffness patterns of butterfly wings (Papilionoidea)," *Journal of Research on the Lepidoptera*, Volume 35, pp. 61-77, 1996 (2000).
65. Sensenig, A.T., and Shultz, J.W., "Mechanics of Cuticular Elastic Energy Storage in Leg Joints Lacking Extensor Muscles in Arachnids," *The Journal of Experimental Biology*, Volume 206, pp. 771-784, The Company of Biologist Ltd., 2001.
66. Pennycuick, C. J., Lock, A., "Elastic Energy Storage in Primary Feather Shafts," *Journal of Experimental Biology*, Volume 64, 1976, pp. 667-689.

67. Pornsin-Sirirak, T. N. and Tai, Y.C., "Flexible Parylene Actuator For Micro Adaptive Flow Control".
68. Ho, S., Nassefa, H., Pornsinsirirak, N., Yu-Chong Taib, Chih-Ming Ho, "Unsteady Aerodynamics and Flow Control for Flapping Wing Flyers," *Progress in Aerospace Sciences*, Volume 39, pp. 635-681, 2003.
69. Broeren, A. P., Bragg, M. B., "Unsteady Stalling Characteristics of Thin Airfoils at Low Reynolds Number," *Fixed and Flapping Wing Aerodynamics for Micro Air Vehicle Applications*, Volume 195, pp. 191-213, *Progress in Astronautics and Aeronautics*, Edited by Mueller, T. J., Published by AIAA, Reston, VA.
70. Cummings, R. M., Morton, S. A., Siegel, S. G., and Bosscher, S., "Numerical Prediction and Wind Tunnel Experiments for a Pitching Unmanned Combat Air Vehicle," 41st Aerospace Sciences Meeting, AIAA, Reno, NV, Jan. 2003.
71. Brandon, J. M., "Dynamic Stall Effects and Applications to High Performance Aircraft," NASA Langley Research Center, Hampton, Virginia.
72. Burner, A. W., Fleming, G. A., Hoppe, J. C., "Comparison of Three Optical Methods for Measuring Model Deformation," 38th AIAA Aerospace Sciences Meeting and Exhibit, Paper 2000-0835, 10-13 January 2000, Reno, NV.
73. Fleming, G. A., Bartram, S. M., Waszak, M. R., and Jenkins, L. N., "Projection Moiré Interferometry Measurements of Micro Air Vehicle Wings," SPIE Paper No. 4448-16.
74. Mooney, M., "A Theory of Large Elastic Deformation," *Journal of Applied Physics*, pp. 582-592, January 1940.
75. Fulop, W., "The Rubber Membrane and the Solution of Laplace's Equation," *British Journal of Applied Physics*, Volume 6, pp. 21-23, January 1955.
76. Yang, W., H., Hsu, K., H., "Indentation of a Circular Membrane," *Journal of Applied Mechanics*, Paper No. 70-WA/APM-33, 227-230, March 1971.
77. Wan, K., Liao, K., "Measuring Mechanical Properties of Thin Flexible Films by a Shaft-Loaded Blister Test," *Thin Solid Films*, Volume 352 (1999), pp. 167-172, May 1999.
78. Liu, K., K., Ju, B., F., "A Novel Technique for Mechanical Characterization of Thin Elastomeric Membrane," *Journal of Physics D: Applied Physics*, Volume 34 (2001), pp. 91-94, July 2001.
79. Albertani, R., Boria, F., Bowman, S., Claxton, Crespo, A., Francis, C., Ifju, P., Johnson, B., Jung, S., Lee, K. H., Morton, M., Sytsma, M., "Development of Reliable and Mission Capable Micro Air Vehicles," University of Florida, MAE Dept., 9th International MAV Competition, South Korea, 2005.

80. Ifju, P. G., Ettinger, S., Jenkins, D. A. and Martinez, L., "Composite Materials for Micro Air Vehicles," SAMPE Conference 2001, Long Beach, CA, May 6-10, 2001.
81. Uccelli, A., *I libri del volo di Leonardo da Vinci*, Hoepli In., pp. XXVIII, 132, 1952.
82. Moolman, V., *The Road to Kitty Hawk*, Time Life Books, Alexandria, Virginia, 1980.
83. "Calibration and Evaluation of Multicomponent SG Balance," NASA Interlaboratory Force Measurements Group Meeting Report, JPL, April 1964.
84. Barlow, J. B., Rae, W. H., and Pope, A., *Low Speed Wind Tunnel Techniques*, John Wiley & Sons, New York, 1999.
85. *Calibration and Use of Internal Strain Gage Balances with Application to Wind Tunnel Testing, Recommended Practice R-091-2003*, AIAA, Reston, Virginia, 2003.
86. Jacobs, E. N., "Sphere Drag Tests in the Variable Density Wind Tunnel," NACA Technical Note No. 312, 1947.
87. Kline, S. J., and McClintock, F. A. "Describing Uncertainties in Single Sample Experiments," *Mechanical Engineering*, Volume 75, No. 1, January, 1953.
88. Pankhurst, P. C., Holder, D. W., *Wind Tunnel Technique*, Sir Isaac Pitman & Sons, Ltd., London, 1952.
89. Peters, W. H. and Ransom, W. F., "Digital Imaging Techniques in Experimental Stress Analysis", *Optical Engineering*, Volume 21(3), pp. 427-431, 1982
90. Sutton, M. A., Cheng, M., Peters, W. H., Chao, Y. J. and McNeill, S. R., "Application of an Optimized Digital Correlation Method to Planar Deformation Analysis", *Image and Vision Computing*, Volume 4(3), pp. 143-151, 1986.
91. Sutton, M. A., Turner, J. L., Bruck, H. A., Chae, T. A., " Full Field Representation of the Discretely Sampled Surface Deformations for Displacement and Strain Analysis, " *Experimental Mechanics*, 1991: Volume 31(2): pp.168-77.
92. Helm, J. D., McNeill, S. R. and Sutton, M. A., "Improved 3-D Image Correlation for Surface Displacement Measurement", *Optical Engineering*, Volume 35(7), pp. 1911-1920, 1996.
93. Vic-3D Digital Image Correlation Software, Correlated Solutions, Inc.
94. Schreirer, H. W., Braasch, J. R. and Sutton, M. A., "Systematic Errors in Digital Image Correlation Caused by Gray-value Interpolation", *Optical Engineering*, Volume 39(11), pp. 2915-2921, 2000.

95. Albertani, R., Stanford, B., Hubner, J. P., and Ifju, P., "Characterization of Flexible Wing MAV's: Aeroelastic and Propulsion Effects on Flying Qualities," AIAA Atmospheric Flight Mechanics Conference, San Francisco, CA, 2005.
96. Albertani, R., Stanford, B., Hubner, J. P., and Ifju, P., "Aerodynamic Characterization and Deformation Measurements of a Flexible Wing Micro Air Vehicle," SEM Annual Conference, Portland, OR, 2005.
97. Albertani, R., Stanford, B., Hubner, J. P., Lind, R. and Ifju, P., "Experimental analysis of deformation for flexible-wing Micro Air Vehicles," AIAA SDM Conference, Austin, TX, 2005.
98. Albertani, R., Hubner, J. P., Ifju, P.G., Lind, R., and Jackowski, J., "Experimental Aerodynamics of Micro Air Vehicles," SAE World Aviation Congress and Exhibition, Reno, NV, 2004.
99. Hooker, J. R., Burner, A. W., and Valla, R., "Static Aeroelastic Analysis of Transonic Wind Tunnel Models using FE Methods," AIAA Paper 97-2243.
100. Burner, A. W., Wahls, r. a., Goad, W. K., "Wing Twist Measurements at the National Transonic Facility," NASA Technical Memorandum 110229, Langley Research Center, Hampton, Virginia, February 1996.
101. Blakelock, J. H., Automatic Control of Aircraft and Missiles, John Wiley & Sons, New York, 1965.
102. Selig, M. S., McGranahan, B. D., "Wind Tunnel Aerodynamic Tests of Six Airfoils for Use on Small Wind Turbines," NREL Report NREL/SR-500-34515, October 2004.
103. Holman, J., P., Experimental Methods for Engineers, 7th Edition, Mc Graw Hill, New York, 2001.
104. Box, G., E., P., Hunter, W., G., Hunter, J., S., Statistics for Experimenters An Introduction to Design, Data Analysis and Model Building, John Wiley & Sons, New York, 1978.
105. Farlow, S., J., Self-Organizing Methods in Modeling GMDH Algorithms, Marcel Dekker, Inc., New York and Basel, 1984.

BIOGRAPHICAL SKETCH

Roberto Albertani earned his master's degree in aeronautical engineering at the Polytechnic University in Milan, Italy, in 1980. His working career has spanned from subsonic and transonic experimental aircraft aerodynamics, aerodynamics of propulsion, and wind turbines structural design, fabrication and operations. He has been actively involved in the design and manufacturing of US Navy composite mine hunters and composite RIB (Rigid Inflatable Boat) for the US SOCOMM, as well as high technology composite sail boats and large wind turbine blades. He has also been engaged in numerous contract specification design projects. The highlight and most enjoyable endeavors of his career were to be staff designer and team senior scientist for two editions of the prestigious America's Cup sailing race and to serve as team member of the Italian sailing team at the 1996 Olympic Games.